Beyond Gravity ...:

Searches for New Fundamental Interactions

Mark Alan Palmer

A DISSERTATION
PRESENTED TO THE FACULTY
OF PRINCETON UNIVERSITY
IN CANDIDACY FOR THE DEGREE OF
DOCTOR OF PHILOSOPHY

RECOMMENDED FOR ACCEPTANCE
BY THE DEPARTMENT OF PHYSICS

November 1993

Abstract

This thesis describes two pieces of apparatus designed to look for a composition-dependent intermediate-range force. Both instruments employ variants of the torsion balance technique. The first measures static torques by means of a capacitance bridge detection and feedback system. The second employs a dynamic technique which looks for shifts in the period of a torsion pendulum. Results from the static experiment, obtained at a site with a significant slope in the terrain, have been used to place limits on couplings to baryon number, isospin, and linear combinations of the two. For a coupling to baryon number, we find the product of the strength, α_0, and the range, λ, of the interaction to be $\alpha_0\lambda = -0.04 \pm 0.07\,\mathrm{m}$ for $25 < \lambda < 400\,\mathrm{m}$ growing linearly to $\alpha_0\lambda = -0.05 \pm 0.09\,\mathrm{m}$ at $\lambda = 1600\,\mathrm{m}$. For longer ranges, out to 5 km, we find $|\alpha_0| < 10^{-4}$. Constraints on a coupling to isospin are similar in magnitude, while for couplings to $B - L$ and L the limits are approximately 26 times smaller.

The dynamic apparatus has not yet been used to look for new interactions. Non-linear behavior was found to be a major source of systematic error. This behavior may have contributed to one of the early positive results in this field for which no explanation has been found. The behavior was characterized and steps taken to minimize such effects.

The final portion of the thesis is a review of experiments looking for departures from Newtonian gravity over ranges of meters to kilometers. Current limits constrain departures from the Newtonian inverse-square law at terrestrial scales at the level of one part in 10^3 (1σ). There is also no evidence for the existence of any composition-dependent effects at these ranges.

This thesis is fondly dedicated to my son, George David, who arrived while this work was in progress and made my world a much richer place by his presence.

Acknowledgements

There are a great many people who have contributed to this project and to whom I am deeply indebted. Two have been around since the outset. The first is my advisor, Val Fitch, who has generously shared his time and wealth of knowledge over the years. He has impressed me repeatedly with his physical insight and ability to design experimental apparatus—I can only hope that some of his skill rubbed off. Marius Isaila was the other member of our team. His knowledge of electronics and readiness to be a sounding board for various ideas were invaluable throughout my stay at Princeton. I will long retain many fond memories of their fine company in the mountains of Montana during our experimental runs.

Very special thanks are due Bob Dicke who provided many useful suggestions from his own experience with torsion balances and commiserated with us as we encountered many of the same difficulties he had seen in his experiments three decades ago. I would also like to thank Frank Shoemaker for a number of discussions about various aspects of the apparatus design, John Wheeler for sharing his thoughts about gravity, and Mark Dragovan who kindly agreed to read and comment on this tome.

The various pieces of equipment that had to be constructed for these experiments would never have reached completion without the assistance of the Elementary Particles Lab staff: Howard Edwards, Bill Sands, Bill Groom, Bob Klemmer, Al Nelson, Sam Morreale, Dick Rabberman, and Dave Hopkins. In particular Bill Groom played a crucial role in the construction of our precision torsion balances while Howard Edwards and Bill Sands were invaluable sources of information and help where mechanical design was concerned. Several other members of the university staff also contributed significantly. Bart Gibbs freely gave time to discussions about electronic design and testing; Joe Horvath was a major resource for all things chemical; and,

Harry Olson taught me the basics of drawing quartz fibers.

Over the course of this work, several of my fellow students were particularly helpful. Steve Strong and Emory Bunn both took on, as short term projects, some aspect of the development and testing of the apparatus. Doug Wright was a good friend and a great help when it came to generating a thesis in LaTeX. I owe Josh Klein, my office-mate, a special debt of gratitude for insuring that all the paperwork associated with completing this degree reached the proper destinations while I was 800 miles away from Princeton.

I would also like to thank the National Science Foundation for the three years of support it provided through its graduate student fellowship program.

Finally, I would like to thank my wife, Pamela, for her help and support in putting this thesis together.

Contents

Abstract iii

Dedication iv

Acknowledgements v

Table of Contents vii

List of Tables xi

List of Figures xii

I The Princeton Experiments 1

1 Introduction 2
- 1.1 Departures from Newtonian Gravity 4
- 1.2 A Yukawa Potential 5
  - 1.2.1 Composition-Dependent Aspects of the Yukawa Potential . . . 6
  - 1.2.2 The Experimental Value of G 7
- 1.3 Departures from the Inverse-Square Law 7
- 1.4 The Role of the Eötvös Experiment 9
  - 1.4.1 Principles of the Eötvös Experiment 9
  - 1.4.2 The Reanalysis of the Eötvös Experiment 13
    - 1.4.2.1 The Eötvös Data 14
    - 1.4.2.2 Some Details of the Reanalysis 15
- 1.5 New Experimental Efforts 20

2 Theoretical Speculations 24
- 2.1 Some Scalar Interactions 25
  - 2.1.1 Dilatons 25
  - 2.1.2 Axions 27
  - 2.1.3 Axion-like Scalars 30
  - 2.1.4 Other Sources of Scalar Interactions 30
- 2.2 Vector Interactions 31
  - 2.2.1 Hyperphotons 33
  - 2.2.2 A Supersymmetric Vector Boson 34

2.3 Gravity Theories 36
2.3.1 Supergravity 37
2.3.2 A Kaluza-Klein Proposal 39
2.4 Summary and General Phenomonology 40
2.4.1 Ranges 41
2.4.2 Charges 41
2.4.3 Competing Forces 42

3 Some General Considerations 45
3.1 Signal Strength at a Terrestrial Site 46
3.2 Torsion Balance Sensitivity 47
3.2.1 Torsion Fibers 48
3.3 Systematic and Noise Constraints in Torsion Balance Measurements . 49
3.3.1 The Thermal Noise Limit 49
3.3.2 Vibrational Noise 52
3.3.3 Gravitational Gradients 55
3.3.4 Temperature Drifts 58
3.3.5 Gas Perturbations 61
3.3.6 Rotation Effects 61
3.3.7 Magnetic Contamination 62
3.3.8 Electrostatic Effects 64

4 The Static Measurement 65
4.1 The Apparatus 66
4.1.1 The Torsion Balances 67
4.1.2 The Detection and Feedback System 71
4.1.3 Summary of Torsion Balance Parameters 76
4.2 The Experimental Site 77
4.2.1 Baryon Content 78
4.2.2 Isospin Content 80
4.2.3 Other Source Charges 81
4.3 Data 82
4.4 Some Comments on Noise and Systematic Effects 85
4.4.1 Noise 86
4.4.2 Systematic Effects 87
4.4.2.1 Gravitational Gradients 87
4.4.2.2 Signal Drifts and Thermal Effects 88
4.4.2.3 Levelling Effects 89
4.4.2.4 Magnetic Contamination 89
4.4.2.5 Electrostatic Effects 90
4.4.3 Summary of Systematic Effects 91
4.5 Limits on New Interactions 91

5 The Dynamic Measurement **94**
5.1 A Period Measurement with a Spherical Balance 95
5.2 The Apparatus 96
5.2.1 The Torsion Balance Housing 97
5.2.2 The Torsion Balance Prototypes 100
5.2.3 The Suspension and Rotation Systems 101
5.2.3.1 The Quartz Suspension 102
5.2.3.2 The Tungsten Suspension 103
5.2.3.3 Summary 103
5.2.4 The Optical Detection System 103
5.2.5 The Electronics and DAC System 106
5.3 Some Critical Issues for a Dynamic System 110
5.3.1 The Rotation Scheme 110
5.3.2 Operation at Atmospheric Pressure 113
5.3.2.1 Fluid Viscosities and Reynolds' Numbers 113
5.3.2.2 Oscillatory Characteristics of the Fluid 115
5.3.2.3 Relative Damping Times 117
5.3.3 Coupled Modes 119
5.4 A Study of System Nonlinearities 122
5.4.1 A Relative Period Measurement 122
5.4.2 Sources of Nonlinear Effects 124
5.4.3 The Nonlinear Data 127
5.4.4 Implications of the Fiber Nonlinearities 129
5.5 Characteristics of the Current System 130
5.5.1 Noise 130
5.5.2 Systematic Effects 131
5.5.2.1 Nonlinearities with the Quartz Suspension 131
5.5.2.2 Fiber Drifts 132
5.5.2.3 Electronics 132
5.5.2.4 Gravitational Gradients 134
5.5.2.5 Temperature Dependence 135
5.5.2.6 Levelling Changes 137
5.6 Final Comments 137

II A Review of Recent Experiments **140**

6 Composition-Independent Limits **141**
6.1 Composition-Independent Experiments 142
6.2 Gauss' Law Experiments 142
6.3 Modulated Terrestrial Source Experiments 144
6.4 Tower Experiments 146
6.5 Borehole and Ocean Measurements 153

6.6 Summary of Composition-Independent Tests 158

7 Composition-Dependent Limits 161
7.1 Galilean Experiments 162
7.2 Torsion Balance Experiments 165
7.2.1 Terrestrial Source Mass Experiments 166
7.2.2 Local Source Mass Experiments 168
7.2.3 A Modulated Terrestrial Source Experiment 171
7.3 Other Composition-dependent Tests 172
7.3.1 A Beam Balance Experiment 172
7.3.2 Neutral Buoyancy Techniques 172
7.4 Summary of Composition-Dependent Tests 174

8 Conclusion 179
8.1 Torsion Balances 180
8.2 Some General Comments 180

A Pre-1986 Limits 182

B Charge Content of the Stable Elements 187

C Toroid and Sphere Scaling Relations 191

D Thermal Noise in a Period Measurement 193

E The Effects of Fluid Oscillations 196
E.1 A Summary of the Oscillatory Solutions 196
E.2 Fluid Oscillations Within a Hollow Sphere 198

F Scaling of the Nonlinearity 202

List of Tables

1.1 The Eötvös Results 14

3.1 Fiber Material Mechanical Properties 49
3.2 Temperature Coefficients of Fiber Materials 59
3.3 Magnetic Susceptibilities 63

4.1 Electronic Feedback Parameters 75
4.2 Torsion Balance Parameters 78
4.3 Expected Differential Accelerations for Copper and Polyethylene . . . 80
4.4 Measured and Calculated Gravitational Gradients 83
4.5 Results from the Static Displacement Experiment 86
4.6 Thermal Noise Levels 87
4.7 Sensitivity to Magnetic Effects 90
4.8 Measurement Uncertainties and Systematic Effects 91
4.9 Baryon and B–L Composition Dependent Limits 92

5.1 Torsional Characteristics 104
5.2 Dynamic and Kinematic Viscosities of Air and Helium. 114
5.3 Reynolds' Numbers for Various Modes 114
5.4 Oscillatory Damping Parameters 116
5.5 Relative Lifetimes of the Oscillatory Modes 117
5.6 Amplitude Dependence of the Oscillator Period 128
5.7 Systematic Period Differences 139

6.1 Some Typical Tower Gravity Contributions and Uncertainties 150
6.2 Borehole Gravitational Gradients 154
6.3 Composition Independent Limits 159

7.1 Vector Charge Differences 162

B.1 The Stable Elements and Their Charges 188
B.1 The Stable Elements and Their Charges (*Continued*) 189
B.1 The Stable Elements and Their Charges (*Continued*) 190

List of Figures

1.1 Short Range Interactions and Boreholes 8
1.2 Early Limits on New Interactions 10
1.3 The Principle of the Eötvös Experiment 11
1.4 Baryon Dependence of the Eötvös Data 15
1.5 The Torsion Balance Signal from an Intermediate Range Interaction . 17
1.6 The Ideal Torsion Balance Experiment 18
1.7 Cavendish and Boys Experiments 23

3.1 Gravitational Gradients Near a Cliff 57

4.1 The Static Displacement Apparatus 68
4.2 Toroidal Torsion Balance 69
4.3 Cavendish Balance 70
4.4 Vertical Gradient Balance 71
4.5 Capacitance Bridge Detector 72
4.6 Block Diagram of the Static Displacement Apparatus 73
4.7 Resonant Circuit 76
4.8 Signal Mixing to Give Torsion and Pendulum Outputs 77
4.9 Terrain at Mt. Maurice 79
4.10 Chart Recorder Data 84
4.11 A Fifth Force Data Run 85

5.1 The Dynamic Apparatus 96
5.2 The Torsion Balance Housing 98
5.3 The Spherical Torsion Balance Prototype 100
5.4 The Optical Detection System 104
5.5 Block Diagram of the Dynamic Apparatus 107
5.6 The Four-Quadrant Photodiode Detector 108
5.7 Amplitude Stabilization 111
5.8 Observed Damping of the Torsion Mode 118
5.9 Coupled Modes of the Torsion Pendulum 119
5.10 Linear Damping Errors in the Period Amplitude Dependence Tests . 124
5.11 Nonlinear Effects on the Oscillator Period 126
5.12 Nonlinear Data Obtained with Tungsten 128
5.13 Nonlinearities with Quartz Fibers 132
5.14 Long Term Stabilization of the Torsional Period 133
5.15 Temperature Dependence with Quartz Fibers 136

5.16 Period Data with Quartz Torsion Fiber 138

6.1 Tower Gravity Residuals 152
6.2 Composition-Independent Limits 160

7.1 Baryon Coupling Limits 176
7.2 Isospin Coupling Limits 177
7.3 B–L Coupling Limits 178

A.1 The Cavendish Technique 183

D.1 Phasor Treatment of Noise in the Oscillator Phase 194

Errata:

Beyond Gravity ...:

Searches for New Fundamental Interactions

Mark Alan Palmer

On page 18, in line 2, "Second, Keyser, *et al.*, noted ..." should read "Second, Keyser, *et al.* [40], noted ..."

On page 32, Equation 2.13 should read:

$$F = -\frac{Gm_1m_2}{r^2}\left[1 + \alpha_0\left(\frac{B_1}{\mu_1}\right)\left(\frac{B_2}{\mu_2}\right)\right];$$

in line 15, $\alpha_0 = f^2/Gm_H^2$ should read $|\alpha_0| = f^2/Gm_H^2$; and Equation 2.14 should read:

$$|\alpha_0| < 10^{-5}.$$

On page 42, in line 9, "We follow the convention of Fischbach and ..." should read "We follow the convention of Fischbach, *et al.* [157], and ...", where Reference 157 (to be added on page 212) is given by:

[**157**] E. Fischbach and C. Talmadge, Modern Physics Letters A **4** (1989) 2303–2315.

On page 47, in line 3 of footnote 1, "...the book by Strong [84] which ..." should read "...the book by Strong [84, See chapter 5] which ..."

On page 48, in line 1, "...thus we expect the sensitivity, in general, to scale roughly as ..." should read "...thus we expect the sensitivity, in general, to scale roughly as [88] ..."

On page 63, in lines 2 and 3 of Table 3.3, "...values for ethylene and and long-chain alkanes." should read "...values for ethylene and and long-chain alkanes. Values based on Reference 85."

On page 78, in the second entry of Table 4.2, "0.008 cm diameter ..." should read "0.005 cm diameter ..."

On page 87, in the third to last line, "...of the gravitational, $\partial g_x/\partial z$ field when slightly tilted." should read "...of the gravitational field, $\partial g_x/\partial z$, when slightly tilted."

On page 94, in line 5, "...design work, Boynton, *et al.* [88], had already published ..." should read "...design work, Boynton, *et al.* [135], had already published ..."

On page 112, in line 5, "...amplitude measurement between the four measurement positions result." should read "...amplitude measurement between the four measurement positions."

On page 121, in line 17, "...the magnitude of a mass element..." should read "...the magnitude of the torque on a mass element..."

On page 150, in the third entry of Table 6.1, "...density of 5 kg/cm [113]" should read "...density of 5 kg/cm [113])"; and, in the caption of Table 6.1, "...uncertainty in the measured values." should read "...uncertainty in the measured values (based on References 113-119)."

Pages 153 to 155—*NOTE ADDED:*
The possibility of making a high sensitivity borehole measurement in a region with a characteristic density of about 3.6 g/cm^3 as was mentioned on page 154, in footnote 5, was noted by Stacey, *et al.* [158], in a review of geophysical gravity measurements which also extensively covers the material of pages 153 to 155. Reference 158 (to be added on page 212) is given by:

[158] F.D. Stacey, G.J. Tuck, G.I. Moore, S.C. Holding, B.D. Goodwin and R. Zhou, Reviews of Modern Physics **59** (1987) 157-174.

On page 167, in line 11, "...Boys-technique." should read "...Boys technique."

On page 171, in line 16, there is a missing reference. "We mention one final variant of the torsion balance approach." should read "We mention one final variant of the torsion balance approach [159]." where Reference 159 (to be added on page 212) is given by:

[159] W.R. Bennett, Jr., Physical Review Letters **62** (1989) 365-368.

On page 175, in line 2, "...it was noted by Boynton [88]..." should read "...it was noted by Boynton [135]..."

On page 186, in line 2, "...strengths comparable to gravity disappear." should read "...strengths comparable to gravity disappear [27]."

On page 207, in line 2 of Reference 90, "...Metals Park, Ohio, 1985)." should read "...Metals Park, Ohio, 1985) p. 20-20."

Part I

The Princeton Experiments

Chapter 1

Introduction

During the past two decades, considerable attention has focused on the possibility of a new fundamental interaction which would act over ranges of meters or kilometers. The initial impetus for this interest came from various theoretical speculations which suggested the possibility of finite-range scalar and vector partners of the infinite-range graviton [1–5]. In particular, Fujii extensively considered a scalar-tensor gravity theory where symmetry-breaking arguments suggested a range of several kilometers for the scalar component [3]. Another interesting line of speculation came from Scherk who, working in the context of supersymmetric gravity theories, considered both massive vector and scalar partners of the graviton [6–8]. All of these speculations suggested that a new interaction was likely to have roughly gravitational strength. Thus, its existence would imply noticeable departures from the Newtonian inverse-square law on terrestrial scales. Although none of these theoretical ideas could be considered compelling, they served to highlight the lack of precise experimental constraints on the behavior of gravity at these distances. In fact, it was realized that direct observations could not exclude departures from Newtonian gravity as large as 40% of gravitational strength [9] when the first of these new interactions was suggested.

In order to clarify the situation, several experiments were designed and carried out to test for gravitational departures from $1/r^2$ behavior at laboratory and terrestrial scales (*i.e.*, from centimeters to meters, and meters to kilometers, respectively) [10–

15]. By the early 1980's, attention was drawn especially to geophysical experiments which measured the gravitational acceleration as a function of depth beneath the earth's surface. These measurements suggested a departure from the gravitational inverse-square law at the 1% level over distances of hundreds to a thousand meters.

In 1986, interest in this area was further heightened when Ephraim Fischbach and his colleagues published results from a reanalysis [16] of the Eötvös experiment [17]. The Eötvös experiment (hereafter referred to as EPF) was performed by Baron Roland von Eötvös and his co-workers Pekár and Fekete during the first decade of this century. EPF compared the gravitational acceleration of numerous test bodies towards the earth. The data was originally interpreted as a null result, showing no variation in the gravitational acceleration due to composition, at the level of 5 parts in 10^9. Later refinements of the experiment by Roll, Krotkov and Dicke (RKD) [18] and by Braginsky and Panov (BP) [19] extended this limit to 3 parts in 10^{11} and 9 parts in 10^{13}, respectively, thus establishing the *equivalence principle* for gravitational and inertial mass to great precision. To everyone's surprise, the Fischbach reanalysis revealed a striking dependence of the EPF data on the baryon content of the comparison materials.

The apparent conflict of the reanalyzed EPF data and the later experiments can potentially be resolved by noting that the RKD and BP experiments looked for a composition dependence in the gravitational acceleration of test bodies towards the sun. Thus they were only sensitive to composition-dependent effects acting over distances of 1.5×10^8 km or more. In this light, the correlation found in the EPF data to the baryon content of the comparison materials does not indicate a violation of the equivalence principle for long-range tensor gravity but is consistent with the presence of a new interaction acting over terrestrial scales. Thus the Fischbach group

proposed a new interaction, the *fifth force*, coupling to the baryon content of normal matter as an explanation for both the EPF and anomalous geophysical results. Since the publication of their analysis, over 20 additional experiments have been conducted, and many more proposed, to look for a composition dependence or failure of inverse-square law behavior in gravity.

The first part of this thesis will consider the motivations for new intermediate-range interactions and describe two torsion balance experiments which have been designed and built at Princeton to look for composition-dependent effects. The second part provides a review of the experimental work conducted since 1986 to search for new interactions with ranges of meters to kilometers.

1.1 Departures from Newtonian Gravity

Our basic notions of gravity, in the classical limit, have persisted unchanged since Newton published the *Principia* in 1687 [20]. Newton's law of gravitation contains two fundamental principles

- *That there is a power of gravity tending to all bodies, proportional to the several quantities of matter which they contain.*[1]
- *In two spheres mutually gravitating each towards the other, if the matter in places on all sides round about and equi-distant from the centres is similar, the weight of either sphere towards the other will be reciprocal to the distance between their centres.*[2]

which are embodied in the familiar force law

$$F = \frac{Gm_1m_2}{r^2}. \tag{1.1}$$

[1] Book III. Proposition VII. Theorem VII.
[2] Book III. Proposition VIII. Theorem VIII.

Newton further observed[3] that the force of gravity on different bodies towards the earth appeared independent of their composition. Thus the mass defined by Newton's second law $F = ma$ and that in the gravitational law were equivalent. In the Newtonian theory, this could only be viewed as an interesting coincidence. Einstein, however, elevated this principle to much greater importance when he used it as a basis for his General Theory of Relativity [21].

The question of whether the gravitational force is independent of composition is an age-old theme in physics. Galileo may or may not have tested it by dropping balls of varied composition from the leaning tower of Pisa but he did consider the rate at which such balls rolled down an inclined plane [22]. Newton and Bessel considered the periods of simple pendula [23]. Over the years many investigators pursued tests of the equivalence principle to successively greater degrees of precision. These tests culminated in the high sensitivity torsion balance experiments of this century which were briefly described above. These experiments, however, all concentrated on long-range gravity. Furthermore, the $1/r^2$ description of gravity was rooted in the motion of the planets. Until recently, little attention was paid to what might happen at shorter ranges.

1.2 A Yukawa Potential

We will consider a Yukawa interaction mediated by a massive gauge boson. If the boson has mass m_b, then the interaction will be apparent over a range given by its Compton wavelength

$$\lambda = \frac{\hbar}{m_b c}. \tag{1.2}$$

[3]Book III. Proposition VI. Theorem VI.

If we consider boson masses in the range 0.02–200 neV, the interaction will act over distances of 1 m to 10 km. Since, among the known fundamental interactions, it is only the gravitational force which acts between neutral objects at these distances, it has become standard to treat such an interaction as part of a total "gravitational" potential, irrespective of whether it is intrinsically associated with gravity or not. Such a potential is the sum of a Newtonian and a Yukawa term which we write as

$$V(r) = -\frac{G_\infty m_1 m_2}{r}\left(1 + \alpha e^{-r/\lambda}\right) \tag{1.3}$$

where G_∞ is the Newtonian gravitational constant and α and λ are the strength and range parameters describing the new interaction. The corresponding force between two test masses is then

$$F(r) = -\frac{G_\infty m_1 m_2}{r^2}\left[1 + \alpha\left(1 + \frac{r}{\lambda}\right)e^{-r/\lambda}\right]. \tag{1.4}$$

1.2.1 Composition-Dependent Aspects of the Yukawa Potential

The above description emphasizes the $1/r^2$ nature of a departure from Newtonian gravity at the expense of any composition-dependent aspects of the interaction. In general both features may be present. If the interaction couples to some charge C of matter and C_1 and C_2 are the charges of the two masses in Equation 1.3, then α contains information about the proportionality of that charge to the mass of each object and the intrinsic coupling strength of the interaction, α_0. Thus we define

$$\alpha = \alpha_0\left(\frac{C_1}{\mu_1}\right)\left(\frac{C_2}{\mu_2}\right), \tag{1.5}$$

where the $\left(C_i/\mu_i\right)$'s give the charge per unit mass. Any equivalence principle violating effect is completely contained in α.

1.2.2 The Experimental Value of G

We also note that, for mass separations much smaller than the range of the Yukawa contribution, the force between two masses is given by:

$$F(r) \approx -\frac{G_\infty m_1 m_2 (1+\alpha)}{r^2} \tag{1.6}$$

Our best experimental value for the Newtonian gravitational constant comes from the torsion balance experiment of Luther and Towler [24]. This experiment measured the force between gravitating masses at a separation of 7 cm. In the presence of an interaction coupling to bulk matter and acting over distances of meters or more, their value, $G_{lab} = (6.6726 \pm 0.0005) \times 10^{-8}\,\mathrm{cm^3 sec^{-2} g^{-1}}$, does not represent the true Newtonian gravitational constant. The relationship between the two is given by

$$G_\infty \approx \frac{G_{lab}}{(1+\alpha)} \tag{1.7}$$

which must be taken into account in any calculations.

1.3 Departures from the Inverse-Square Law

In 1981, Stacey and Tuck [13] published a survey of borehole, mine, and marine measurements of the variation of the gravitational force as a function of depth beneath the earth's surface. The observed variations were consistent with the value of G being O(1%) larger than the standard laboratory value. A careful exposition of this Airy method to determine G will be left to Chapter 6. For the moment, we note that, if these borehole measurements are treated as indicative of new physics, they can be readily explained by the presence of an intermediate-range repulsive interaction. In this scenario, a test mass on the earth's surface will experience an effective gravitational acceleration which is smaller than the purely Newtonian acceleration.

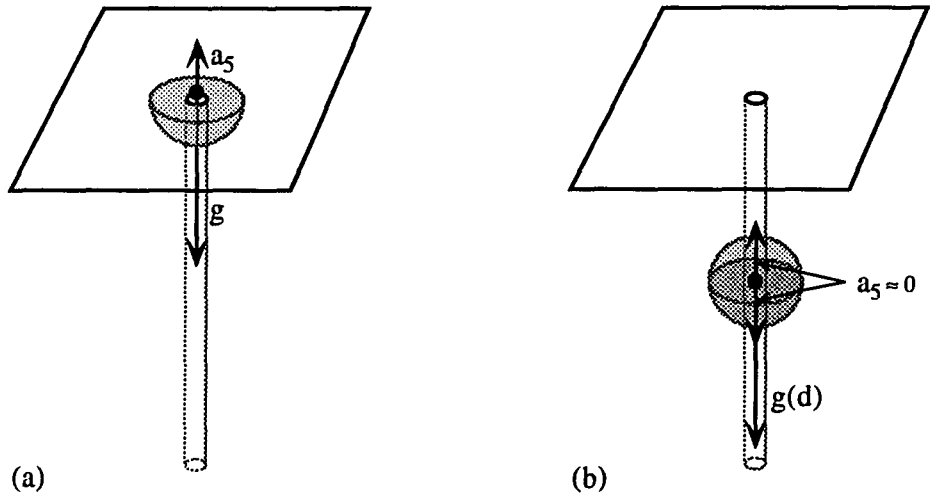

Figure 1.1: (a) Acceleration on a test mass on the earth's surface where the shaded region is within range to contribute to a short range repulsion. (b) Deep inside the earth short range repulsions from the two shaded regions above and below the test mass cancel leaving a net acceleration due only to Newtonian gravity.

At depths greater than the range of the interaction, short range repulsive contributions from the material immediately above and below the test mass approximately cancel (See Figure 1.1). Thus the value obtained deep inside the earth will roughly correspond to the purely Newtonian value of G.

The reliability of the measurements considered by Stacey and Tuck was not immediately clear, however. It was suggested that the observed trend could be explained by a systematic error in the measurement of rock densities in the geological layers through which the boreholes passed. This would lead to an incorrect calculation of the expected Newtonian gravity profile below the surface. Holding and Tuck [14] conducted an experiment in 1984 at the Hilton mine in Queensland, Australia where they carefully addressed this issue. They obtained data which also appeared to disagree with the laboratory value of G. The scale of the Hilton experiment was determined by the approximately 1 km depth of the borehole. In terms of a Yukawa coupling, the

Hilton results suggested a departure from Newtonian gravity over ranges of hundreds of meters to a kilometer or so.[4]

In addition to the geophysical analyses, several reviews of extant data providing information on gravitational departures from $1/r^2$ behavior were carried out from the mid-1970's to the mid-1980's [9, 25–28]. These reviews covered all ranges for which gravitational data was available. Figure 1.2 summarizes the limits that were inferred from tests at laboratory, terrestrial and astrophysical scales. More detailed information on how these various limits were set can be found in Appendix A. The important feature of the figure from our point of view is the substantial window just above the laboratory scale with no significant limits on possible interactions at the level of a percent of gravitational strength or smaller. Note, in particular, that the initial results from the Hilton mine experiment were not in any conflict with limits from other sources.

1.4 The Role of the Eötvös Experiment

Because of the importance of the Eötvös technique to current composition-dependent searches, we will take a few moments to consider that experiment in some detail.

1.4.1 Principles of the Eötvös Experiment

The principles of the Eötvös experiments are demonstrated in Figure 1.3. Two test masses, A and B, of different composition are suspended from opposite ends of a torsion balance arm. The key to the original EPF experiment is that the total force exerted on each mass results from the sum of a gravitational force and an inertial

[4] In order not to confuse the reader about the current experimental situation, it must be mentioned that, in light of more recent developments, these early Hilton mine results are no longer considered compelling.

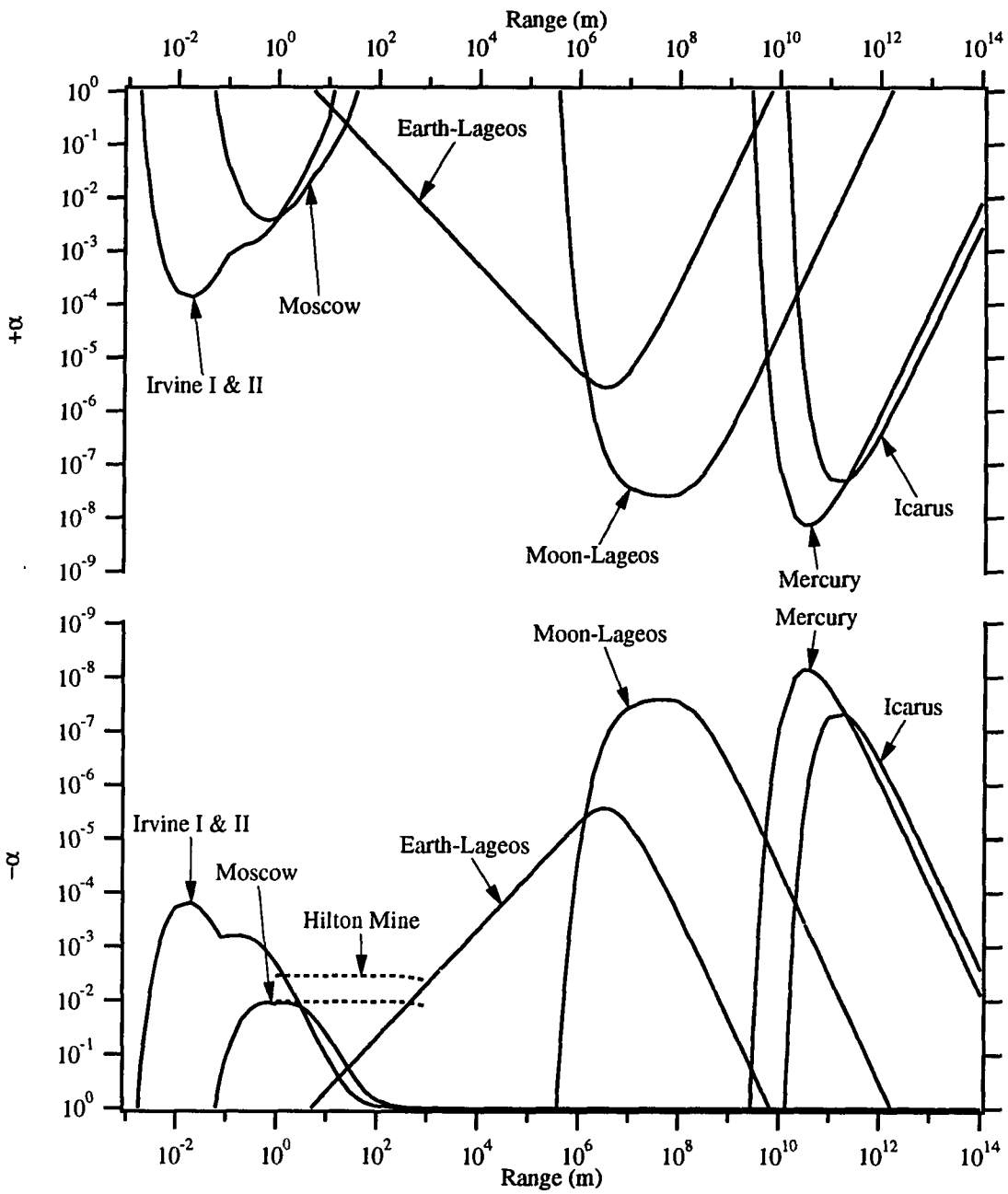

Figure 1.2: 1σ limits on departures from the gravitational inverse-square law. This assumes a single Yukawa term added to the Newtonian potential as given in Equation 1.3. The upper plot is for positive values of the strength parameter, α, corresponding to an attractive interaction while the lower plot is for a repulsive interaction. Excluded regions are above the solid limit curves in the upper plot and below the solid limit curves for the lower plot. The range of interaction strengths consistent with the early mine results are enclosed by the pair of dashed lines.

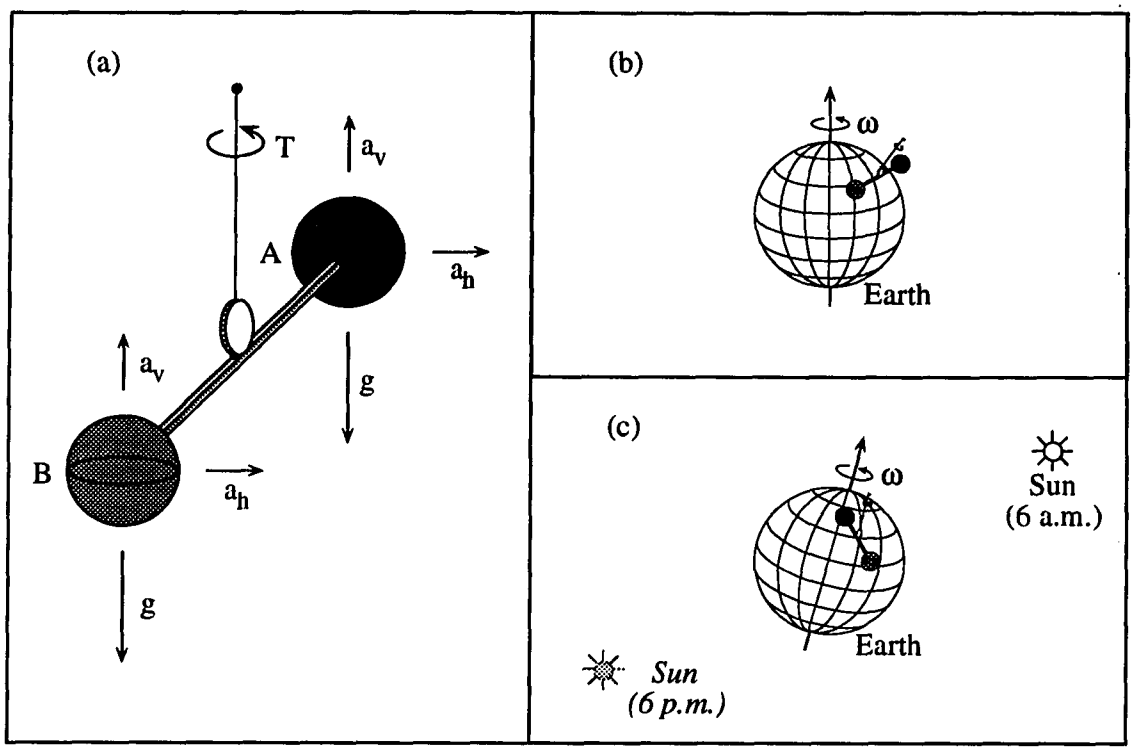

Figure 1.3: (a) The principle of the Eötvös experiment; (b) as carried out by Eötvös, Pekár and Fekete; (c) as carried out in the Roll, Krotkov, Dicke and Braginsky, Panov experiments.

force which are acolinear. We can obtain the size of the effect on the two objects, which have gravitational masses m_{Ag} and m_{Bg} and inertial masses m_{Ai} and m_{Bi}, by considering the conditions for static equilibrium of the balance—for a long thin suspension fiber the net force and torque vectors must lie along the axis of the fiber. The net force and torque on the balance are given by:

$$\vec{F} = (m_{Ag} + m_{Bg})\,\vec{g} + (m_{Ai} + m_{Bi})\,\vec{a}_c \tag{1.8}$$

$$\begin{aligned} \vec{T} &= \vec{r}_A \times \vec{f}_A + \vec{r}_B \times \vec{f}_B \\ &= (m_{Ag}\vec{r}_A + m_{Bg}\vec{r}_B) \times \vec{g} + (m_{Ai}\vec{r}_A + m_{Bi}\vec{r}_B) \times \vec{a}_c \end{aligned} \tag{1.9}$$

where $\vec{r}_A$ and $\vec{r}_B$ are the position vectors of A and B, and $\vec{a}_c$ is the centrifugal force field. Since we require these vectors to be parallel, the magnitude of the observed

torque may be written as:

$$\left|\vec{T}\right| = \frac{\vec{F}\cdot\vec{T}}{\left|\vec{F}\right|} \tag{1.10}$$

In our case $g \gg a_c$ and the magnitude of the force along the wire is approximately $\left|\vec{F}\right| = (m_{Ag} + m_{Bg})\, g$. Taking the origin of our coordinate system as the point midway between the centers of the two masses, we obtain to lowest order:

$$\left|\vec{T}\right| \approx m\left(\frac{m_{Bi}}{m_{Bg}} - \frac{m_{Ai}}{m_{Ag}}\right)\vec{r}_B \cdot \left(\vec{a}_c \times \frac{\vec{g}}{g}\right) \tag{1.11}$$

where

$$m = \frac{m_{Ag}m_{Bg}}{(1/2)\,(m_{Ag} + m_{Bg})}. \tag{1.12}$$

Clearly, a non-zero torque requires a breakdown in the equivalence of gravitational and inertial mass for the two test bodies. Since the centrifugal field points outward from the axis of the earth's rotation, we see that the maximum signal is obtained when the arm of the balance is oriented in an East-West direction. We also require the balance to be located at a latitude such that there is a significant component of the centrifugal force in the plane of rotation of the balance. Such a situation is shown in Figure 1.3(b).

A crucial facet of this experiment is the fact that there is no way in which to make a measurement with the signal source turned off. Note, however, that upon rotation of the entire balance by 180^0, the signal reverses sign. Thus a real world measurement requires comparing the torques measured in two different configurations—switching between these configurations without introducing extraneous systematic effects is one of the primary challenges to the experimentalist. The Dicke, *et al.*, and Braginsky and Panov experiments avoided this systematic difficulty by comparing the accelerations of the test masses in the gravitational field of the sun and utilizing the earth itself

as a gigantic, ultrastable turntable. Their experimental arrangement is shown in Figure 1.3(c). In this case the arm of the torsion balance is oriented in a North-South direction and the accelerations of the two masses towards the sun are compared at 6 a.m. and 6 p.m. A failure of the equivalence principle couples directly into a torque around the fiber axis.

1.4.2 The Reanalysis of the Eötvös Experiment

The 1986 reanalysis of EPF by Fischbach, *et al.* [16], demonstrated a strong correlation between the baryon content of the materials used by Eötvös and the signals he obtained. Their initial motivation for the reanalysis was an apparent energy dependence in the parameters of the neutral kaon system which could be explained by an interaction coupling differently to the particle and antiparticle [29–32]. One explanation for such a dependence is a hyperphoton field coupling to the strangeness or hypercharge (Y=B+S) of the kaons (This is discussed in more detail in Chapter 2). Fischbach, *et al.*, noted that a hypercharge coupling in the kaon system would imply a coupling to baryon content for normal matter. They asked the question of whether other data from existing experiments might shed further light on such an interaction. Since the baryon content of normal matter is a function of the binding energy, the effect of such an interaction is composition-dependent and should be apparent as a violation of the equivalence principle. Hence the reanalysis of EPF. In addition, the vector nature of such a coupling guarantees a repulsive interaction between like charges. A massive hyperphoton field was thus consistent with the observed departures from Newtonian gravity in the borehole measurements of G.

Comparison Materials	$10^3\Delta\left(B/\mu\right)$	$10^8\Delta\eta$
Cu-Pt	+0.94	+0.4± 0.2
Magnalium-Pt	+0.50	+0.4± 0.1
Ag-$FeSO_4$	0.00	0.0± 0.2
Schlangenholtz-Pt	-0.50	-0.1± 0.2
Asbestos-Cu	-0.74	-0.3± 0.2
$CuSO_4 \cdot 5H_2O$-Cu	-0.86	-0.5± 0.2
$CuSO_4$(soln.)-Cu	-1.42	-0.7± 0.2
Water-Cu	-1.71	-1.0± 0.2
Tallow-Cu	-2.03	-0.6± 0.2

Table 1.1: The Eötvös results as reanalyzed by Fischbach, *et al.* [16].

1.4.2.1 The Eötvös Data

Moving now to the EPF data, Table 1.1 lists the pairs of materials that were compared by EPF and their baryon content differences. Dicke, *et al.* [18], noted in 1964 that there was a spread in the EPF data that was somewhat larger than might be expected from the quoted standard errors. They attributed it possibly to some sort of "systematic disturbances of the [torsion] balance." In particular, they expressed concern over the fact that, for an observer to approach the Eötvös apparatus in the proper position to make an observation, the gravitational torque exerted by the observer would be large enough to perturb the measurement. Bod, *et al.* [33], note that Eötvös was aware of this problem and that measurements were made rapidly with respect to the torsion balance natural frequency to minimize such an effect. There seems little else that Eötvös and his colleagues could have done other than state their results as a limit on the equivalence of gravitational and inertial mass, irrespective of any misgivings they, themselves, might have had about the spread of their data points. Certainly they could not have been expected to find a correlation

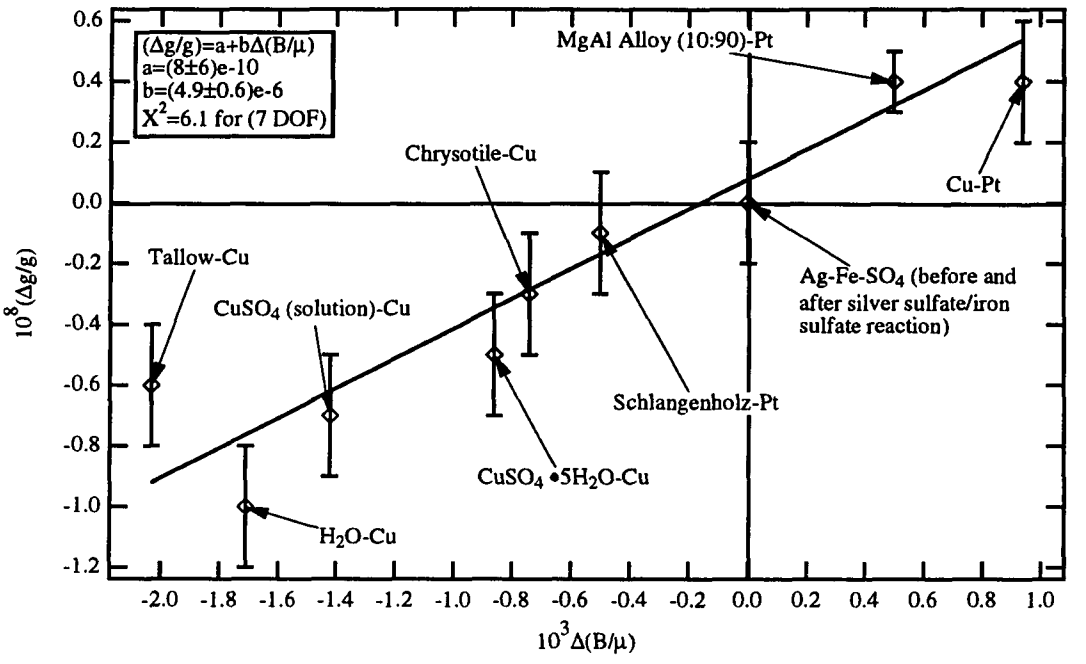

Figure 1.4: The baryon dependence of the Eötvös data as demonstrated by Fischbach, *et al.* [16].

to baryon content when that concept would not be developed until decades after their experimental work was complete.

1.4.2.2 Some Details of the Reanalysis

The range of baryon contents of the materials tested by EPF provided an important probe of the hypothesized interaction. The correlation between the EPF signal and the baryon content is plotted in Figure 1.4. The correlation by itself is highly suggestive. Nevertheless, the sensitivity of the EPF experiment to such an interaction must be carefully considered before we can say that the correlation is indeed due to such an interaction. The initial analysis by Fischbach, *et al.*, assumed a uniform and spherical earth as the source of the new interaction. In this scenario, the acceleration

vector due to a new interaction lies along the same line as $\vec{g}$ which is acolinear with the effective local gravity vector, $\vec{g}_{eff} = \vec{g} + \vec{a}_c$. Again applying the conditions of static equilibrium to the torsion balance we arrive at the analog of Equation 1.11:

$$\left|\vec{T}\right| \approx m\vec{r}_B \cdot \left[(\vec{a}_{A5} - \vec{a}_{B5}) \times \left(\frac{\vec{g}_{eff}}{g_{eff}}\right)\right] \tag{1.13}$$

where $\vec{a}_{A5}$ and $\vec{a}_{B5}$ represent the *fifth force* accelerations on the two masses each with mass m. Unfortunately, this model is wrong. Torsion balances are intrinsically sensitive to horizontal forces. As was pointed out by Eckhardt [34], for an ideal rotating earth in hydrostatic equilibrium, the force due to an intermediate range interaction will be perpendicular to the local surface (See Figure 1.5). Thus it will be precisely parallel to the direction of $\vec{g}_{eff}$, and no torque will be felt by a torsion balance. Thus an EPF-type experiment is sensitive only to departures of the local mass distribution from hydrostatic equilibrium [35–38]. One sees immediately that the ideal situation is to place a torsion balance apparatus looking for such an interaction next to a large topological feature on the earth's surface. This provides a large horizontal component of the force due to any new interaction—a location halfway down the face of a cliff of extent greater than the range of interest provides the maximum signal (See Figure 1.6). This sensitivity to local mass distributions made a quantitative interpretation of the EPF results impossible without detailed information about the local topology of the Budapest site at which the work was done.

Before proceeding further, it should be noted that there were several points of contention over this analysis. Since the issues received so much attention at the time, they will be briefly summarized here for completeness. First, it was noted by Thodberg [39] that, in the context of the spherical earth model, the Fischbach group made a sign error which made the interaction appear repulsive, in agreement with the borehole results. The proper sign indicated an attractive interaction. The

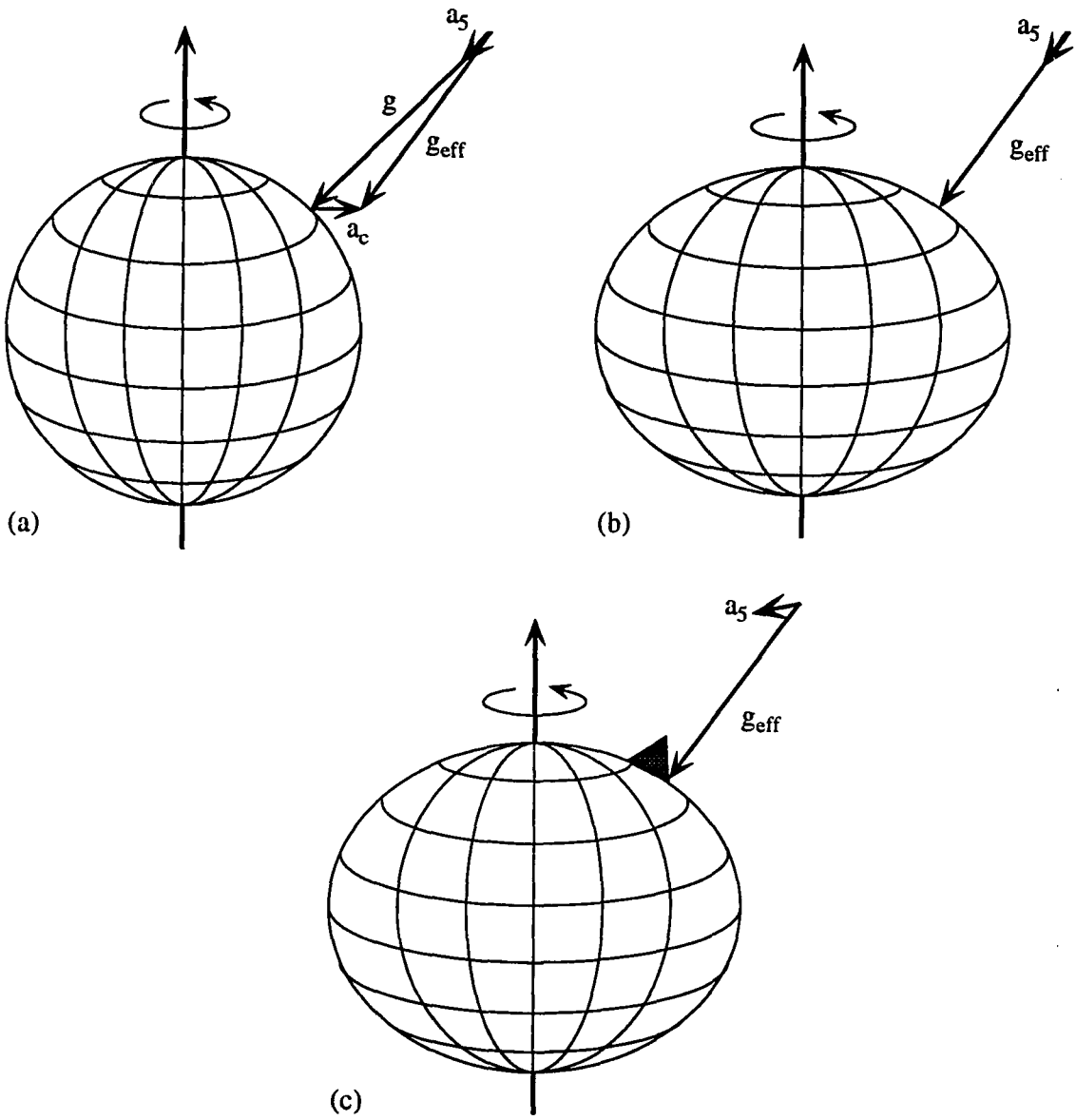

Figure 1.5: The torsion balance signal from an intermediate-range interaction: (a) in a spherical earth approximation, one incorrectly assumes that $\vec{g}_{eff} = \vec{g} + \vec{a}_c$ and $\vec{a}_5$ are acolinear; (b) consideration of an earth in hydrostatic equilibrium, gives no horizontal component of an intermediate range interaction and thus no signal in an EPF experiment; (c) local mass distributions uniquely determine the torsion balance signal.

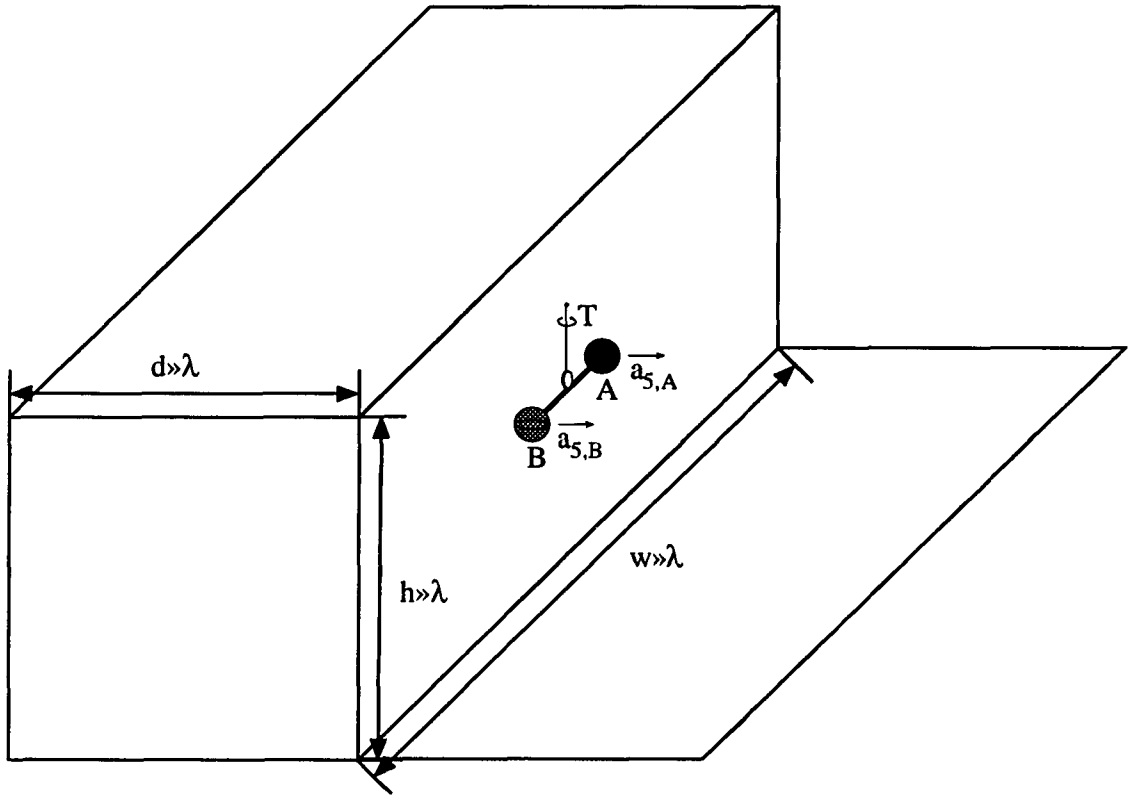

Figure 1.6: The ideal torsion balance experiment where the balance is located at the middle of the face of a cliff which extends for distances much larger than the range of the interaction in all three dimensions.

dominant sensitivity to local mass distributions, however, makes this point moot. Second, Keyser, *et al.*, noted the omission of some of the EPF data—in particular, the tallow and schlangenholz points were originally omitted because of uncertainty in their precise compositions. Also a comparison of radioactive $RaBr_2$ in a brass vial versus platinum was omitted. Each of these data was subsequently dealt with to everyone's satisfaction. Finally, perhaps a more questionable omission was the set of data obtained by Eötvös' student Renner. These data were thoroughly reviewed by Dicke, *et al.* [18], who found that the quoted statistical errors had been uniformly

underestimated by roughly a factor of 3.[5] Keyser, *et al.* [40], and Fischbach, *et al.* [38], have considered the Renner data in terms of a baryon coupling. If the questions just raised about the data are ignored, the central values obtained do not show such a correlation. The lack of a correlation, however, may be attributed to the fact that the terrain at the location of the Renner experiment was much more symmetric than at the Eötvös site [33]. Thus, none of these considerations affect the fundamental issue of a baryon content dependence in the EPF data which needs to be explained.

An alternative explanation of the EPF correlation was proposed by Chu and Dicke [41]. They suggested that a thermal gradient across the EPF apparatus would lead to a pressure gradient since the experiment was not operated under vacuum. Such a gradient could couple into a torque on the balance if the masses at each end were of different cross sections. If the gradient were steady in time and its direction determined by external features of the room in which the experiment was operated, the signal obtained would mimic a real signal upon rotation of the apparatus. Chu and Dicke were able to make a reasonable fit of the EPF data in this scenario using cross sections for the masses based on information provided by reference [17]. As pointed out by Fischbach, *et al.* [42], however, the mechanism by which a constant thermal gradient could be maintained over thousands of hours [33] of operation time is unclear.

To summarize the information provided on new interactions from the reanalysis of EPF, all that can be said is that a correlation corresponding to a specific form of composition dependence, baryon content, was found. At the time when new experiments were starting to attack the situation, there was insufficient information

[5]They also expressed concern over the fact that the scatter of the individual data points was too small to be representative of the proper statistical errors.

available to say anything concrete about the range of the interaction based on that data. A possible explanation requiring no new physics had been proposed but was certainly no more compelling than the explanation requiring new physics. This last comment is made somewhat tongue-in-cheek because the innate point of view of the physicist is that no new physics should be introduced until there is a substantial degree of certainty that the framework of standard physics simply cannot accommodate the observations.

1.5 New Experimental Efforts

After the EPF reanalysis, the need for new experimental tests to clarify the situation was very plain. Immediately upon publication of the Fischbach article, a range of experiments covering the geophysical and composition dependent effects were proposed and pursued at a number of institutions. In view of the fundamental importance of the Eötvös results, we decided to pursue a new round of torsion balance experiments at Princeton, *à la* Dicke, to search for an apparent violation of the equivalence principle.

The correlation of the EPF data to baryon content suggested that any new experiments should carefully choose the comparison materials in order to maximize sensitivity. Since the mass of normal matter scales nominally as the baryon number of the material, this requires considering departures from this proportionality, *i.e.*, considering the binding energy differences of the comparison materials. Clearly the maximum contrast occurs between samples of iron and hydrogen. These materials, however, are not well-suited for incorporation into an apparatus for measuring small differential accelerations. Table B.1 in Appendix B lists the baryon content of the

stable elements. It also lists the "isospin"[6] and "B-L" contents which will be of interest in later discussions. A reasonable choice for a high baryon content material is copper. Although not the easiest material to machine, copper parts can be manufactured very readily. Also, the availability of high purity forms, makes it a prime candidate from the point of view of being able to minimize systematic effects from ferromagnetic impurities. A choice for a low baryon content material is somewhat more difficult to arrive at. Of the metallic elements with low baryon content, Li is a poor choice because of its high reactivity on contact with moisture. Beryllium offers a viable choice, although particular care must be taken when machining it due to its carcinogenic properties. A final class of possibilities are plastics with their intrinsically high hydrogen content. These materials are often easily machined or can be molded into the necessary component shapes. We chose polyethylene, -CH_2-, which maximizes the hydrogen content of the plastic and is easily machined as our low baryon content material. This choice yields $\Delta(B/\mu) = 2.3 \times 10^{-3}$. This is to be compared with $\Delta(B/\mu) = 2.5 \times 10^{-3}$ for copper vs. beryllium or iron vs. beryllium, and the maximum contrast of $\Delta(B/\mu) = 9 \times 10^{-3}$ for iron vs. hydrogen.

Two pieces of apparatus for composition-dependent searches have been constructed at Princeton. Both utilize a torsion balance, however they differ in their methods of detecting torques. The first is a variant of the Cavendish experiment [43] which looks for static angular displacements of a torsion balance due to an external torque. In our case, instead of measuring the angular displacements, an electronic feedback torque is applied to the balance to maintain it in its equilibrium position. The size of the feedback torque then is a direct measure of any external torques acting on the system.

[6]Note that the isospin values quoted in the table are the negative of I_3. This is a convention that has been universally adopted in these searches, presumably since it makes the isospin value for most bulk matter positive.

Our second experiment employs the method of Boys [44]. In this type of experiment the frequency of the torsion pendulum is measured. If an external field is present which increases (decreases) the restoring torque on the balance then the frequency of oscillation will increase (decrease). Figure 1.7 illustrates the two techniques in the context of a terrestrial source experiment. Part (a) shows the Cavendish-type technique where the "composition dipole" axis of the torsion balance is oriented perpendicular to the line joining the centers of mass of the torsion balance and the source mass. In this scenario, the torque on the balance is measured in one orientation and then the entire apparatus is rotated precisely 180^0. If there is an external differential force acting on the balance, then the sign of the measured torque will reverse. In part (b) the Boys-type technique is shown. Here the dipole axis of the balance is oriented parallel to the line joining the centers of mass of source and balance. If there is a differential force on the two masses, the restoring torque for the oscillation will increase (from the value due to the fiber alone) in one orientation and decrease in the other, leading to a difference in the oscillation frequency between the two orientations.

In order to make a precision measurement, it is necessary to minimize the sensitivity to the Newtonian gravitational field. Thus the current torsion balance efforts typically utilize balances for which the mass distribution is cylindrically symmetric or is composed of discrete masses mounted in a pattern which reduces the sensitivity to gravitational gradients through several multipole orders. A major challenge associated with this comes from maintaining the necessary mechanical tolerances while making the two halves of the balance from different materials which typically have substantially different densities.

Further details of the techniques and results from our two pieces of apparatus will be found in Chapters 3–5.

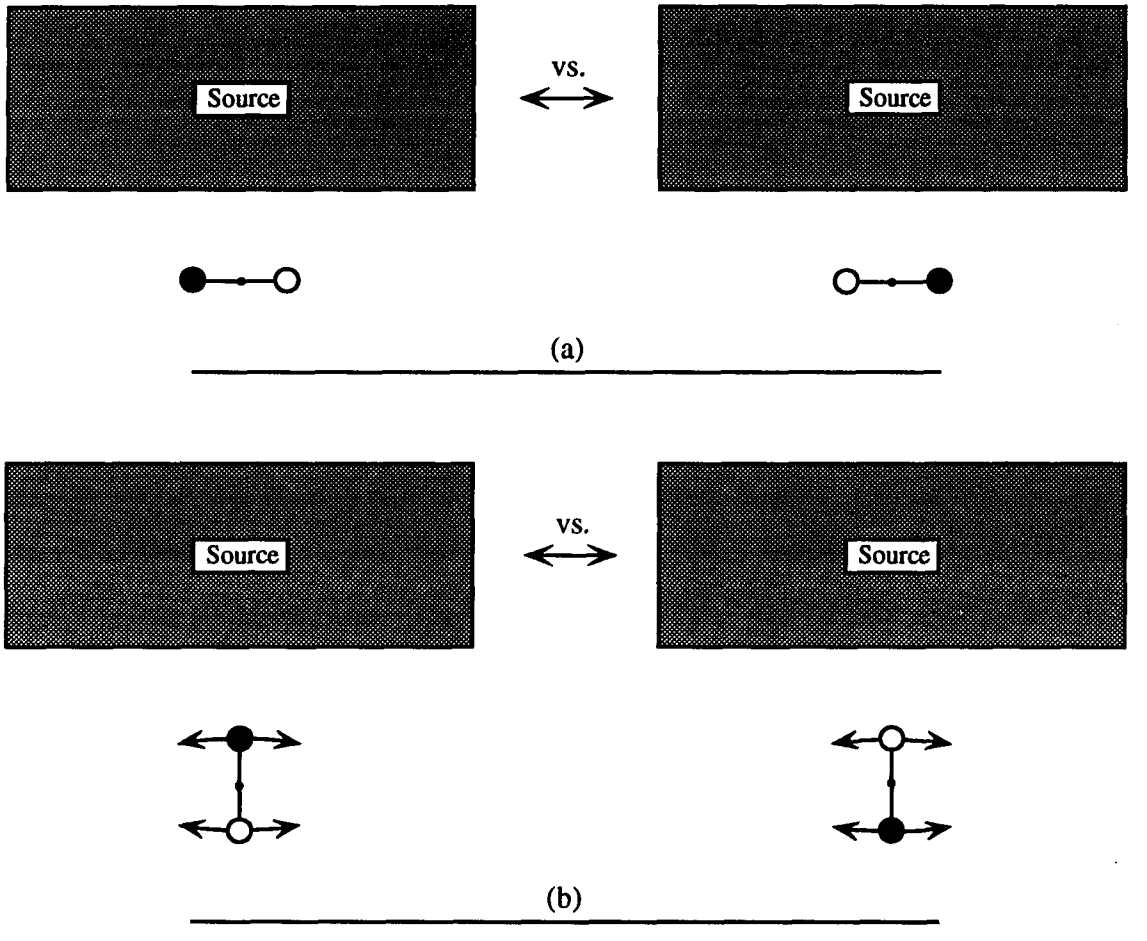

Figure 1.7: (a) Sketch of the Cavendish arrangement which looks for a shift in the static angular displacement of the torsion balance upon a rotation of the apparatus by 180^0; (b) the Boys arrangement which looks for a shift in the torsion balance frequency upon a 180^0 rotation of the apparatus.

Chapter 2

Theoretical Speculations

In this chapter we survey several theoretical suggestions for new fundamental interactions. These speculative ideas come from two main sources. The first is high energy physics where, over the years, a variety of new particles and interactions have been proposed in attempts to explain specific observations not fully accommodated by existing theory. Attempts to unify the four known forces of nature into a single, quantum-mechanically satisfactory framework provide another bountiful source of such suggestions. Our current understanding of spontaneous symmetry-breaking provides a mechanism for the bosons mediating any new interactions to acquire mass and thus act over finite ranges. It is particularly interesting that simple symmetry-breaking arguments suggest the terrestrial scale as an interesting place to look for new physics.

Before beginning our survey, a couple preliminary comments are in order. First, what is presented here is not intended to be, in any way, an exhaustive review of theoretical concepts and possibilities, but rather a brief look at several ideas which seem particularly relevant and illuminating to our search for intermediate-range interactions. Secondly, we emphasize, yet again, that all of the possibilities mentioned here are purely speculative. The existence of any of these proposed interactions is ultimately an experimental question.

2.1 Some Scalar Interactions

It has long been wondered why we see no long-range fundamental scalar interaction [45] when both vector and tensor interactions of that type are present. This was the impetus for the development of the Jordan [46] and Brans-Dicke [47] scalar-tensor theories of gravity. Furthermore, Brans and Dicke noted that a long-range scalar contribution to gravity could allow general relativity to be made compatible with Mach's principle [48–50]. Nevertheless, no evidence for such an interaction has ever been seen. In 1970, Wagoner considered a more general form for scalar-tensor theories of gravity [1] which included the Brans-Dicke theory as a special case. Wagoner's formulation led, in the static limit, to a gravitational potential with both the standard Newtonian part and a contribution from the scalar field which plausibly had finite range. He assessed the existing observational constraints on the theory and found that scalar coupling constants only slightly weaker than the tensor coupling constant were possible.

2.1.1 Dilatons

Fujii also considered the possibility of a scalar field coupled with tensor gravity [2,3]. Fujii's scalar particle was the Nambu-Goldstone boson associated with scale invariance, the dilaton. This possibility has also been considered, more recently, by Peccei, Solà and Wetterich [51]. The dilaton mass is found to scale as:

$$m_d \approx \frac{\mu^2}{M_P}, \tag{2.1}$$

where M_P is the Planck mass and μ is an undetermined mass scale. It is argued in both cases that a plausible value of the dilaton mass may be obtained by by considering μ to come from hadronic physics This makes μ on the order of Λ_{QCD} and

leads to interaction ranges on the order of kilometers. Perhaps the most intriguing aspect of Fujii's speculations was the rather precise prediction for the deviation from the Newtonian inverse-square law that resulted. His interaction generated a potential given approximately by:

$$V(r) \approx -\frac{G_\infty}{r}\left(1+\frac{1}{3}e^{-r/\lambda}\right) = -\frac{3G_0}{4r}\left(1+\frac{1}{3}e^{-r/\lambda}\right) \tag{2.2}$$

where G_∞ is the proper Newtonian gravitational constant that would be measured outside the range of the second term while G_0 is the value of G that would be measured by a Cavendish type experiment operating at separations of laboratory scale. O'Hanlon, eschewing a quantum mechanics based theory, developed a classical analogue of Fujii's theory including a mass term for the scalar field with precisely the same form for the potential [4]. The large coupling to such a scalar field was quickly excluded for the boson mass range suggested by Fujii (See Figure 1.2). At very short ranges, i.e. smaller than a few millimeters, this form cannot be ruled out. However, probes that operate between the high energy scale and the laboratory scale are difficult to devise leaving a large region of the $\alpha - \lambda$ plane unexplored.

The dilaton interaction suggested by Peccei, Solà and Wetterich was constructed to provide a mechanism to solve the "cosmological constant problem," *i.e.*, as a method to drive the vacuum energy density to zero. Their dilaton, the cosmon, couples primarily to mass but has equivalence principle violating corrections which effectively couple to baryon number and the third component of isotopic spin. In what they consider to be the most likely scenario for their coupling, the effective charge of normal matter looks like:

$$C_{nucleus} \approx f\left[m - \sigma B - \delta\left(N - Z\right)\right] \tag{2.3}$$

where f is a strength parameter and σ and δ specify the relative contributions from the baryon and isospin portions of the interaction. Peccei, *et al.*, give

$$1 : \frac{\sigma}{m_H} : \frac{\delta}{m_H} \approx 1 : \frac{1}{20} : \frac{1}{250} \tag{2.4}$$

as the hierarchy of these contributions to the interaction. Although the composition-independent part of this interaction dominates, it would probably be easiest to detect in a composition-dependent experiment due to the much greater precision with which a differential force measurement can be made.

2.1.2 Axions

Another particle that can potentially lead to long range interactions between normal matter is the axion [52,53]. The axion is the Nambu-Goldstone boson associated with Peccei-Quinn symmetry-breaking—a mechanism to solve the "strong CP" problem of QCD.[1] Moody and Wilczek have examined in detail the possible manifestations of the axion in intermediate-range force experiments [56,57]. The axion has pseudoscalar couplings to fermions and because of instanton fields can also couple to quarks via a CP-violating scalar vertex. This leads to the possibility of three types of axion-mediated static interactions which are distinguished by the combination of interaction

[1] The strong CP problem arises when quantum chromodynamics is combined with the electroweak theory in the standard model. There is a P and CP violating term in the QCD Lagrangian which, in the limit of massless quarks, can be transformed away but which, in the real world, is potentially non-zero (See, for example, the discussion of Kolb and Turner [54, Chapter 10]). Such a CP-violating term should lead to an electric dipole moment of the neutron. This can be seen classically by considering the transformation of $\vec{\sigma} \cdot \vec{E}$ under CP: $\vec{\sigma} \cdot \vec{E} \xrightarrow{CP} -\vec{\sigma} \cdot \vec{E}$. The experimental limit on this value for the neutron is $EDM \leq O\left(10^{-24} e - cm\right)$ [55]. We can make a rough estimate the size of a CP-violating parameter in QCD by a simple dimensional argument: $EDM \approx e \cdot \ell \cdot \Theta_{CP-violating}$, where e is the electric charge, ℓ is a distance determined by QCD, and Θ is the CP-violating parameter. Taking ℓ as the hadronic scale gives $EDM \approx 10^{-14} \Theta e - cm$ which implies that the CP-violating parameter is 10^{-10} or less. Why so small? In the context of the axion, the Peccei-Quinn symmetry-breaking mechanism dynamically forces this parameter to zero.

vertices which contribute. They are:

$$V_{mon-mon}(r) = -\frac{g_{s1}g_{s2}}{4\pi r}e^{-m_a r} \tag{2.5}$$

$$V_{mon-dip}(r) = -g_{s1}\left(\frac{g_{p2}}{M_2}\right)\left(\frac{\hat{\sigma}_2\cdot\hat{r}}{8\pi}\right)\left(\frac{m_a}{r}+\frac{1}{r^2}\right)e^{-m_a r} \tag{2.6}$$

$$\begin{aligned} V_{dip-dip}(r) = & -\frac{1}{16\pi}\left(\frac{g_{p1}}{M_1}\right)\left(\frac{g_{p2}}{M_2}\right)\left[(\hat{\sigma}_1\cdot\hat{\sigma}_2)\left(\frac{m_a}{r^2}+\frac{1}{r^3}+\frac{4\pi}{3}\delta^3(r)\right)\right. \\ & \left.-(\hat{\sigma}_1\cdot\hat{r})(\hat{\sigma}_2\cdot\hat{r})\left(\frac{m_a^2}{r}+\frac{3m_a}{r^2}+\frac{3}{r^3}\right)\right]e^{-m_a r} \end{aligned} \tag{2.7}$$

where g_s and g_p represent scalar and pseudoscalar coupling constants, respectively, m_a is the axion mass, $\hat{\sigma}$ is the spin vector, and M is the mass of the fermion to which the axion couples. The first is a monopole-monopole coupling which would be evident as a coupling between nucleons. The second is a monopole-dipole coupling which could be detected as a coupling between bulk matter and spin-polarized material. The third type leads to spin-spin interactions. Equation 2.5 gives the coupling of particular interest to us since it would be the source of an interaction coupling to bulk matter. Since it represents a coupling between nucleons it will scale only approximately as the mass and would be detectable, in principle, as a deviation from $1/r^2$ behavior in a composition-independent test of Newtonian gravity or as a baryon dependence in an Eötvös-type experiment. This assumes that the axion mass is such that it would actually be detectable in these macroscopic experiments.

There are two parameters which specify the mass and couplings of the axion. The first is the Peccei-Quinn symmetry breaking scale, F_{PQ}. The second is the QCD CP-violating parameter, Θ. The discussion in Footnote 1 of the previous paragraph gives the accepted upper limit on the CP-violating parameter $\Theta \approx 10^{-10}$. In terms of these parameters, the coupling constant for an axion-mediated coupling between nucleons is [56]:

$$g_{sNN} = \frac{\Theta}{F_{PQ}}\frac{2m_u m_d}{(m_u+m_d)^2}\langle N|\,\sigma\,|N\rangle \tag{2.8}$$

where m_u and m_d are the masses of the up and down quark and $\langle N|\,\sigma\,|N\rangle$ is the pion-nucleon σ term. If we take $\langle N|\,\sigma\,|N\rangle \approx$60 MeV, $m_u \approx$4.5 MeV, and $m_d \approx$7.5 MeV, this yields:

$$\frac{g_{sNN}^2}{4\pi} = 63MeV^2\left(\frac{\Theta}{F_{PQ}}\right)^2 \tag{2.9}$$

The mass of the axion is approximately determined by the inverse scale of QCD and the scale of the symmetry-breaking according to [54]:

$$m_a \approx \frac{\Lambda_{QCD}^2}{F_{PQ}}. \tag{2.10}$$

With this last relation, it should be noted that the coupling constant given in Equation 2.8 is proportional to the axion mass. As is pointed out by Kolb and Turner, the Peccei-Quinn symmetry-breaking scale is unspecified from the point of view of resolving the strong CP problem and could plausibly lie anywhere between roughly the weak scale and the Planck scale. This gives rise to potential axion masses in the region 1 peV–1 MeV corresponding to Yukawa ranges of 200 fm–200 km. High energy experiments, however, constrain the mass to lie below about 10 keV. Furthermore, if the axion mass were less than about 1 μeV, then the mass density due to axions in the universe would exceed the critical density. Finally, consideration of the cooling of the cores of stars further constrains the axion mass to lie between 1 μeV and 1 meV or around a few eV. This corresponds to ranges of hundreds of microns to tens of centimeters in the first case and submicron ranges in the second (The reader is referred to Chapter 10 of reference [54] which provides a comprehensive summary of these constraints and continuing experimental efforts.). For an axion of mass in the 10^{-6}–10^{-3} eV mass range, Equation 2.9 implies coupling strengths in the range 10^{-44}–10^{-50}. If we write this in terms of α as given in Equation 1.3, this corresponds to $\alpha \approx 10^{-6}$–10^{-12}.

Thus we see that the axion coupling provides a route to couplings weaker than gravity. Furthermore, the coupling to nucleons described here is expected to yield exactly the sort of baryon number dependence noted in the EPF data. Its range, however, is too short for it to be a candidate for the interactions of interest here.

2.1.3 Axion-like Scalars

By axion-like scalars, I mean Nambu-Goldstone bosons which arise from the breaking of some global symmetry and which have induced scalar couplings because of the CP-violating term in the QCD Lagrangian described above. Chang, *et al.* [58], have considered these couplings in the context of equivalence principle violations. The phenomonology of such interactions closely parallels that of the axion but with the details of the couplings being specific to the particular model. Nevertheless, couplings which are weaker than gravitational strength are likely, as is exemplified by the axion, because they vary inversely as some potentially large symmetry-breaking scale. A general expression for the mass of the boson in such models as:

$$m_b \approx \frac{\Theta m_u m_Q}{F} \tag{2.11}$$

where m_Q is a mass which might be as large as the top quark mass. If m_Q is taken to lie somewhere in the region 10 MeV–100 GeV and F in the region 10^9–10^{12} GeV (as is suggested by axion limits), this gives interaction ranges from less than 1 m to 10^4 km.

2.1.4 Other Sources of Scalar Interactions

Taylor and Veneziano [59] have considered the scalar dilatons which naturally arise in string theories. These dilatons couple naturally to mass, but radiative corrections lead to an equivalence principle violating portion of the interaction. Scalar

interactions also appear in theories which attempt to unify gravity with the other fundamental interactions. Scalar and vector interactions in these theories are particularly interesting to fifth (and sixth!) force searches because they naturally have couplings of gravitational strength. These theories will be considered later in this chapter. From the viewpoint of particle physics, gravitational strength couplings seem much too small to be natural in most interactions [60]. The exception is in the case of a Nambu-Goldstone boson which results from the spontaneous breakdown of a global symmetry which has anomalies. This is the case with the axion and cosmon which were described above. In such cases, a coupling is introduced which is inversely proportional to the scale of the symmetry-breaking and directly proportional to the size of the anomaly (presumably quite small). This leads to very small coupling constants for sufficiently large symmetry-breaking scales. The mass associated with such a boson is generically determined by the scale of the dynamics involved, Λ_{dyn} and the symmetry-breaking scale, F:

$$m_b \approx \frac{\Lambda_{dyn}^2}{F_{S.B.}}. \tag{2.12}$$

As we have already seen, macroscopic range interactions are readily accommodated by substitution of plausible parameters into Equation 2.12. At this point we will turn our attention to the consideration of some candidates for new vector interactions.

2.2 Vector Interactions

Perhaps one of the most persuasive lines of reasoning for the existence of new interactions is that explored by Lee and Yang during the mid-1950's [61]. Gauge invariance leads to charge conservation laws. They asked, in particular, the question whether a gauge invariance should be associated with each and every apparently conserved

charge. Yang and Mills attempted to base a theory for the strong interactions on just such a gauge invariance connected to the approximately conserved charge, isotopic spin [62]. Some years later Néeman considered his "fifth interaction,"a coupling to strangeness [63]. Finally, Lee and Yang considered the apparent conservation of "heavy particles," *i.e.*, baryons [61]. We will consider this last hypothesis in a bit more detail.

Application of a locally gauge invariant transformation to the baryonic wave function proceeds in complete analogy to the gauge transformation of electromagnetism. Such a transformation gives rise to an infinite range vector coupling between the "heavy particles." For interactions between like charges, the coupling will be repulsive and, since baryon content is not precisely proportional to mass, should give rise to a baryon dependence in the EPF data. The modification to the gravitational force law would look like (in our notation):

$$F = -\frac{Gm_1m_2}{r^2}\left[1 - \alpha_0\left(\frac{B_1}{\mu_1}\right)\left(\frac{B_2}{\mu_2}\right)\right] \tag{2.13}$$

where $\alpha_0 = f^2/Gm_H^2$ and f is the baryon charge. Lee and Yang used the EPF result to place an upper limit of

$$\alpha_0 < 10^{-5} \tag{2.14}$$

for the strength of such a coupling. We can only wonder how the knowledge of a correlation to baryon number in the EPF data would have influenced the further development of gauge theories at the time.[2]

[2]A particularly controversial point would presumably have been the apparent attractive nature of the coupling indicated by the experimental data. In the case of a long range force as envisioned by Lee and Yang, the initial rotating spherical earth approximation used in the Fischbach reanalysis would have been the correct way to interpret the experiment. The apparent attractive nature of the interaction would have been crucial to any further developments (See Chapter 1). Note that the Roll, Krotkov, Dicke and Braginsky and Panov experiments had not yet been carried out so that there would have been no reason, a priori, to consider a short range effect.

2.2.1 Hyperphotons

A hyperphoton coupling to hypercharge or the third component of isospin was first suggested by Bernstein, Cabibbo and Lee [64] and separately by Bell and Perring [65] as a possible explanation for the decay of the long lived component of the kaon system $K_2^0 \to 2\pi$ which would not require explicit CP violation in the weak interactions. The presence of an external field giving a potential energy difference between K^0 and $\overline{K^0}$ leads to a small real shift in the diagonal elements of the kaon mass matrix. The eigenvalue problem for the weak decay modes, which in the limit of CP invariance and no external fields yields the CP eigenstates K_1 and K_2, then diagonalizes to states which can be characterized as dominantly CP= +1 or CP= −1 but with each state having a small admixture of the "wrong" CP component. Thus the long lived, dominantly CP= −1 state can decay to a CP= +1, two pion final state. If ϵ is the parameter describing the admixture, and we allow the possibility that the potential is not necessarily due to a vector interaction, then $\epsilon \propto \gamma^J$, where J is the spin of the field and γ is the usual relativistic factor [64]. The energy dependence of the 2π decays quickly ruled out the possibility of a vector interaction as the source of the $K_2^0 \to 2\pi$ decays. In general, the observation that

$$\frac{B\left(K_\ell^0 \to \pi^+\pi^-\right)}{B\left(K_\ell^0 \to \pi^0\pi^0\right)} \neq \frac{B\left(K_s^0 \to \pi^+\pi^-\right)}{B\left(K_s^0 \to \pi^0\pi^0\right)} \tag{2.15}$$

indicates that the two pion decay modes for K_ℓ^0 and K_s^0 cannot both be due strictly to decays of a K_1^0 component in each wave function.

Weinberg pointed out that a hyperphoton coupled to hypercharge would necessarily be massive since hypercharge is not absolutely conserved [66–68]. This can be seen in the following way. The equation of motion for a massive vector field is:

$$\partial_\sigma\left(\partial^\sigma A^\nu - \partial^\nu A^\sigma\right) + m^2 A^\sigma = J^\sigma. \tag{2.16}$$

Taking the divergence of this equation then yields:

$$m^2 \partial_\nu A^\nu = \partial_\nu J^\nu. \tag{2.17}$$

We see immediately that a nonconserved charge requires a massive hyperphoton.

For normal matter, the hypercharge is simply the baryon number (Y=B+S). Thus the massive hyperphoton coupled to hypercharge provides a plausible mechanism for a finite range interaction between bulk matter. For the ranges of interest in the interaction window described above, and since accelerator experiments are conducted near the earth's surface, such a coupling would also be expected to show up in data from the neutral kaon system and give rise to an energy dependence of the neutral kaon parameters. Such an energy dependence was considered by Fischbach, *et al.* [29–32, 69], in a series of papers which analyzed results from several experiments of the late 1970's that were carried out at higher energies than had previously been used in kaon studies.[3]

2.2.2 A Supersymmetric Vector Boson

Another possibility for a vector interaction, which is satisfying to an experimentalist because of its explicit predictions of the charge dependence of the force, is the U, proposed by Fayet, which appears as a supersymmetric partner for the spin-1/2 goldstino (or as a supergravity partner of the spin-3/2 gravitino) [72–74]. Fayet emphasizes that such a boson is *required* in many supersymmetric theories to make the unobserved supersymmetric lepton and quark partners massive via spontaneous breaking of the supersymmetry. He considers, in particular, the extension of the standard model

[3]At present, however, the failure to see hyperphotons via the decay $K^+ \rightarrow \pi^+ + \gamma_H$ at the level of 1.7×10^{-9} [70] strongly constrains the possibility that this particle could be the mediator of an intermediate-range force having roughly gravitational strength (See Reference 71 and references therein).

gauge group SU(3)×SU(2)×U(1) to SU(3)×SU(2)×U(1)×U(1) where the extra U(1) group is the source of the new spontaneous symmetry-breaking. The U potentially couples to both axial and vector currents leading to both "bulk matter" and spin-dependent interactions [75], which is similar to the case of the axion described above. Also, it would, in general, be expected to mix with the Z^0—as long as its coupling is small, the standard model predictions of Z behavior would not be significantly altered [76].

Fayet's U has a mass given by:

$$M_U \geq \frac{g''}{g} M_W = \frac{g''}{\sqrt{g^2 + g'^2}} M_Z = 123GeV \times g'' \tag{2.18}$$

where g and g' are the weak interaction coupling constants and g'' is the coupling associated with the new U(1) gauge group. The expression is stated as an inequality because additional Higgs fields may serve to increase the U mass above this basic value [75]. If in fact the U is considered a partner of the gravitino, it is natural to expect g'' to be of gravitational strength. If we take

$$(g'')^2 \approx G_N m_H^2 = 0.5 \times 10^{-38} \tag{2.19}$$

we see that

$$M_U \approx 10^{-8} \text{ eV} \;\Rightarrow \lambda_U \approx 20 \text{ meters} \tag{2.20}$$

leading to effects that are detectable in macroscopic experiments. If we require a potential coupling to be somewhat weaker than gravity as is required by the experimental limits, then the U range would correspond to terrestrial scales.

The general form of the charge for the vector coupling of the U is given by [77]:

$$C_V^U = aB + b_e L_e + b_\mu L_\mu + b_\tau L_\tau + cQ \tag{2.21}$$

where B, L and Q are baryon number, lepton number and electric charge, respectively, and where the coefficients of the various terms are model dependent. In the case of neutral bulk matter this becomes

$$C_V^U(bulk) = aB + b_e L_e. \tag{2.22}$$

For the purpose of composition-dependent experiments, the charge given by Equation 2.22 will effectively appear as:

$$C_V^U(bulk) = \left(a + \frac{b_e}{2}\right) B - \left(\frac{b_e}{2}\right)(N - Z). \tag{2.23}$$

From the point of view of grand unified theories (GUT's), restrictions can be placed on the form of Equation 2.21. These theories often imply the nonconservation of B and L but still retain (B-L) as a good quantum number. In this case the U couplings become [77]:

$$C_V^U = a(B - L) + cQ \;\Rightarrow\; C_V^U(bulk) = a(B - L) = \frac{a}{2}[B + (N - Z)] \tag{2.24}$$

where L now refers to the total lepton number.

2.3 Gravity Theories

Certain lines of speculation come directly from attempts to unify gravity with the other known forces in a single quantum mechanically satisfactory theory. It is interesting to note that such attempts typically result in both vector and scalar components of the gravitational field. Because of the repulsive nature of the vector interaction between like charges, the concept of "antigravity"[4] was revived in this context [7].

[4] "Antigravity," in its original context, was meant to indicate that antiparticles might "fall up" in the gravitational field of normal matter. In the current context, that of a vector interaction, an antiparticle would actually be more strongly attracted to a matter source than a matter particle.

Because these extra components are fundamentally linked to gravitation, they naturally have gravitational strength, thus circumventing the concerns about the small intrinsic coupling constants noted in Reference 60 and in Section 2.1.4 above.

Another point which can be made about interactions intrinsically linked to gravity is an estimate for the "natural" range of such interactions. For a boson mass arising from spontaneous symmetry-breaking via the Higgs mechanism, the relationship between the boson mass and the symmetry-breaking scale is given by [8]:

$$m_b = g\,\langle\phi\rangle \tag{2.25}$$

where g is the coupling constant. For g of gravitational strength, Equation 2.25 becomes:

$$m_b = \sqrt{G\mu^2}\,\langle\phi\rangle = \frac{\mu\,\langle\phi\rangle}{M_{Planck}}. \tag{2.26}$$

If μ and ϕ are both taken to lie in the range of $\Lambda_{QCD} - \Lambda_{electroweak}$, we have:

$$m_b \approx 10^{-12}\text{–}10^{-6} eV \tag{2.27}$$

which is equivalent to ranges from tens of centimeters to hundreds of kilometers.

2.3.1 Supergravity

Much of the speculation about new interactions with gravitational strength originated with Scherk [6–8] in the context of extended supergravity theories. He considered, in particular, N=2 and N=8 supergravity models.

In the case of an N=2 theory he noted the appearance of a vector field, a "graviphoton," associated with normal tensor gravity. The resulting gravitational potential between fundamental particles, in the limit of a massless vector field, is given by [8]:

$$V(r) = -\frac{G}{r}\left(m_1 m_2 - \frac{g_1 g_2}{4\pi G}\right). \tag{2.28}$$

The coupling constant, g, is given by $g = \pm m\sqrt{(4\pi G)}$, where the + sign is for a particle and the − sign is for the antiparticle . Thus the potential becomes:

$$V(r) = -\frac{Gm_1m_2}{r}(1 \mp 1) \tag{2.29}$$

where the upper sign corresponds to a particle-particle interaction and the lower corresponds to a particle-antiparticle interaction. Note that, in the case of self-conjugate particles, the vector interaction disappears [6]. This implies that the gravitational potential between matter (or between antimatter) vanishes while the gravitational field between particle and antiparticle would be twice the "normal" value. The vanishing of the potential between like objects constitutes "antigravity" as defined by Scherk. In order for such an interaction to be compatible with observation, however, it would also be necessary for symmetry-breaking to occur, giving the vector field a finite range.

In the case of an N=8 model (here, Scherk begins with a five-dimensional model which is compactified to four dimensions), the tensor component of gravity is accompanied by both a vector and a scalar component. Scherk gives the gravitational interaction between fundamental particles as:

$$V(r) = V_T(r) + V_V(r) + V_S(r) \tag{2.30}$$

where

$$V_T(r) = \frac{-Gm_1m_2}{r} \tag{2.31}$$

$$V_V(r) = \frac{\pm 4Gm_1m_2}{r} \tag{2.32}$$

$$V_S(r) = \frac{-3Gm_1m_2}{r} \tag{2.33}$$

with the upper sign in V_V for particle-particle(antiparticle-antiparticle) interactions and the lower for particle-antiparticle interactions—as in the N=2 case, the vector

interaction disappears for self-conjugate particles. Note that there is again a competition of the three terms for matter-matter interactions which, in the case of all three fields being massless, gives no gravitational interaction between particle or antiparticle pairs. The same considerations apply here as they did for N=2 and symmetry-breaking is required for this model to be in any way compatible with observation.

An important point to note for any attempt to use either of these models as a phenomenological template in the search for new interactions is the nature of the "mass" to which each boson couples [6]. The above interactions are those between the fundamental particles of the theory—not interactions between bulk matter. The spin-2 graviton couples to the stress-energy tensor and thus the actual mass of bulk materials. In the case of the vector interaction, the coupling must be to some charge of the particles. In Scherk's models, this charge is proportional to the mass of the fundamental fermions involved. Thus for protons and neutrons, he suggests that the vector coupling to protons and neutrons is to the bare mechanical masses of the quark constituents. Scherk takes the scalar interaction to couple to the trace of the stress energy tensor so that the scalar interaction sees the rest mass of composite particles.

2.3.2 A Kaluza-Klein Proposal

Bars and Visser have proposed a five-dimensional Kaluza-Klein gravity model [78] in some ways similar to the $N = 8$ supergravity model as described by Scherk. Their model includes a five-dimensional vector interaction which, upon compactification to four dimensions yields both a scalar and a vector interaction of roughly gravitational strength. Symmetry breaking provides a method to make both of the bosons associated with these interactions massive.

They note, as did Scherk, the need to specify the precise form of the "mass charge"

to which their vector interaction should couple. They prefer not, however, to assign it *a priori* to the bare mechanical mass of the fundamental fermions in their theory, allowing for a potentially more complicated effective charge when considering couplings to composite objects. This leads them to an effective vector charge of the form:

$$C_{V,eff} = C_V^n(B - Z) + (C_V^p + C_V^e)Z = C_V^n(B - \epsilon Z) \tag{2.34}$$

where $\epsilon = (C_V^n - C_V^p - C_V^e)/C_V^n$ and n, p, and e stand for neutron, proton, and electron, respectively. In the case of coupling to bare mechanical masses (with m_u=4.5 MeV, m_d=7.5 MeV, m_e=0.5MeV), this implies $\epsilon \approx 0.17$. For the scalar interaction, they assume, in the same manner as Scherk, a coupling to the trace of the stress-energy tensor so that the scalar coupling for composite particles is to the rest mass.

The authors emphasize the potential generalization of their compactification scheme to superstring theories. From a purely phenomenological point of view, the interactions of the Bars and Visser model are indistinguishable from the supergravity models of Scherk.

2.4 Summary and General Phenomonology

In the preceding sections we have seen that there are a variety of theoretical speculations which lead us to wonder about the presence of heretofore unseen interactions. None of these speculations is absolutely compelling because they are just that, speculations. The question does exist, however, as to whether a "theory of everything" can be arrived at without introducing something new.

2.4.1 Ranges

One thread that runs through most of the above speculations is that the range of a new interaction may be written as:

$$\lambda \approx \frac{M}{\Lambda^2} \tag{2.35}$$

where M is some large mass scale, typically the Planck scale or the scale at which a global symmetry is broken, and Λ is determined by the scale of the hadronic or weak interactions. The resulting forces may then act over distances of up to hundreds or even thousands of kilometers. This places renewed emphasis on the use of classical techniques to probe for new physics. In some sense, the methods needed to look for new interactions have come full circle during the span of the $20th$ century.

2.4.2 Charges

The effective charge for a scalar interaction is not necessarily simply characterized. In quantum gravity models there is a predilection to let the scalar field couple to the trace of the stress-energy tensor so that the effective charge is the rest mass of the materials involved. If the coupling is to rest mass, the scalar interaction would only be apparent in composition-independent searches for new forces, *i.e.*, searches which rely on looking for a deviation from $1/r^2$ behavior of gravity. Less simple scenarios are, in general, also possible as is illustrated by the coupling of the cosmon to the anomalous part of the trace of the stress-energy tensor. Such couplings would manifest themselves both as a violation of $1/r^2$ behavior as well as in violations of the equivalence principle.

For vector couplings, the situation is somewhat more straightforward (However, see the discussion in Section 2.4.3 below.). A vector coupling to bulk matter, com-

posed of protons, neutrons and electrons, can be characterized by the effective charges of these three basic constituents. This leads to an effective vector charge of the form:

$$C_{V,eff} = C_V^n N + (C_V^p + C_V^e)Z = C_V^n B + (C_V^p - C_V^n + C_V^e)L. \tag{2.36}$$

A coupling to $B-L$ as might be suggested by a gauge coupling to the conserved charge of a GUT corresponds to $C_V^p = C_V^n = -C_V^e$; a coupling to the third component of isospin, $N - Z$, (note the opposite sign convention from that normally used in high energy physics) corresponds to $C_V^p = -C_V^n$, $C_V^e = 0$. Since $Z = L$ for bulk matter, an effective charge can be defined as some linear combination of N and Z, or, equivalently, B and I_3. We follow the convention of Fischbach and define a mixing angle, θ_5, which characterizes the mixing between the latter two quantities

$$\frac{C_5}{\mu} = \left(\frac{B}{\mu}\right)\cos(\theta_5) + \left(\frac{I}{\mu}\right)\sin(\theta_5). \tag{2.37}$$

This expression will be used for the analysis of various experimental results later in this paper.

2.4.3 Competing Forces

Goldman, Hughes and Nieto have considered in detail the phenomonology of quantum theories of gravity [79–82]. In the static limit, the total potential with scalar, vector, and tensor terms may be written as:

$$V(r) = -\frac{Gm_1m_2}{r}\left(1 \mp ve^{-r/\lambda_V} + se^{-r/\lambda_S}\right) \tag{2.38}$$

where v and s are the coupling strengths of the vector and scalar couplings, respectively, and the corresponding λ's are their ranges. Note that the minus sign in Equation 2.38 corresponds to the interaction between two matter or two antimatter masses while the plus sign gives the coupling in the matter-antimatter case. In the

context of the same spontaneous symmetry-breaking process giving mass to both the vector and scalar, we can consider the case where both bosons acquire roughly the same mass. If we now ignore, for the moment, the complicated information about the couplings that are contained in the values v and s and algebraically set $v \approx s$, we see that a composition independent test of the $1/r^2$ would lose all sensitivity to the pair of interactions. This sort of cancellation is not unreasonable, for instance, when considering a vector coupling to baryon number and a scalar coupling to $T^{\mu}{}_{\mu}$. In this case the sensitivity of, say, a borehole or tower experiment would be roughly 10^{-3} of the sensitivity for either interaction alone. For a composition-dependent search, however, the full sensitivity to the vector part of the interaction would be maintained.

Nieto and Goldman argue that more precise cancellations may in fact occur. To support this possibility they have suggested several exotic vector and scalar couplings which depart from the forms for the effective charge given in Section 2.4.2 [82]. For instance, they suggest, among others, a vector coupling to the dilatation current

$$J^{\mu} = X_{\nu} T^{\mu\nu} \tag{2.39}$$

which would yield a gravivector interaction precisely proportional to mass for composite systems. They also consider graviscalar couplings to the square of the field-strength tensor for the gauge fields. This scenario leads to interaction terms roughly proportional to the baryon and lepton numbers. They point out that tuning the various coupling coefficients which result could allow a rather precise cancellation of a vector coupling to some combination of baryon and lepton numbers by the scalar field.

Clearly, scenarios can be devised which make the partners of the graviton invisible to the current round of experiments looking for composition-dependent and independent interactions. However, the tailoring of the interactions to explain the current

lack of experimental evidence for one or both seems, at best, not very compelling. In the event that such a cancellation does occur, and if we restrict ourselves to experiments which operate in the static limit, the only method available for verifying the existence of the vector and scalar parts of gravity is to weigh some antimatter in which case the two contributions sum instead of cancel. For vector and scalar contributions which don't cancel, a combination of composition-dependent and independent tests employing normal matter can, in principle, fully characterize the pair of interactions without resorting to antimatter tests [83].

Chapter 3

Some General Considerations

Before proceeding to a description of the specific pieces of apparatus used in the Princeton experiments, we will consider some general issues of torsion balance sensitivity to signal, sensitivity to systematic effects, and noise performance. We do this in the context of a linearly damped harmonic oscillator which is subject to a constant external signal or systematic torque and various noise torques. The equation of motion can be written as

$$I\ddot{\theta} + 2\beta\dot{\theta} + \kappa\theta = \tau(t) \tag{3.1}$$

where I is the moment of inertia, β is the inverse time constant (for the oscillator *amplitude*), κ is the torsion constant, and τ represents all externally applied torques. With these parameter definitions the homogeneous solution is given by

$$\theta_h(t) = e^{-\beta t}(A\sin\omega_1 t + B\cos\omega_1 t) \tag{3.2}$$

where $\omega_1^2 = \omega_0^2 - \beta^2$ with $\omega_0^2 = \sqrt{\kappa/I}$. For a composition-dependent external torque which couples differentially to the two halves of the torsion balance, we have

$$\tau_{signal} = \tau_s \sin\psi \tag{3.3}$$

where ψ is the angle between the dipole axis of the torsion balance and the horizontal component of the composition dependent acceleration and τ_s is the maximum torque which can be exerted. Thus we have $\sin\psi \approx +1$ or -1 for a Cavendish-type

experiment and $\sin\psi \approx \psi \approx +\theta$ or $-\theta$ for a Boys-type experiment. For a Cavendish measurement, we may ignore the dynamic terms in Equation 3.2 and write the sensitivity, S_C, as

$$S_C = \Delta\theta = \frac{\tau_s}{\kappa}. \tag{3.4}$$

For the Boys measurement, the external torque effectively increases or decreases the torsion constant by τ_s, depending on the orientation. Thus the dynamic sensitivity, S_B, which is determined by the induced shift in the oscillator frequency, can be written as

$$S_B = \frac{\Delta\omega}{\omega} \cong \frac{\tau_s}{2\kappa}. \tag{3.5}$$

Note that the dynamic technique has only half the intrinsic sensitivity of the static technique. Hence it might be argued that a static measurement is the method to pursue. Response to noise and systematic effects are somewhat different for the two methods, however, making such a judgement impossible, *a priori*.

3.1 Signal Strength at a Terrestrial Site

Terrestrial source experiments are sensitive to any horizontal component of the earth's gravitational field. As was mentioned in Chapter 1, the optimal experimental location is half-way down the face of a cliff which is much larger in extent than the range of interest. In practice, the experimental site is typically a location exhibiting terrain with large slope. In this case we can define an effective tilt, θ_t, of the terrain which is obtained by averaging over the range of the force and which corresponds to the angle of inclination necessary for an "infinite" plane of material to exert the same force as the actual source-mass distribution. The maximum torque exerted on a torsion

balance configured as a composition dipole, with two masses m, is then given by

$$\tau = \frac{3}{2R_\otimes}\left(\frac{\alpha_0\lambda}{1+\alpha_0}\right)\left(\frac{\rho_{local}}{\rho_\otimes}\right)\left(\frac{C_\otimes}{\mu_\otimes}\right)\left(\frac{C_2}{\mu_2}-\frac{C_1}{\mu_1}\right) mg\ell\sin(\theta_t) \tag{3.6}$$

where $R_\otimes$, $\rho_\otimes$, and $C_\otimes/\mu_\otimes$ are the earth's radius (assumed to be far larger than λ), mean density (5.5 g/cm^3), and effective charge per unit mass, respectively. ρ_{local} is the local mass (rock) density, the C_i/μ_i are the effective charges of the test masses and ℓ is the effective moment arm of the torsion balance. Note that, for small α_0, this technique is sensitive to the product, $\alpha_0\lambda$, of the strength and range of the interaction.

3.2 Torsion Balance Sensitivity

Equations 3.4 and 3.5 express the sensitivity in terms of two parameters, τ_s and κ. This statement is actually somewhat misleading. Since τ_s is proportional to the masses of the two materials used and since the maximum mass that can be employed is determined by the tensile strength of the torsion fiber, both τ_s and κ can be expressed in terms of fiber properties. We want to examine the general scaling of the sensitivity to differential forces with respect to fiber size and strength. The maximum load which can be supported by a fiber scales approximately as r^2 where r is the fiber radius.[1] The torsion constant of the fiber scales approximately as r^4/L, where L is the length of the fiber. Ignoring the precise torsion balance geometry, the mass to be supported by the fiber scales roughly as R^3 where R is the characteristic linear dimension of the balance. Hence the magnitude of the signal torque, τ_s, scales as

$$\tau_s \propto MR \propto R^4. \tag{3.7}$$

[1]It should be mentioned that the fiber sizes utilized in these experiments have diameters of order 25 μm and that the mechanical properties of fibers in this range begin to have significant contributions from surface effects (See for example the book by Strong [84] which summarizes the situation in the case of quartz). This results in departures from the precise scaling relationships derived in this section. These departures will not affect any of our conclusions, however.

Thus we expect the sensitivity, in general, to scale roughly as

$$S \propto Lr^{-4/3}. \tag{3.8}$$

In practice, the scaling relationship departs from this form due to the specific geometry of the torsion balance used (See Appendix C). The use of spherical shell and toroidal geometries tends to lessen the $1/r^p$ dependence of the sensitivity. In fact, an idealized toroid shows no r dependence.

In the end, finite fabrication tolerances limit how small the torsion balance can reasonably be made—for instance, the relative contribution from gravitational gradients will grow as δ/R as $R \to 0$ for a fixed tolerance δ. We have found that balances with characteristic dimensions of a few inches are reasonable to build and mount for use.

3.2.1 Torsion Fibers

We must also consider that there is a choice of fibers available with which to hang our torsion balance. It is standard to load a fiber to a substantial fraction of its breaking strength in order to maximize signal. This fraction is typically around 50% . Thus r^2 of the fiber scales as the inverse of its tensile strength, S_{tens}, and the torsion constant scales as

$$\kappa_{wire} \propto r^4 \propto \frac{1}{S_{tens}^2}. \tag{3.9}$$

Table 3.1 shows the mechanical properties of the principal fiber types we have employed. The obvious choice of fiber material in this context is tungsten with its tensile strength more than twice that of steel. This choice is complicated, however, by the fact that tungsten is polycrystalline. In a static experiment this results in fiber creep where the equilibrium angle of the fiber periodically undergoes a shift because of a

Fiber Material	Young's Modulus (10^{11}dynes/cm^2)	Rigidity Modulus (10^{11}dynes/cm^2)	Tensile Strength (10^{11}dynes/cm^2)
Tungsten	35.5	14.8	0.41
Be-Cu Alloy	12.7	5.0	0.13
Quartz	7.1	3.1	0.11
Carbon Steel	20.0	8.11	0.15

Table 3.1: The mechanical properties of some fiber materials we have employed are shown. Tungsten and steel values come from Reference 85; Be-Cu Alloy from Reference 86; and quartz values from References 84 and 87.

realignment of the crystals. In a dynamic experiment it is manifested as nonlinearities in the restoring torque of the fiber leading to an amplitude dependence of the oscillator frequency.

3.3 Systematic and Noise Constraints in Torsion Balance Measurements

As has already been pointed out, the scaling relations obtained above give only a very incomplete picture of the measurement capability of a torsion balance. Fundamental noise limitations and a host of potential systematic effects combine to place significant constraints on the attainable precision and accuracy of these measurements. The following sections provide a survey of several sources of such limitations. The reader is referred to the accompanying chapters on the two Princeton experiments for more specific details of the impact of these effects on our two pieces of apparatus.

3.3.1 The Thermal Noise Limit

Thermal noise sets an unavoidable lower limit on the size of forces that can be measured by torsion balances. We now consider contributions to τ in Equation 3.1 which

are due to thermal excitations of the system. We can immediately write down the size of such contributions by considering the equipartition theorem. In the context of measuring a static angular displacement this gives a mean square noise amplitude

$$\tfrac{1}{2}\kappa\left\langle\theta^2\right\rangle = \tfrac{1}{2}k_BT. \tag{3.10}$$

This expression, however, greatly exaggerates the thermal limit that can be achieved in typical torsion balance experiments if careful signal averaging is carried out. The reason, as was pointed out by Boynton [88], is that such excitations of the torsion balance remain coherent over many cycles.[2] To see how this works, consider starting a measurement of the displacement at time t=0 where the result will be obtained by averaging the signal over an integral number of oscillator cycles. Since the system is in thermal equilibrium, there will be some initial angular displacement and velocity due to thermal excitation. On average these will be given by:

$$\theta_0^2 = \frac{k_BT}{\kappa} \tag{3.11}$$

$$\dot{\theta}_0^2 = \frac{k_BT}{I}. \tag{3.12}$$

Using these values as boundary conditions to specify the constants in Equation 3.2 gives:

$$\theta(t) = e^{-\beta t}\left[\theta_0\left(\cos\omega_1 t + \frac{\beta}{\omega_1}sin\omega_1 t\right) + \frac{\dot{\theta}_0}{\omega_1}\sin\omega_1 t\right]. \tag{3.13}$$

and the resulting "noise signal" averaged over one cycle is

$$\frac{1}{P}\int_0^P \theta(t)dt \approx \frac{1}{2Q}\sqrt{\frac{k_BT}{\kappa}} \tag{3.14}$$

to lowest order in

$$Q^{-1} = \frac{\beta P}{\pi}, \tag{3.15}$$

[2]In the interest of accuracy, we note that Dicke, *et al.* [18], had pointed out that signal averaging over integral cycles of the oscillator period would yield a greatly improved thermal noise limit in their 1964 paper.

where P is the balance period. Now we must also consider the noise which enters the system during the measurement cycle. It will be found that it is this source which dominates the sensitivity limit. To estimate this contribution, we recall Nyquist's theorem for thermal fluctuations in a dissipative system [89] which specifies the mean square thermal torque as

$$\left\langle \tau_{noise}^2 \right\rangle = 4k_B T \left(2\beta I\right) \Delta f \tag{3.16}$$

where $2\beta I$ gives the dissipation in the system and Δf is the bandwidth. We identify Δf with the inverse sampling time which we will take as one period of the oscillator. The mean square fluctuation can now be estimated as

$$\begin{aligned} \left\langle \theta^2 \right\rangle &\approx \frac{1}{\kappa^2} \left\langle \tau_{noise}^2 \right\rangle \\ &\approx \frac{4k_B T \left(2\beta I\right)}{\kappa^2 P} \\ &\approx \frac{2k_B T}{\pi \kappa Q} \end{aligned} \tag{3.17}$$

so that the RMS noise amplitude from this contribution scales as $\sqrt{Q^{-1}}$ which dominates the amplitude uncertainty given in Equation 3.14 for large Q. Thus Equation 3.17 represents the thermal noise limit for single-cycle averaging in a static measurement. If we extend the averaging over N cycles, we obtain

$$\left\langle \theta^2 \right\rangle \approx \frac{2k_B T}{N \pi \kappa Q}. \tag{3.18}$$

There are two standard methods which can be used to minimize the size of $\langle \theta^2 \rangle$ as given by Equations 3.17 and 3.18. First, Q can be maximized by operating the torsion balance in high vacuum, thereby minimizing the damping contribution due to the viscosity of the gas in the apparatus. Second, the system can be "cooled" by introducing electronic damping. Such damping provides an effective route to remove energy from the system without introducing the thermal fluctuations which

are inherent when the dissipation is into a reservoir with which the system is in thermal equilibrium. If we specify the electronic Q-factor as

$$Q_{elec} = \frac{\omega}{2\beta_{elec}}, \tag{3.19}$$

where β_{elec} is the inverse time constant due to the electronics, and we assume that the electronic damping is much larger than the viscous damping, the effective temperature of the system is

$$T_{eff} \approx T\left(\frac{Q_{elec}}{Q_{viscous}}\right) \tag{3.20}$$

which offers substantial noise performance improvement for high-Q systems.

In the case of a period measurement in a dynamic system, thermal noise results in a random walk of the oscillator phase [88] which, in turn, causes variations in the measured period. Appendix D estimates the impact of these variations on the measured period. The resulting mean-square fractional uncertainty in the period measurement is given by Equation D.12

$$\left\langle\left(\frac{\Delta P}{P}\right)^2\right\rangle \approx \frac{k_B T}{4\pi N \kappa Q \theta_0^2}$$

Note that the RMS timing uncertainty scales as $1/\theta$ so that operating at fairly large amplitudes improves the noise performance. Substantial improvement is also obtained by using oscillators with large Q.

3.3.2 Vibrational Noise

For the two Princeton experiments the noise levels have been dominated by vibrational as opposed to thermal noise. There are three general sources of such noise to be considered: seismic noise, weather-related noise, and man-made noise (*i.e.*, "cultural" noise). There are several specific mechanisms by which we expect such vibrations to

couple into the torsion mode of our oscillators. In principle, angular excitations of the foundation on which the apparatus rests provide a direct excitation. We expect, however, that linear motions of the foundation are the dominant source of of vibrational input to each apparatus. Thus we will examine some obvious mechanisms for linear motions to influence our torsion signals.

First we consider a situation where the natural twist of a fiber is a function of the tension, or equivalently the stretch, of the fiber. Such a dependence is evidenced by the behavior of fibers when tension is initially applied—for instance, in the case of our tungsten fibers, a fiber typically undergoes a period of "untwisting" upon application of tension which persists for days to weeks. We write this dependence as

$$\theta_0(\ell) = a(\ell - \ell_0) + b(\ell - \ell_0)^2 + \ldots \tag{3.21}$$

where θ_0 is the equilibrium angle of the torsion balance and ℓ_0 is the unperturbed length of the suspension fiber. Vertical excitations of the balance lead to an oscillatory torque from the shifts in the equilibrium angle. With the typical fiber loadings and lengths employed in these experiments, the vertical stretch mode has a frequency, $f \geq 10$ Hz, much higher than the natural frequency of the torsion oscillation. The torsion amplitude response is thus suppressed from the equivalent DC response by a factor f_0^2/f^2. Furthermore, at these frequencies, passive vibrational isolation is a fairly effective method of preventing unwanted balance excitations.

As was noted by Dicke, *et al.* [18], the presence of the second, nonlinear, term in Equation 3.21 leads to a mean displacement of the equilibrium angle of the torsion balance when the stretch mode is excited. If the torsion balance is operated in high vacuum so that the Q of this mode is extremely large, this can pose a problem for an experiment measuring a static displacement. By operating our experiments in air (or helium), the lifetime of a mode with the characteristic frequency of the stretch mode

is relatively short, of order a few hundred seconds, so that any major angular offsets from this source will die away quickly on the typical integration timescale of our static measurement. In the case of a dynamic measurement, it is the time-dependence of the mean displacement which will affect the period measurement. But again, the short lifetime of this mode at atmospheric pressure makes it possible to selectively remove segments of data when major oscillations of this type have been excited.

Horizontal motions of the torsion balance suspension point result in excitation of the pendulum modes of the balance. These excitations can couple to our torsion signal in several ways. In principle there is a stretch coupling, as just discussed, associated with this mode due to the time-varying tension on the fiber as the pendulum swings back and forth. However, for small oscillations this effect is presumably small. Probably a more significant coupling to the torsion mode arises from the bending stresses induced around the suspension points as the balance oscillates. Such stresses are also expected to change the effective equilibrium angle of the balance, thus driving torsion oscillations. The lowest order contributions to such a coupling presumably have the same form as has already been discussed. Another mechanism by which the pendulum modes of the balance are expected to affect any measurement is by the resulting physical displacements coupling into the detection system employed. In the case of our static displacement apparatus, movement of the balance vane (See Chapter 4) relative to the other components of the capacitance bridge resulted in systematic shifts of the torsion signal. In the case of our dynamic apparatus, side-to-side displacements of the optical elements on top of the balance lead to angular shifts in the detection system which will appear as timing shifts if there is movement of the balance between successive zero crossings (See Chapter 5 for details of this detection system). A final, more direct manner in which the pendulum modes can couple to

the torsion mode is via the moment of inertia tensor. If the balance experiences a rocking motion which is not around a principal axis, torques will be generated about the other axes of the balance. These types of issues had to be considered in some detail for the dynamic apparatus and we will defer a detailed description of this effect until Chapter 5.

An important point to note with any of these mechanisms is that the fundamental excitation frequencies are considerably higher than the torsion balance frequency. As has already been mentioned in the case of the stretch mode, this results in "filtering" of the excitation so that the excited torsion amplitude is smaller by a factor of f_0^2/f^2 than would be the case for a DC torque applied to the balance. Furthermore, the higher frequencies result in increased damping of these modes at atmospheric pressure due to excitation of wave motions in the fluid (See Appendix E). Finally, for frequencies above about 1 Hz, passive vibrational isolation techniques become effective. Both Princeton experiments have relied heavily on passive isolation. Thus proper isolation of the apparatus minimizes excitation of most of these modes. The lowest frequency mode of the balance is the simple pendulum mode which oscillates at very near 1 Hz for all of our balance configurations. Excitations of this mode are highly suspect as the major source of vibrational noise coupling into our torsion signals.

3.3.3 Gravitational Gradients

Terrestrial sites which are useful for intermediate-range interaction searches are inevitably associated with large local gravitational gradients. As a result, care must be taken to insure that the torsion balances employed possess sufficient symmetry not to introduce spurious signals from standard Newtonian couplings. In principle it is not difficult to design a torsion balance possessing a mass distribution where the mass

multipole moments vanish to several orders. Limits are imposed on the implementation of such designs, however, due to imperfect fabrication and assembly capabilities. In particular, the ability to maintain a high degree of symmetry is sorely tested by the need to construct a composition-dipole balance from comparison materials with very different physical properties (note that the densities of polyethylene and copper used in our balances differ by an order of magnitude). We have employed balances with toroidal and spherical geometries during the course of our research. The details of each design will be provided with the descriptions of the specific experiment. Nevertheless, we will take a moment here to provide some estimates of the level at which gravitational effects may become important.

The presence of a balance quadrupole moment results in couplings to the first order derivatives of the gravitational field. The most demanding operational situation arises when the balance is located at the edge of cliff. This configuration provides half of the maximum signal sensitivity but also maximizes the local gravitational gradients. Figure 3.3.3 shows the calculated gradients for a torsion balance mounted at a height of 30 cm above ground level near the edge of a 160 m high ideal cliff. This approximates the situation that would exist at the Palisades cliff along the Hudson River overlooking New York City, a potential experimental site. Our coordinate system takes the x-axis to point outward from the cliff, the y-axis along the cliff face, and the z-axis vertical. For a quadrupole which is not azimuthally symmetric there will be couplings to the horizontal gradients of g_x and g_y. For a toroidal balance geometry, the dominant effect comes from considering a balance tilt coupling to the $\partial g_x/\partial z$ and $\partial g_y/\partial z$ derivatives as the balance rotates. Let's take a toroid of mass 200 g with radius 5 cm and negligible cross-section which is tilted at an angle of 1 mrad from horizontal. A vertical gradient of 10^3 Eötvös results in an anomalous

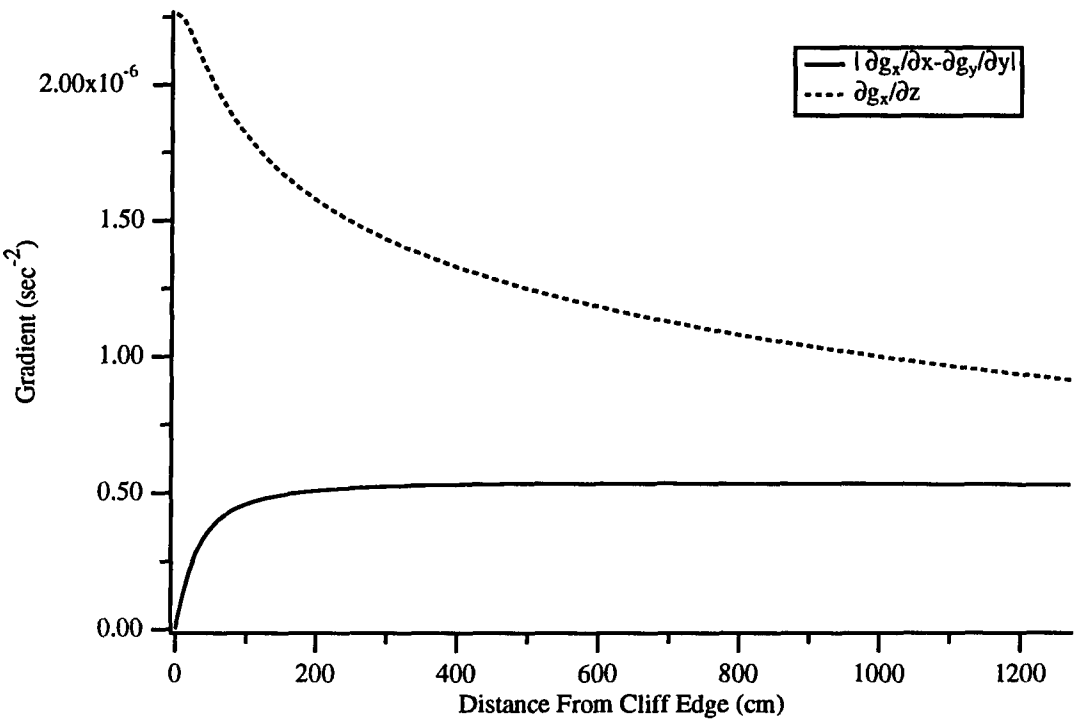

Figure 3.1: Gravitational gradients near the edge of an "ideal" cliff of infinite width and depth and a height of 160 meters.

signal of 5×10^{-6} dyne-cm upon 180° rotation which would appear as an anomalous acceleration of 8 nGal.[3] An equivalent torque would be exerted on a "barbell" balance, with the same total mass and a 10 cm length, by a 75 kg man standing 1.7 m away at an angle of 45° with respect to the balance axis.

The situation described above is vastly improved by choosing an experimental site with approximately uniform slope—a 30° slope giving the same source strength as a location at the top of a cliff. This leads to vertical gradients that are more than an order of magnitude smaller and somewhat reduced horizontal gradients. Furthermore, the assumption of a 1 mrad tilt is rather gross if care is taken with the mounting of

[3]Note that a Galileo is a convenient unit of measure commonly used by geophysicists. $1 Galileo(Gal) \equiv 1 cm/s^2$. Another convenient unit which will be of use shortly is the Eötvös which is a measure of gravitational gradients. 1 Eötvös (E) = 1nGal/cm = $10^{-9}s^{-2}$.

the balance. Our balances have typically been constructed with a 10.2 cm outer diameter so that 1 mrad corresponds to a 0.01 cm vertical displacement from side to side. This represents only a modest levelling of the balance and, using simple mechanical techniques, we should be able to verify the toroid tilt to nearly an order of magnitude better than this. The point of this argument is that a carefully designed and assembled toroid should allow differential acceleration measurements at the level of 0.1 nGal at a suitable site.

Further improvements can be attained by minimizing the quadrupole moment of the torsion balance. With a cylindrical geometry, masses to null the quadrupole moment can be located above and below the toroid on the vertical axis. With our second apparatus we pursued a spherical geometry in hopes of minimizing multipole contributions to all orders. The details of our torsion balance designs are contained in the following two chapters.

3.3.4 Temperature Drifts

Sensitivity to temperature variations is unavoidable in a mechanical measuring device. We broadly divide these variations into two classes:

1. Temperature-induced mechanical changes in the apparatus which result in a time-varying output signal correlated with the temperature, and;
2. Thermal gradient effects which can introduce spurious signals and instabilities in the gas which surrounds the apparatus.

In each of our experiments, we have observed diurnal drifts associated with the first category. This section will consider some mechanisms for these drifts. Note that our experimental situation in this case is somewhat more tractable than that faced by Dicke, *et al.*, since our fundamental measurement timescale is not set by the rotation of the earth.

Fiber Material	Temperature Coefficient of the Rigidity Modulus, $\gamma(^\circ C^{-1})$	Coefficient of Linear Expansion, $\alpha(^\circ C^{-1})$
Tungsten	(about)-2×10^{-4} (See footnote)	4.43×10^{-6}
Quartz	$+1.3\times10^{-4}$	0.3×10^{-6}

Table 3.2: Temperature coefficients of fiber materials. Tungsten values are based on Reference 90 while those for quartz are from chapter 5 of Reference 84.

In a Cavendish-type experiment, the most direct link of temperature variations to the torsion signal is via a mild temperature dependence of the equilibrium angle of the fiber. Further variations presumably result from temperature induced changes in the detector geometry. Overall, the situation may be quite complex and our approach has been to analyze data sets that span periods of smoothly varying signal and take the drifts into account during the fitting process.

For the Boys technique, it is possible to be somewhat more quantitative in our assessment. Temperature-induced changes of the apparatus geometry should only enter dynamically since a static shift in the detector alignment will not affect the timing measurement. In this case, we expect the timing variations to be dominated by a temperature dependence of the torsion constant of the suspension fiber and by changes in the geometry of the torsion balance itself. Table 3.2 gives values for the temperature coefficients of our primary torsion fiber materials.[4] There are a couple things to note about these numbers. First, the temperature dependence of the torsion constant, $\kappa = {}^{\pi Z r^4}/_{2\ell}$, is dominated by changes in the modulus of rigidity as

[4]The temperature dependence of the rigidity modulus, γ, for tungsten contained in Table 3.2 is a very rough estimate based on the change in the Young's modulus over a 1000° C interval. Since the rigidity modulus is related to Young's modulus by $Z = Y/2(1+\nu)$, where $\nu \approx 0.28$ is Poisson's ratio for tungsten, we expect the rigidity modulus to scale roughly as the Young's modulus with any temperature dependence in Poisson's ratio to enter as a correction. The gross temperature range used to estimate the Young's modulus temperature coefficient renders these numbers suitable only for very gross estimates of the temperature dependence, however. Temperature dependences in our dynamic apparatus appeared substantially smaller than the above estimate would imply.

opposed to dimensional changes of the fibers. Secondly, the temperature dependence has opposite sign for the two materials (tungsten is polycrystalline whereas quartz is a vitreous material). Thus we expect the temperature dependence of the torsion period from this source to be

$$\frac{\Delta P}{P} = -\frac{1}{2}\gamma\Delta T \tag{3.22}$$

Thermal expansion and contraction of the torsion balance affect the period of oscillation via the moment of inertia. To lowest order the moment of inertia behaves as

$$\Delta I \approx 2I\Delta T \tag{3.23}$$

where α is the coefficient of linear expansion and the induced period shift is

$$\frac{\Delta P}{P} \approx \alpha\Delta T. \tag{3.24}$$

For most materials, α is a few parts in 10^5. Thus the balance portion of the temperature effect is smaller, but not negligibly so, than our estimated fiber contributions. Our estimate for the overall temperature dependence of the period is then

$$\frac{\Delta P}{P} \approx \left(-\frac{1}{2}\gamma_{fiber} + \alpha_{balance}\right)\Delta T. \tag{3.25}$$

Thus we expect temperature drifts to enter the dynamic experiment at least at the level of $\left(\Delta P/P\right) \approx$ a few $\times 10^{-5}$ per degree C.

Another temperature-related effect is pressure gradients introduced in the gas surrounding the balance due to thermal gradients in the apparatus. We will discuss this issue in the following section.

3.3.5 Gas Perturbations

The presence of thermal gradients across the apparatus leads to pressure differences and thus convection currents which can exert forces on the torsion balance. These effects were already mentioned in Chapter 1 as a possible explanation for the EPF data requiring no new physics. They can be minimized by requiring a high degree of symmetry in the torsion balance so that the two halves do not present different cross-sections to any convective air flow in the system. Horizontal temperature gradients are minimized by using multiple layers of insulation and conducting surfaces around the balance and providing a large thermal reservoir in the form of a thick-walled aluminum housing. We seem to have been successful in maintaining the overall thermal stability of the atmosphere in the inner portions of each apparatus by maintaining a small vertical temperature gradient. In our early tests, we saw evidence for atmosphere instabilities during periods of substantial temperature variations in the form of wild fluctuations in our output signal. Measurements made with moderate temperature stability and the vertical temperature gradient being maintained have shown no evidence for this type of effect.

3.3.6 Rotation Effects

As has already been mentioned, the requirement that the apparatus be rotated to make a measurement substantially increases its susceptibility to a variety of systematic effects. Needless to say, any rotation must be undertaken with great care in order to prevent a major shock to the fiber which could result in an irreversible change in the fiber's properties. Once the rotation of the apparatus to its new orientation has been accomplished, concern focuses on whether the top of the fiber has experienced a slight bend due to a levelling difference between the two positions. As was discussed

in Section 3.3.2, such a bend is expected to shift the equilibrium angle of the fiber at some level, thus leading to a systematic signal in a static deflection experiment. The situation in the case of a dynamic experiment is somewhat better since we know that twists in thin fibers tend to propagate along the local fiber axis and should "penetrate" around any bend. Nevertheless, a small levelling dependence cannot be dismissed out of hand.

Another concern of this type, which is directly associated with the rotation process, is excitation of the pendulum modes of the balance by the rotations between positions. Such an excitation will occur if the top suspension point of the torsion fiber fails to lie on the rotation axis. Mechanical tolerances in the apparatus lead us to expect that a misalignment of several thousandths of an inch are likely. Since apparatus rotations typically take place on time scales much longer than the periods of the pendulum modes, however, they drive these modes only very weakly. For instance, with the most rapid rotations used with our dynamic apparatus, the amplitude of the induced pendulum oscillations is estimated to be no more than microradians. In general, we have implemented a delay after each balance rotation, to allow unwanted oscillations to die away, before beginning to analyze the data in each position.

Other systematic effects which become apparent upon rotation of the apparatus, such as gravitational gradient and magnetic field couplings, have been or will be discussed separately.

3.3.7 Magnetic Contamination

Ferromagnetic contamination of the torsion balance is a primary source of concern when considering systematic effects. The most obvious method for introducing such contamination comes during the fabrication process. If care is not taken with the

Material	Magnetic Susceptibility per gram of material χ_{mass} (cgs units)
Copper	-0.09×10^{-6}
Polyethylene	-0.55×10^{-6}

Table 3.3: Magnetic susceptibilities of our torsion balance materials. The polyethylene value is an estimate based on the available values for ethylene and long-chain alkanes.

cutting tools used to make the balance components, a small tool chip can be embedded in the piece being fabricated or adhere to its surface in some hard to clean spot. We expect such a chip to be highly magnetized due to the stress it undergoes while shearing away from the body of the tool. Noting that the saturation magnetization for iron is roughly 1.7 kG, we consider a chip that is partially magnetized at the level of 100 G and has size $0.001 \times 0.001 \times 0.01$ cubic inches. The torque experienced by such a chip in the earth's magnetic field is of order 10^{-6} dyne-cm. A torque of this size would mimic a true differential acceleration of 5 nGal when using our toroidal balance.

We also consider the magnetic susceptibilities of our torsion balance materials. Both copper and polyethylene exhibit diamagnetism as is shown in Table 3.3. Clearly, it is the polyethylene which dominates the contributions from this source. If the local magnetic field were due entirely to a dipole at the center of the earth, the contribution to the torque on the balance from this source would be entirely negligible. As things stand, unless there is a local concentration of magnetic material to distort the earth's magnetic field and cause anomalously large gradients, we can ignore diamagnetic effects, even in the absence of magnetic shielding around our torsion balance. It would require a local gradient of roughly 1 mG/cm to mimic a fifth force differential

acceleration at the 0.1 nGal level.

3.3.8 Electrostatic Effects

We make brief mention of one final category of systematic effects. Since our torsion balances have employed an insulator as one of the dipole materials, the buildup of charge on a portion of the balance surface is a potentially significant systematic effect. To minimize any buildup, we aluminized and grounded all insulating surfaces. Even with proper grounding, however, contact potentials might still lead to electrostatic effects. Typical surface areas for our balances reach the hundreds of square centimeters level and typical separations within the torsion balance housing are of order centimeters. With moment arms also on the order of centimeters, this could lead to torques on the order of 10^{-6}dyne $-$ cm for a contact potential of 0.1 V, a non-negligible number. One way to avoid this would be to encase the balance in a uniform outer shell (For the vast majority of our tests with our dynamic apparatus, we have employed an aluminum shell null balance for that reason). An important point is, however, that if the amount of charge buildup remains constant and the position of the torsion balance remains fixed with respect to the housing, then such an effect only appears as an offset torque and does not hurt a differential measurement. In the case of our static apparatus, the entire balance housing was rotated with the balance and the relative position of the balance within the housing precisely maintained. We note that any time variation of a contact potential would be expected to contribute to the overall drift of our torsion signal.

Chapter 4

The Static Measurement

We have already described the relatively unexplored region in the α-λ plane for meter to kilometer ranges that existed during the mid-1980's (See Figure 1.2). The aim of the first Princeton experiment was to search for a baryon-dependent interaction of finite range using a device with sufficient sensitivity to constrain a coupling constant at or below the level suggested by the borehole measurements of G described in Chapter 1. This corresponds to $\alpha_0 \sim 10^{-2}$ and $100\,\mathrm{m} < \lambda < 5\,\mathrm{km}$. In order to pursue this goal, an apparatus based on the torsion balance was constructed to compare the relative forces acting on copper and polyethylene in the presence of a horizontal component of gravity due to a major topological feature (See Figure 1.6) [91].

By the time the experiment was completed, substantial interest had also arisen in looking for isospin-dependent forces. The choice of copper and polyethylene as comparison materials was fortuitous in this context. Hydrogen, along with its very low binding energy, exhibits a third component of isospin which is opposite in sign to all of the elements except helium. Thus we were able to place a useful limit on this type of coupling as well. We have also considered the resulting limits on couplings to the bare quark masses as suggested by Scherk [6] and Bars and Visser [78], and to the GUT charge $(B - L)/\mu$. The vector charge differences for these two materials

(based on Table B.1) are:

$$\Delta\left({}^{B}/_{\mu}\right) = 2.24 \times 10^{-3} \tag{4.1}$$

$$\Delta\left({}^{I}/_{\mu}\right) = 0.21 \tag{4.2}$$

$$\Delta\left(\frac{B-L}{\mu}\right) = 0.12. \tag{4.3}$$

4.1 The Apparatus

The apparatus design was governed in large part by the necessity of making 180° rotations of the torsion balance to obtain a signal and the need for a relatively portable instrument for remote site operation. In order to maintain the alignment of the detection system with respect to the rotating portion of the apparatus, the detector elements were completely contained within the torsion balance housing and underwent rotations along with the balance. In order to monitor the angular position of the torsion balances, an aluminum vane was attached to the underside of each. This vane hung between pairs of capacitor plates at either end forming part of an RF capacitance bridge. Signals from this bridge were used to generate a DC feedback voltage which was then applied back to the capacitor plates around the vane. This feedback allowed us to operate the apparatus in a null mode where any external torques on the balance were precisely countered by the applied voltage. Thus the feedback voltage became a direct measure of any differential forces acting on the torsion balance masses.

The instrument was designed to operate at atmospheric pressure to insure that vibrational modes would be quickly damped. In particular, oscillations of the pendulum mode of the balance which would directly affect the capacitance bridge alignment could be kept under control. In terms of portability, this was favorable because there was no need for high vacuum equipment.

A sketch of the torsion balance housing is shown in Figure 4.1. The capacitance bridge and torsion balance were located in a 15 cm O.D. aluminum cannister with 6 mm wall which was mounted on a 28 cm diameter by 1.2 cm thick aluminum baseplate. The entire plate and cannister assembly was suspended as a simple pendulum by a single 0.05 cm steel wire to minimize levelling variations upon rotation. To provide rotation capability, the suspension point of the baseplate was driven by a small electric motor. A precision rotation stage was mounted on the top of the aluminum cannister. This stage allowed angular positioning of the balance vane to nominally center it with respect to the capacitance bridge. A microscope tube with ladder gear was mounted in turn on this rotation stage and provided a means to vertically position the balance. Layers of mu metal sheet were placed both inside and outside the cannister for magnetic shielding. Finally, the entire apparatus was placed in an insulated box for temperature stability. To prevent thermal inversions, the temperature at the top of the box was maintained 2.0–2.5 °C higher than at the bottom during the various data runs. For vibrational insulation, the feet of the box were placed on "lossy" rubber sheets interleaved with lead bricks.

4.1.1 The Torsion Balances

A set of three torsion balances was used in the experiment. Two balances with discrete masses allowed us to check the local gravitational gradients at the remote site while a cylindrically symmetric balance, in the form of a toroid, was used in the fifth force measurement.

The toroidal balance, which we affectionately called the "bagel," is shown in Figure 4.2. The toroid had an outer radius of 5.04 cm and a 2.54×2.54 cm^2 cross section. The density ratio of copper to polyethylene is approximately 10. Thus, to

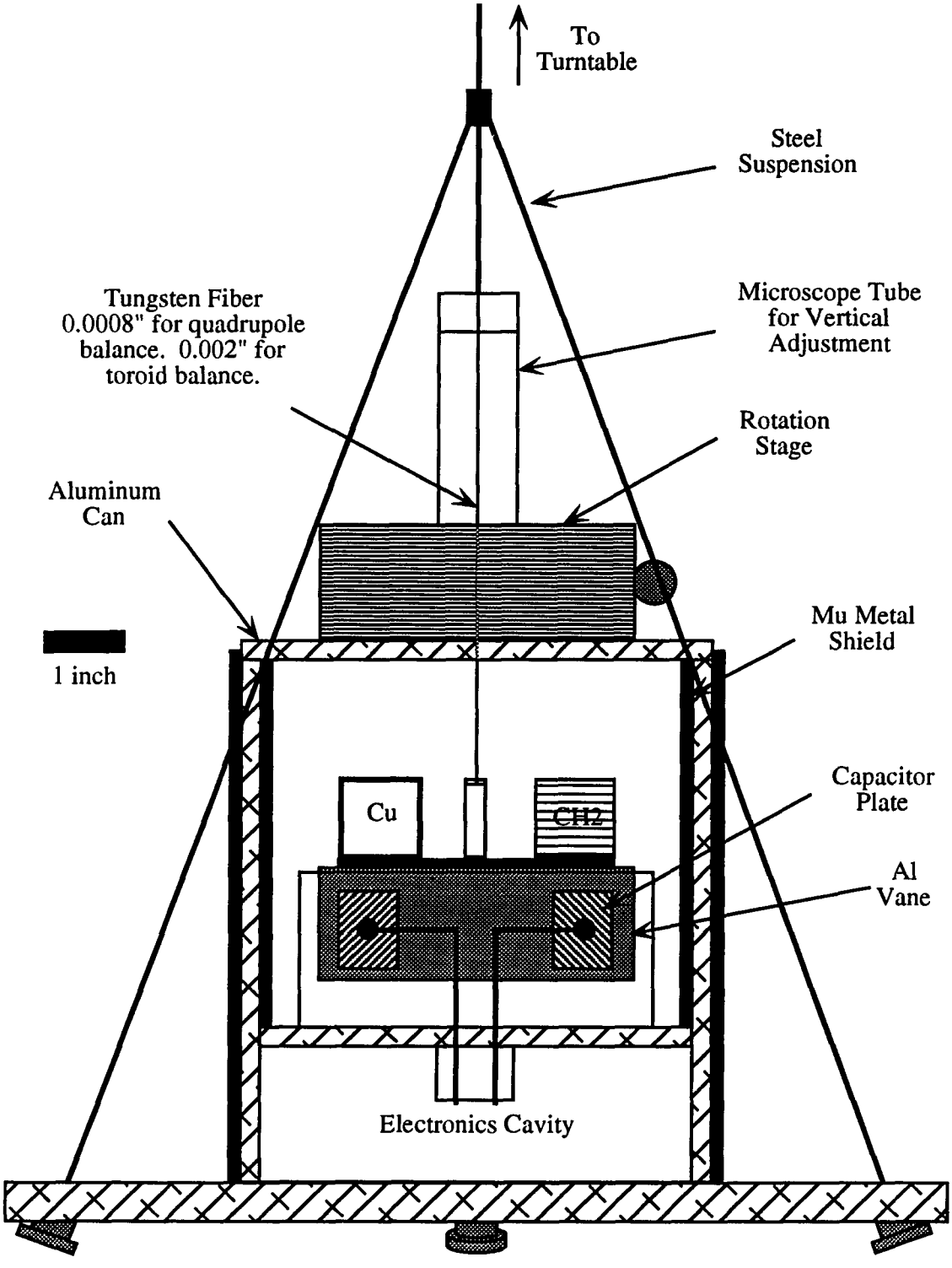

Figure 4.1: A sketch of the torsion balance housing used in the static displacement apparatus.

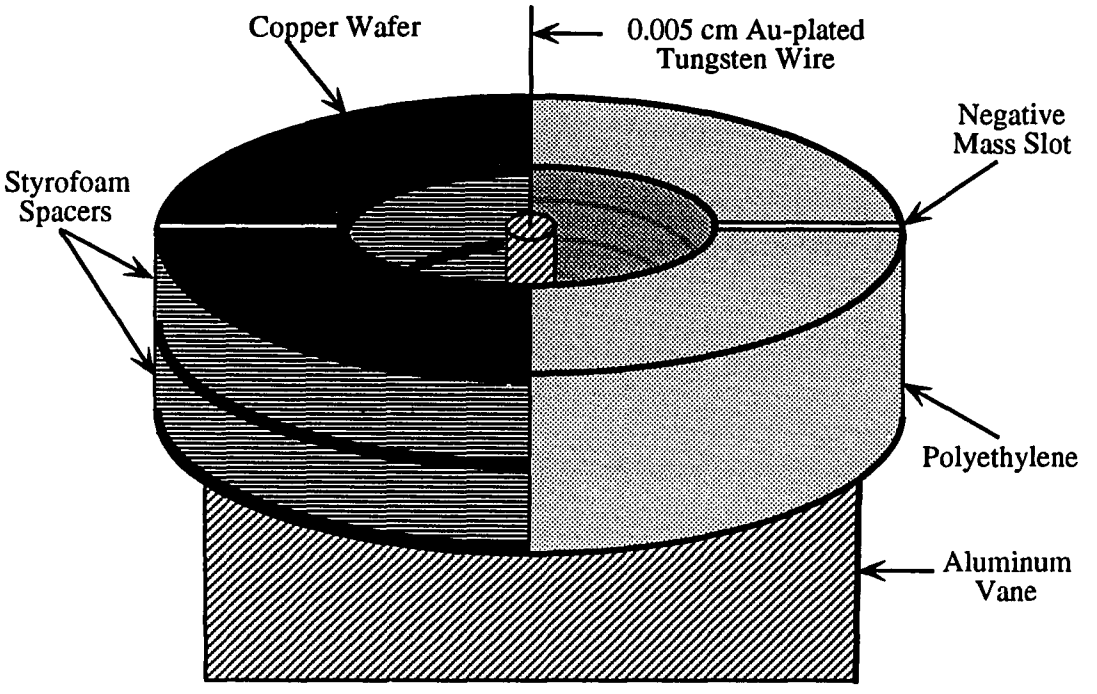

Figure 4.2: The toroidal torsion balance used to obtain fifth force data

match the masses and the cross sections of the two halves, the polyethylene half was solid while the copper half consisted of three layers (the top and bottom layers were nominally 0.76 mm thick while the center layer was 0.89 mm) separated by styrofoam spacers. The total mass of the polyethylene was 65.753 g while the copper was 65 g. The combined mass of the copper and styrofoam was trimmed to match the polyethylene mass. To eliminate any possible systematic effects due to charge build-up on the insulating surfaces, the outer vertical surface of the toroid was sheathed with a grounded sheet of aluminized mylar. Attached beneath the "bagel" was an aluminum vane, an integral part of the position sensing system. The quadrupole moment of the vane was compensated by a slot of material removed from the toroid itself. This balance was suspended by a 0.005 cm diameter gold-plated tungsten wire which had been annealed under tension. This wire also served to electrically ground

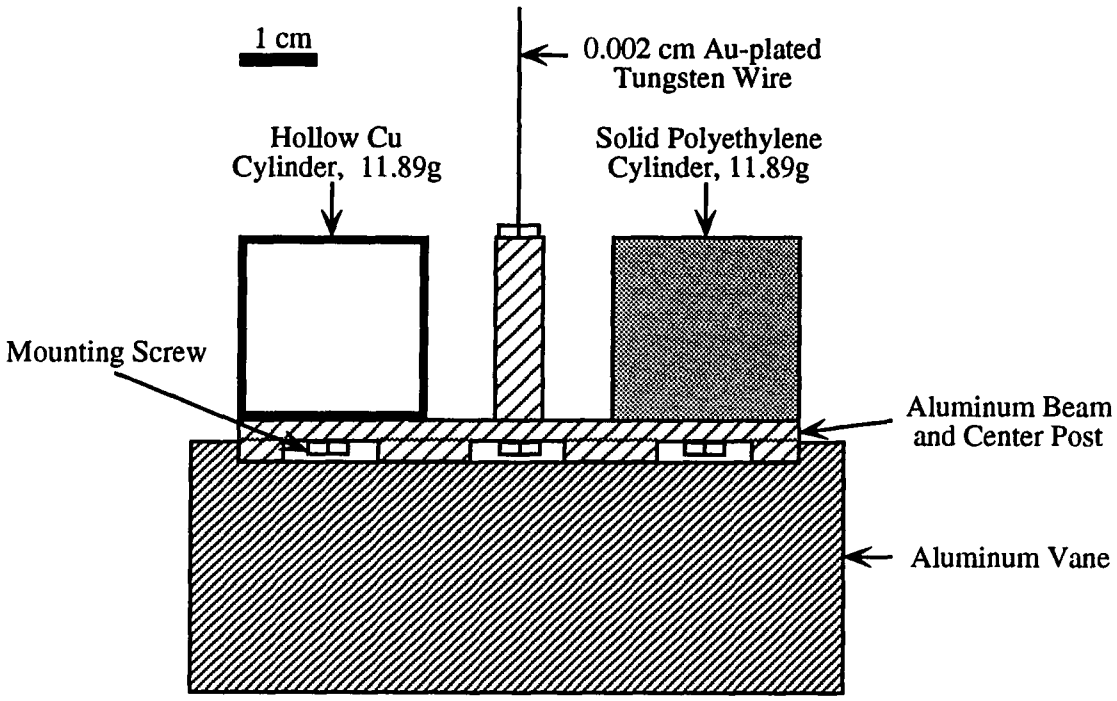

Figure 4.3: The torsion balance used to calibrate the apparatus via a Cavendish measurement and to measure horizontal gravitational gradients at the YBRA site in Montana.

the balance to the rest of the apparatus.

The first of the two gravitational gradient balances, the "Cavendish balance" (CB), consisted of two 11.89 g right circular cylinders, one of polyethylene (solid with an aluminized surface) and the other of copper (hollow with end caps). Each cylinder was 2.54 cm tall and 2.54 cm in diameter and the two were separated by 5.08 cm (See Figure 4.3). This balance was used to measure horizontal gravitational gradients at the remote site and to calibrate the detection system in a Cavendish experiment at Princeton. The final balance, the vertical gradient balance (VGB), shown in Figure 4.4, was designed to measure $\partial g_x/\partial z$ since this was the gradient of primary concern with respect to measurements made with the toroid (Recall from Section 3.3.3 that misalignment of the suspension point on the toroid results in a

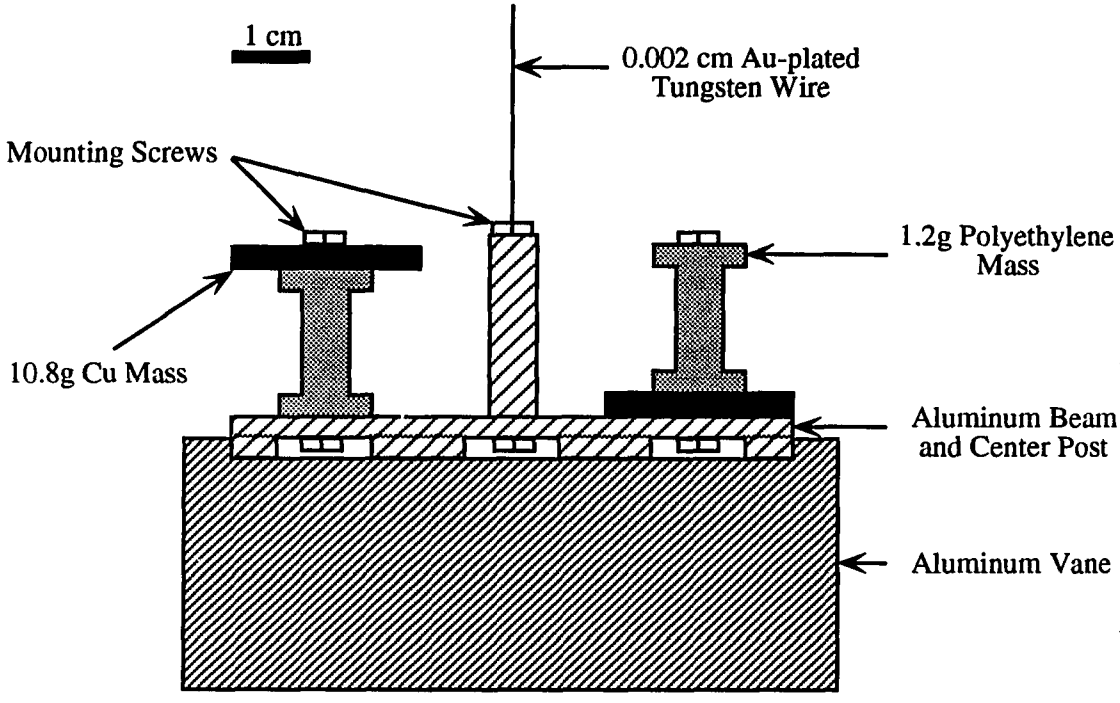

Figure 4.4: The vertical gradient torsion balance used to measure $\partial g_x/\partial z$ at the YBRA site in Montana.

tilt which directly couples to this gradient term). This balance consisted of two 10.8 g copper disks (2.54 cm diameter × 0.24 cm thick) mounted on 2.3 cm tall, 1.2 g aluminized polyethylene posts. The two masses were inverted with respect to each other so that the centers of mass of were vertically displaced by 2.00 cm. Both of these balances were suspended by a 0.002 cm diameter gold-plated tungsten suspension wire.

4.1.2 The Detection and Feedback System

A key feature of the apparatus was the capacitance bridge detection and feedback system as shown in Figure 4.5. The ends of the aluminum vane beneath each torsion balance hung between pairs of capacitor plates which formed part of a 4 MHz

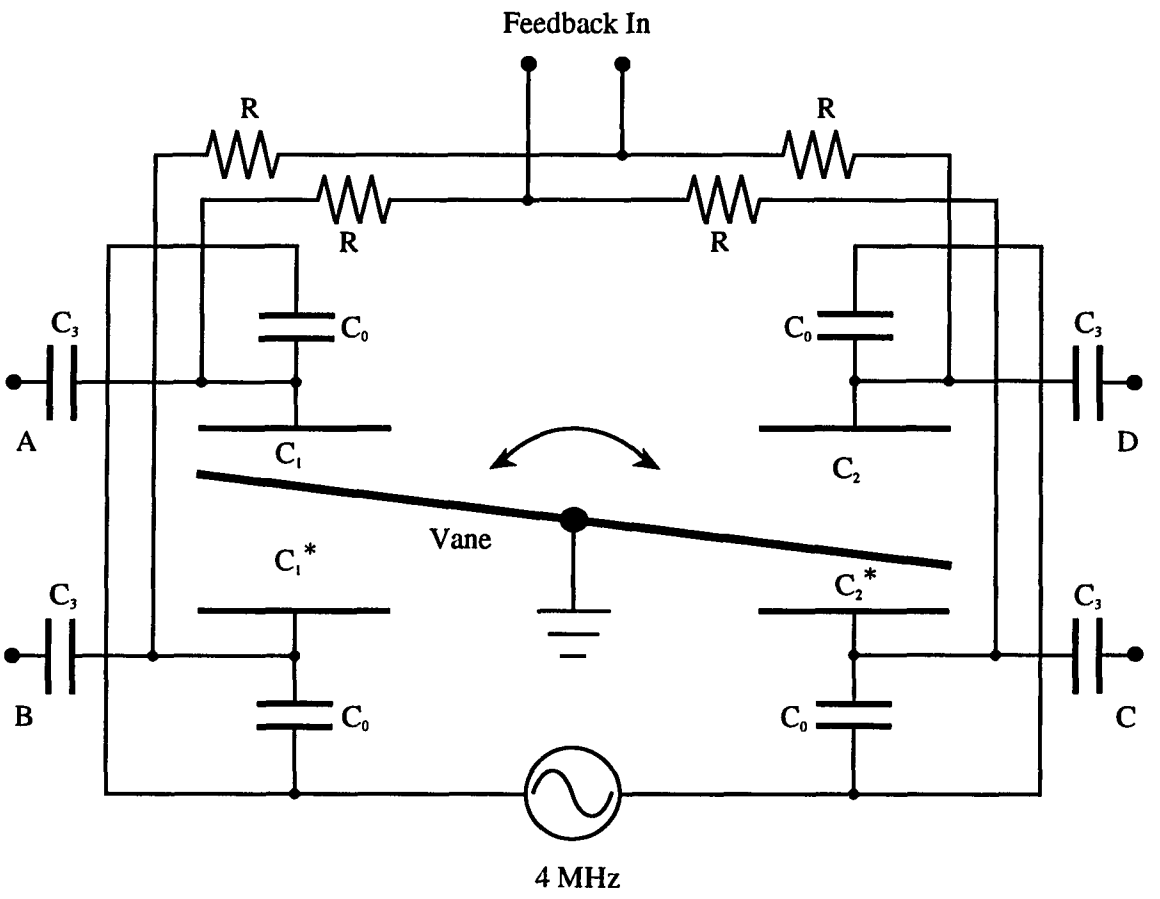

Figure 4.5: The capacitance bridge system which was used to detect angular displacements of the torsion balance as well as pendulum motions in the direction perpendicular to the aluminum vane. DC feedback for the torsion mode was applied through the inner plates of the bridge.

capacitance bridge. Signals from the bridge were differentially amplified, mixed and demodulated to yield both torsion and pendulum displacement signals (pendulum signals were for displacements in the direction perpendicular to the vane). In the case of the torsion mode, a DC feedback voltage was applied to the capacitor plates to maintain the angular alignment of the balance. This feedback voltage provided a direct measure of the external torque on the system, independent of the gain of the amplifier. For the pendulum mode, recall that the entire torsion balance housing

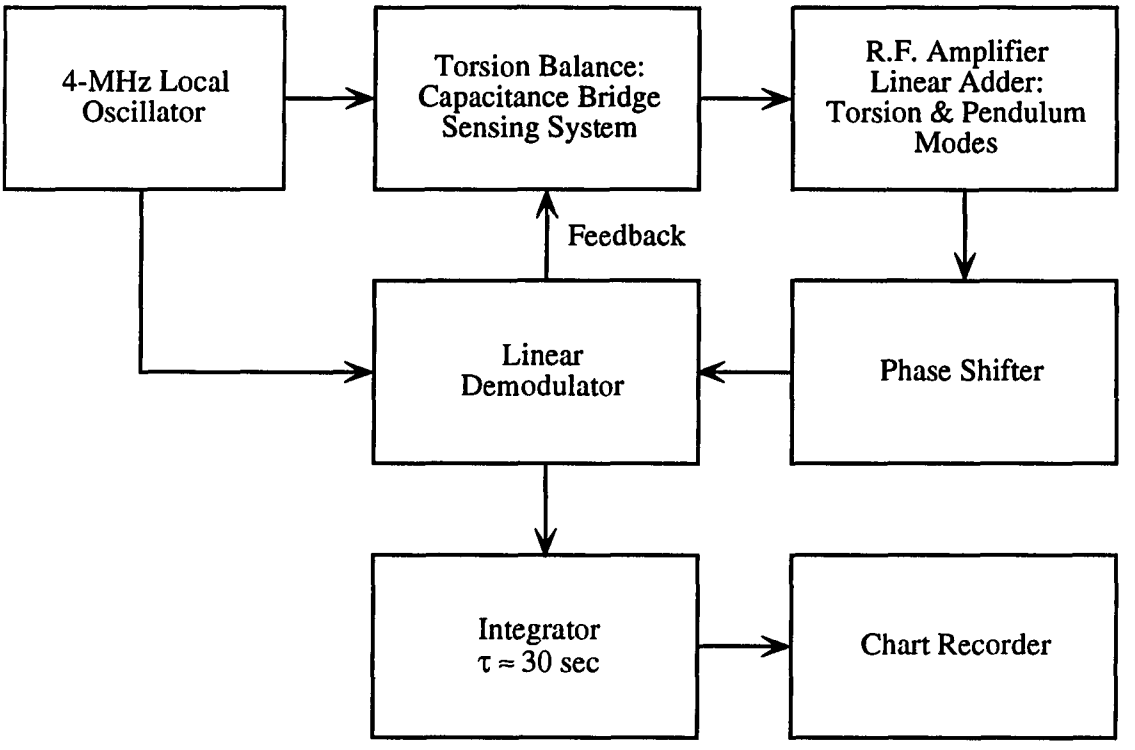

Figure 4.6: A block diagram of the static displacement apparatus.

was suspended as a simple pendulum. This permitted us to use an active levelling system in the dimension sensed by the capacitance bridge. This system consisted of a magnet mounted as the bob on a simple pendulum whose motion was constrained to one dimension. The pendulum angle could be controlled by running a current through a pair of small speaker coils adjacent to the magnet. Note that sensitivity to pendulum displacements in the direction parallel to the vane was minimized by constructing the vane to extend well beyond the fixed capacitor plates at each end as can be seen in Figure 4.1. A block diagram of the detection and feedback system is shown in Figure 4.6.

The maximum signal from the capacitance bridge detector is obtained when C_0 and the vane-to-fixed plate capacitances, C_i, are made equal. This was nominally the

case with our bridge. If we consider a small displacement of the vane from its center position, the change in amplitude of the voltage, ΔV_i, on one of the fixed capacitor plates is

$$\Delta V_i \approx \frac{V_0}{4}\left|\frac{\Delta s_i}{s_0}\right|. \tag{4.4}$$

where V_0 is the amplitude of the driving voltage, s_0 is the separation between vane and fixed plate when the vane is perfectly centered, and Δs_i is the displacement of the vane from the centered position relative to a given fixed plate. If we consider a displacement that is purely torsional and take the sum of the signals from all four fixed plates we have

$$\Delta V_{torsion} \cong V_0 \frac{\Delta\theta}{\theta_0} \tag{4.5}$$

where $\theta_0 = {}^{s_0}/_{l_c}$ and l_c is the effective moment arm of the capacitor plates. Feedback for the torsion mode was generated by applying a DC voltage difference to each pair of fixed capacitor plates. By maintaining a constant voltage difference between the fixed plates and shifting the central value up and down, an electrostatic force could be applied to each end of the torsion balance's vane. The force exerted on a centered vane is given by:

$$F = \frac{(V_2^2 - V_1^2)\, C_i}{2s_0} \tag{4.6}$$

where V_1 and V_2 are the voltages applied to the fixed plates on either side of the vane. If we now call the total voltage difference between the plates V and ΔV the average of V_1 and V_2, we may write the feedback torque applied to the balance as

$$T_{FB} = \frac{C_i V \Delta V l_c}{s_0}. \tag{4.7}$$

Parameter	Value
Vane-to-Fixed Plate Capacitance, C_i	3.3 pF
Internal Bridge Capacitance, C_0	3.5 pF
Vane-to-Fixed Plate Separation, s_0	0.14 cm
Capacitor Moment Arm	2.86 cm
Feedback Voltage Difference, V	9.4 V
DC Gain, G_0	$\sim$ 5000
4 MHz Oscillator Voltage	1 V
Velocity Feedback Time Constant, $\hat{\tau}$	0.17 sec

Table 4.1: Nominal values of the capacitance bridge detection and feedback parameters.

We can use Equation 4.5 to write $\Delta V = GV_0\Delta\theta/\theta_0$, where G is the overall gain of the electronics, which lets us define an electronic torsion constant for the system

$$\kappa_{FB} = GCVl_c\left(\frac{V_0}{s_0\theta_0}\right). \tag{4.8}$$

This electronic torsion constant completely dominated the torsion constants of the fibers used in this experiment. A final point to make about the feedback system was the inclusion of velocity feedback for the torsion mode. Differentiating a portion of the demodulated torsion signal provided an effective amplifier gain given by

$$G = G_0\left(1 + i\omega\hat{\tau}\right) \tag{4.9}$$

This results in a Q-factor for the balance

$$Q = \frac{2}{\omega_{FB}\hat{\tau}}, \tag{4.10}$$

where ω_{FB} is the resonant frequency of the balance with feedback applied. A summary of the pertinent capacitance bridge parameters is given in Table 4.1.

We return now to consideration of the AC signals generated by the bridge circuit. These signals were coupled to the externally mounted amplifier electronics via

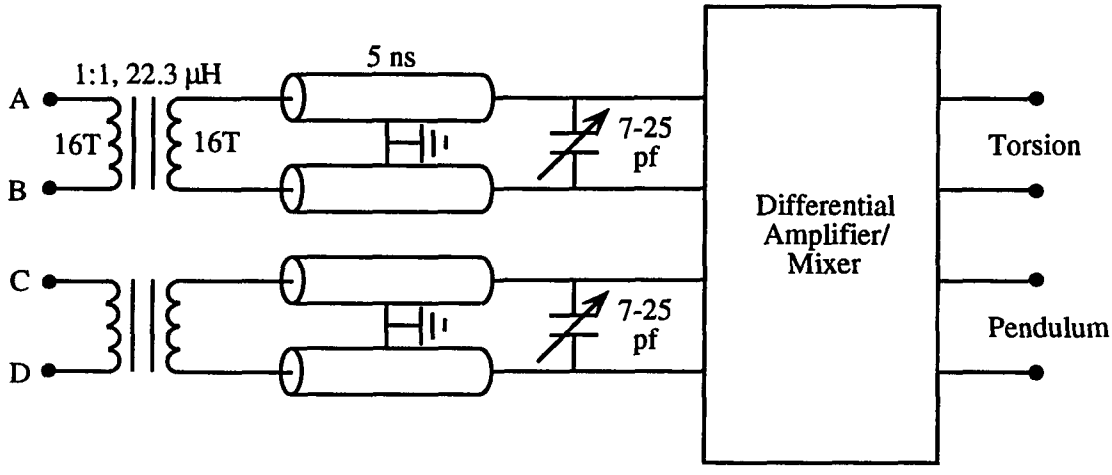

Figure 4.7: The resonant circuit used to couple the capacitance bridge signals from the torsion balance housing to the externally mounted amplifier circuitry.

a passive resonant circuit. The use of a tuned circuit in this instance obviated the need for a heat-producing preamplifier circuit within the confines of the torsion balance housing (This was particularly important since the capacitance bridge circuitry was located immediately beneath the body of the torsion balance. This is the worst possible position for a heat source because of thermal convection.). The details of this circuit are shown in Figure 4.7. After differentially amplifying the (A,B) and (C,D) output pairs, mixing was carried out to give both torsion and pendulum output signals. The mixing scheme is shown in Figure 4.8. These outputs were further amplified and phase-shifted before demodulation to provide the DC feedback signals.

4.1.3 Summary of Torsion Balance Parameters

We finish our description of the apparatus with a summary of some key torsion balance parameters shown in Table 4.2. Surveying these numbers, it is interesting to note that the 3 nrad angular displacement for a 10 nGal differential acceleration corresponds to a movement of only 1 Angstrom of the torsion balance vane relative to the fixed

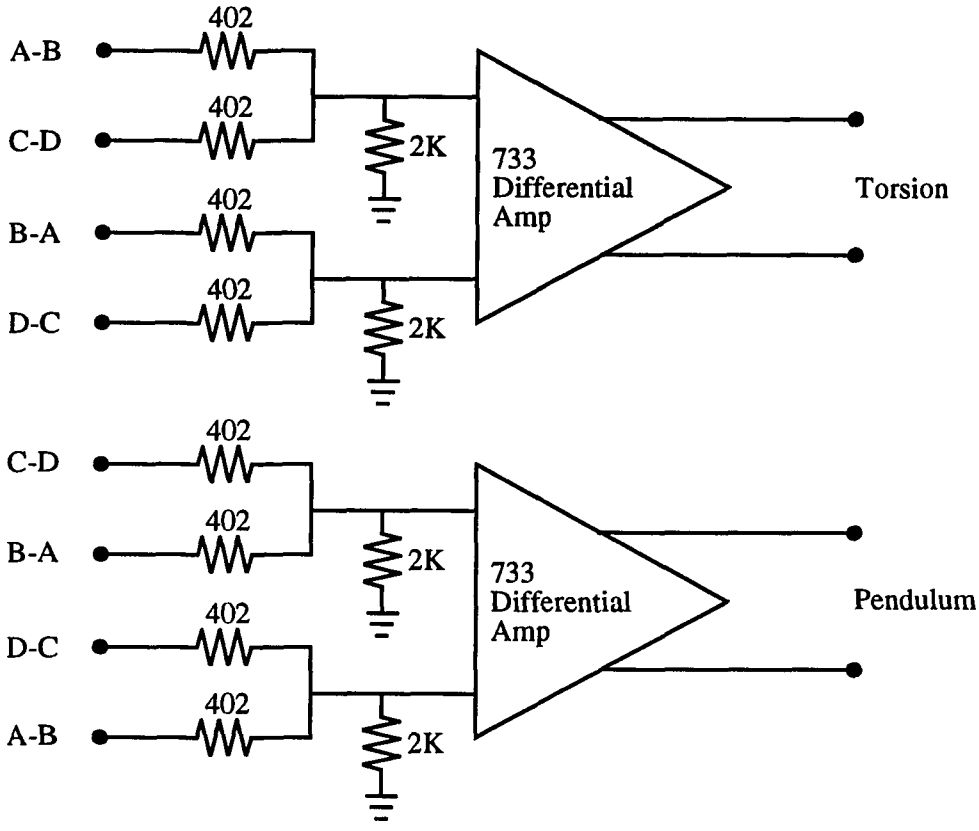

Figure 4.8: The signal mixing scheme used to produce both torsion and pendulum output signals.

capacitor plates.

4.2 The Experimental Site

The site chosen for the experiment was the Yellowstone Bighorn Research Association Camp situated on the slopes of Mt. Maurice near Red Lodge, Montana. Below the camp the terrain slopes away towards the North with a tangent of 0.16 while above the camp the slope has a tangent of roughly 0.5 to the peak roughly 2 km away. An important feature of the local geology is a nearly vertical tear fault of 5 km width and 1 km depth which is centrally positioned beneath the camp. Thus the material

Parameter	Value
Torsion Constants:	
0.002 cm diameter ×20 cm Au-plated W wire	0.1 dyne-cm
0.008 cm diameter ×20 cm Au-plated W wire	5 dyne-cm
Electronic Feedback	5×10^2 dyne-cm
Toroidal Balance Periods:	
Free	137 sec.
With Feedback	14 sec.
Quality Factors:	
No Velocity Feedback	$O(10^2)$
With Velocity Feedback	13
Angular Displacements (Toroidal Balance):	
Free (for $\Delta a = 10$nGal)	0.3μrad
With Feedback (for $\Delta a = 10$nGal)	3 nrad
Effective Dipole Moment Arm (Toroidal Balance)	2.49 cm

Table 4.2: Torsion balance parameters.

to the North of the camp was composed primarily of sedimentary rocks with densities of 2.3–2.4 g/cm^3, while, towards the South, the rock was primarily pre-Cambrian granite with a density of 2.7 g/cm^3 as shown in Figure 4.9. Details of the terrain were obtained from U.S. Geological Survey topographical maps.

4.2.1 Baryon Content

Since the baryon content of normal matter is approximately 1 per amu, the source fields for an intermediate-range baryon coupling could be computed by a simple integration over the local source mass distribution. Recall Equation 3.6 which gives the torque exerted on a torsion balance by an intermediate-range interaction in a region

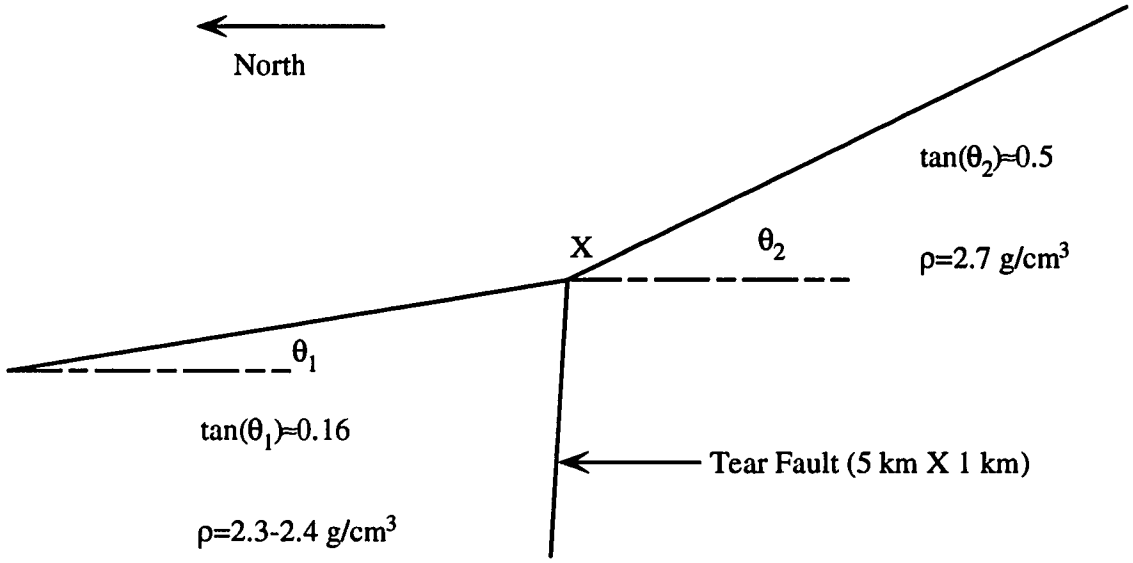

Figure 4.9: A sketch of the average terrain at the YBRA Camp on the slopes of Mt. Maurice just outside of Red Lodge, Montana. The position of the apparatus is denoted with an X.

with uniform slope:

$$\tau = \frac{3}{2R_{\otimes}} \left(\frac{\alpha_0 \lambda}{1+\alpha_0} \right) \left(\frac{\rho_{local}}{\rho_{\otimes}} \right) \left(\frac{C_{\otimes}}{\mu_{\otimes}} \right) \left(\frac{C_2}{\mu_2} - \frac{C_1}{\mu_1} \right) mg\ell \sin(\theta_t) .$$

The local topography for the Mt. Maurice site was numerically integrated over a 100 km^2 region, with the density discontinuity at the tear fault being taken into account (a typical density value of 2.33 g/cm^3 was used for all material below the fault), for a Yukawa potential with various values of the range. The results of this integration were stated in terms of an effective tilt of the terrain. For a coupling to baryon content, assuming a repulsive interaction 1% of gravitational strength, values of the expected horizontal component of the differential acceleration between copper and polyethylene are shown in Table 4.3.

λ (m)	a_H (10^2 nGal	ϕ (deg)	$\langle \sin(\theta_t) \rangle$
25	0.21	0	0.35
50	0.41	358	0.35
100	0.80	355	0.34
200	1.55	353	0.33
400	2.98	352	0.32
800	5.34	352	0.28
1600	8.43	354	0.22

Table 4.3: Horizontal component of a differential acceleration between copper and polyethylene assuming a coupling to baryon content with intrinsic strength $\alpha_0 = -0.01$ and range λ. ϕ indicates the direction relative to North and θ_t is the effective slope angle.

4.2.2 Isospin Content

When considering a coupling to isospin, which is highly dependent on the local chemical composition, the integration over the source becomes much more difficult. The local geology can be broken into three regions:

I. Above the tear fault the rock is primarily pre-Cambrian granite from the Beartooth uplift, possibly with some amphibolite and granodiorite inclusions (on the order of a percent). Interstitial water content is estimated to be less than 0.5%, with an absolute upper limit of no more than 1%;

II. At distances greater than roughly 1.5 km downslope Tertiary sediments of the Fort Union Formation of the Bighorn Basin predominate. These sediments are primarily composed of sandstones and shales with substantial clay mineral content and numerous coal beds. Substantial hydrogen content is present both from the carbonaceous material and from water occupying the pore space of the rock;

III. Just below the tear fault the material is primarily porous clastic sediments of the same origin as the Fort Union Formation along with an overlying granitic conglomerate eroded directly from the pre- Cambrian granite above. Also some Paleozoic and Mesozoic sedimentary material was introduced by the extensive local thrusting of the mountain range.

In region I the mineral content of the rocks has been fairly extensively studied [92,93]. This gives $I/\mu = (6.6 \pm 1.4) \times 10^{-3}$, where the errors represent limits on the value that are dominated by our lack of knowledge about the precise water content of the rock. In region II the isospin content is determined primarily by hydrogenous materials (carbonaceous deposits and water) present in the formation. Contributions from the rock were estimated based on chemical analyses of the major mineral components of the Fort Union Formation [94]. The contribution from the hydrogenous materials was estimated using neutron-density logs from various wells drilled in the formation [95]. Stating the hydrogenous material content as the equivalent amount of water, the well logs indicate 8-18% water content in the porous formation. The resulting isospin value for this region was $I/\mu = (-7 \pm 9) \times 10^{-3}$, where, again, the quoted uncertainty represents limits on the value as opposed to a statistical error. In region III very little information existed with which to evaluate the chemical composition of the sediments and, furthermore, no detailed information was available as to the degree of water saturation of the local strata. The most significant point that could be made was to note that, particularly at short ranges (i.e., a few tens of meters) the isospin content was expected to be strongly influenced by the overlying granitic conglomerate in this region. Thus, the most conservative position was to take an upper limit as the value obtained for region I.

4.2.3 Other Source Charges

In the case of a coupling to B–L, we return to writing the generalized charge as (Equation 2.37)

$$\frac{C_5}{\mu} = \left(\frac{B}{\mu}\right) \cos(\theta_5) + \left(\frac{I}{\mu}\right) \sin(\theta_5)$$

which gives, for normal matter,

$$\left(\frac{B-L}{\mu}\right) = \frac{1}{\sqrt{2}}\left(\frac{C_5}{\mu}\right) \tag{4.11}$$

at $\theta_5 = 45°$. Considering the relatively small contribution from the isospin values obtained in the previous section we are able to write

$$\left(\frac{B-L}{\mu}\right) = 0.50 \pm 0.01 \tag{4.12}$$

for all of the geology around our site. Thus we can directly apply the source integration used for the baryon coupling, with a suitable change in normalization, to set limits in this case.

Finally, considering a coupling to the lepton and bare mechanical quark masses (m_u=4.5 MeV, m_d=7.5 MeV, and m_e=0.5 MeV) corresponds to setting $\theta_5 \approx 3.9°$ in Equation 2.37. Thus, for all practical purposes, this coupling is indistinguishable from a coupling to baryon number.

4.3 Data

Calibration data for the capacitance bridge detection and feedback system was obtained at Princeton using the CB torsion balance. A 23.7 kg source mass was moved from a position adjacent to one mass (Adjacent in this case means at a distance of 21 cm from the center of the torsion balance at an angle of 35° with respect to the torsion balance dipole axis) to a corresponding position adjacent to the other mass. The change in torque was used to generate an effective value for C_i/s_0 as defined by Equation 4.7. This calibration yielded

$$C_i/s_0 = 16.1 \pm 0.6$$

where both parameters are measured in centimeters.

Results from gravitational gradient measurements using the CB and VGB torsion balances at the YBRA site are given in Table 4.4. In the case of the Cavendish

	Measured (10^2 Eötvös)	Calculated (10^2 Eötvös)
$\partial g_x/\partial x - \partial g_y/\partial y$	6.0 ± 1.0	4.05
$\partial g_x/\partial y$	-2.6 ± 1.0	-2.0
$\partial g_x/\partial z$	0.82 ± 0.12	1.03

Table 4.4: Measured and calculated gravitational gradients. Positive x is North, y is West, and z is up. Recall that 1 Eötvös $=10^{-9}\text{sec}^{-2}$.

balance, the torque exerted by the first derivatives of the gravitational field is given by:

$$\begin{aligned} \tau(\theta) &= 2m\ell^2 \left[\left(\frac{\partial g_x}{\partial x} - \frac{\partial g_y}{\partial y} \right) \sin\theta\cos\theta + \frac{\partial g_x}{\partial y}\cos^2\theta - \frac{\partial g_y}{\partial x}\sin^2\theta \right] \\ &= 2m\ell^2 \left[\frac{1}{2}\left(\frac{\partial g_x}{\partial x} - \frac{\partial g_y}{\partial y} \right) \sin(2\theta) + \frac{\partial g_x}{\partial y}\cos(2\theta) \right]. \end{aligned} \tag{4.13}$$

Measurements were made with the balance displaced by $\pm 15°$ from the normal operating orientation (*i.e.*, with the balance dipole axis perpendicular to the direction of maximum slope on the mountain) to give the horizontal gradient values in Table 4.4. These measurements served as a rough check of our numerical integration of the topography. In view of their sensitivity to the details of the nearby mass distribution, for which precise knowledge was lacking, the observed agreement between calculated and measured values seemed quite satisfactory.

The search for a composition-dependent interaction was conducted using the toroidal balance. The balance was oriented so that the axis of the composition dipole was perpendicular to the average line of maximum slope. In order to make the comparison measurements in the required two balance orientations, slow 180° rotations ($\sim$10°/min) to prevent jarring to the balance were followed by 30 minute periods

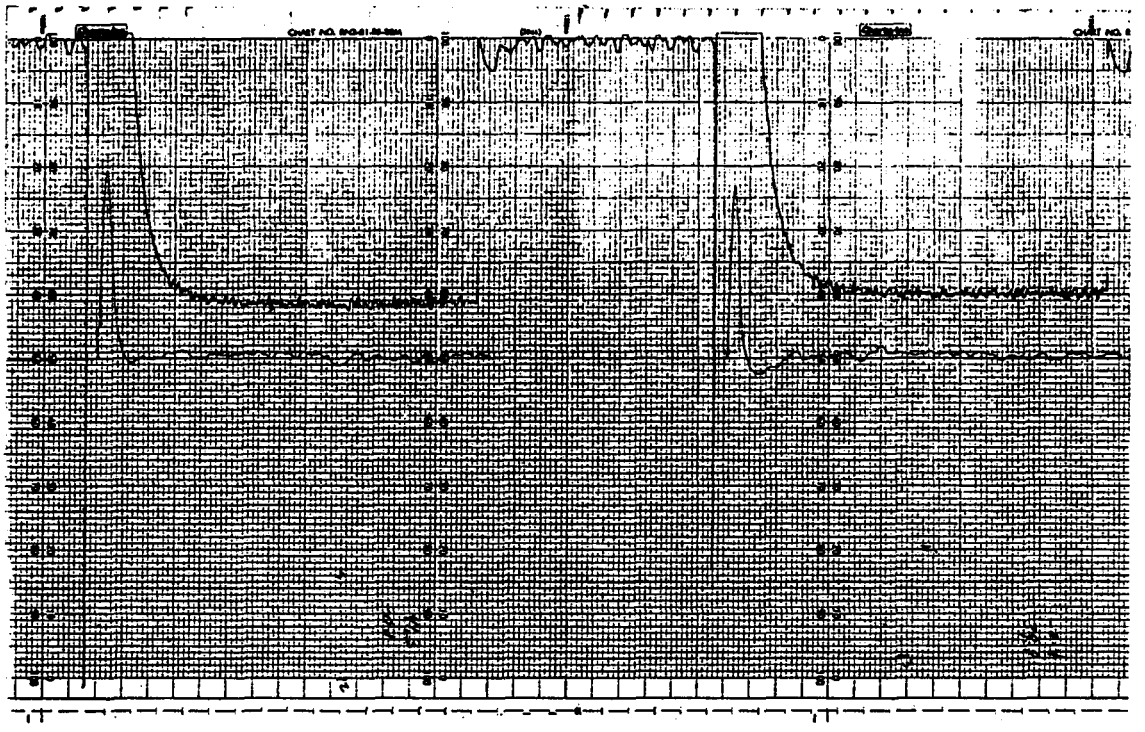

Figure 4.10: Chart recorder data showing both torsion and pendulum signals obtained with the toroidal torsion balance. The pendulum signal is the lower of the two and was recorded at 10 V full scale. The torsion signal is at 500 mV full scale. The chart segment is approximately 85 minutes long.

during which the apparatus remained stationary. Data from the last 8 minutes of each stationary period was read from the chart recorder trace by means of a "Dicke Integrator."[1] These readings were repeated separately by all three observers with a typical scatter of ± 0.5 mV. Figures 4.10 and 4.11 show some typical data obtained with the toroidal balance. Least squares fitting of large segments of the data to simple functions proved difficult due to slow instrumental drifts. On time scales of a few to several hours, however, second order polynomial fits with the signal difference between 0° and 180° as a free parameter proved adequate. Errors in these fits were

[1] A Dicke Integrator is a ruler-shaped piece of lucite with a fine, centered lined scribed along its length. It allows a rather simple, but accurate, visual integration of chart recorder data.

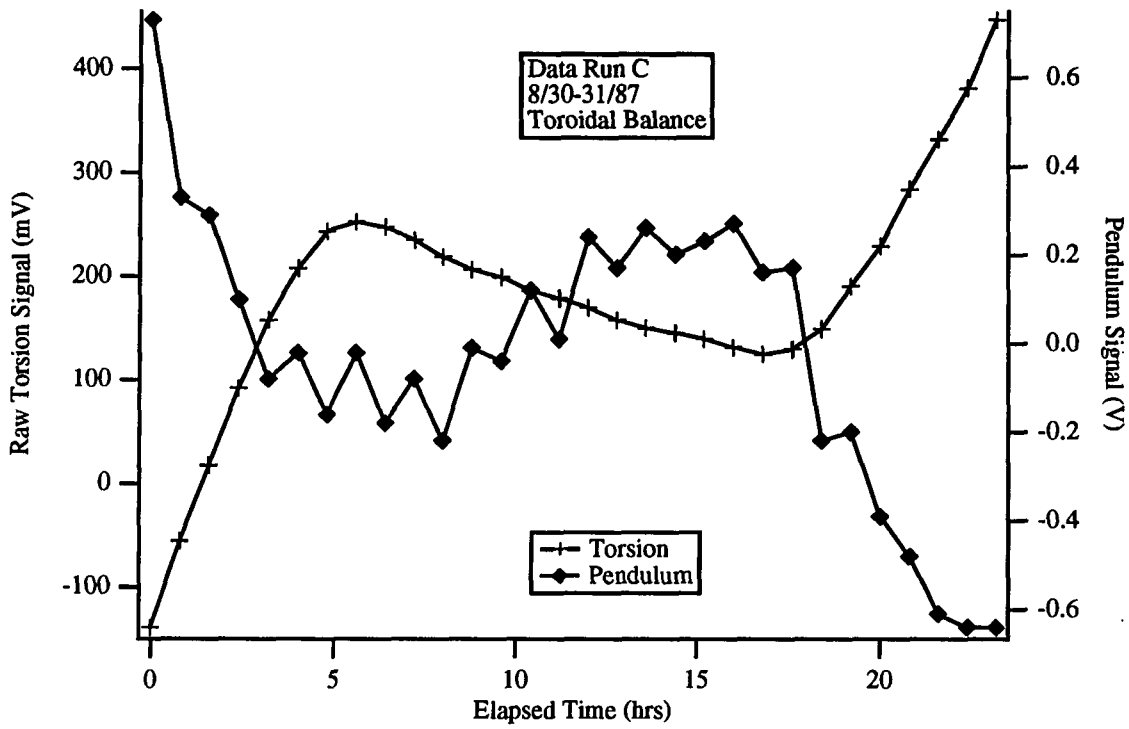

Figure 4.11: A plot of data obtained with the toroidal balance over a 24-hour period.

taken to be identical from point to point and were adjusted to give a χ^2 equal to the number of degrees of freedom. The results from these fits and their weighted average are given in Table 4.5 along with the corresponding acceleration differences between the copper and polyethylene.

4.4 Some Comments on Noise and Systematic Effects

In stating a null result, the responsibility rests with the experimenter to demonstrate that the apparatus is capable of detecting a signal and that a true signal is not in some way negated by systematic effects. With respect to the first requirement, we note that measurements made with the VGB balance involved measuring a 10^{-5} dyne-cm torque with an uncertainty of 15%. Furthermore, this value was in good agreement with the

Number of Rotations	Signal (mV)	Horizontal Acceleration ($10^{-2}\mu$Gal)
13	3.50 ± 1.46	4.85 ± 2.03
6	-1.45 ± 7.53	-2.02 ± 10.5
10	0.04 ± 0.86	0.06 ± 1.20
12	-0.14 ± 1.81	-0.20 ± 2.51
8	-1.60 ± 3.35	-2.22 ± 4.65
10	-0.96 ± 1.84	-1.33 ± 2.56
6	-0.47 ± 4.08	-0.65 ± 5.67
10	-0.10 ± 1.22	-0.14 ± 1.69
6	0.23 ± 0.51	0.32 ± 0.70
5	-0.33 ± 1.04	-0.46 ± 1.44
Weighted Mean	0.21 ± 0.35	0.30 ± 0.49

Table 4.5: Results from ten runs obtained in Montana under widely varying external conditions.

expected torque from our calculated value of the vertical field gradient. For the composition-dependent measurement, the same torque corresponds to a differential acceleration of 30 nGal with an uncertainty of a few nGal, thus demonstrating our ability to make measurements at the requisite sensitivity levels.

In order to assure ourselves that a true signal was not masked in any way, I will discuss the operating characteristics and sensitivity to systematic effects of our apparatus before interpreting the data of the previous section in terms of the existence of a new fundamental interaction.

4.4.1 Noise

It was described in Chapter 3 how careful signal averaging yields an improved thermal noise limit over that naively suggested by the equipartition theorem. Alternatively, the noise levels can be improved by "cooling" the system electronically. The latter

approach was followed with this apparatus. As has already been mentioned, the Q of the system with electronic velocity feedback was some two orders of magnitude smaller than would be expected in the absence of feedback. This leads, via Equation 3.20, to the values given in Table 4.6. In fact, the observed noise levels were noticeably higher

	Torque Noise (dyne-cm)	Readout Noise (mV)	Differential Acceleration Uncertainty (nGal)
Without Velocity Feedback	4.5×10^{-6}	0.50	7.0
With Velocity Feedback	$\sim 0.45 \times 10^{-6}$	0.05	0.7

Table 4.6: Calculated thermal noise levels from equipartition for the static displacement experiment.

than this—typical levels were a few to several millivolts corresponding to differential accelerations of tens of nGal. These noise levels were observed to vary on a diurnal schedule and were attributed in large part to vibrations in the building—in particular due to creakings associated with expansion and contraction of the building during the large external temperature swings associated with a mountain site. Movement near the balance was kept to a minimum to prevent additional vibrational noise from human sources. For the data sets shown in Table 4.5, each of which lasted for no more than several hours, variations in the noise level over time was small enough that our assumption of equal measurement uncertainties throughout the run was justified.

4.4.2 Systematic Effects

4.4.2.1 Gravitational Gradients

As has already been mentioned, an ideal toroidal balance couples to the vertical gradient of the gravitational, $\partial g_x/\partial z$ field when tilted slightly. Fabrication and assembly tolerances in the vertical dimension also contribute. We ascribe an effective tilt to the "bagel" of no more than 2 mrad. Using the measured vertical gradient value, this

leads to spurious gravitational torques upon rotation of 2.4×10^{-7} dyne-cm. Further couplings to horizontal gradients result due to departures from cylindrical symmetry and failures to make precise 180° rotations. We mention again that the primary design departure from this symmetry was the presence of the aluminum vane beneath the balance. The quadrupole moment of this piece was compensated, however, by introducing a corresponding region of negative mass in the volume of the toroid. Even in the absence of compensation, the quadrupole moment of the vane coupled with a roughly 5 mrad uncertainty in the rotation size yields a spurious torque of only 8×10^{-8} dyne-cm, or roughly $1/3$ the tilt coupling. We estimate the true coupling to horizontal gradients to be roughly an order of magnitude smaller than the tilt coupling. Thus the overall sensitivity to gravitational gradients is no more than $\sim 2.7 \times 10^{-7}$ dyne-cm which corresponds to 15% of the quoted error bars for our material-dependent result.

4.4.2.2 Signal Drifts and Thermal Effects

Daily drifts of the torsion balance signal were attributable to two major sources:

1. Unwinding of the torsion fiber; and,
2. Temperature induced drifts which led to diurnal variations in the equilibrium angle of the balance.

The widely varying rate of drift was the primary limitation in fitting the torsion data. Peak drift rates reached $\sim$ 100 mV/hour while using the toroidal balance. Substantial segments of data existed, however, where the drifts were much more manageable, at the level of $<$ 10 mV/hour. Nevertheless, the wide range of external conditions at the remote site which drove these drifts is quite evident in the range of the errors associated with the various fits in Table 4.5. Such variations also make it unlikely

that any sort of static temperature gradient could have masked a true signal.

As has already been mentioned, the top of the apparatus was maintained at an elevated temperature with respect to the bottom to prevent thermal inversions of the atmosphere inside the torsion balance housing. During periods of stable running, no "burps" were noted and we considered this technique quite adequate.

4.4.2.3 Levelling Effects

Tests with the toroidal balance at the YBRA site, showed a small levelling dependence for pendulum displacements perpendicular to the torsion balance vane at the level of

$$\frac{\Delta V_{torsion}}{\Delta V_{pendulum}} = \frac{0.09\text{mV}}{\text{V}}.$$

Note that a pendulum signal of 1 V corresponds to an angular displacement of about 5μrad. The pendulum mode signals were monitored throughout the data runs and a correction was applied to all data. On any single rotation this correction was never more than ± 0.04 mV, much smaller than our quoted errors.

4.4.2.4 Magnetic Contamination

Magnetic tests were conducted on the toroidal torsion balance at Princeton. Magnetic fields were generated using a 154 turn coil mounted on the outside of the wooden box housing the apparatus. Comparisons were made between states with the coil on in one polarity, with the coil off, and with the coil on with reversed polarity. With both polarities, the torque signal was dominated by the diamagnetic susceptibility of the polyethylene giving results in excellent agreement with the effect expected based on the diamagnetic susceptibilities given in Table 3.3 for copper and polyethylene. Magnetic couplings from this source alone would have been negligible at the YBRA

Parameter	Value
Magnetic Field at Torsion Balance	4.0 G
Field Gradient at Torsion Balance	0.28 G/cm
Signal Averaged over both Polarities	18.5 ± 5.0 mV
Diamagnetic Torque	$(8.7 \pm 2.4) \times 10^{-5}$ dyne-cm
$\Delta\chi_{mass}(\mathrm{Cu} - (\mathrm{CH}_2)_n)$	$(0.46 \pm 0.12) \times 10^{-6}$ (cgs)
Asymmetry Signal Between Polarities	7.5 ± 4.2 mV
Magnetic Moment	$(4.5 \pm 2.5) \times 10^{-6}$ dyne-cm/G

Table 4.7: Summary of the magnetic tests conducted on the toroidal balance at Princeton.

site even without the presence of magnetic shielding around the balance. In addition to the diamagnetic effects, which were independent of polarity, an asymmetry corresponding to the direction of the applied field indicated that the balance was contaminated with a small permanent magnetic dipole. The dipole was sufficiently strong to imitate an anomalous acceleration of approximately 4 nGal in the earth's field. The presence of magnetic shielding around the balance reduced the effect by a factor of at least 5–10 making the effect at most several percent our final quoted errors. One final point that should be mentioned is that, since the magnetic shields were fixed to the torsion balance housing and thus rotated with the balance, any residual magnetization of the shields themselves would not affect our measurement because they would remain constant with respect to the torsion balance.

4.4.2.5 Electrostatic Effects

The possible impact of electrostatic effects on our measurement was outlined in Section 3.3.8. In particular, the fields due to a contact potential between different parts of the torsion balance or some charge trapped on the polyethylene can directly generate a torsion signal on rotation. This will occur if the position of the balance, relative to

the surrounding surfaces of the balance housing, changes. Such displacements in this apparatus result from levelling differences between the two operating orientations. Thus the levelling tests, described above, place strong constraints on contributions to the torsion signal from this source. In light of the small size of the observed levelling dependence of the torsion signal, this was not a major source of experimental error.

4.4.3 Summary of Systematic Effects

Table 4.8 summarizes the contributions from the various sources just discussed to the torsion signals of Table 4.5. These numbers are to be compared with the quoted error

Source	Contribution to Signal (nGal)
Thermal Noise	0.7
Observed Noise	2–10
Gravitational Gradients	0.8
Levelling (before applying correction)	0.6
Magnetic Contamination	< 0.8

Table 4.8: Summary of the noise and systematic contributions to the fifth force signal at the YBRA Camp.

on our final result of 4.9 nGal.

4.5 Limits on New Interactions

Our results, when interpreted in terms of a coupling to baryon number, yield the limits shown in Table 4.9 and plotted in Figure 7.1. As was noted in Section 4.2.3, a coupling to the lepton and bare mechanical quark masses is practically indistinguishable from a coupling to baryon number and these limits apply to that situation as well.

Range (m)	Baryon Limit	B–L Limit
$25 < \lambda < 400$	$\alpha_0\lambda = -0.04 \pm 0.07$ m	$\alpha_0\lambda = (-1.5 \pm 2.6) \times 10^{-3}$
1600	$\alpha_0\lambda = -0.05 \pm 0.09$ m	$\alpha_0\lambda = (-2 \pm 5) \times 10^{-3}$
$1600 < \lambda < 5000$	$\lvert\alpha_0\rvert < 10^{-4}$	$\lvert\alpha_0\rvert < 4 \times 10^{-6}$

Table 4.9: Limits on the coupling to baryon and B–L content based on the YBRA data. The values and errors at 400 m grow linearly with range to the values given at 1.6 km.

For a coupling to B–L, the constraints on $\alpha_0\lambda$ are somewhat tighter. In this case

$$\left(\frac{B-L}{\mu}\right)_{\otimes} \Delta\left(\frac{B-L}{\mu}\right) = 6.0 \times 10^{-2} \tag{4.14}$$

in comparison to

$$\left(\frac{B}{\mu}\right)_{\otimes} \Delta\left(\frac{B}{\mu}\right) = 2.24 \times 10^{-3} \tag{4.15}$$

for a coupling to baryon number. These results are also shown in Table 4.9 and are plotted in Figure 7.3.

It is discussed in Chapter 7 how an effective charge, which is a linear combination of baryon number and isospin as given by Equation 2.37, disappears for typical geological sources very near the region of pure isospin coupling. Using our conservative position that, for short ranges, the isospin content of the rock above and below the Mt. Maurice tear fault must be treated as equal (See Section 4.2.2, the source charge disappears for $\theta_5 \approx 90.4°$. In terms of the region of compatibility between the Thieberger and Boynton results that is described in Section 7.4, we obtain $\alpha_0 = (2.3 \pm 4.0) \times 10^{-3}$ in marginal agreement with those experiments. Assuming a value for the isospin content of the downhill side more in line with the typical values for the Fort Union Formation worsens the agreement. Considering a coupling to pure isospin, and maintaining our conservative position that the isospin values for the source are equal for a short distance on either side of the tear fault, yields limits

on $\alpha_0\lambda$ which are 60% larger than the baryon limits for ranges out to 100 m or so. At ranges of a few hundred meters or more, the isospin content of the source should be more characteristic of the Fort Union Formation values. There the isospin limits are the same as those obtained for a pure baryon coupling to well within the experimental error.

Chapter 5

The Dynamic Measurement

Our second torsion balance apparatus had three goals in mind. The first was to see whether we could improve the sensitivity of our measurement by one to two orders of magnitude. Secondly, we were interested in trying a slightly different technique than we used for the first apparatus—*i.e.*, the method of Boys. At the time we started our design work, Boynton, *et al.* [88], had already published a result obtained with an apparatus employing the Boys technique. As will be described in Chapter 7, this result showed a small non-zero effect. We hoped to characterize the technique sufficiently to determine whether that effect might be systematic in origin. As has already been mentioned, our experience with nonlinearities associated with the torsion fibers employed may provide an explanation for the effect seen in that experiment. The third goal was to design a torsion balance which would still allow us to make a fairly direct comparison with the materials employed by Thieberger when he obtained a positive result at the Palisades along the Hudson River. Thus we decided to continue using copper and polyethylene as comparison materials and to construct a torsion balance compatible with making measurements at the Palisades. The large gravitational gradients present near the edge of a cliff prompted us to design a prototype balance with approximately spherical symmetry in an attempt to remove gravitational multipole couplings to all orders. This has the added advantage of insuring that the rotation axis of the balance must be very nearly a principal axis, irrespective of fabrication

and assembly tolerances. Unfortunately, systematic effects with this apparatus have prevented us from achieving all of our goals.

5.1 A Period Measurement with a Spherical Balance

The principles of a Boys measurement have already been described.[1] We take a moment, however, to calculate the sensitivity that can be achieved using a torsion balance with a spherically-symmetric mass distribution, *i.e.*, a torsion balance constructed of two hemispherical shells of differing composition. When making a period measurement, we can consider orienting the composition-dipole parallel (anti-parallel) to the horizontal component of an external field. Then, depending on the sign of the effect, the period of the torsion oscillation will be longer (shorter) than its unperturbed value. Upon rotating the orientation of the balance by precisely 180°, the effect will reverse sign giving a period which is shorter (longer). For our spherical-shell balance, the period shift between these two orientations is given by

$$\frac{\Delta P}{P} = -\frac{\Delta\omega}{\omega} \cong \frac{3\Delta a_5}{8\omega^2 R} \tag{5.1}$$

where P and ω are the period and frequency, respectively, R is the radius of the shell, and Δa_5 is the differential acceleration due to a *fifth force*. For the torsion balances we have employed, $R \approx 5\,\mathrm{cm}$ and $P \approx 130\,\mathrm{sec}$ (quartz) or $P \approx 280\,\mathrm{sec}$ (tungsten). Thus making a timing measurement good to 1 part in 10^8 provides timing sensitivity to differential accelerations of $\leq 0.3\,\mathrm{nGal}$. Furthermore, if we take the minimum timing unit to be fixed, the sensitivity improves as the cube of the torsion balance period. As was discussed in Chapter 3, longer periods require smaller balances so that fabrication tolerances become more important when considering systematic effects. Furthermore,

[1] See Equations 3.3 and 3.5 and the accompanying text. Also see the general comments in the introduction, p. 22.

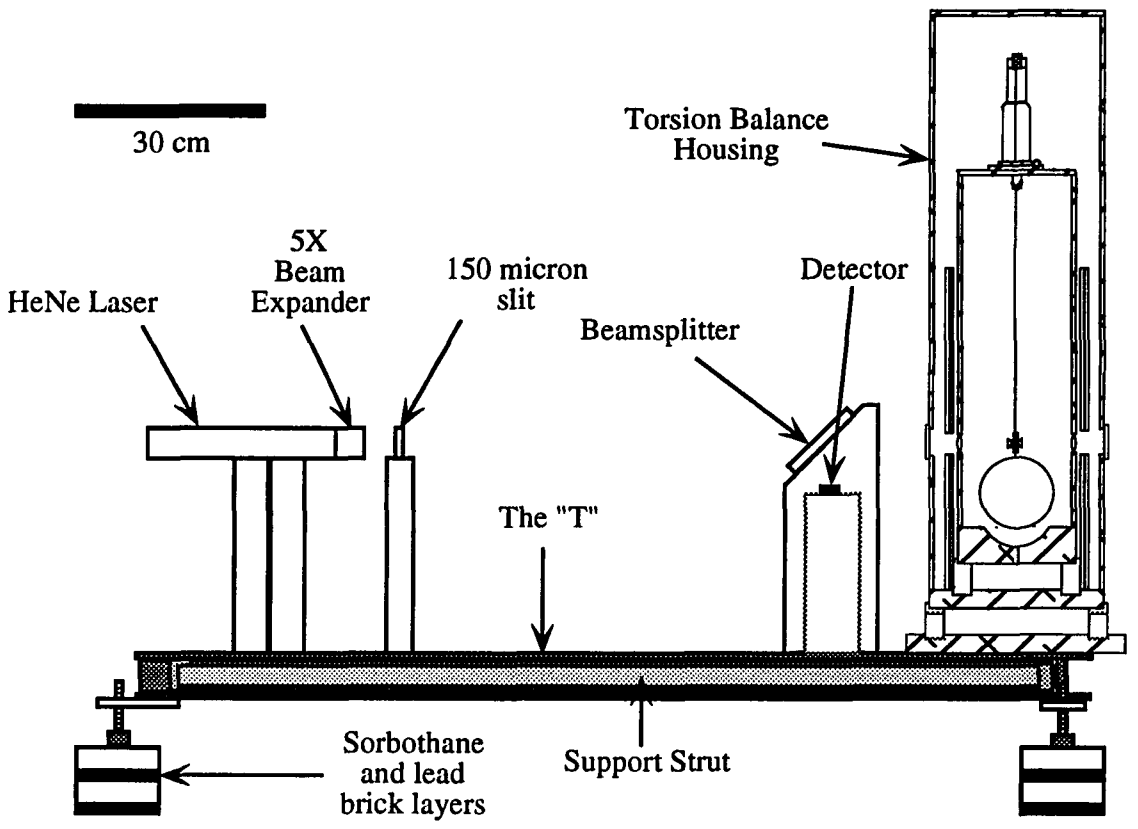

Figure 5.1: A side view of the dynamic apparatus showing the torsion balance housing, the major components of the optical detection system, and the I-beam frame on which all of the above components were mounted.

timing drifts over timescales of hours force us to keep the period short enough so that timing comparisons spanning several rotations of the balance can be made in a fraction of a day. Typically a measurement in a single position lasts for at least 15 cycles. Thus, given the above constraints, periods greater than a few hundred seconds are difficult to implement.

5.2 The Apparatus

A sketch of the apparatus is shown in Figure 5.1. The torsion balance is housed inside a pair of concentric aluminum cannisters which are mounted on a large I-beam

frame. The aluminum frame, which consists of two sections of I-beam welded together in the shape of a "T", holds the components of the optical detection system along its stem and mountings for the stepper motor which drives the balance rotations on the crosspiece, adjacent to the cannisters. To insure the rigidity of the frame, reinforcing struts run between the ends of the crosspiece and stem of the "T". Three-point levelling of the apparatus is provided by adjustable "feet" at the three ends of the of the "T". These feet rest on interleaved layers of Pb bricks and 1.3 cm sorbothane sheets[2] for passive vibrational isolation. All of the above components reside inside a large, insulated wooden box which is temperature controlled.

5.2.1 The Torsion Balance Housing

An expanded view of the torsion balance housing is shown in Figure 5.2. The inner housing is a 15 cm ID aluminum cannister with a 6 mm wall. The overall height (including the cap and baseplate) is 65 cm in order to permit the use of balance suspensions nominally 60 cm in length. The components necessary to mount and adjust the torsion balance are located on the cap of this inner can. These components will be described in detail in Section 5.2.3. Two 2.5 cm diameter holes, slightly above the level of the torsion balance, were cut on opposite sides of the inner can. As part of the optical detection system, 40 cm *f.l.* lenses were mounted in each of these holes. Ultimately, only one was employed in the detection system. Thermal contact of the inner housing with the rest of the apparatus was minimized by mounting the baseplate on a 2.5 cm thick ring of G-10 which was 4.4 cm high. This ring was in turn mounted to the baseplate of the outer housing. The temperature of the inner can was

[2]Sorbothane is a rubber-like material which approximates a Newtonian liquid for sufficiently high frequency vibrations. It is commonly used when particularly good vibrational isolation of a large piece of machinery is needed.

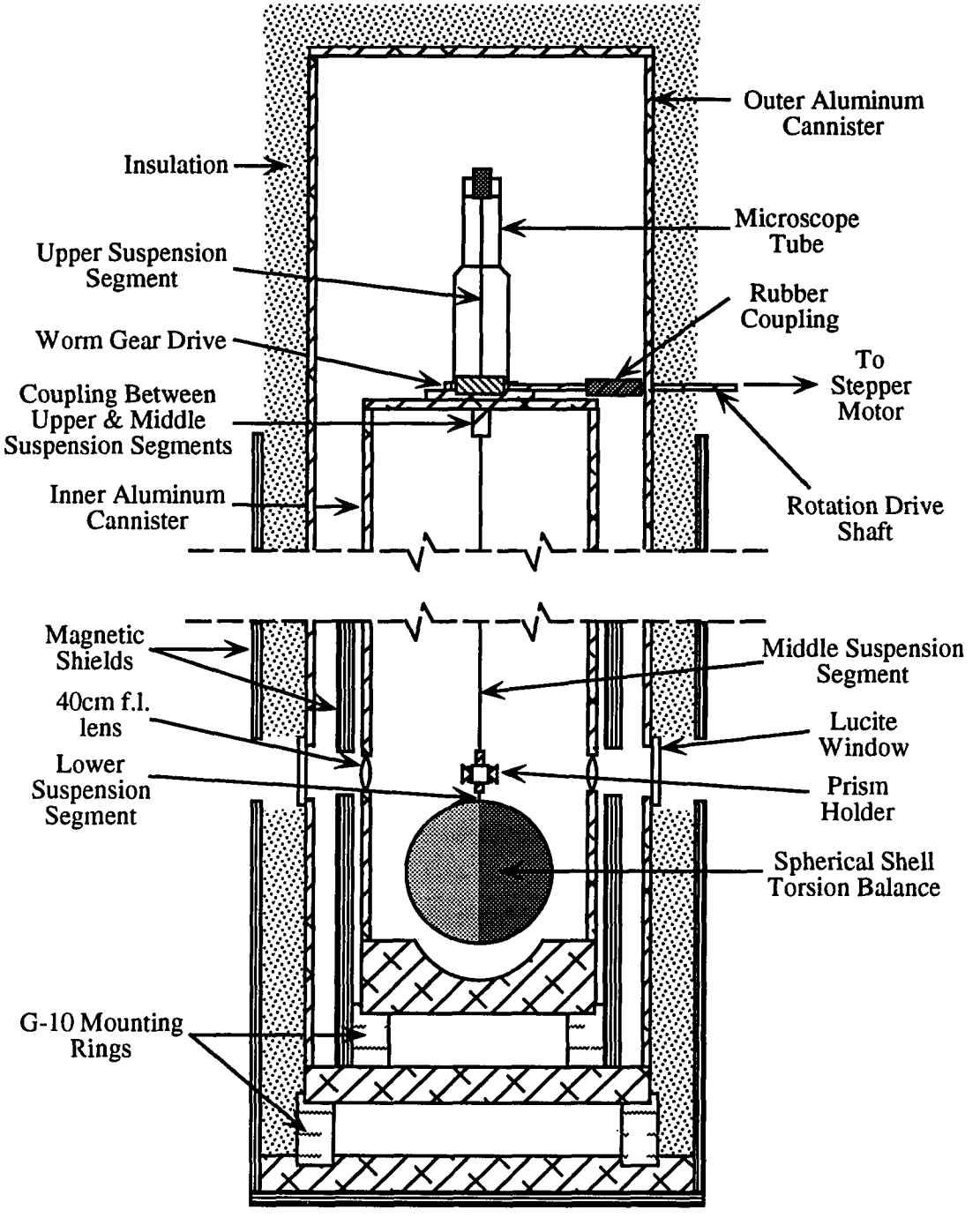

Figure 5.2: The torsion balance housing. The various components are described in the text. Note that, in the picture, the stepper motor shaft is shown rotated 90° from its true orientation with respect to the optical axis for ease of view.

monitored during all runs to follow the temperature dependence of the measurements.

The outer housing, including top and bottom plates, is 102 cm tall with a 23 cm ID and 6 mm thick walls. Heating elements are mounted on the outer surface of this cannister as well as on the top and bottom plates. These heating elements, which are all counter-wound to prevent generation of magnetic fields near the balance, provide the innermost layer of thermal control for the apparatus. As with the static apparatus, the top is normally maintained at a slightly higher temperature than the bottom to prevent convection instabilities in the atmosphere inside the cans. The temperature difference from the top of the housings to the support frame is nominally 1°C. The baseplate for this cannister, in the same manner as the baseplate of the inner housing, is mounted on a G-10 ring to minimize the thermal coupling to the rest of the apparatus. In this case the G-10 ring is mounted to yet another aluminum baseplate which is in turn bolted to the frame on which the apparatus rests. To further aid in thermal isolation, the outer housing is surrounded by several centimeters of insulation. The outer housing is sealed and gas fittings (not shown) are present to allow the system to be operated in other than an air atmosphere. Normal operation is carried out under helium (the reasons for this will be discussed further in Section 5.3.2.1) with a slow flow of the gas being maintained in the space between the two cans.

Two magnetic shields are shown in Figure 5.2. Each consists of an outer layer of relatively low permeability Netic material with a high permeability Co-Netic inner layer. The system has been operated with none, one or both of these shields in place. Typical operation has been with the shields absent in order to allow magnetic tests on the system using a set of externally mounted coils.

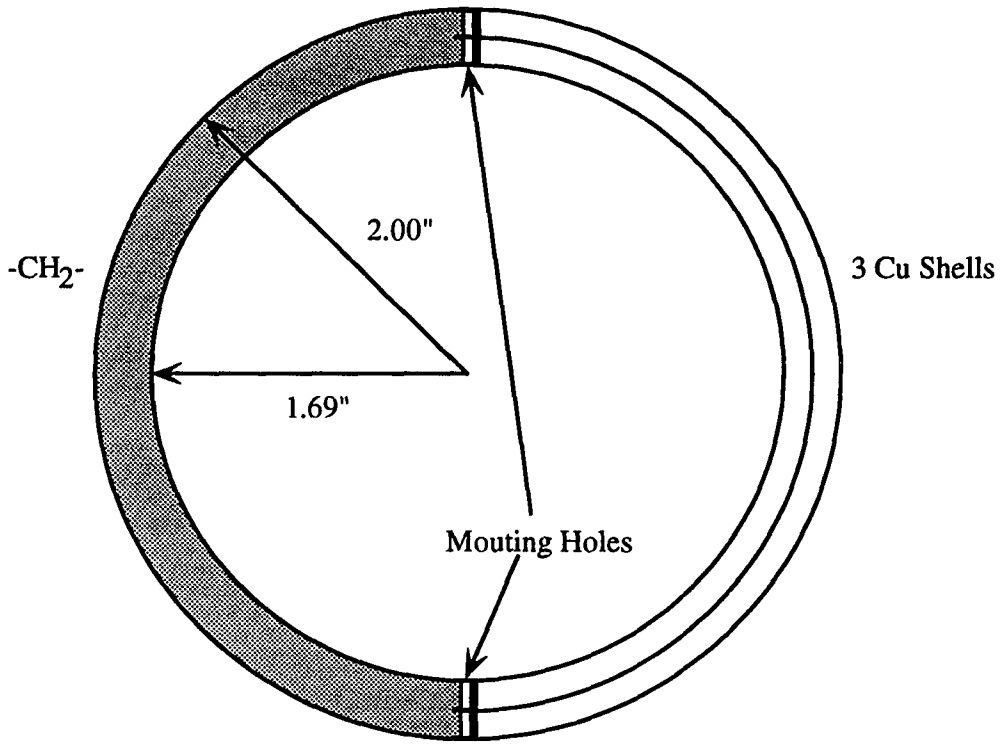

Figure 5.3: The spherical torsion balance prototype constructed of polyethylene and copper. The three shell construction of the copper half allows matching of the first three mass moments of each half. The balance departs from spherical symmetry via the overlap of the copper and polyethylene where the two halves join.

5.2.2 The Torsion Balance Prototypes

The prototype torsion balance, shown in Figure 5.3, is a spherical shell with hemispheres of differing composition. The nominal mass of the balance is 204.6 g. The design was intended to minimize couplings to the large gravitational gradients expected at a site next to a major topological source. The primary departure from spherical symmetry resulted from a region of overlap which provided the means to join the two halves. This ring, with a nominal mass of 6 g, results in residual quadrupole couplings to the earth's gravitational field. The polyethylene half has a thickness of approximately 7.9 mm while the Cu half is made of 3 electroplated shells ranging

in thickness from approximately 180 μm to 410 μm. The three-shell construction allowed matching of the mass, centroid, and moment of inertia of the two halves of the balance. The shells were fabricated by machining an aluminum mandrel with a hemispherical surface, electroplating a layer of copper onto it, and then polishing the copper surface, on a lathe, with repeated weighings to generate the correct mass for the shell. Subsequently the edge of the hemisphere was trimmed at the correct distance from the "nose" of the shell in order to provide the proper overlap of the components of the two halves. Finally, the aluminum mandrel was etched away in a concentrated sodium hydroxide solution. To minimize charge buildup, the entire surface of the polyethylene half was aluminized by vacuum deposition.

For test purposes, the actual balance currently in use is one fabricated entirely of aluminum. It has a shell thickness of 0.25 cm, a mass of 200.7 g, and a moment of inertia of 3.3×10^3 gcm^2. This balance has the advantage of not having a quadrupole mass ring around the seam joining the two halves, however, fabrication tolerances lead us to expect small variations in the moment of inertia around the principal axes. A "worst-case" distribution of the mass places an upper limit of $1\frac{1}{2}\%$ on this asymmetry.

5.2.3 The Suspension and Rotation Systems

Two primary fiber suspension systems have been employed over the course of testing this apparatus, one for use with tungsten fibers and the other for use with quartz. To describe the current system, I will begin with the fittings on the balance, itself, and work upwards and outwards to the other components.

5.2.3.1 The Quartz Suspension

Two 1.6 mm diameter aluminum "plugs" fit into each of the mounting holes shown in Figure 5.3. These plugs have a 110 μm feedthrough hole running their entire length which aligns a 100 μm gold-plated tungsten wire passing through the center of the balance. The wire extends approximately 6 mm above the top surface of the balance and enters a similar fitting on the bottom of the aluminum fixture which holds the four right-angle prisms for the optical system. A gold-plated copper collar, with a 100 μm center hole, holds one end of the quartz torsion fiber and fits into the top of the optics fixture. The 43 cm long torsion fiber, which has a vacuum-deposited layer of gold on its surface to ground the balance, is $75 - 100\,\mu$m in diameter. The upper end of the quartz is held by an identical collar which fits into an aluminum coupling to an upper suspension fiber, of copper or beryllium-copper wire, which is thick enough to prevent a large contribution to the torsion constant of the system but which takes up any bending in the suspension due to levelling changes upon rotation. It also helped prevent breakage of the quartz fiber during the process of loading the balance into the housing. The upper suspension point is located at the top of a moveable microscope tube with its optics removed. This tube allows vertical positioning of the balance and the balance optics to within 25 μm. The microscope tube is mounted on a precision bearing and gear assembly which allows rotation of the suspension point. These rotations are driven from a stepper motor via a worm gear drive. The gearing ratio results in 12,000 steps per single revolution of the torsion balance suspension, *i.e.*, a 0.5 mrad positioning resolution. The angular velocity and phase of the rotations relative to the balance oscillation are computer controlled.

5.2.3.2 The Tungsten Suspension

The suspension system when using a tungsten torsion fiber was somewhat simpler. In this case, a 1.6 mm stainless steel pin was used to directly mount the prism holder to the top of the torsion balance. A 50 μm diameter, gold-plated tungsten fiber was crimped into another 1.6 mm SS pin with a 100 μm hole through its center. This pin fit into the top of the prism holder. The top of the tungsten fiber was fed through and soldered to a a cylindrical copper mount using a low temperature silver solder. The mount, with a precision weight attached, was suspended as a simple pendulum during the soldering process to insure that the tungsten fiber exited the mount parallel to its axis. Wicking of the solder along the tungsten fiber provided a gradual tapering in the effective diameter to that of the torsion fiber. This helped to prevent small levelling changes at the top of the suspension from coupling strongly to the torsion constant of the system.

5.2.3.3 Summary

Table 5.1 provides a summary of the torsional characteristics of the two suspension systems.

5.2.4 The Optical Detection System

In the context of making a dynamic measurement, we required a detection scheme that would perturb the overall cylindrical symmetry of the interior of the apparatus as little as possible. This led us to implement a simple optical lever-arm detection system that would only require a set of on-axis mirrors on the torsion balance (we actually employed precision right-angle prisms) and a set of access windows in the torsion balance housing.

Suspension Segment	Torsion Constant (dyne-cm/rad)
Suspension Method I:	
50 μm×60 cm Au-Plated W Fiber	1.7
Suspension Method II (Quartz):	
Top Segment–	
310μm×13cm Cu Wire	3.7×10^3
380μm×14cm Be-Cu Wire	8×10^3
Main Segment–	
75-100μm×43cm Quartz Fiber	7.4
Bottom Segment–	
100μm×3–6mm Au-Plated W Fiber	$2.7–5.4\times10^3$

Table 5.1: Torsional characteristics of the elements of the two balance suspensions.

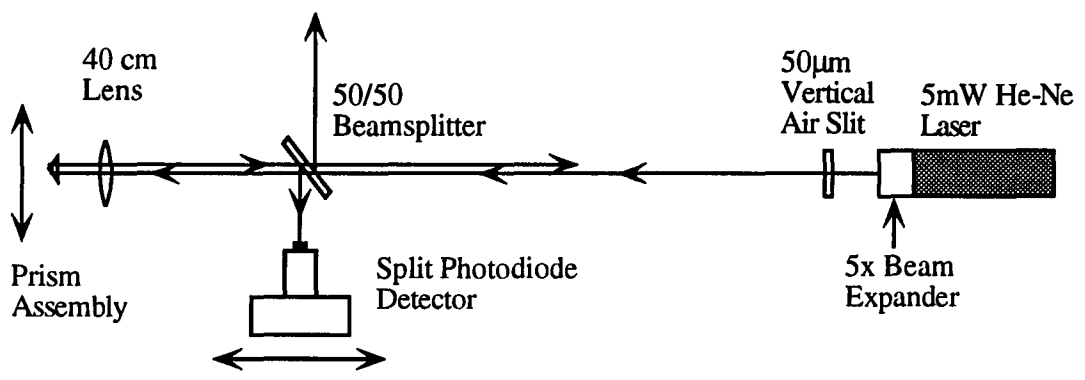

Figure 5.4: The optical detection system

Figure 5.4 shows the components of the optical detection system. The beam from a 5 mW, randomly polarized, He-Ne laser passes through a 5-times beam-expander and is used to illuminate a 150 μm × 3 mm vertical slit. Light from the slit is imaged with an approximate demagnification of 1 to 2.3 on a Siemens SFH204 four-quadrant photodiode detector. The detector, composed of four 100 μm × 100 μm active regions, has 12 μm spacing between adjacent quadrants. The effective moment arm from the prisms to the detector is nominally 26 cm. The diodes in the detector are

ganged "vertically" (See Figure 5.6) to provide two channels for horizontal position measurement of the beam as it sweeps by at each half-cycle of the torsion balance oscillation. The optical elements on the torsion balance are 5 mm, precision, right-angle prisms mounted to provide retroreflection in the vertical dimension. The front of each prism is angled upward by nominally 12 mrad to prevent front surface reflections from propagating through the optical system. An angular tolerance of $\pm 150\,\mu$rad in the retro-reflection dimension results in $\pm 40\,\mu$m uncertainty in the vertical position of the image at the detector—much smaller than the 1.3 mm vertical spot size. Horizontal positioning of the prisms with respect to the plane of the torsion fiber axis is $\pm 125\,\mu$m leading us to expect apparent angular offsets between the four 90° positions of ± 0.25 mrad. The observed angular offsets between the four positions are considerably larger than this due to angular tolerances of the prisms in the horizontal plane which are much poorer than the corresponding vertical values. Typical measured horizontal variations between the positions are ± 1.5 mrad which ends up being a very critical tolerance affecting the amplitude stability in the balance rotation scheme described below. Another point to consider concerning the mounting tolerances of the prisms, is the torque which can be exerted on the balance due to light pressure. Certainly such a torque, to lowest order, results in an offset of the equilibrium angle and not a shift in the period, but it gives us an idea of the level at which such effects become important. The total power impinging on the balance optics is about $100\,\mu$W so that the corresponding torque when the balance optics are horizontally displaced by $125\,\mu$m is 7×10^{-10} dyne-cm or 3% of the torque expected from a differential acceleration of 0.1 nGal. Two antireflection-coated 40 cm *f.l.* lenses are mounted on opposite sides of the wall of the inner can. Only one of these is used by the optical system while the other provides visual access to the inside

of the apparatus for inspection of the balance and to aid in the initial alignment of the optical system. The double passage of the laser beam through one of these lenses provides the necessary focusing of the slit image. Access through the outer housing is provided by two lucite windows adjacent to these lenses which are inclined at a small angle to the vertical, again to eliminate stray reflections in the optical path. In addition to the split-photodiode detector, there are also two phototransistor detectors mounted 2.2 cm to either side of the central detector which allow a time-of-flight (TOF) measurement of the oscillation amplitude at each half-cycle.

5.2.5 The Electronics and DAC System

A block diagram of the electronics is shown in Figure 5.5. The major components of the electronics are:

- Circuitry associated with amplifying, filtering, and triggering on the difference signal from the split-photodiode detector.
- Circuitry for amplifying, differentiating and triggering on the phototransistor signals which provide for the time-of-flight measurement of the balance amplitude.
- A 32-bit clock to provide single-cycle period measurements with a precision of better than 1 part in 10^8 for all of the balance/suspension configurations we have employed.

In addition, there are modules for monitoring and controlling the apparatus temperature and a stepper motor controller which is computer driven. All data is collected and the apparatus is controlled by a Macintosh computer.

The four-quadrant photodiode detector, with the diodes ganged to provide a differential position measurement in the horizontal dimension, is the basis of the precision timing circuitry. The detector and one of the associated current-to-voltage converters are shown in Figure 5.6. Signals from the two channels are amplified and combined

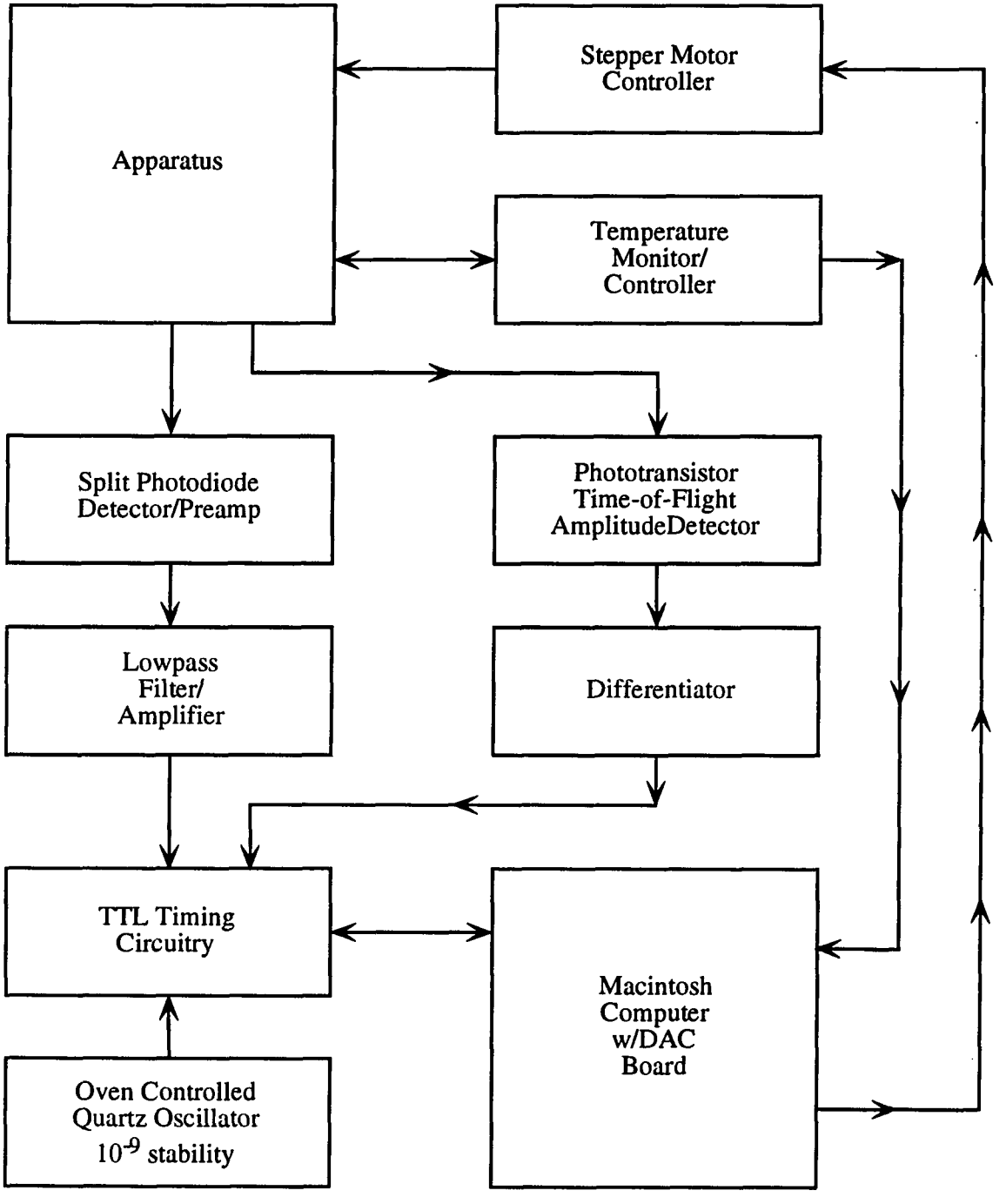

Figure 5.5: Block diagram of the dynamic apparatus

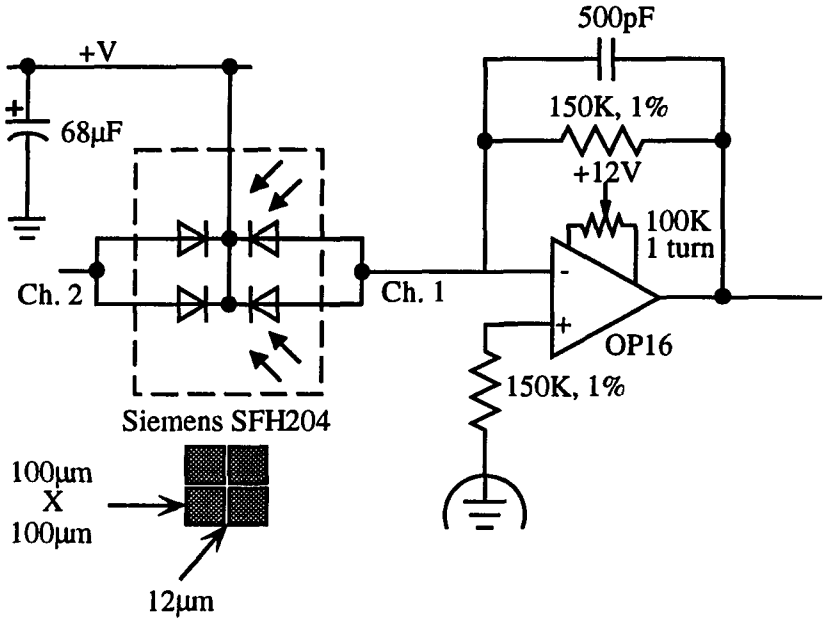

Figure 5.6: The four-quadrant photodiode detector. The quadrants are ganged in pairs to provide precision position information in the horizontal dimension.

to yield a difference signal. The zero-crossing of the difference signal upon equal illumination of the two photodiode channels is used to trigger latches in the clock circuitry which hold the current timing value. This value is then read and stored by the computer. The characteristic frequency of the difference signal is determined by the speed at which the laser spot sweeps over the detector. Typical signal widths, as determined by the interval between the half-height points on the leading edge of the first-activated photodiode pair and the corresponding point on the trailing edge of the second pair are ≥ 20 msec under normal operating conditions.[3] The other key characteristic of the difference signal is the voltage slew rate at the zero-crossing. This is typically a few mV/μsec for the balance amplitudes and periods we employ. Thus,

[3]This value of the signal width corresponds to operating with a quartz-suspended torsion balance, which has a nominal period of 130 sec, and an amplitude slightly less than 1 rad. The largest widths seen have resulted from operating a tungsten-suspended balance at oscillation amplitudes of a few tenths of a radian. The nominal 280 sec period of such a balance gives rise to widths of O(100 msec).

triggering of the timing circuitry as the analog signal passes through zero is relatively insensitive to electronic noise, with noise levels of several millivolts producing timing uncertainties of a few microseconds in the period measurement (See Section 5.5.2.3 for additional discussion of electronic effects on the timing signal).

Signals from the two phototransistor detectors which provide time-of-flight amplitude information are amplified and then differentiated to provide a zero-crossings in the electronic signals corresponding to the beam being centered on each detector. This technique, although offering a simpler set of amplification and trigger electronics than for the split-photodiode detector, provides timing measurements which are intrisically much less precise than those provided by the central detector. The resulting amplitude measurements are good to about 3 parts in 10^3 under normal operating conditions.

The clocking circuitry consists of a 32-bit TTL counter which is driven by a 10 MHz oven-regulated, quartz crystal oscillator. The oscillator has a rated long-term stability of 1 part in 10^9, an order of magnitude better than the timing precision that we require. The clocking signal is divided such that timing triggers from the central photodiode detector are binned into 1 μsec intervals. Triggers on all three timing channels (the central and two TOF channels) as the balance passes through its equilibrium position result in a "read signal" being sent to the Macintosh computer which then collects the timing information which has been latched for all three channels. At the end of the read cycle, all latches are reset in preparation for the next set of timing triggers.

The Macintosh computer, in addition to recording the timing signals, controls the rotations of the balance between the four operating positions, monitors the temperature at various points inside and outside the apparatus and carries out real-time

analysis of the balance dynamics.

5.3 Some Critical Issues for a Dynamic System

There are several aspects of conducting measurements with a dynamic system that merit particular attention. This section provides details associated with the rotation scheme that is used for angular transport of the balance between measurement positions and also serves to excite the oscillations in each position. It then goes on to consider the effects of a viscous medium on the balance dynamics. Finally, an estimate of the impact of the torsion mode coupling to the other normal modes of the balance is made.

5.3.1 The Rotation Scheme

During normal operation the torsion balance is periodically rotated by 90° increments and data is recorded in each position for anywhere from 8 to 45 cycles of the oscillator. Instead of rotating the entire apparatus, as was done with the static experiment, the transport between positions is accomplished by a rotation of the top of the suspension fiber. The phase and angular velocity of each rotation is designed to excite the balance amplitude to a specific initial value for each set of measurements.

In order to clarify this scheme, consider an ideal undamped oscillator with amplitude θ_0 and angular frequency ω. As the oscillator passes through its equilibrium position (which nominally corresponds to the laser spot crossing the split photodiode detector) a rotation of the top of the suspension fiber is begun. This rotation is in the same direction as the balance motion, with constant angular velocity $\omega\theta_0$, so that the top of the suspension fiber rotates in phase with the torsion balance. If this rotation continues for 90° and then stops, the balance will undergo oscillations with the same

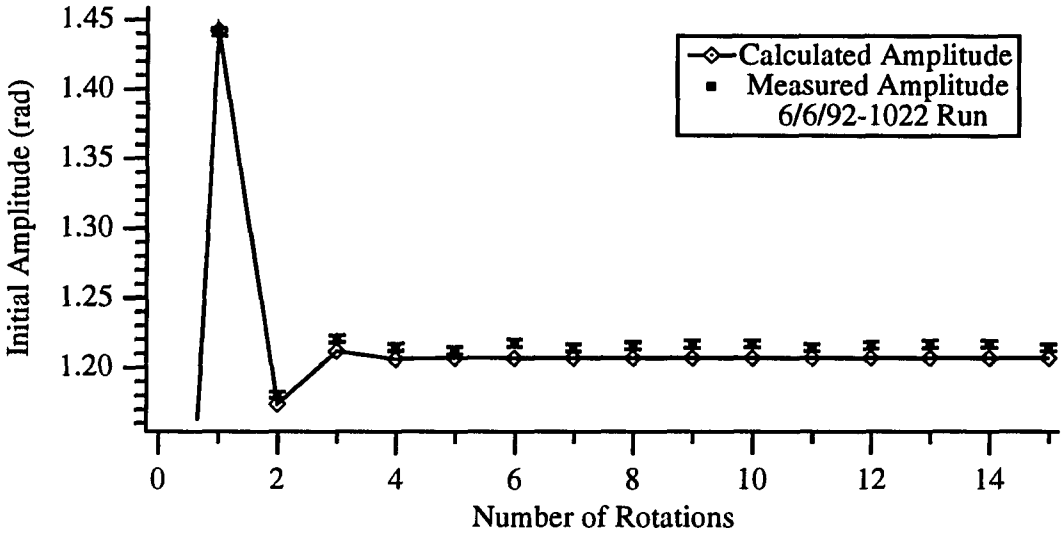

Figure 5.7: Amplitude stabilization as a function of the number of 90° rotations of the torsion balance with a quartz suspension. The amplitude values correspond to the initial amplitude in each new balance orientation. The period and damping time were 132.6 sec and 5.8×10^3 sec, respectively, and the rotation time between positions was 30 sec.

amplitude as before but with its equilibrium position shifted by 90° .

In a lightly damped system, the situation is only slightly more complicated. Here, the amplitude of the balance at the start of a rotation may be considerably smaller than its initial amplitude in that position. For instance, period measurements lasting 45 cycles of the oscillation (when using a quartz torsion fiber and operating in a helium atmosphere) result in a final amplitude only 40% of the initial amplitude. By rotating the suspension point of the fiber with an angular velocity larger than that of torsion balance, however, the oscillation can be re-excited to its original amplitude. With this rotation scheme a stable steady-state value for the initial amplitude in each position is reached within several rotations of the balance. This is demonstrated in Figure 5.7 which shows the calculated and observed initial amplitude in each position as a function of the number of rotations for a torsion balance initially at rest. The

small discrepancy between the modelled and measured values is attributable to modelling errors on the order of 1% and an uncertainty in the amplitude calibration at the level of a few percent. Statistical errors in the measured values are negligible at the scale of the plot. The error bars represent a systematic uncertainty in the time-of-flight amplitude measurement between the four measurement positions result. In practice, when starting the balance from rest, the amplitude stabilizes to within a few parts in 10^3 in a dozen rotations or less. Unfortunately, systematic variations in the amplitude at this level coupled significantly to nonlinearities in the tungsten torsion fibers we initially employed.

Systematic variations in the oscillation amplitude arise when the four prisms mounted on top of the torsion balance are not precisely separated by 90° angles. As was noted in Section 5.2.4 the typical angular tolerances involved are $\sim \pm 1.5$ mrad. As a result, when the driving rotation is started immediately upon an incoming trigger from the optical system, the relative phase variations from position to position induce amplitude variations. These variations then couple to nonlinearities in the system giving systematic changes in the measured period between positions. To minimize this problem, real time control of the phase of the driving rotation by the computer to compensate for these angular errors was implemented.

A potential drawback to our rotation scheme is the fact that the entire torsion balance housing is not rotated along with the balance. Thus, the torsion balance rotates with respect to all external components and may be susceptible to a wider variety of systematic effects.[4]

[4]For instance, consider that any magnetic shielding will remain fixed so that magnetic contamination of the balance could couple to a residual magnetization of the shield.

5.3.2 Operation at Atmospheric Pressure

As with the previous apparatus, it was decided operate the dynamic experiment at atmospheric pressure. This provides damping for the various non-torsional modes which might be excited by external vibrations coupling into the apparatus or parasitically by the excitation of the torsion mode (See Section 5.3.2.3 below). At the same time this raises concerns about the influence of the surrounding fluid on the oscillating balance. In particular, the characteristics of our apparatus require us, first of all, to consider the fluid as a potential source of nonlinear contributions to the balance dynamics. Secondly, the nature of the oscillatory solutions to the Navier-Stokes equation must be detailed and the effects of fluid oscillations on the balance dynamics outlined.

5.3.2.1 Fluid Viscosities and Reynolds' Numbers

We begin by considering the fluid dynamics regime in which the balance operates. The transition between linear and nonlinear fluid dynamics is characterized by the value of the Reynolds' number

$$\mathcal{R} = \frac{\rho u \ell}{\eta} = \frac{u\ell}{\nu}, \tag{5.2}$$

where ρ is the density of the fluid, u is the velocity of the object moving through the fluid, ℓ is the characteristic dimension of the object, and η is the dynamic viscosity. The ratio $\nu = \eta/\rho$ is the kinematic viscosity. We see immediately that nonlinearities will be minimized by the use of low density gases. Table 5.2 gives the viscosity values for air and helium which have both been employed in this experiment. For a sphere of radius R undergoing torsion oscillations with frequency ω, the expression for the

Parameter	Air	Helium
Dynamic Viscosity (μPoise)	182.7	194.1
Kinematic Viscosity (cm^2/sec)	0.15	1.0

Table 5.2: Dynamic and kinematic viscosities of air and helium. These values were obtained from Reference 85, pp. B · 19 and F · 9, 47–48.

RMS Reynolds' number is

$$\mathcal{R} = \frac{\theta_0 \omega R^2}{2\nu} \tag{5.3}$$

while for translational oscillations it is

$$\mathcal{R} = \frac{x_0 \omega R}{2\nu}, \tag{5.4}$$

where θ_0 and x_0 give the oscillation amplitude in each case. Table 5.3 summarizes the situation for several modes of our torsion balance. Since the Reynolds' numbers for

Mode	Characteristic Frequency, f (Hz)	RMS Reynolds' Number	
		Air	Helium
Torsion Oscillation (Tungsten)	3.64×10^{-3}	2	0.3
Torsion Oscillation (Quartz)	7.70×10^{-3}	4	0.6
Simple Pendulum Mode	0.64	0.4	0.06
Vertical Stretch Mode	10	1	0.15

Table 5.3: Reynolds' numbers for the major torsion balance configurations employed in the dynamic experiment. The values are calculated for a 5 cm diameter sphere. Torsion mode numbers assume a 1 rad amplitude; simple pendulum mode numbers, 100 μrad; and vertical stretch mode, 10 μm.

the torsion mode approach or surpass unity for our system, the possible effects of nonlinear damping on the period measurement cannot be ignored. Nonlinear behavior of the torsion mode will be considered in detail in Section 5.4. For small excitations of the other normal modes we can reasonably make all estimates using the linear equations.

5.3.2.2 Oscillatory Characteristics of the Fluid

A proper treatment of the effects of the surrounding fluid on the dynamics of our torsion balance must include the oscillatory nature of the balance motions. Thus we must consider the explicit time-dependence contained in the Navier-Stokes equation when calculating the effects of the surrounding gas on the torsion balance oscillations [96]. Appendix E outlines the important details of the time-dependent calculations; we simply summarize the principal results here.

In comparison to the steady-state calculation of the fluid coupling to a sphere undergoing translation or rotation, the time-dependent calculations introduce two corrections. First, there is an inertial correction due to the acceleration of the fluid as the balance moves back and forth. Due to the low density of the gas, this correction can be ignored. Secondly, the outward propagation of waves in the fluid, taking energy from the balance, results in increased damping of the various modes. The outgoing waves are characterized by their penetration depth, δ, which can be written as

$$\delta = \sqrt{\frac{2\nu}{\omega}} \tag{5.5}$$

where ω is the angular frequency of the oscillatory mode being considered. In the case of our hollow sphere, a penetration depth smaller than the radius of the balance results in the internal fluid effectively decoupling from the motion of the balance walls with the result that *both* the external and internal fluid volumes significantly damp such an oscillation. The damping of a sphere, of radius R, undergoing oscillatory motion can be described by defining an effective viscosity as

$$\eta_{\text{eff}} = \eta_0 f\left(\frac{R}{\delta}\right) \tag{5.6}$$

where $f\left(R/\delta\right) \rightarrow 1$ as $R/\delta \rightarrow 0$. Values of R/δ for the various modes are summarized in Table 5.4. Using Equation E.4, we can write $f\left(R/\delta\right)$ for translational motions as

Mode	R/δ	
	Air	Helium
Torsion Oscillation (Tungsten)	1.4	0.54
Torsion Oscillation (Quartz)	2.0	0.78
Simple Pendulum Mode	18	7.0
Wag Mode	39	15
Vertical Stretch Mode	72	28

Table 5.4: Values of the oscillatory damping parameter, R/δ, for the major modes of the balance.

$$f\left(\frac{R}{\delta}\right) \approx 2\frac{R}{\delta} \tag{5.7}$$

where this expression includes contributions from both the external and internal volumes of fluid. It also assumes a negligible shell thickness for the sphere and $R/\delta \gg 1$. Thus damping of the last three modes in Table 5.4 are dramatically increased in comparison to the Stokes' Law value in the limit of uniform motion. In contrast, the relatively small values of R/δ which are found for the torsion oscillations result in a much smaller change in the effective damping. In the limit of $R/\delta < 1$ Equation E.7 gives

$$f\left(\frac{R}{\delta}\right) \approx \left[\frac{1+\frac{2R}{\delta}+2\left(\frac{R}{\delta}\right)^2+\frac{2}{3}\left(\frac{R}{\delta}\right)^3}{1+\frac{2R}{\delta}+2\left(\frac{R}{\delta}\right)^2}+\frac{4}{525}\left(\frac{R}{\delta}\right)^4\right] \tag{5.8}$$

where the final term is due to the internal fluid and clearly does not contribute significantly (the internal fluid essentially co-rotates with the balance). In the case of the quartz-suspended balance operating in a helium atmosphere, this expression indicates roughly a 10% increase in the damping of the torsion mode due to oscillatory effects.

5.3.2.3 Relative Damping Times

Our main interest in the results from the previous section is to compare the lifetimes of the various modes. Since the non-torsion modes may be parasitically excited during the driving of the torsion mode,[5] the lifetimes of these unwanted oscillations need to be substantially shorter than the torsion mode lifetime. The calculated relative lifetimes for operation of the torsion balance are given in Table 5.5.

Mode	Relative Lifetime
Torsion Oscillation	1.0
Simple Pendulum Mode	0.16
Wag Mode	0.07
Vertical Stretch Mode	0.04

Table 5.5: Calculated relative lifetimes of the oscillatory modes of the balance, normalized to the torsion mode value, for helium operation.

In practice, the torsion mode lifetime is actually somewhat shorter than indicated by the above calculations. This is illustrated in Figure 5.8 which plots $\pi/Q = \beta P$ versus the balance period for the various system configurations we have employed. The observed damping is roughly 50% larger than would be expected based on the discussion of linear damping effects thus far. However, we have ignored the fact that the balance oscillates in a confined space. The added damping can be largely explained by the small separation between the balance and the spherical "cup" at the bottom of the inner can housing which holds the balance during transport of the entire apparatus (See Figure 5.2). The damping from this source can be estimated by considering the torques exerted between two concentric spheres of similar radius

[5]For instance, if the balance suspension point fails to lie precisely on the axis of rotation, the pendulum mode will be excited directly by a rotation of the balance. This excitation is small because the rotation velocities are determined by the torsion mode frequency which is much smaller than pendulum mode frequency. Nevertheless, a 250 μm offset from the axis can result in pendulum amplitudes of up to 10 μrad. The resulting displacements of the prisms on top of the balance result in timing errors at the tens of microseconds level.

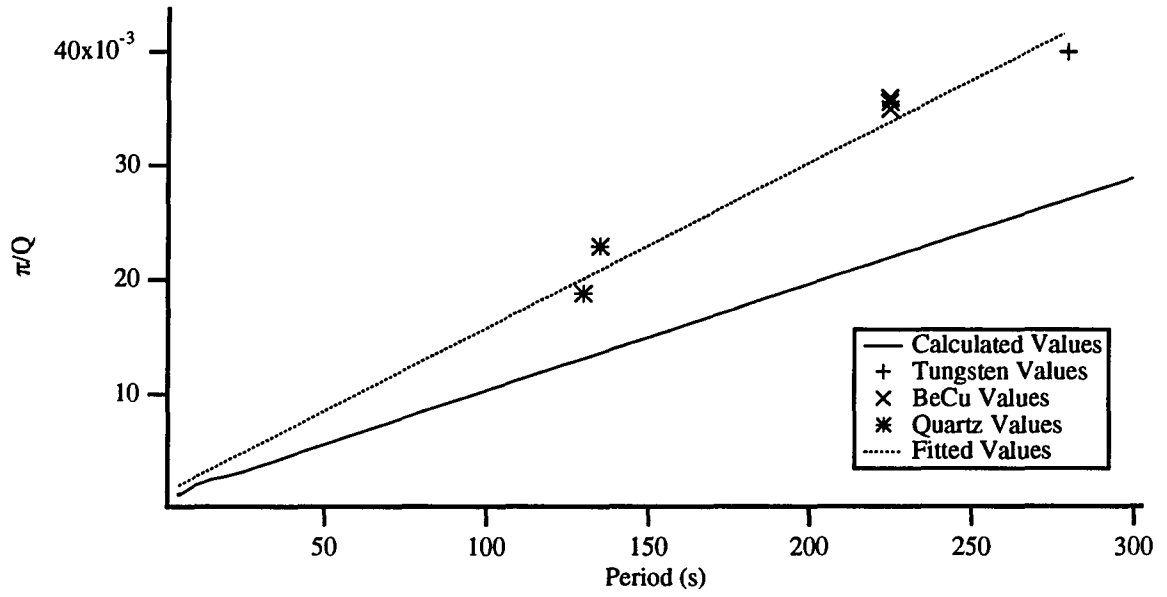

Figure 5.8: The plot shows the observed damping of the torsion balance expressed as $\pi/Q = \beta P$ as a function of the period. The solid line shows the calculated values based on Equation 5.8 while the dotted line is a fit of the observed values which is constrained to pass through the origin. The fit indicates roughly 50% more damping than expected.

rotating with angular velocity Ω with respect to one another.[6] The total viscous torque in that case is given by

$$T = \frac{8\pi\eta R^3\Omega}{3}\left(\frac{R}{s}\right) \tag{5.9}$$

where s is the separation between the shells. We compare this value with the standard damping expression for a sphere, $8\pi\eta R^3\Omega$. The mean spacing between our two surfaces is roughly 1 cm or about a quarter of the balance radius and just under 30% of the surface of the balance is subtended by the "cup". Thus we expect an increase in the damping of about 40–50% from this source. Fortunately, this effect is small enough that it does not seriously alter the relative damping times of the unwanted modes in comparison to the torsion mode.

[6]See Reference 96, p. 65.

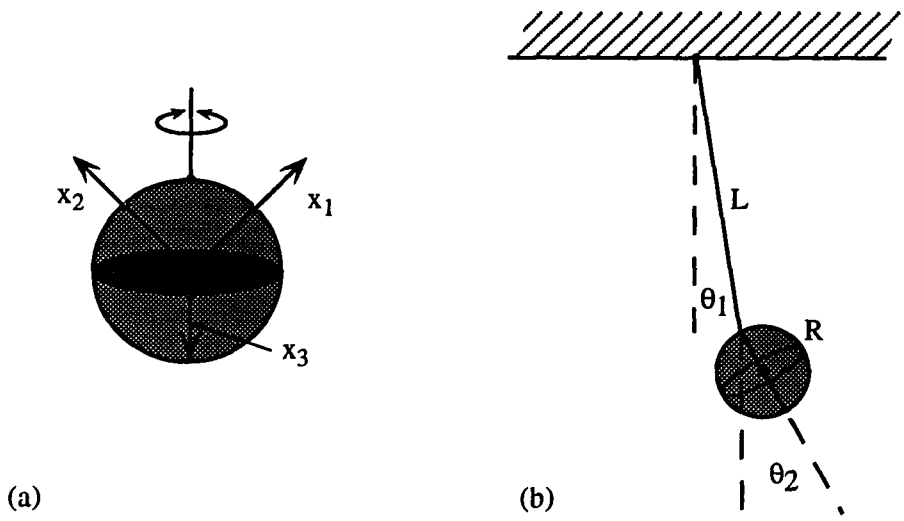

Figure 5.9: (a) The "worst-case" geometry for a coupling of the torsion mode to the pendulum modes of the balance due to a mass asymmetry. (b) The compound pendulum problem. The moment of inertia asymmetries under consideration drive the corresponding normal modes.

5.3.3 Coupled Modes

Departures of the torsion balance mass distribution from spherical symmetry will, in general, result in a coupling between the torsion and compound pendulum modes of the system. In order to estimate the impact of such a coupling, we consider a situation where a spherically symmetric mass distribution, with moment of inertia I, is perturbed to give $I_1 = I \neq I_2 = I_3$. Thus, if the torsion axis does not lie along a principal axis, torsional motion of the balance will result in a torque around an axis lying in the horizontal plane. Figure 5.9(a) shows the worst case scenario where the torsion axis lies 45° away from a principal axis. With this geometry, Euler's equations give the torque around the x_3 axis as

$$T_3 = \frac{\Delta I_{12}\dot{\theta}^2}{2} \tag{5.10}$$

where $\dot{\theta}$ is the angular velocity around the torsion axis. Figure 5.9(b) illustrates the compound pendulum problem. The torsion oscillation drives the normal modes of the pendulum well below their resonant frequency and we consider the energy stored in these modes as they displace to balance the driving torque [97]. As long as the torsion oscillations are not too large, we can make our estimates assuming that the pendulum modes are excited in only one dimension. A simple energy conservation argument then gives the torque on the torsion mode as

$$T_{tors}\dot{\theta} = -\frac{dE}{dt} \tag{5.11}$$

where E is the potential energy imparted to the pendulum modes. The energy stored in each mode is given by

$$E_i = \frac{T_i^2}{2\kappa_i} \tag{5.12}$$

where T_i is the projection of the torque of Equation 5.10 on the ith mode and κ_i is the torsion constant of that mode. We can make a quick estimate of the total energy involved by examining the constants associated with the simple pendulum mode, which has $\kappa \approx Mg\,(L+R)$, and the "wag" (θ_2 oscillations) mode, which has $\kappa \approx MgR$. Most of the energy enters the mode with the lower torsion constant and we roughly estimate the total energy in the pendulum modes as

$$E_{tot} \sim \frac{T_3^2}{\kappa_{wag}} = \frac{T_3^2}{MgR} \tag{5.13}$$

where T_3 is given in Equation 5.10. Writing the torsion oscillations as $\theta\,(t) = \theta_0 \sin \omega t$ and defining $\Delta\kappa = T_3/\theta$, we can write the fractional induced change in the torsion constant as:

$$\frac{\Delta\kappa}{\kappa_{suspension}} \sim \frac{(\Delta I_{12})^2\,\dot{\theta}^2}{2MgRI_{sphere}}. \tag{5.14}$$

Letting $\dot{\theta} \rightarrow \omega$, *i.e.*, the maximum value of $\dot{\theta}$ for a 1 rad amplitude oscillation, we obtain

$$\frac{\Delta\kappa}{\kappa_{suspension}} \sim \frac{1}{2}\left(\frac{\Delta I_{12}}{I_{sphere}}\right)^2 \left(\frac{\kappa_{suspension}}{\kappa_{wag}}\right) \tag{5.15}$$

where the second factor falls in the range 5×10^{-6}–5×10^{-7} for the torsion fibers we have employed and the size of $\Delta I_{12}/I \approx 0.015$ is determined by the fabrication tolerances of the torsion balance.[7] This leads us to expect period variations

$$\frac{\Delta P}{P} < 10^{-9} \tag{5.16}$$

due to couplings between modes, an order of magnitude smaller than our desired measurement accuracy.[8]

It should also be mentioned that, even in the absence of a mass asymmetry as just described, the torsion mode will couple to the pendulum modes via the Coriolis effect which also causes torques in the horizontal plane. An order of magnitude estimate, however, shows that this effect is much too small to present difficulties. The Coriolis force on a particle of mass m is given by:

$$\vec{F} = 2m\vec{\omega}_{earth} \times \vec{v}_r \tag{5.17}$$

where $\vec{v}_r$ is the velocity of the particle in the rotating frame. Setting $v_r \sim \omega_{torsion} R$, the magnitude of a mass element on the surface of the sphere is

$$T_m \sim 2m\omega_{earth}\omega_{torsion}R^2 \tag{5.18}$$

[7]The "worst-case" estimate for the difference in the two moments comes from considering the initial machining tolerances associated with the production of the aluminum shell balance. These lead to mass variations between the two hemispheres of the balance at the 1% level. Assuming this asymmetry is concentrated at a single point on the surface of the sphere results in the maximum difference in the moments between two principal axes ($\sim 1\frac{1}{2}\%$). It should also be pointed out that an attempt by Strong [97] to measure the moment of inertia asymmetry in our first prototype of a composition-dipole sphere indicated a similar size asymmetry as we have employed here.

[8]A related effect is the "reverse" of the problem just described. If we consider orienting the x_1 and x_2 axes of Figure 5.9(a) so that they lie in a vertical plane and exciting a rocking oscillation of the balance, then the rocking motion will drive the torsion mode directly. The driving frequency is well above the torsion frequency so the induced amplitude is fairly small. A quick estimate gives a period variation of a part in 10^9 for a 1 mrad rocking amplitude.

and the total torque on the sphere is of order

$$T_{Coriolis} \sim 2I\omega_{earth}\omega_{torsion}. \tag{5.19}$$

If we consider the ratio of this torque to the Eulerian torque from above, we see that

$$\frac{T_{Coriolis}}{T_3} \sim \left(\frac{I}{\Delta I_{12}}\right)\left(\frac{\omega_{earth}}{\omega_{torsion}}\right) \sim 0.1 \tag{5.20}$$

which indicates that this effect is indeed negligible.

5.4 A Study of System Nonlinearities

Nonlinearities associated with the torsion fibers have been a dominant characteristic of the dynamic system. These nonlinearities lead to a substantial amplitude dependence in the measured period and can be considered one of the main limitations of the technique. With tungsten torsion fibers, amplitude dependent period shifts were observed to be as large as several parts in 10^5. This section will describe the tests conducted to study this effect.

5.4.1 A Relative Period Measurement

Because of long-term drifts in the balance period and the relatively long duration of a period measurement in a single position, conducting separate experimental runs at different amplitudes was not an effective way to study the amplitude dependence of the period. Furthermore, the change in oscillation amplitude over the course of a measurement spanning 15 or more cycles of the oscillator results in substantial "smearing" of the amplitude information. In order to make a better relative measurement of the period's amplitude dependence, individual timing measurements as the amplitude of the balance slowly decayed in a single position were compared. The prescription for

this comparison consisted of taking an "averaged" value of the current period given by

$$\mathcal{P}_i = \frac{P_i + P_{i+1}}{2} \tag{5.21}$$

$$= \frac{t_{i-1} + 2t_i + t_{i+1}}{2} \tag{5.22}$$

where the t_i's represent the raw timing values obtained for three successive half-cycles of the torsion pendulum. To clarify the motivation for this approximation, note that the timing measurements in the experiment are obtained at a small but finite angular offset from the torsion pendulum's equilibrium angle. Thus, for a linearly damped oscillator, the t_i are given by

$$t_i \approx \frac{P}{2} + \frac{1}{\omega}\left[(-1)^i\left(\frac{\theta_m}{\theta_0}e^{\frac{i\beta P}{2}}\right) - (-1)^{i-1}\left(\frac{\theta_m}{\theta_0}e^{\frac{(i-1)\beta P}{2}}\right)\right] \tag{5.23}$$

where θ_m is the offset angle, θ_0 is the initial amplitude of the oscillation, and β is the inverse decay time (*for the amplitude*). The use of Equation 5.21 removes the exponential damping dependence to $2nd$ order.[9] Further corrections can be applied to the $\mathcal{P}_i$ values to remove higher order contributions from the exponential terms in Equation 5.23.[10] Figure 5.10 shows the departure expected for a linearly damped oscillator with a "typical" offset of $\theta_m = 5\,\text{mrad}$. The approximation rapidly

[9]It should be noted that the $2nd$ order linear damping contributions to P_i and P_{i+1} do not precisely cancel due to the slightly different amplitudes at which the two values are obtained. The uncancelled portion, at this level of approximation, is independent of the amplitude, however, and results in a small but equal shift of the calculated period values for all amplitudes. Thus, since we are interested only in amplitude-dependent variations, it has no impact on our analysis. Another point worth mentioning here is that this form also removes the effect of a direction dependence of the propagation delay through the electronic triggering circuitry. This effect arises because two trigger channels are used in triggering from the split-photodiode difference signal. The two channels are based on which direction the beam sweeps across the detector. A difference in the propagation delay between the two channels results in a systematic difference between even and odd half-cycle timing measurements and also between the values of $t_{i-1} + t_i$ and $t_i + t_{i+1}$ which are obtained. The effect on Equation 5.21 disappears to lowest order, however.

[10]An additional correction can also be applied for the fact that the half-cycle timing intervals used in the exponentials of Equation 5.23 are only first order approximations to the true intervals between zero-crossings. Under normal running conditions these corrections are quite small.

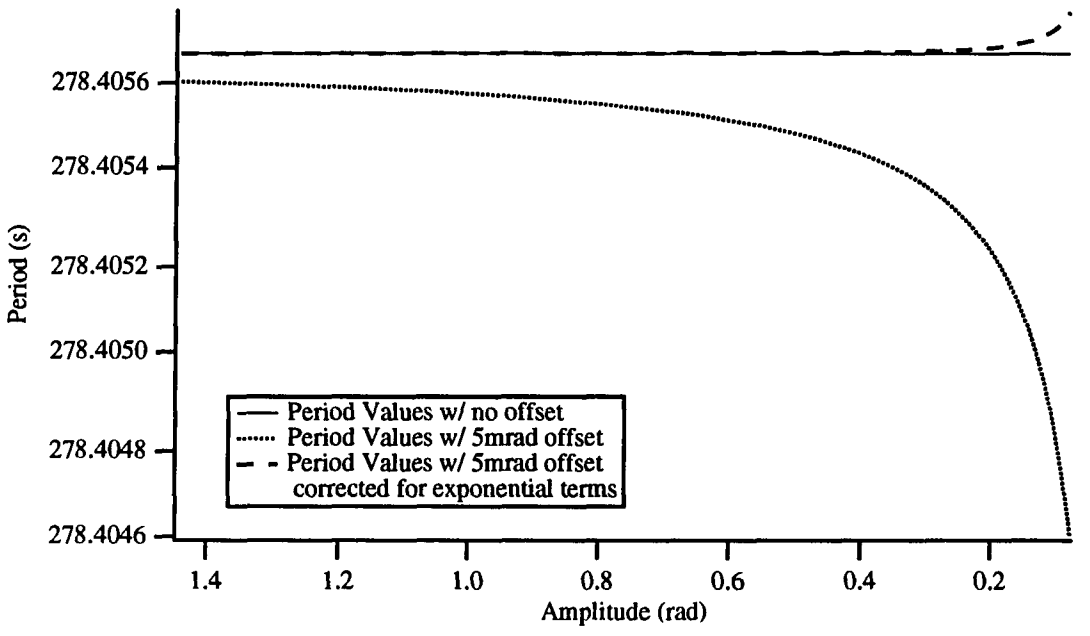

Figure 5.10: Errors in the $\mathcal{P}_i$ values due to a 5 mrad offset angle. The solid line shows the period of a balance with a natural period of 278.4 sec and a Q of 78.5. The dotted line shows the uncorrected $\mathcal{P}_i$ values while the dashed line shows these values when corrected for the exponential terms in Equation 5.23.

breaks down, however, when the ratio θ_m/θ_0 grows too large. Thus, at small initial amplitudes, this technique becomes subject to relatively large systematic variations. Given the size of the nonlinear effects involved, this level of approximation was more than sufficient to make the relative comparison of period values as the amplitude decayed.

5.4.2 Sources of Nonlinear Effects

Nonlinearities in the system can result from fluid dynamics effects and from nonlinear behavior of the torsion fibers. The significant role of the torsion fibers was first suggested by the observation that the method of fiber preparation significantly affected

the instabilities in the observed period.[11] When considering nonlinearities in the fibers, we have modelled the effects due to the first two nonlinear corrections to the restoring torque.

We consider an effective potential for the torsion mode given by:

$$V(\theta) = \frac{1}{2}\kappa\theta^2 + \frac{1}{3}\alpha\,|\theta|^3 + \frac{1}{4}\gamma\theta^4. \tag{5.24}$$

The presence of the $|\theta|^3$ term is due to the symmetry of the shear stress when the fiber is twisted in either direction. The expected amplitude dependence of these two extra terms is most readily seen by a simple energy conservation argument.[12] Noting that the kinetic energy in the oscillator is $\frac{1}{2}I\dot{\theta}^2$ we write

$$\frac{1}{2}I\dot{\theta}^2 = \frac{1}{2}\kappa\left(\theta_0^2 - \theta^2\right) + \frac{1}{3}\alpha\left(|\theta_0|^3 - |\theta|^3\right) + \frac{1}{4}\gamma\left(\theta_0^4 - \theta^4\right). \tag{5.25}$$

If we define $\hat{\alpha} = \alpha/I$ and $\hat{\gamma} = \gamma/I$, we then have

$$\int dt = \int \frac{d\theta}{\sqrt{\omega_0^2\left(\theta_0^2 - \theta^2\right) + \frac{2\hat{\alpha}}{3}\left(|\theta_0|^3 - |\theta|^3\right) + \frac{\hat{\gamma}}{2}\left(\theta_0^4 - \theta^4\right)}} \tag{5.26}$$

which leads to

$$\frac{P}{4} = \int_0^{\theta_0} \frac{d\theta}{\sqrt{\omega_0^2\left(\theta_0^2 - \theta^2\right) + \frac{2\hat{\alpha}}{3}\left(\theta_0^3 - \theta^3\right) + \frac{\hat{\gamma}}{2}\left(\theta_0^4 - \theta^4\right)}}. \tag{5.27}$$

The expression in the square root can be expanded to first order in both $\hat{\alpha}$ and $\hat{\gamma}$ and (after some manipulation) integrated to give

$$\begin{aligned} P &\cong P_0\left(1 - \frac{4\hat{\alpha}}{3\pi\omega_0^2}\theta_0 - \frac{3\hat{\gamma}}{8\omega_0^2}\theta_0^2\right) \\ &\cong P_0\left(1 - \frac{4\alpha}{3\pi\kappa}\theta_0 - \frac{3\gamma}{8\kappa}\theta_0^2\right) \end{aligned} \tag{5.28}$$

[11] Initially, our torsion fibers were heat-treated under tension before mounting the torsion pendulum. Improved performance was obtained, however, by hanging the torsion pendulum on an untreated fiber and allowing it to work anneal in the apparatus over a span of about two weeks.

[12] This treatment can be found in any number of texts on classical mechanics. See for example Reference 98.

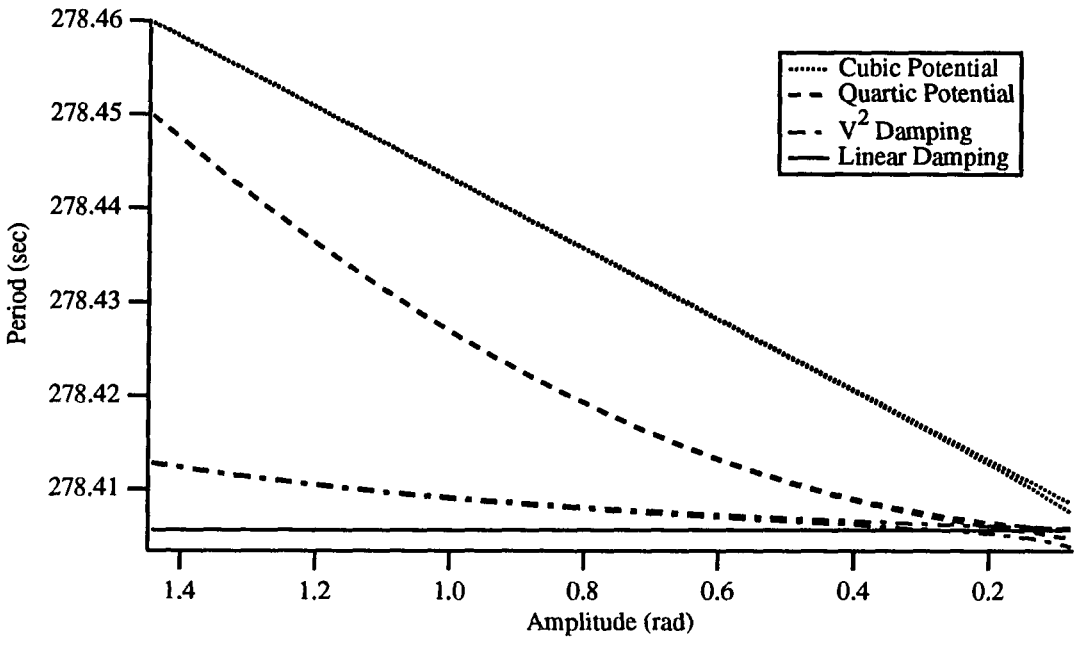

Figure 5.11: Nonlinear effects on the oscillator period for cubic and quartic terms in the torsion potential and a "v^2" damping term. Period values quoted are the $\mathcal{P}_i$'s as defined in Equation 5.21. The "tails" on the curves at low amplitude represent the breakdown of the $\mathcal{P}_i$ approximation due to a 10 mrad offset angle.

Thus the two nonlinearities are distinguishable by their linear or quadratic variations in the period.

As has already been mentioned, the other potential source of nonlinear effects is nonlinear damping of the torsion balance since the RMS Reynolds' number for the torsion oscillation approaches unity. We have considered an additional "v^2" damping term of the form

$$\tau\left(\dot{\theta}\right) = -\delta\left|\dot{\theta}\right|\dot{\theta} \tag{5.29}$$

It is found, however, that, when considering reasonable values of the coefficient δ, the direct effect on the measured period from this source is much smaller than that from fiber nonlinearities.

The three nonlinear effects just described have been numerically modelled as per-

turbations to the linearly damped harmonic oscillator. Figure 5.11 shows the $\mathcal{P}_i$ values expected for an oscillator with an undamped period of 278.4 sec and a Q of 78.5 corresponding to typical characteristics of our tungsten-suspended balance. The nonlinear coefficients employed for the plot correspond to fiber nonlinearities consistent with the measured period variations seen at 1 rad operating amplitude. Note that the amplitude dependence corresponds to negative nonlinear coefficients in the torsion potential so the oscillator potential is "soft". In the case of the v^2 damping, the coefficient corresponds to the RMS damping at 1 rad amplitude being roughly $1/2$ of the peak linear damping value. Since the observed damping of the balance is dominated by linear effects (See Section 5.3.2.2), this significantly exaggerates the size of the nonlinear damping contribution.

5.4.3 The Nonlinear Data

Figure 5.12 shows data obtained with a single tungsten fiber at three different operating amplitudes. These data were obtained over a span of two months in mid-1991. The fourth plot in the set shows the slopes obtained from fitting each of the data sets to a straight line as a function of amplitude. Every effort was made to use data obtained during periods in which long-term drifts of the torsion balance period were small. Note, however, that the sensitivity of low amplitude oscillations to fiber drifts is quite evident in the spread of values seen in the plot of the low amplitude slopes.

The data are clearly consistent with the dominant source of nonlinearities being the α term in Equation 5.24. Weighted means of the slopes at each of the three amplitudes are given in Table 5.6. The results from the two higher amplitude measurements are in excellent agreement with each other, while the low amplitude value differs by about 10% from the other two. Perhaps as much as a quarter of the effect

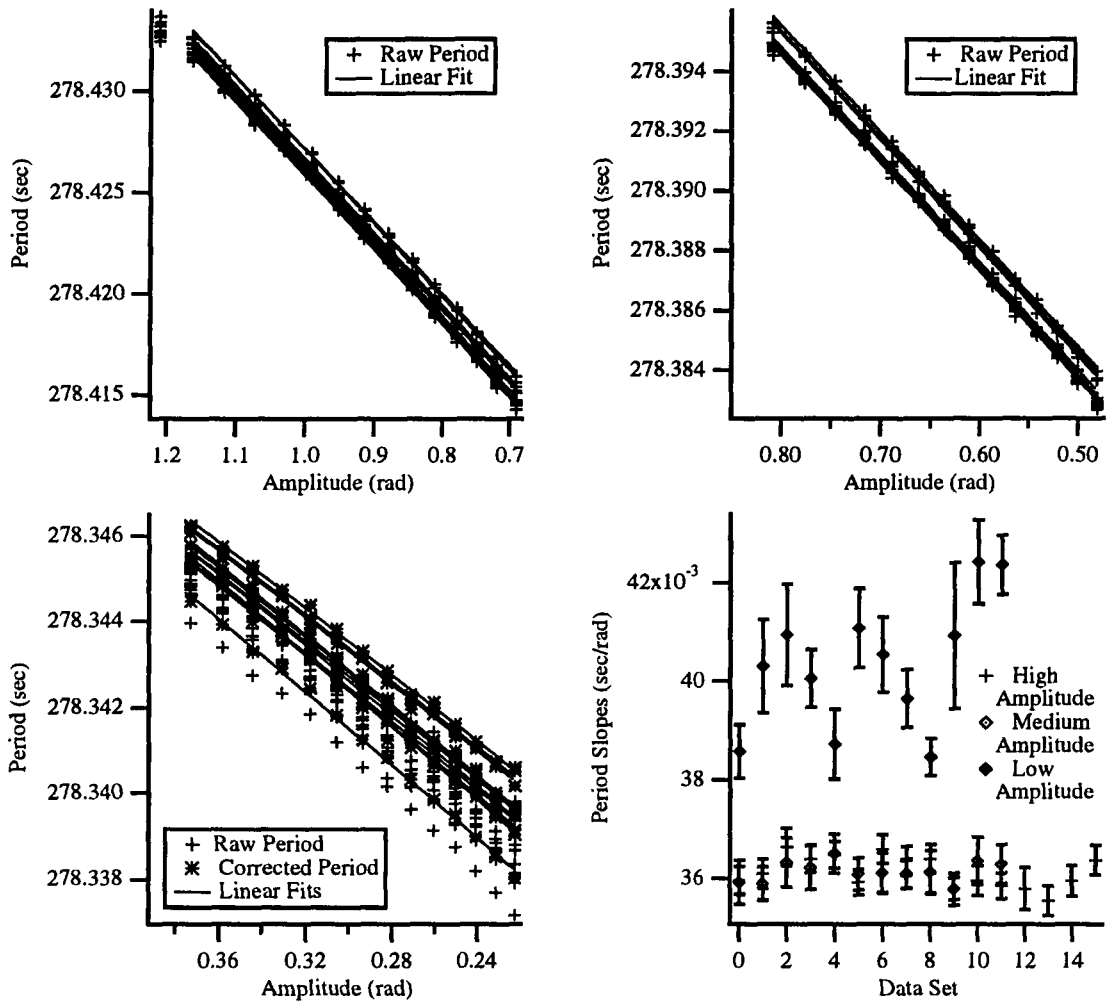

Figure 5.12: Nonlinear data obtained with a single tungsten torsion fiber at three different starting amplitudes. Corrections as described in Section 5.4.1 were applied to the low amplitude values. Also shown are the measured slopes in the period as obtained from a linear fit of the data for each regime.

Mean Amplitude (rad)	Slope in Period (msec/rad)	α/κ
0.30	39.8 ± 0.4	$(3.37 \pm 0.03) \times 10^{-4}$
0.64	36.1 ± 0.2	$(3.06 \pm 0.02) \times 10^{-4}$
0.93	36.1 ± 0.1	$(3.06 \pm 0.01) \times 10^{-4}$

Table 5.6: Amplitude dependence of the oscillator period at three operating amplitudes.

may be due to a small average drift of the balance period over the course of the data-taking. Furthermore, the breakdown of our timing approximation in the limit of low amplitudes makes the low amplitude value less reliable than the other two.

5.4.4 Implications of the Fiber Nonlinearities

The above amplitude dependence indicates that a period measurement at the level of 1 part in 10^8 would require a knowledge of the amplitude to better than a part in 10^4. The unacceptability of such a large systematic sensitivity led us to pursue the development of quartz torsion fibers as a possible replacement for tungsten.

As was mentioned at the beginning of this chapter, one of the goals of this experiment was to gain some insight into this technique in the interest of determining whether the non-zero result published by Boynton, *et al.* [88], might be due to some undiscovered systematic effect. The strong amplitude dependence exhibited by our tungsten fibers seems a plausible possibility. In order to estimate the impact of such a nonlinearity on Boynton's apparatus, we need to consider how the nonlinearities scale with fiber size. An estimate of this scaling is given in Appendix F. From the arguments there, we expect

$$\frac{\alpha}{\kappa} \propto \frac{r}{L}. \tag{5.30}$$

Boynton's torsion balance employed a 10 μm diameter fiber which was approximately 15 cm long in comparison to our own 50 μm by 60 cm fiber. Thus we expect the ratio of coefficients for the Boynton experiment to be about 80% of those that we observed. Boynton's signal corresponded to a $\pm 4 \times 10^{-6}$ fractional variation in the period of his torsion balance. With the above scaling, this would require ± 40 mrad variations in the amplitude of his balance to explain the effect. It is not clear, however, why amplitude variations sufficient to cause this effect would have been present during

his experimental run at a remote site near Index, Washington but not during several diagnostic tests in the laboratory [88].

5.5 Characteristics of the Current System

After nearly a year of development, we were able to successfully mount a torsion balance on a nominal $100\,\mu$m quartz torsion fiber. As will be shown below, the amplitude dependent shifts in the period were substantially reduced with this system. The following sections describe several key operating characteristics of the system in order to evaluate its potential for detecting weak forces.

5.5.1 Noise

Uncertainties in the period measurement due to thermal noise have been considered in detail in Section 3.3.1 and Appendix D. The salient features of this type of noise are that the phase of the oscillator undergoes a random walk from cycle to cycle so that the fractional phase and period uncertainties grow as $1/\sqrt{N}$ (where N is the number of cycles) and, furthermore, that they scale as $1/\theta_0$ (where θ_0 is the amplitude of oscillation). Using Equation D.12 and assuming oscillation amplitudes near 1 rad, we find that the thermal noise uncertainty for a single cycle period measurement is at or below a part in 10^8 for the quartz and tungsten fibers used in our experiment.

The single-cycle noise levels we actually observe are considerably higher than this. The RMS scatter in timing values in a given position is typically several tens of microseconds (*i.e.*, several parts in 10^7 of the balance period). The size of this scatter is found to be highly dependent on the level of activity in the building in which the apparatus is located. Thus we attribute the dominant source of noise to vibrational couplings into the apparatus. The most likely mode to be excited

vibrationally is the simple pendulum mode with a natural frequency of a fraction of a Hertz. This is the lowest frequency mode of the balance except for the torsion mode, and lies in the frequency region where our passive vibrational isolation is expected to fail. Furthermore, timing errors due to displacements of the prisms will be O(1μsec/μrad). Thus small excitations of this mode can readily generate timing noise of the size observed.

Before leaving the topic of noise, it should be noted that the noise in this type of system can be divided into two classes. Broadband excitation of the torsion mode directly results in a $1/\sqrt{N}$ behavior of the fractional uncertainty in the period measurement. In contrast, random noise in the timing measurements will simply produce some fixed uncertainty in the initial and final timing values. Thus, this latter type of noise will cause the fractional uncertainty in the period to scale roughly as $1/N$ for an N-cycle measurement. Electronics noise and noise due to motion of the optics fall in this category. Least squares fits of the balance period yield uncertainties in the period value which are consistent with the noise in our system being dominated by random timing measurement noise.

5.5.2 Systematic Effects

5.5.2.1 Nonlinearities with the Quartz Suspension

Nonlinearities with a quartz torsion fiber were indeed found to be significantly smaller than was the case with tungsten. Figure 5.13 shows a plot of the period versus amplitude obtained during a recent data run. The observed amplitude dependence is roughly a factor of 130 smaller than was seen with the earlier tungsten suspension. With an amplitude dependence of this magnitude, maintaining the amplitude stability to 3 mrad implies 1 μsec shifts in the measured period.

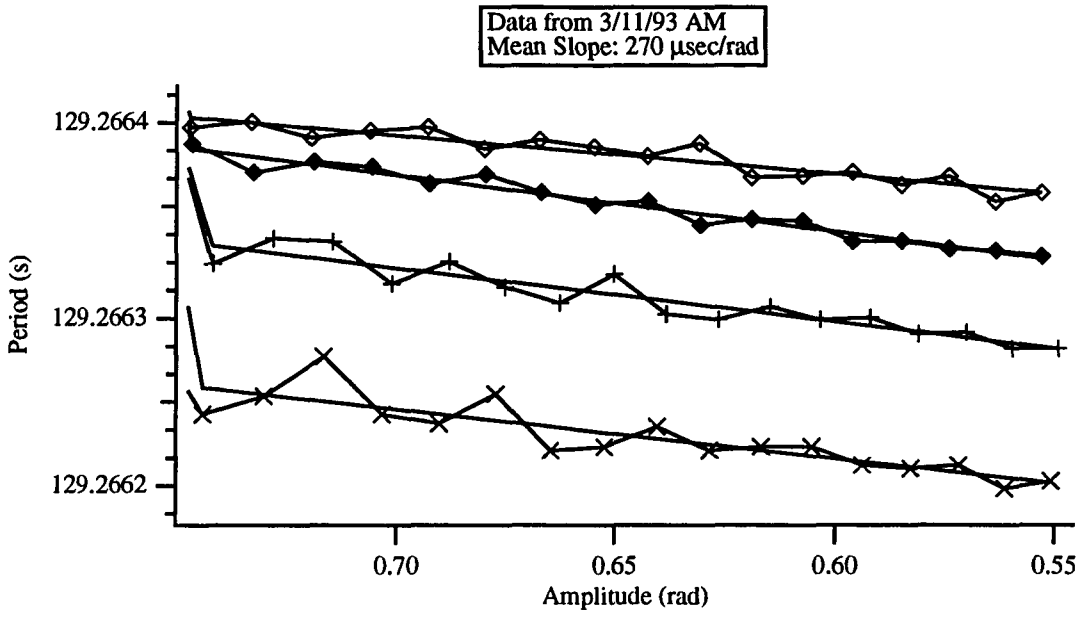

Figure 5.13: Nonlinear behavior shown by a quartz torsion fiber. The average slope is 270 μsec/rad, about 130 times smaller than was obtained with a tungsten fiber.

5.5.2.2 Fiber Drifts

Long term drifts in the period due to the gradual stabilization of the torsion fiber present difficulties for a precision period measurement. Figure 5.14 shows the long term change in the measured period which were observed for tungsten, beryllium-copper, and quartz suspension fibers. The long stabilization time (3 months) with the quartz suspension is particularly problematic form the point of view of mounting balances in the field for, more or less, immediate use. We are reminded of Eötvös' practice of letting his tungsten fibers hang for years before use in his apparatus [33].

5.5.2.3 Electronics

Filtering of the split-photodiode signal results in a frequency dependent propagation delay of the zero-crossing signal through the electronics. Since the amplitude of the

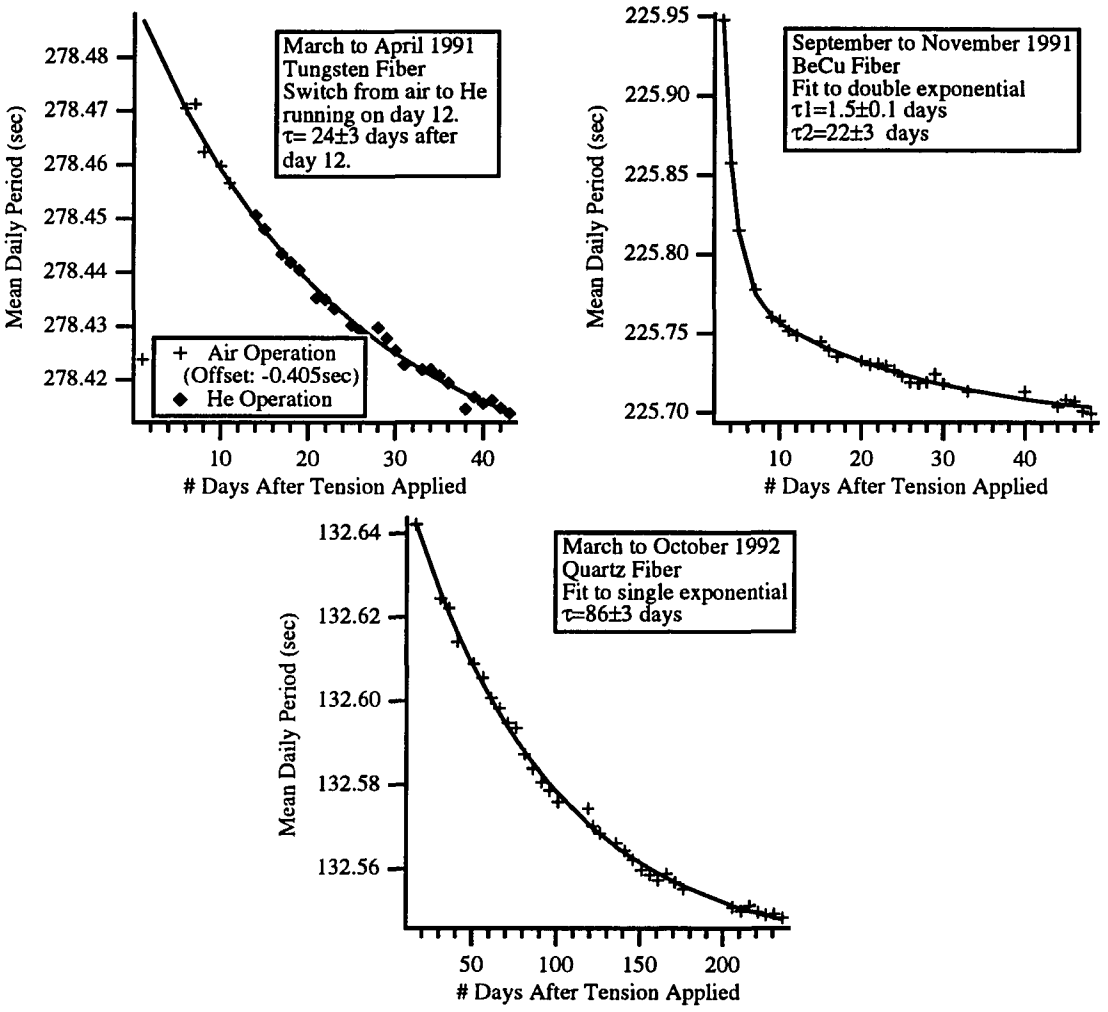

Figure 5.14: Long term stabilization of the torsional period as observed for tungsten, beryllium-copper, and quartz torsion fibers. Data shown in the case of tungsten shows a transition between air and helium operation. The air values have been offset to line up with the helium values

torsion balance decays significantly during the course of a measurement in a single position, the electronic signal width as the laser beam sweeps across the detector grows with time. We have extensively modelled the filter characteristics of our electronics and find that the measured period will typically vary by less 20 microseconds over the amplitude range at which we operate the torsion balance (i.e., approximately 0.4 to 1 radians). When making a measurement in a single position, this amplitude dependence should be reasonably linear as the oscillation dies away and will simply look like a small correction on top of the effects of the nonlinear torsion fiber.

5.5.2.4 Gravitational Gradients

In this section we briefly depart from the current setup to discuss the gravitational gradient couplings that may be expected with the composition-dipole torsion balance prototype.

If we assume for the moment that our copper/polyethylene spherical torsion balance is ideal except for the mass ring where the two halves overlap, the balance will couple to gravitational gradients by not having the suspension point bisect the edge of the mass ring, thus causing the ring to be slightly tilted from the vertical. The coupling of the ring to the $\partial g_x/\partial z$ derivative of the gravitational field at the Palisades (See Section 3.3.3) due to a $50\,\mu$m mounting error imitates a differential acceleration of 0.1 nGal (Recall that our 1 part in 10^8 timing sensitivity corresponds to 0.3 nGal with the quartz suspension). A second, more dramatic, coupling is to the horizontal derivatives of the field. This coupling is of the same form as was shown in Equation 4.13 for the gravitational gradient tests with the Cavendish balance in the previous experiment. This will result in roughly a part in 10^6 timing variation between the $0°/180°$ pair of positions and the $90°/270°$ pair of positions at the Palisades

site. This characteristic is potentially useful as a built-in calibration of the timing signal. It also results in systematic signals due to angular positioning errors, however. Our data indicates that the repeatability of the torsion balance angular positioning is $< 0.5\,\mathrm{mrad}$. Thus positioning errors should result in variations in the 180° timing comparison of less than 5 parts in 10^{10}. All in all, a reduction of the ring mass by an order of magnitude in any new version of the sphere, would result in negligible couplings to the gradients in the gravitational field except for the one providing the calibration. The calibration signal would then be roughly ten times the basic balance sensitivity.

5.5.2.5 Temperature Dependence

Day to day drifts in the period values we measure are dominated by the temperature dependence of the torsion period (this is after the long-term drifts associated with the break-in of the torsion fiber have subsided sufficiently). Figure 5.15 shows observed temperature dependence with a quartz fiber during a run where incomplete sealing of the apparatus allowed particularly large variations in the temperature in the apparatus. A long-term linear drift in has been removed from the period values. Diurnal temperature variations measured on the inner can housing are typically in the several tenths of a degree Celsius range. The temperature coefficient we measure in the case of our quartz suspension is approximately $-0.7\,\mathrm{msec}/^\circ\mathrm{C}$. The resulting period variations are somewhat large for our ultimate $1\,\mu\mathrm{sec}$ timing goal. Nevertheless, they are adequate for the current levels of testing. Furthermore, selecting data that is obtained during periods of relatively low drifts allows adequate comparison of the timing values at the level of a few microseconds.

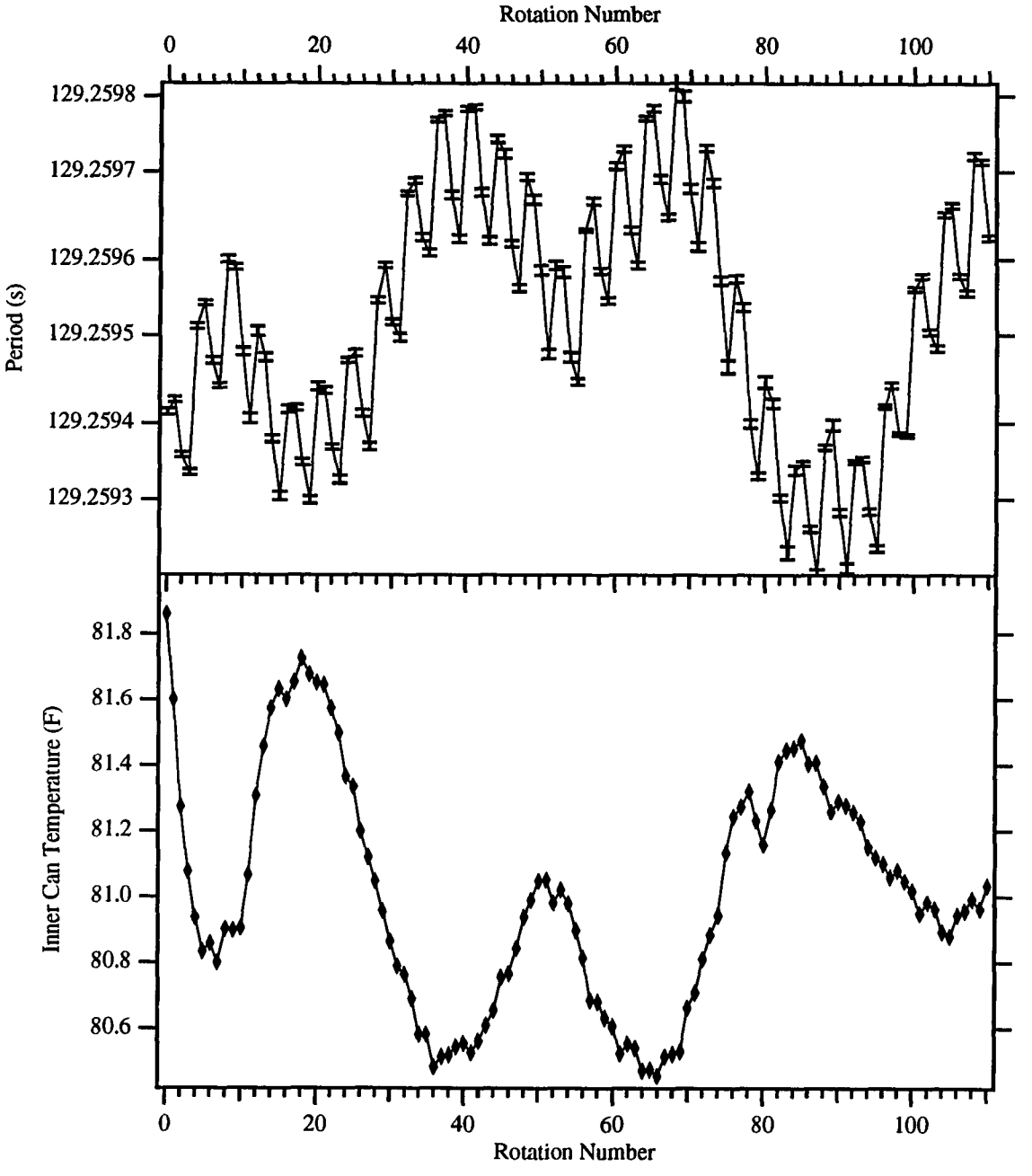

Figure 5.15: Temperature dependence exhibited by a quartz fiber during a period of relatively large temperature excursions. A linear drift has been removed from the period values.

5.5.2.6 Levelling Changes

Small levelling changes in the rotation mechanism of the apparatus as the balance is transported from position to position may affect the effective length of the torsion fiber, and thus induce a systematic variation in the observed period. As was described in Section 5.2.3, the torsion balance suspension is designed to minimize such effects. Measurements of the levelling dependence by varying the level of the support frame by ± 3 mrad indicate a change of $<30\,\mu$sec in the period.[13]

5.6 Final Comments

The performance of the dynamic apparatus has been rather disappointing to date. Persistent difficulties with various systematic effects have prevented its being used directly in any search for new interactions. Initial operation using tungsten torsion fibers was plagued by the nonlinear behavior described earlier. A brief interlude with a beryllium-copper fiber also showed significant systematic variations in the period. In our first attempt to work with a quartz torsion fiber, operation was characterized by large drifts in the torsion period as the fiber slowly stabilized over the space of several months. Furthermore, it was discovered that a permanent-dipole magnetic contaminant had been introduced with one of the suspension fittings. In our latest round of operation, the magnetic contamination has been removed but a residual systematic shift in the torsion period between our four measurement positions remains.

Figure 5.16 shows a segment of data taken at an oscillator amplitude of 0.773 rad. The segment spans roughly 11 hrs from a recent run. The individual data points are

[13]The relatively large size of this limit in comparison to our $1\,\mu$sec timing sensitivity is due to major thermal drifts in the apparatus during a levelling run. This is because the apparatus enclosure must be opened to access the levelling screws on the apparatus frame each time a levelling change is made.

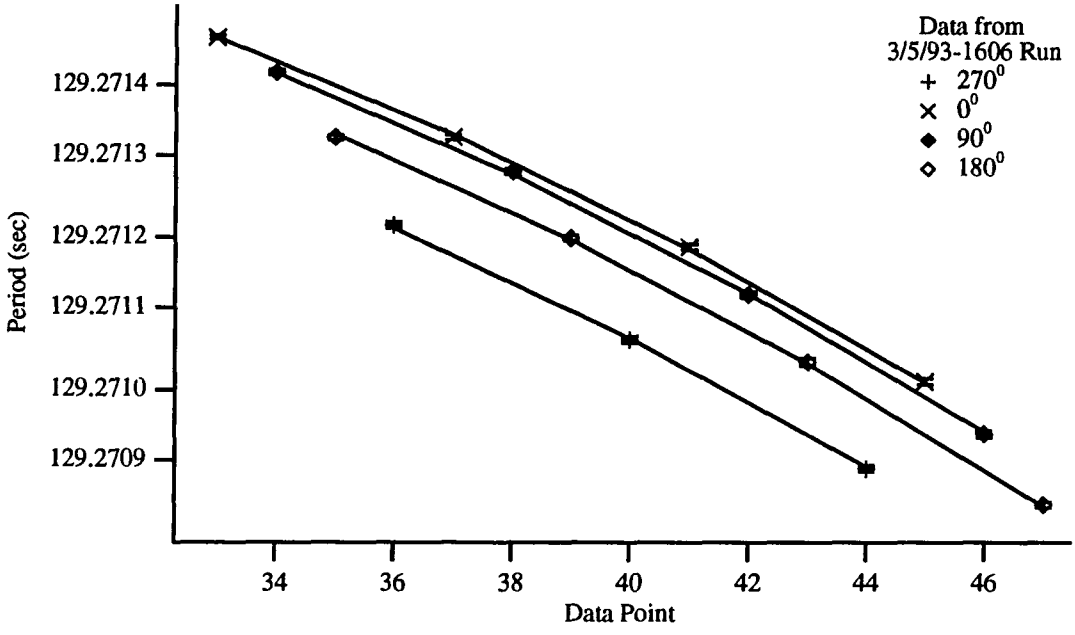

Figure 5.16: An approximately 11 hr segment of data from a data run in March 1993. Period values are least squares fits to a linearly damped function spanning approximately 0.168 radians of amplitude. Solid curves indicate least squares fits of the periods in each position to a 2nd order polynomial with the separation between the four sets of traces as a free parameter.

the results of least squares fits of the timing values in each position to the functional form of a linearly damped oscillator for 13 cycles of the torsion oscillation. Temperature variations through this segment of the run did not exceed 0.07°C. The period values for the four positions were fitted to a second-order polynomial where the period differences between the four positions were treated as free parameters. The resulting difference values are given in Table 5.7. The hopeful aspect of these numbers is the fact that the uncertainty in the timing differences is only 3 μsec, within a factor of three of our sensitivity goal, with data spanning less than four complete rotations of the apparatus. Clearly, if systematic effects can be fully understood and corrected, the apparatus has the potential to make measurements of differential accelerations at the level of a few tenths of a nGal with an integration time of a few days. We note

Positions Compared	Period Difference (μsec)	External Torque (dyne-cm)
0 – 270	152 ± 3	$(2.54 \pm 0.05) \times 10^{-6}$
90 – 270	136 ± 3	$(2.27 \pm 0.05) \times 10^{-6}$
180 – 270	88 ± 3	$(1.47 \pm 0.05) \times 10^{-6}$

Table 5.7: Systematic differences in the torsion balance period between the four measurement positions based on a χ^2 fit to a second-order polynomial with the differences as free parameters. The resulting χ^2 per degree of freedom was 0.9. The corresponding torque values are corrected for the finite amplitude of the oscillation.

that achieving a sensitivity of 0.1 nGal with this apparatus at the Palisades, would yield limits on composition-dependent interactions that are within a factor of two of the most sensitive terrestrial source results to date [99].

Part II

A Review of Recent Experiments

Chapter 6

Composition-Independent Limits

This chapter is the first of two devoted to a survey of experiments conducted from the late 1980's to the present whose goal has been to place better limits on interactions with ranges from meters to kilometers. These experiments can be classified as composition-independent tests, which test the $1/r^2$ behavior of gravity, and composition-dependent tests, which are, in essence, tests of the equivalence principle. This chapter provides an overview of the first category of experiments and summarizes the current experimental limits on new interactions in the region of interest. The following chapter surveys the corresponding composition-dependent limits.

Before beginning the survey, one ambiguity about the results of composition-independent tests should be made clear. The various tests which are described here use various laboratory and terrestrial source masses (most, however, employ LaCoste-Romberg gravimeters and thus have equivalent detector masses). In particular, water and rock terrestrial sources have both been employed. Thus the limits on inverse-square law departures from these experiments can only be directly compared if the nature of the interaction charge is known. In the absence of evidence for composition-dependent departures from Newtonian gravity, the comparisons which follow, and which are based simply on the masses of the source and detector, hold.

6.1 Composition Independent Experiments

Composition-independent tests fall into several categories which are listed roughly in order of increasing range at which the technique becomes sensitive.

1. Cavendish(Boys)-type experiments to measure G as a function of range.
2. Gradiometer verifications of Gauss' Law.
3. Beam balance/gravimeter tests with time-varying terrestrial source masses.
4. Tower measurements of g as a function of height above the earth.
5. Borehole and ocean measurements of g as a function of depth.
6. Orbit measurements to compare G at various distances.
7. Orbital precession measurements to detect deviations from general relativistic predictions.

Several experiments relating to first and last two categories are briefly summarized and the corresponding limits described in Appendix A. The limits discussed there are those which defined the unexplored "interaction window" at ranges of meters to kilometers which has been the subject of so much recent experimental effort. The following sections consider the remaining four types of experiments which have been used to place limits on new interactions in that region.

6.2 Gauss' Law Experiments

An elegant test of the $1/r^2$ form of the gravitational force is the verification that

$$\nabla^2\Phi = 0 \tag{6.1}$$

in the absence of sources. For a Yukawa potential, Φ_α, however, Equation 6.1 no longer holds. Consider a source mass at a distance r from a detector capable of

measuring $\nabla^2\Phi$. Then the intermediate-range part of the total potential is given by

$$\Phi_\alpha = -\frac{\alpha G m}{r} e^{-r/\lambda} \tag{6.2}$$

This leads to

$$\nabla^2\Phi_\alpha = -\frac{\alpha G m}{\lambda^2 r} e^{-r/\lambda}. \tag{6.3}$$

Over the past several years, Moody, *et al.*, have pursued the development of superconducting gravity gradiometers with the necessary sensitivity to measure $\nabla^2\Phi$ [100–103]. Their apparatus consists of six spring-mass accelerometers mounted on the faces of a precision cube with the axes of the individual accelerometers perpendicular to the corresponding faces of the cube. Each pair of accelerometers sharing an axis is coupled together by a superconducting circuit which is used to measure both the common mode and differential accelerations of the two masses. The precise details of the accelerometer design can be found in reference [102]. The cube is oriented with its diagonal along the local vertical in order for all three gradiometers to be equally biased in the earth's field. It is important to note that, in practice, a static measurement is not possible so that the position of the gradiometer must change with respect to the source mass and the two signals compared. The method of Moody, *et al.*, is to use a simple pendulum (nominal mass of 1500 kg) source [104]. This method also has the potential to be used at a location with a modulated terrestrial source as described in the next section. The errors peculiar to this experiment come from 3 main sources. First, since there is a finite separation between each accelerometer in a pair, the gradiometer is sensitive to higher order derivatives of of the gravitational field. Also, any angular acceleration of the detector introduces a differential acceleration between mass pairs which imitates a real signal. Finally, misalignment of the six individual accelerometers leads to addition errors when the signals from the three axes are summed.

Moody and Paik have recently reported results from their 3-axis gradiometer experiment with effective ranges on the order of a few meters [104]. Their sensitivity to gravitational gradients is at the level of $10^{-13}\,\mathrm{sec}^{-2}$.They quote a 2σ limit on α of $(0.9 \pm 4.6) \times 10^{-4}$ for $\lambda = 1.5\,\mathrm{m}$. The more general limits placed by their experiment are shown in Figure 6.2 later in this chapter. They hope to improve their current signal-to-noise ratio by constructing a better source.

6.3 Modulated Terrestrial Source Experiments

By modulated terrestrial source we mean a large (i.e. larger than can be accommodated in a laboratory) concentration of mass which is varied on a periodic basis. This cryptic statement essentially translates to measuring the gravitational acceleration due to a body of water whose height is varied on a daily basis. Bodies of water with well characterized and substantial height variations (i.e. on the order of tens of meters) are readily available in the form of artificial lakes and reservoirs. There have been two principal experiments of this type which have attempted to place significant constraints on departures from Newtonian gravity.

These experiments rely on comparing the gravitational acceleration at a point when a layer of material of density ρ is present versus when the layer is removed. In order to understand the size of the effect, consider the gravitational acceleration due to an infinite layer of thickness t. Application of Gauss' Law reveals

$$g_{slab} = 2\pi G\rho t \tag{6.4}$$

independent of the distance from the layer. A typical height variation of the water level in a reservoir is of order tens of meters. Taking $t = 10\,\mathrm{m}$, and assuming the material is water, this corresponds to a change in the gravitational acceleration of

approximately $4 \times 10^{-4}\text{cm/sec}^2 = 4 \times 10^{-4}$ Gal. Now, in the presence of an intermediate range Yukawa-type interaction, the acceleration due to an infinite slab is given by:

$$\Delta a = 2\pi G\rho \left[t + \alpha\lambda e^{-z/\lambda}\left(1 - e^{-t/\lambda}\right)\right] \tag{6.5}$$

where z is the distance from the slab at which the measurement is made. To obtain a feeling for the requisite sensitivity for placing limits on the strength of the interaction, consider the case of $\lambda = t$ and $z \ll t$. Then placing a limit on α at the level of 1% of gravity requires a measurement precision at the level of $2\,\mu$Gal which is possible, for instance, using standard gravimeters.[1] Before proceeding further, it should also be mentioned that substantial corrections must be applied to the infinite layer approximation assumed here in any real experiment. The fractional corrections are of order z/R and t/R where R is a measure of the horizontal extent of the body of water. For both of the experiments described below, the measurement sites are about 150 m from the nearest shoreline. For a 10 m thick layer, the resulting 7% correction would swamp any fifth force contribution at the levels of interest.

There are two experiments of this type, since the time of the Eötvös reanalysis, which have placed limits at effective ranges of tens of meters. The first, by Moore, *et al.* [106, 107], employed a beam balance with the two masses separated by a vertical distance of approximately 12 m. The experiment was located on a tower in the middle of the Splityard Creek reservoir in Brisbane, Australia. The hydroelectric reservoir

[1] LaCoste-Romberg D and G gravimeters are the standard measuring instrument for all of the terrestrial gravity experiments described in this chapter. They have sensitivities on the order of $1\,\mu$Gal and are easily portable to experimental sites. Marson and Faller [105] provide a review of these standard tools of the geophysicist. For our purposes, it is important to note that the spring-mass acceleration measurement system employed must be calibrated at sites of known gravitational acceleration over the range of accelerations to be employed. As with any measurement system employing a mechanical spring as a force (or torque) sensor, mechanical drifts are present and must be taken into account for high sensitivity measurements. The units are sealed and temperature-controlled for environmental isolation although some sensitivity to ambient temperature and pressure remains. Finally, the masses used in these gravimeters are normally tungsten.

was subject to level changes of up to 10 m and this 10 m range was bracketed by the two balance masses. Note that the beam balance method doubles the size of the effects given by Equations 6.4 and 6.5. This experiment was able to place limits on the existence of a Yukawa interaction at the level of 2% of the gravitational strength.

The second experiment, by Müller *et al* [108], was conducted at the Hornberg Lake hydroelectric reservoir in Germany. In this case two sets of three LaCoste-Romberg gravimeters were employed. One set was located on a 60 m tower in the middle of the lake while the second set was located in a tunnel underneath the lake offering access to the tower. Variations in the water level of 5 to 22 meters provided the signal of interest. The tower gravimeters were at an effective range of 68 m from the slab while, for the tunnel gravimeters, this value was 39 m.[2] The limits placed by this experiment were at the level of 0.7% of gravitational strength.

The limits placed by both experiments are shown in Figure 6.2. A final comment is in order about any hopes for more experiments of this type. The inability to make vertical acceleration measurements at much better than the level of 1 μGal, 1 ppb of the gravitational acceleration, precludes any significant improvement in sensitivity beyond the limits of the experiment by Müller, *et al.* [108].

6.4 Tower Experiments

The existence of stable towers with heights of several hundred meters allows probes of new interactions at ranges of roughly tens to hundreds of meters. The analysis of such data requires precise knowledge of the gravitational field of the earth because any variation in the force on a test mass as a function of height is dominated by the

[2]The effective range is the distance from the test mass to each mass element in the slab weighted by the mass elements contribution to the vertical acceleration on the test mass.

variation in the earth's gravitational field. Before considering how well the Newtonian portion of the force can be determined, we calculate the size of an acceleration due to an intermediate-range force. Since the range is finite, we calculate the difference in acceleration between a test mass at height z above a semi-infinite slab of density ρ and a test mass on the surface of the slab due to a Yukawa interaction:

$$\Delta a = 2\pi G_\infty \alpha\lambda \left(e^{-z/\lambda} - 1\right). \tag{6.6}$$

Note that, for ranges much longer than the height of the measurement, the tower experiment is sensitive to the product, $\alpha\lambda$, of the strength and range of the interaction. We can calculate the acceleration gradient to which we must be sensitive in this limit for an interaction with a strength of 0.1% of gravity. Assuming a local density of $2.5\,\mathrm{g/cm^3}$, this corresponds to da/dz =1 E=1 nGal/cm.

Modelling of the gravitational field above the earth's surface is accomplished by the method of "upward continuation." Upward continuation extrapolates the vertical component of the gravitational field to points above the surface based on a finite sampling of the surface gravity in the vicinity of the tower. This is accomplished by considering Laplace's equation outside the volume bounded by the surface of the earth after having explicitly taken into account non-harmonic contributions to the effective gravitational potential (*i.e.*, inertial accelerations due to the earth's rotation, tidal effects, and the fact that air is present so that the region under consideration is not truly sourceless). Thomas [109] and Romaides, *et al.* [110] have given the details of the upward continuation procedures used for the tower experiments at a Nevada and a North Carolina tower, respectively. At current levels of sensitivity in these experiments, it is simply necessary to consider the gravity field above a boundary plane on

which the vertical component of the gravitational field is specified.[3] It is important to note that, in cylindrical coordinates, the z-component of the gravitational field as well as the gravitational potential are harmonic functions above our boundary plane. This allows us to consider the Dirichlet boundary value problem for the z-component of the gravitational field. The solution is given by [111, see Equation (1.44)]

$$W(\vec{x}) = -\frac{1}{4\pi}\oint_S W(\vec{x}')\frac{\partial G_D}{\partial n'}da' \tag{6.7}$$

where W is the harmonic function, G_D is the Green's function for the Dirichlet boundary conditions, and n' is in the direction of the unit normal pointing downward. The necessary Green's function for the plane is

$$G_D(\vec{x},\vec{x}') = \frac{1}{|\vec{x}-\vec{x}'|} - \frac{1}{|\vec{x}+\vec{x}'|}. \tag{6.8}$$

If we now set $W = g_z$ and restrict ourselves to points lying on the vertical axis passing through the origin, Equation 6.7 becomes

$$g_z(0,0,z) = \frac{z}{2\pi}\int_0^\infty r'dr'\int_0^{2\pi} d\theta'\frac{g_z(r',\theta',0)}{(r'^2+z^2)^{3/2}} \tag{6.9}$$

which has the obvious interpretation from electrostatics as the integral over the induced surface charge on a grounded and conductive boundary plane.

There are several geophysical details which complicate the simple picture above. The reader is referred to the standard text by Heiskanen and Moritz [112] for a general treatment of the techniques of physical geodesy and to the recent experimental references (see below) for the details of the geophysical models actually employed—only a cursory summary of some important principles will be given here. First of all, the raw gravitational acceleration given by Equation 6.9 is *not* the quantity that is

[3]Current experimental limits are at roughly the 0.1% level while corrections to any calculation due to curvature of the earth will enter at the level of $z/R_\otimes$, where $R_\otimes$ is the earth's radius. For towers of several hundred meters in height this corresponds to a correction of $O(10^{-4})$.

calculated in practice. Instead it is the gravity anomaly, Δg, which is the difference between the observed gravity and the gravity expected due to a rotating spherical or ellipsoidal earth model (with the effects of the atmosphere taken into account) which is employed. This explicitly removes the nonharmonic contributions from the quantity undergoing upward continuation. Local topology can be taken into account by extrapolating the surface gravity measurements down to the reference ellipsoid (the method of Bouguer reduction). This effectively removes the contribution of the local mass above the reference ellipsoid and takes into account the change in gravity due to the free-air gradient between the two levels. Thus the gravity anomalies are obtained on the reference ellipsoid surface from which the upward continuation integral can be calculated. The change in gravitational acceleration up the tower then consists of three parts:

1. The component due to the basic ellipsoidal model;
2. The contribution of the upward continued anomaly field;
3. The contribution from the topological mass which was effectively removed by the Bouguer reduction.

Note that this type of analysis has several variants which depend primarily on modifications to the earth model employed in # 1, which can shift some contributions to the gravity field from # 2 to # 1. It also depends on the definition of the reference surface to be used in the calculation.

Several purely experimental complications arise due to the LaCoste-Romberg gravimeters used in the gravity measurements (see the previous section). Calibration, drift and temperature dependence must be considered. Also, tidal corrections must be applied to each gravity measurement. Another source of concern in these experiments has been tower motion. Finally, the free-air gradient of approximately

Source	Contributions to $g(z) - g(0)$ in μGal
Free-Air Gradient	150×10^3
Intervening Atmosphere	50
Tower Mass (assuming a linear mass density of 5 kg/cm [113]	3
Fifth Force with $\alpha = 0.01$ and $\lambda = 100\,\mathrm{m}$	100
Upward Continuation Uncertainty	15–80
Gravimeter Measurement Uncertainty	10–20
Tidal Correction Uncertainty	5
Gravimeter Position Uncertainty (1 cm)	4
Accelerations Due to Tower Motion	<5

Table 6.1: Nominal contributions to the gravity change from the base to the top of a 500 m tower and sources of uncertainty in the measured values.

$3\,\mu$Gal/cm necessitates precise knowledge of each measurement location over the entire height of the tower. Table 6.1 provides nominal values for the various contributions to the gravity differences measured between the top and the base of a "typical" 500 m tall tower.

Gravity measurements have been obtained at three tower sites. The first experiment to publish results was that of the group of Eckhardt, *et al.* [113,114], conducted at the 600 m WTVD tower in Garner, North Carolina, which seemed to indicate a significant departure from Newtonian gravity. Their initial analysis indicated an anomalous acceleration of $-500 \pm 35\,\mu$Gal at a height of 562 m. This was interpreted as evidence for an *attractive* Yukawa interaction with $\alpha = 0.0204$ and $\lambda = 311\,\mathrm{m}$. In order to make the result compatible with other experimental indications of a repulsive interaction, it was also shown that the data could easily accommodate the presence of two competing interactions, a scalar and a vector, as had been suggested by quantum

gravity models. Romaides, *et al.* [110], provide details of the upward continuation models used in the analysis. Their gravity survey included direct measurement of g at 77 sites within 5 km of the tower and gravity measurements from the Defense Mapping Agency at 1784 sites between 5 and 220 km from the tower. Bartlett and Tew [115] suggested that most of the anomalous effect could in fact be explained by incomplete characterization of the local surface terrain in their analysis (they noted that the azimuthally averaged terrain around the WTVD tower indicated that the tower was effectively situated on a hill) combined with a statistical bias towards making their surface gravity survey at easily accessible locations (typically locations on high ground, "to avoid local swamps" [115]). The Eckhardt group subsequently extended their gravity surveys and the degree of terrain modelling used in their analyses. Jekeli, *et al.* [116], quoted a final result consistent with Newtonian gravity and placing an upper limit on the coupling strength of a single Yukawa force of 10^{-3}.

A second tower experiment was conducted by Thomas, *et al.* [117], at a 465 m tower at Jackass Flats, Nevada. The experimental site was a desert plain, with a line of sight extending for 5 km, allowing a precise surface gravity map to be obtained. Direct gravity measurements were obtained at 281 sites within 2.6 km of the tower and were supplemented by 60,000 gravity measurements within 300 km of the tower available from the databases of the USGS and NOAA. They obtained a null result with a measured gravity residual of $-60 \pm 95\,\mu$Gal at a height of 454 m.

The third tower experiment, by Speake, *et al.* [118,119], was conducted on a 300 m tower at Erie, Colorado which the authors point out was situated on flat and easily surveyed terrain. Their gravity survey included 265 sites within 8 km of the tower and was supplemented by Defense Mapping Agency data at 26,000 sites in a roughly 450 km $\times$ 560 km region. At a height of 295 m their gravity residual was $10 \pm 27\,\mu$Gal.

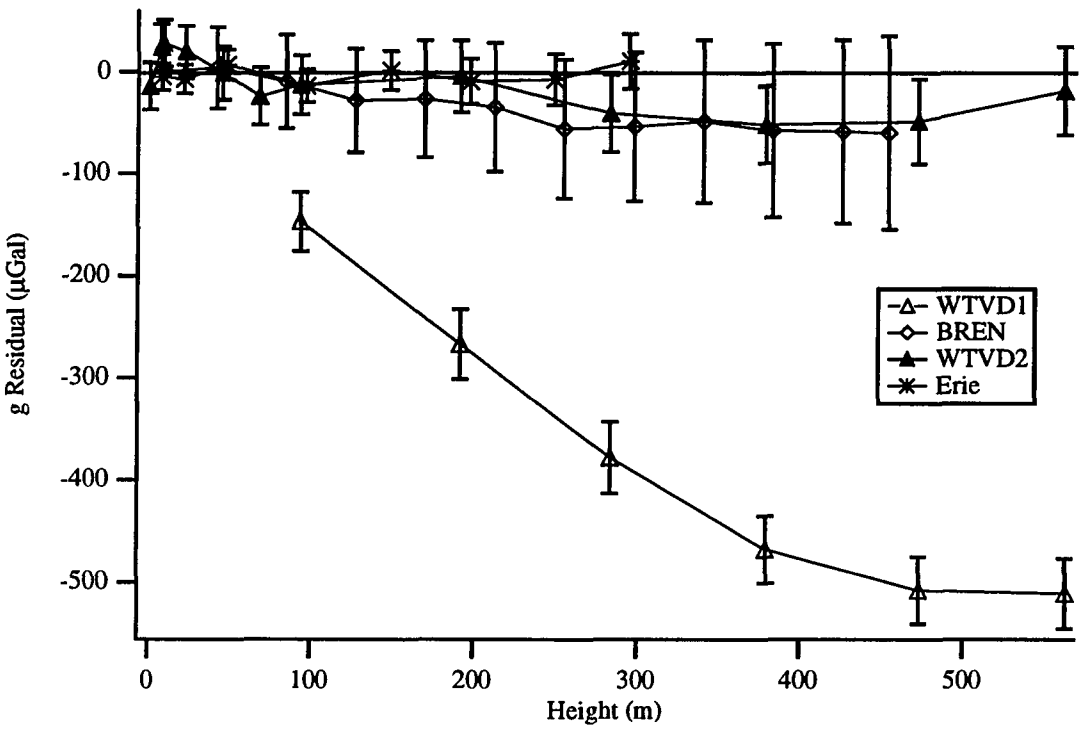

Figure 6.1: Tower gravity residuals as obtained at the three tower sites described in the text (Form of plot based on Reference 119). Results from the WTVD tower are shown from before and after the reanalysis of that data by the Eckhardt group. The need for great care in modelling the earth's field is self-evident.

Gravity residuals from the three tower measurements are plotted in Figure 6.1. Note that the plot labelled WTVD1 shows the results from the original analysis of Eckhardt *et al* while WTVD2 includes the revised modelling of the local terrain. Note that, for all of the measurements, the indicated errors are highly correlated at the various heights. This is due to uncertainties from the upward continuation of the gravity field which dominate the statistical uncertainties in the measurement. 1σ constraints can be placed on the strength, α, of an intermediate range interaction by fitting the central value of the residuals $\pm$ the 1σ uncertainties to the Yukawa form given by Equation 6.6 [117,119]. These limits are shown in Figure 6.2 in Section 6.6.

6.5 Borehole and Ocean Measurements

The role of borehole measurements in the search for new interactions has already received some mention in each of the preceding chapters. The basic principles of this type of measurement of the gravitational acceleration are relatively straightforward. Assume for the moment a spherical, layered, and non-rotating earth. The rate of change of the gravitational acceleration as a function of depth beneath the surface of the earth is given by:

$$\frac{dg}{dr} = -\frac{2g(r)}{r} + 4\pi G_\infty \rho_{local} \tag{6.10}$$

The first term describes the gradient due to the effective point mass source at the center of the earth while the second describes the change due to the mass in the local layer through which the borehole passes (The first term is known as the free-air gradient while the second is the Bouguer term.). Note that we explicitly write the gravitational constant, G, as G_∞ in Equation 6.10 in order to emphasize that, in the presence of an intermediate range force, the Newtonian value of G that should enter is the one that is measured beyond the range of the interaction (as opposed to the measured value which is obtained at small separations in a laboratory).

In the presence of an extra Yukawa interaction, there will be a non-Newtonian acceleration on a test mass given by:

$$\Delta a = 2\pi G_\infty \alpha \lambda \left(e^{-z/\lambda} - 1\right) \tag{6.11}$$

where z is the depth of the measurement. In general, measurements of this type are also presented in the form of a gravity residual:

$$\Delta\left[g(z) - g(0)\right] = \left[g(z) - g(0)\right]_{measured} - \left[g(z) - g(0)\right]_{calculated} \tag{6.12}$$

$$= -2\pi\left[2\rho_{local} z\left(G_\infty - G_{lab}\right) + G_\infty \rho_{local} \alpha\lambda\left(1 - e^{-z/\lambda}\right)\right]. \tag{6.13}$$

Source of Gradient	$10^{-6}\,\mathrm{sec}^{-2}$
Free-Air Gradient	-3.1
Bouguer Term for Rock ($\rho = 2.7\,\mathrm{g/cm^3}$)	+2.3
Bouguer Term for Water ($\rho = 1.0\,\mathrm{g/cm^3}$)	+0.8
Fifth Force with $\alpha = 0.01$	+0.01

Table 6.2: Contributions to the total gravitational gradient in borehole measurements.

Noting that $G_{lab} = G_\infty (1+\alpha)$, we may write this as:

$$\Delta\left[g(z) - g(0)\right] = \frac{4\pi\rho_{local}\alpha G_{lab}}{1+\alpha}\left[z - \frac{\lambda}{2}\left(1 - e^{-z/\lambda}\right)\right]. \tag{6.14}$$

Interpretation of the experimental results in terms of limits on the interaction strength, α, proceeds most simply by considering the derivative of Equation 6.14

$$\frac{d}{dz}\left\{\Delta\left[g(z) - g(0)\right]\right\} = \frac{4\pi\rho_{local}\alpha G_{lab}}{1+\alpha}\left(1 - \frac{1}{2}e^{-z/\lambda}\right). \tag{6.15}$$

It is immediately obvious that the slope of the residual divides into three distinct regions. For $z < \lambda$ the expression in brackets on the r.h.s. of Equation 6.15 approaches $\frac{1}{2}$ while for $z > \lambda$ it approaches 1.[4] The region with $z \approx \lambda$ is the only one where the slope varies appreciably from a constant value. A comparison of the various contributions to the total derivative of the earth's field is given in Table 6.2.

It is useful to compare the derivative of the earth's gravitational field at the surface to the derivative of a Yukawa field of some given strength. The two terms in Equation 6.10 have nominal values $-3.1 \times 10^{-6}\,\mathrm{sec}^{-2}$ and $2.3 \times 10^{-6}\,\mathrm{sec}^{-2}$ (where a local rock density of $2.7\,\mathrm{g/cm^3}$ has been assumed) giving an overall derivative of $-0.8 \times 10^{-6}\,\mathrm{sec}^{-2}$.[5] The corresponding acceleration gradient due to an intermediate

[4] For depths greater than the range of an intermediate range interaction, one expects the anomalous acceleration due to layers above and below the test mass to cancel. The slope of the residual does not disappear, however, because of the fact that the calculated value of the Newtonian acceleration employs the laboratory value of the gravitational constant and thus incorrectly calculates the Newtonian contribution.

[5] Note that a very high sensitivity test could be conducted in a region with local density $3.6\,\mathrm{g/cm^3}$ because the Newtonian contribution to the gradient would disappear.

range interaction with a characteristic strength of 1% of gravity is $1 \times 10^{-8}\,\mathrm{sec}^{-2}$.

In practice, several adjustments must be made to the simple gravity model described by Equation 6.10 in order to make acceptable measurements at the level of possible fifth force contributions to the gravity residuals. First of all, corrections must be applied to the free-air gradient term to take into account the ellipticity and rotation of the earth. These corrections are described by Holding, *et al.* [120], and are not considered to impose any limitations on the technique. Secondly, a correction must be applied due to the breakdown of the uniform layer approximation used in Equation 6.10. This correction consists of considering edge effects of finite layers, much as described in the section on modulated source experiments above. In the case of rock layers, there is the added complication that the layers do not have to be horizontal nor of uniform thickness, which requires accurate characterization of the rock strata around the borehole (boreholes which could be used for these studies have had available core samples from the surrounding area which allowed the necessary layer characterization). A related requirement, which applies to the surface layer, is correction of the gravity gradient for a non-horizontal surface, this is commonly called the terrain correction. For typical durations of measurements, the time-varying tidal component of gravity must be taken into account. One final consideration is the possible existence of mass anomalies deep beneath the borehole. This is not something that can be corrected for, but any positive result must be considered in light of the likelihood that such an anomaly could mimic the contribution due to a new interaction.

As noted in Chapter 2, borehole measurements of G were an important motivation in the consideration of possible new interactions. In the early 1980's, Stacey and Tuck had surveyed a number of borehole-type gravity measurements and came

to the conclusion that they were consistent with a value of G slightly higher than that given by laboratory experiments [13]. Holding, *et al.*, subsequently carried out borehole measurements at two mines in Queensland, Australia [14, 120]. The most significant results were those from the Hilton mine which were shown in Figure 1.2 and which indicated a repulsive deviation on the order of 1% of gravity with a range of a few hundred meters. Questions were initially raised about the knowledge of the local rock density and possible systematic effects from that source. Stacey, *et al.*, strongly argued that density uncertainties were not sufficient to explain the observed effect [121]. Bartlett and Tew examined the possibility that a failure to properly consider the local topology could explain the 1% effect [115]. Stacey, *et al.*, reconsidered their sampling of the terrain and acknowledged that most of their signal could be accounted for by such an explanation [122, 123].

Other borehole experiments were carried out by Hsui [124], Ander, *et al.* [125], and Thomas and Vogel [126, 127].

The Hsui experiment was carried out at a borehole in western Michigan. The central values for G which were obtained were O(0.3%) higher than the laboratory value with a spread of 0.2% . The statistical spread of the data was dominated, however, by a 1% systematic uncertainty in the calculated gravity profile for the borehole. Thus these results were consistent with no effect but were also marginally consistent with an effect of the size originally obtained by Holding, *et al.*

The Ander experiment attempted to avoid the complications of passing through rock strata by measuring gravity in a borehole in the Greenland ice cap. This technique has the disadvantage that the corresponding derivative of the gravitational acceleration is larger than for rock because the free-air gradient and the Bouguer terms of Equation 6.10 do not cancel as completely. Ander, *et al.*, quote an anoma-

lous gravity difference of 3.87 ± 0.36 mGal in going from a depth of 213 meters to 1673 meters which is compatible with an *attractive* interaction with a range on the order of a kilometer and a strength of a few percent of gravity. They note however that they can not exclude the possibility of an underlying mass anomaly as the source.

The Thomas and Vogel experiment was carried out in a borehole at the Nevada Test Site where extensive characterization of the geology was done for nuclear weapons testing. They note an anomalous residual at the level of -4 mGal over a depth of approximately 600 meters. This corresponds to roughly a 4% change in G, with the sign indicative of a repulsive interaction.

The wide variation in borehole results suggests that the technique may be fundamentally limited by the possible presence of underlying mass anomalies at intermediate ranges from the boreholes [127]. Stacey,*et al.*, consider a simple picture of such an anomaly [121]. Assume a spherical mass anomaly lying on the axis joining the borehole and the center of the earth at a depth H, where H is much larger than the maximum depth of the borehole. The gradient in the gravitational field is given by

$$\frac{dg}{dz} = \frac{2GM}{H^3} \tag{6.16}$$

where M is the total mass of the anomaly. Now, if we assume M is spread uniformly throughout a spherical region extending very nearly to the surface, we may write Equation 6.16 in terms of a density contrast, $\Delta\rho$, with respect to the surrounding material

$$\frac{dg}{dz} = \frac{8\pi G\Delta\rho}{3}. \tag{6.17}$$

For a gradient of $7 \times 10^{-8}\,\mathrm{s}^{-2}$, this gives a density contrast of $0.1\,\mathrm{g/cm}^3$, or 2% of the mean density of the earth, which does not seem to be a prohibitively large variation (In particular, in the case of the Nevada experiment, Thomas and Vogel note the

presence of a major seismic reflection boundary at a depth of 10 kilometers may be indicative of a region with the necessary density contrast to explain their results [127]. Better knowledge of large-scale underlying anomalies of this type can be obtained by gravity mapping over substantial regions in the horizontal plane—a task more easily accomplished in an ocean variant of the bore hole experiment.

Zumberge, *et al.*, have conducted an ocean determination of G as a function of depth over a vertical baseline of approximately 5 kilometers [128]. Their experiment was carried out in the northeast Pacific Ocean over a region where the sea floor was relatively flat and there were few variations in the underlying geology. Their gravity surveys included a $15\,\mathrm{km}^2$ sea floor survey, a $50\,\mathrm{km} \times 50\,\mathrm{km}$ sea surface survey. For mass anomalies at longer distances (up to 1000 km) satellite orbital measurements were employed. Their measurement of the local sea water density to approximately 0.01% determined the ultimate sensitivity limit that they could obtain for $\Delta G/G$. Their determination of the local free-air gradient was facilitated by the ability to use satellite altimetry to measure the height of the ocean surface and thus the local geoid. The reader is referred to their article for the details of the submarine and ship gravity measurements. For ranges less than 5 kilometers they obtained $G = (6.677 \pm 0.013) \times 10^{-8}\,\mathrm{cm}^3/\mathrm{gs}^2$, consistent with the laboratory value. This constrains α in our single Yukawa-term model to be $|\alpha| < 2 \times 10^{-3}$ at the 1σ level. The limits are shown in Figure 6.2.

6.6 Summary of Composition Independent Tests

Table 6.3 summarizes various composition independent limits from the above sections. The land-based borehole limits have been neglected because of the apparent difficulty in dealing with systematic effects as described above. The labels given in Table 6.3

Experiment	Type	Nominal Limit on $\lvert\alpha\rvert$	Characteristic Range	Figure 6.2 Labels
Moody & Paik	Gradiometer	$5.5 \times 10^{-4}(2\sigma)$	1.5 m	A
Moore *et al*	Modulated Source	0.02	22 m	B
Müller *et al*	Modulated Source	0.007	39 m, 68 m	C, C′
Thomas *et al*	Tower	0.004	465 m	D
Jekeli *et al*	Tower	0.002	600 m	E
Speake *et al*	Tower	0.002	300 m	F
Zumberge *et al*	Ocean	0.002	5000 m	G

Table 6.3: Recent composition-independent limits on the strength of a Yukawa coupling. All limits are 1σ unless otherwise noted. Results from the land-based borehole experiments are not shown due to systematic uncertainties.

are employed by Figure 6.2 which presents the set of 1σ limits over the entire range of interest.

The experiments of the last few years show no evidence for a departure from the inverse-square law at distances of meters to kilometers. It would seem that increasing the scale of the source mass in the gradiometer test of Gauss' Law may have the greatest potential for placing new limits in the region of tens to hundreds of meters. At ranges of several hundred meters to kilometers, carefully executed ocean and tower experiments provide the best currently available methods.

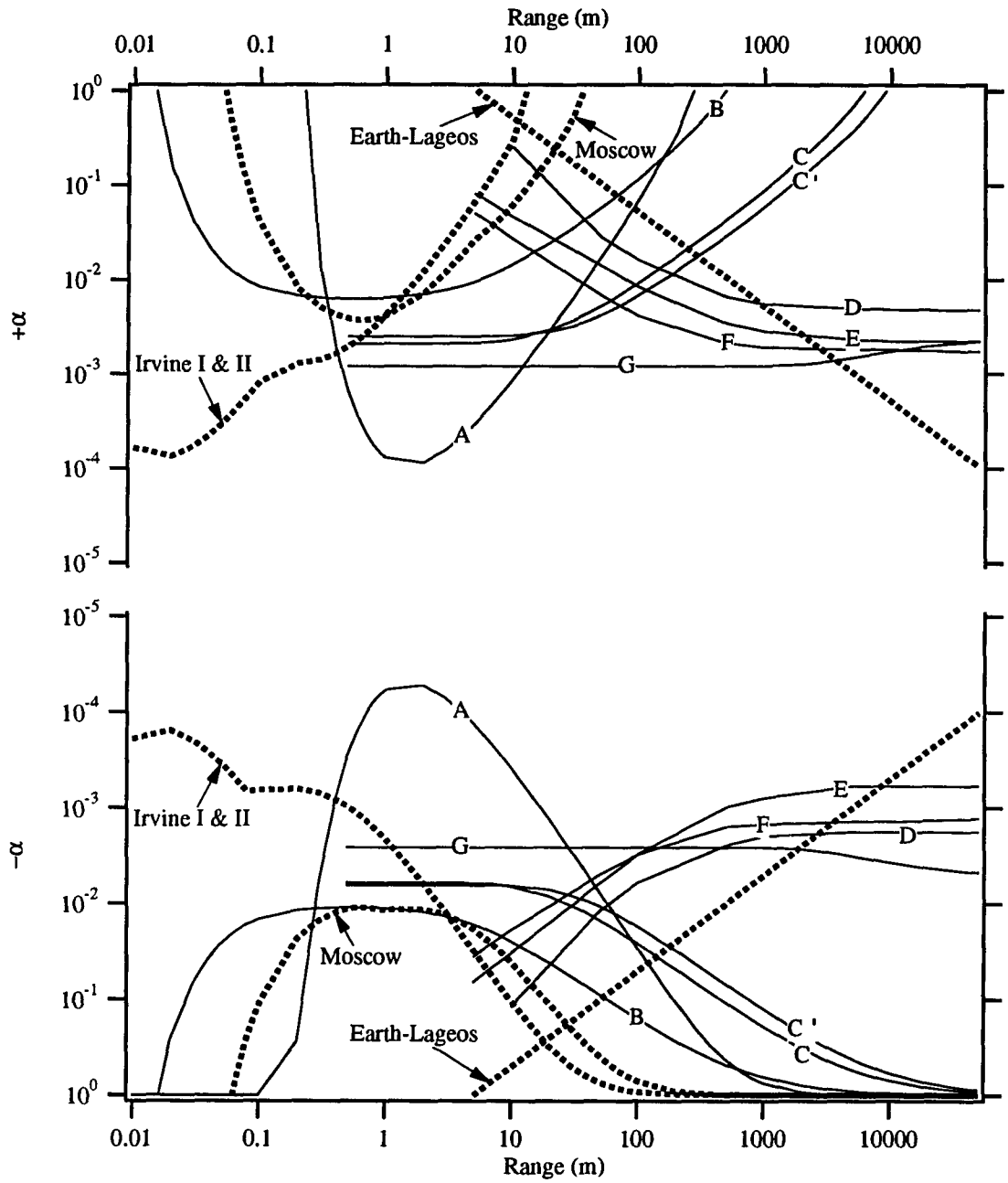

Figure 6.2: Composition-independent limits. The key to the limit curves is in Table 6.3. The upper plot is for positive values of the strength parameter, α, corresponding to an attractive interaction while the lower plot is for a repulsive interaction. Excluded regions are above the solid limit curves in the upper plot and below the solid limit curves for the lower plot.

Chapter 7

Composition-Dependent Limits

The second main class of intermediate range experiments is that of searches for an explicit composition dependence in a new interaction—experiments which look for a violation of the weak equivalence principle. These tests include:

1. Galilean free-fall experiments.
2. Torsion balance experiments.
3. Several novel techniques.

These types of experiments have compared the differential accelerations of a range of test materials to terrestrial and local source masses. The various "vector" charge differences (recall that a fairly common feature of the scalar couplings discussed in the last chapter is a small composition-dependent correction which can be expressed as an effective coupling to a vector charge) of the mass pairs which have been employed are shown in Table 7.1. It is important to realize, in the case of a coupling to some linear combination of charges (see Equation 2.37), the effective charge of a given mass pair will disappear for some mixing angle [129]. Thus, comparisons using more than one pair of test masses are necessary to fully constrain new interactions. We also mention that the source charge disappears for certain linear combinations as well. It was this fact that led to the series of experiments conducted with local source masses, described below, which characterized couplings for which the effective charge

Comparison Materials	$10^3\Delta\left(B/\mu\right)$	$\Delta\left((N-Z)/\mu\right)$	$\Delta\left((B-L)/\mu\right)$	$\Delta\left(L/\mu\right)$
Cu–Be	2.49	-0.023	-0.010	0.012
Cu–Al	0.44	0.052	0.026	-0.026
Cu–$(CH_2)_n$	2.24	0.232	0.117	-0.115
Cu–H_2O	1.72	0.201	0.101	-0.099
Cu–Pb	1.01	-0.121	-0.060	0.061
Cu–Ur	0.71	-0.111	-0.055	0.056
Al–Be	2.05	-0.074	-0.036	0.038
Al–C	0.69	0.036	0.019	-0.018

Table 7.1: Vector charge differences for materials used in the various composition-dependent tests for new interactions.

of terrestrial source masses disappeared.

7.1 Galilean Experiments

Galilean experiments are, in principle, the simplest of the composition-dependent searches—a comparison is made of the accelerations of two test masses with differing compositions as they fall in the earth's field. In experiments of this type, the difficulty of measuring a small differential acceleration on top of the large acceleration due to gravity is minimized by dropping pairs of test masses together and directly measuring relative displacements of the two masses by interferometric means.

If we assume these experiments are operated on flat terrain over a region of uniform density, the relative acceleration due to a composition dependent force is given by

$$\Delta a = \frac{3}{2R_\otimes}\left(\frac{\alpha_0\lambda}{1+\alpha_0}\right)\left(\frac{\rho_{local}}{\rho_\otimes}\right)\left(\frac{C_\otimes}{\mu_\otimes}\right)\left(\frac{C_2}{\mu_2}-\frac{C_1}{\mu_1}\right)g \tag{7.1}$$

where $R_\otimes$, $\rho_\otimes$, and $C_\otimes/\mu_\otimes$ are the earth's radius (assumed to be far larger than λ), mean density (5.5 g/cm^3), and effective charge per unit mass, respectively. The C_i/μ_i are the effective charges of the test masses, while ρ_{local} is the local mass (rock)

density. Note that, for small α_0, this technique is sensitive to the product, $\alpha_0\lambda$, of the strength and range of the interaction. Note also that, for longer ranges, the above approximation must be adjusted to take into account the varying density as a function of depth below the earth's surface. If we consider a force coupling to baryon content with $\alpha_0\lambda = 1\,\mathrm{m}$ and a pair of test masses with $\Delta\left(B/\mu\right) = 10^{-3}$, this corresponds to a differential acceleration of approximately 100 nGal in comparison with the earth's gravitational acceleration of roughly 10^3 Gal. All of these experiments have quoted final uncertainties in the measured differential accelerations of at least 500 nGal. Thus they are primarily useful at setting limits at longer ranges. A primary physical limitation of this type of experiment is the fact that the source mass is the earth. Thus, if the charge of the typical materials composing the earth's crust is intrinsically small, there is no recourse to the loss of experimental sensitivity which results.

There are several potential systematic effects that can affect the results of this type of experiment. First of all, if the centers of mass of the objects being dropped are not superimposed, gradients in the earth's gravitational field can easily mimic a 100 nGal differential acceleration. Residual gas in the dropping chamber results in drag forces which can perturb the measurement. This effect can be minimized by operating at sufficiently high vacuum [130] or by enclosing the masses in a drag-free chamber which surrounds the mass and falls with it [131]. An unavoidable and potentially limiting difficulty is residual motion of the masses at the point of release which can produce an apparent differential acceleration between the two masses [130,132]. Three "dropping" experiments have yielded useful limits out to ranges of 10^6–10^7 m.

The first experiment was conducted by Niebauer, *et al.* [131], and compared the relative accelerations of copper and uranium masses. The masses were housed in a

pair of adjacent dropping chambers mounted to a single base. Sensitivity to horizontal gradients was minimized by making multiple sets of measurements with the locations of the chambers interchanged. Corner cube reflectors were mounted on each mass to serve as reflecting elements in their Michelson interferometer. In order to produce a suitable fringe rate passing across the detector, one mass was always released ahead of the other, thus introducing a sensitivity to vertical gravitational gradients. Again, interchanges, in this case of the first-released mass, were used to remove the sensitivity to this effect. In terms of a coupling to baryon number, they quote a limit of $\alpha_0\lambda = 1.6 \pm 6.0\,\mathrm{m}$ valid for ranges of 10^2–10^6 m.

The second experiment of this type, by Kuroda and Mio [130], utilized a more complicated interlocking mass arrangement in order to compare the relative acceleration of two objects whose centers of mass were precisely superimposed. Their mass comparisons included Al-Be, Al-Cu, and Al-C combinations. Motions of the masses introduced at the point of release appear to have dominated the experimental uncertainty. For a coupling to baryon number their limits imply $\alpha_0\lambda = 2.3 \pm 6.7\,\mathrm{m}$ for ranges of 10^3–10^6 m. At larger distances, out to 10^7 m, the layered structure of the earth becomes important and their limits correspond to $|\alpha_0| < 10^{-5}$.

Carusotto, *et al.* [132], published the last experimental result in this category. Instead of measuring the differential acceleration of two discrete masses, they employed a composition-dipole disk of aluminum and copper in an aluminum shell. Corner cube reflectors were mounted on the rim of the disk and rotational motion around its axis was monitored with a modified Michelson interferometer. The authors note that precession of the disk around its axis, due to angular motions about axes in the plane of the disk upon release, was the major source of experimental error. Their limit for a coupling to baryon number is $\alpha_0\lambda = 6 \pm 18\,\mathrm{m}$.

General limits for couplings to B, $N - Z$, and $B - L$ for these experiments are shown in Figures 7.1, 7.2, and 7.3.

7.2 Torsion Balance Experiments

Torsion balance experiments naturally subdivide into several classes. The most obvious distinction is whether they are operated in a static (Cavendish) or dynamic (Boys) mode. They further differ as to the nature of the source mass employed. When considering an interaction of intermediate range, the largest signal can be obtained when the size of the source mass is of the same order or larger than the range of the interaction. For ranges on the order of tens of meters to kilometers this leads to the use of topological source masses on the earth's surface. If, however, the effective charge of a coupling disappears for typical terrestrial matter, then the use of such a topological source becomes futile. In this case, the only recourse is to local source masses, assembled in a laboratory setting, which are designed to maximize a particular charge by the choice of source material.

There are a variety of systematic effects to which these experiments are sensitive. These were already considered in some detail in the chapters dealing with the two Princeton experiments and will be largely passed over in the sections which immediately follow. I will simply reiterate that sensitivity to gravitational gradients, magnetic fields and thermal effects are of primary concern.

7.2.1 Terrestrial Source Mass Experiments

We recall Equation 3.6 for the sensitivity of a torsion balance to an intermediate-range interaction when located on a slope with uniform tilt, θ_t:

$$\tau = \frac{3}{2R_\otimes}\left(\frac{\alpha_0\lambda}{1+\alpha_0}\right)\left(\frac{\rho_{local}}{\rho_\otimes}\right)\left(\frac{C_\otimes}{\mu_\otimes}\right)\left(\frac{C_2}{\mu_2}-\frac{C_1}{\mu_1}\right) mg\ell\sin(\theta_t)$$

Recall that, for small α_0, the technique is sensitive to the product, $\alpha_0\lambda$, of the strength and range of the interaction. Three groups have conducted experiments employing this type of source at various sites around the country.

The first (and last) group to publish results from terrestrial source measurements was the Adelberger group from the University of Washington [99,129,133,134]. Their campus laboratory is located in the basement of a building built into the side of a hill giving them a site with significant local tilt for the ranges of interest. Their effective value of $\sin(\theta_t)$ is maximum for a range of a few meters with a value of ~ 0.3, steadily falling for longer ranges to ~ 0.15 at 100 m, and to ~ 0.05 at 1 km. The final version of their torsion balance consisted of four, cylindrical test bodies, each weighing 10 g, mounted equidistant around the circumference of a thin, aluminum support tray at a distance of 27.56 ± 0.01 mm from the balance axis. A barbell-like spindle extended through the center of the support tray and the on-axis masses above and below the plane of the test masses were positioned so as to nullify the overall quadrupole moment of the balance. The four test masses, used in combinations of two copper versus two beryllium or two aluminum versus two beryllium, were oriented to provide a composition dipole. Angular sensing was carried out optically. The apparatus rested on a precision turntable which was rotated continuously. A significant reduction in systematic errors due to gravitational gradients and highly reproducible turntable irregularities was achieved by making a series of measurements which alternated the direction of the composition-dipole with respect to the rest of the apparatus and then

comparing the resulting signal differences. The final quoted differential accelerations were

$$\Delta a\,(\mathrm{Cu}-\mathrm{Be}) = (0.8 \pm 1.7) \times 10^{-2}\,\mathrm{nGal}$$

$$\Delta a\,(\mathrm{Al}-\mathrm{Be}) = (2.1 \pm 2.1) \times 10^{-2}\,\mathrm{nGal}$$

where a positive value indicates that the first material was repulsed by the source. The combined limit for a coupling to baryon number from both of these measurements is

$$\alpha_0 = (3.9 \pm 4.1) \times 10^{-6}$$

for $\lambda = 100\,\mathrm{m}$.

A second measurement of this type was conducted by Boynton, *et al.* [135], but employed an oscillating torsion balance in the Boys-technique. The experimental site in this case was at the base of a 130 m cliff in the Cascade Mountains which provided sensitivity to new interactions with ranges between 10 m and 1 km. The torsion balance was a toroid of square cross-section, one-half beryllium and one-half aluminum, with a total weight of 11.4 g and a mean radius of 4.7 mm. It was suspended by a 0.001 cm diameter tungsten fiber. Timing variations in the 975 sec torsion oscillation were measured to the 10^{-6} level. This experiment excited particular interest because it reported a non-zero result:

$$\frac{\Delta P}{P} = (-4.6 \pm 1.1) \times 10^{-6}$$

which corresponds to

$$\alpha_0 = (2.3 \pm 0.6) \times 10^{-4}$$

for a coupling to baryon number at a range of 100 m. Before continuing, it should be mentioned that preliminary results from a later iteration of the experiment were

null [136]. Also, in our own attempt at making a dynamic measurement, we have noted large systematic signals due to nonlinearities in our tungsten torsion fibers (See Section 5.4) coupling to variations in the oscillation amplitude of our torsion pendulum. It is possible that such an effect played a role in this measurement as well.

The final experiment in this category was our own Princeton experiment utilizing a force-sensing, capacitance bridge detection scheme and copper and polyethylene as comparison materials [91]. Details of the apparatus and results are contained in Chapter 4. For comparison with the sensitivities of the other two experiments of this type, we note that the intrinsic strength of a coupling to baryon number was measured as

$$\alpha_0 = (-4 \pm 7) \times 10^{-4}$$

for $\lambda = 100\,\mathrm{m}$.

General limits for couplings to B, N–Z, and B–L for each of these experiments are shown in Figures 7.1, 7.2, and 7.3.

7.2.2 Local Source Mass Experiments

When considering a coupling to isospin, local source experiments (*i.e.*, experiments using laboratory-scale sources) move to the fore. Since all of the relevant distances in these experiments are much smaller than the interaction range of interest, the observed torque for a Cavendish experiment reduces to

$$\tau = \frac{G_{lab} M m \ell}{r^2} \left(\frac{\alpha_0}{1+\alpha_0}\right) \left(\frac{C_s}{\mu_s}\right) \left(\frac{C_2}{\mu_2} - \frac{C_1}{\mu_1}\right) \tag{7.2}$$

where M is the source mass and C_s/μ_s is its charge per unit mass. Thus these experiments provide a direct measurement of the strength of a new interaction but do

not yield significant information about its range. In this type of experiment, the fundamental loss of sensitivity from not employing a source mass with dimensions of the same size as the interaction range is balanced by the ability to know the source mass composition precisely and tailor it to maximize the charge. Further experimental gains have been obtained by being able to move the source mass while leaving the torsion balance undisturbed and by working in a stable laboratory environment instead of at a remote site. Three more groups have published results obtained by operating in this fashion.

Cowsik, *et al.* [137–139], employed a resonant torsion balance technique to publish two results for a coupling to isospin. Their technique looked for excitations of a Pb-Cu dipole torsion balance due to a set of source masses being driven in a circle around their apparatus at the natural frequency of the balance. Their source consisted of a set of Pb masses counterbalanced with similar brass masses, at a radial distance of 105 or 120 cm from the torsion balance. The source masses were arranged to minimize couplings to gravitational gradients. Note, however, that the $(N - Z)$ excess of Pb over brass provided a significant source for an isospin field. The torsion balance itself was a toroid of rectangular cross-section with a mean radius of 8.5 cm and contained approximately 700 g of each comparison material. Their final result gave a limit of

$$\alpha_0 = (-1.0 \pm 1.3) \times 10^{-4}$$

for all ranges greater than 3 m.

The Adelberger group [99, 140] also conducted a laboratory-scale source experiment by placing a 1300 kg Pb source next to their apparatus and operating it in the same fashion as described in the previous section. For an isospin coupling they obtained

$$\alpha_0 = (-0.14 \pm 1.24) \times 10^{-3}$$

for ranges greater than 1.0 m. The same results, when interpreted in terms of a coupling to baryon number provide useful limits at short distances where terrestrial source experiments are subject to the details of the local mass distribution. For this coupling they obtained

$$\alpha_0 = (0.21 \pm 1.90) \times 10^{-3}$$

for ranges greater than 0.5 m.

A final torsion balance experiment of this type was conducted by Newman, *et al.* [141]. This experiment employed a 321 kg Pb source in the form of a ring with its axis horizontal. In much the same way that a proper coil geometry insures a highly uniform magnetic field when using Helmholtz coils, the proper mass ring geometry in this experiment assured that the *difference* in the horizontal component of gravity, *i.e.*, the difference in the fields obtained first with the mass on one side of the apparatus and then with it moved to the opposite side, was highly uniform. The first three derivatives of this horizontal field difference were all zero at the position of the torsion balance, thus minimizing any sensitivity to gravitational gradients. This experiment compared the accelerations of lead and copper leading to

$$\alpha_0 = (-5.7 \pm 6.3) \times 10^{-5}$$

for a coupling to $(N - Z)$ and

$$\alpha_0 = (1.2 \pm 1.3) \times 10^{-3}$$

for a coupling to baryon number. Both limits apply for ranges greater than approximately 1 m.

Before leaving the discussion of local source mass experiments, mention should also be made of the experiment by Kreuzer [142] to verify the equivalence of ac-

tive and passive gravitational mass. Kreuzer placed a Teflon cylinder in a dibromomethane/trichloroethylene solution and varied the temperature (to change the fluid density) around the neutral density point. Outside of the fluid tank, he mounted a Cavendish-type torsion balance and looked for an induced torque on the balance as the block of teflon was moved from side to side. He found that the torques on the balance disappeared to within 5 parts in 10^5 when the condition of neutral buoyancy was met for the teflon in the solution. This result was used to conclude that the passive mass of the two materials, *i.e.*, the mass experiencing the gravitational field of the earth, was indeed equivalent to their active gravitational mass which was generating forces on the torsion balance. Upon the proposal of the fifth force hypothesis, Neufeld reanalyzed this experiment in terms of the limits that could be placed on a coupling to baryon number [143]. With $\Delta\left(B/\mu\right) = 0.75 \times 10^{-3}$, this implied a limit of $\alpha_0 < 6.6 \times 10^{-2}$ which, unfortunately, was not of sufficient sensitivity to constrain a new interaction at the level of interest.

7.2.3 A Modulated Terrestrial Source Experiment

We mention one final variant on the torsion balance approach. Bennett mounted a Pb-Cu torsion balance next to the Little Goose Lock on the Snake River in Washington State. This lock provided a 219 m×25.6 m body of water which varied in height by 30 m as boat traffic passed through. The structure of the lock walls was such that Bennett was able to position his torsion balance only 11.25 m from the edge of the water at a height of 9 m above its lowest level. Mean angular displacements of the torsion balance were compared with the lock full and empty to place limits on the differential acceleration of the two materials. The most stringent limits from this

experiment are for a coupling to isospin, for which Bennett obtained

$$\alpha_0 = (-0.5 \pm 1.1) \times 10^{-3}$$

for our standard range of 100 m.

7.3 Other Composition-dependent Tests

Several experiments eschewed the use of a torsion balance. This section describes results from three such experiments.

7.3.1 A Beam Balance Experiment

Another type of local source mass experiment was conducted by Speake and Quinn [144]. They used a beam balance capable of comparing the masses of two kilogram-sized objects at the level of tens of nanograms (specifically they quote a typical measurement uncertainty, obtained in an overnight series of measurements, of 35 ng). The beam balance was loaded with pairs of 2.3 kg test masses in the combinations of Pb versus graphite and Pb versus copper. In order to carry out a search for a coupling to isospin, they alternately placed 1782 kg Pb and brass source masses beneath the balance. They obtained a null result for coupling to $(N - Z)$ given by

$$\alpha_0 = (-0.8 \pm 2.0) \times 10^{-5}$$

which is valid for $\lambda \geq 1.1$ m and represents the combined result from both the Pb-C and Pb-Cu comparisons.

7.3.2 Neutral Buoyancy Techniques

A novel type of composition-dependent experiment is the comparison of the force on a neutral buoyancy sphere versus that on the fluid it displaces which was pioneered by

Thieberger. In principle, the spherically symmetric geometry guarantees insensitivity to gravitational gradients. Great care must be taken, however, to avoid systematic effects from convective flows in the fluid. In the presence of a differential force, the sphere will achieve a steady state velocity, u, through the fluid given by Stokes' Law [96]

$$\Delta a = \frac{6\pi\eta u R}{m}\left(1 + \frac{3uR}{8\nu}\right) \tag{7.3}$$

where Δa is the differential acceleration, R is the radius of the sphere, and η and ν are the dynamic and kinematic viscosity, respectively. The second term is a correction for the Reynold's number of the fluid.

Thieberger used this technique at the Palisades formation above the Hudson River [145] in 1987. At his location, the cliff extends approximately 160 m above the river and backwards to a distance of about a kilometer before the formation begins to slope downwards to any great extent. He employed a hollow copper sphere, with a diameter of 20 cm and a mass of approximately 5 kg, floating approximately 2 cm below the surface in a tank of water. For stability, the top and bottom of the sphere were equipped with small stems of 3 mm diameter. The stem on top broke the water's surface and its position could be monitored with a television camera. Thieberger observed the copper sphere to move towards the edge of the cliff at a rate of (4.7 ± 0.2) mm/hr corresponding to a differential acceleration of $(8.5 \pm 1.3) \times 10^{-8}$ cm/sec^2. For a range of a 100 m this corresponds to $\alpha_0 = (1.2 \pm 0.4) \times 10^{-2}$ for a coupling to baryon content. This early positive result was a major impetus to continuing searches for new intermediate-range interactions. In light of more recent tests, it must be assumed that some systematic effect produced this result. The possibility of a convection current explanation was widely discussed [146–149], but no entirely consistent explanation was achieved. The symmetry of the sphere was also sufficient to

preclude couplings to gravitational gradients as a source of significant error. Having a portion of the apparatus (the upper stem) break the surface of the water raises the question of some sort of surface tension effect, but this fails to explain the observed size of the effect. Thus, this result remains a bit of an open question.

A second neutral buoyancy sphere experiment was conducted by Bizetti, *et al.* [150], two years later. Their apparatus consisted of a 10 cm diameter, solid nylon sphere suspended in a weakly stratified KBr solution to maintain vertical stability and minimize the possibility of convection currents. The apparatus was located on a ridge extending from the side of a mountain at Vallombrosa, Italy. The effective slope of the local terrain was approximately 30°. This experiment obtained an upper limit on the steady state velocity that could be due to a new interaction of 10 μm/hr which yields a limit on a differential acceleration of $\Delta a < 2.4 \times 10^{-8}$ Gal. For a coupling to baryon number, and again considering a range of 100 m, this gives $\alpha_0 < 2.5 \times 10^{-3}$.

7.4 Summary of Composition-Dependent Tests

Figures 7.1, 7.2 and 7.3 show the the existing composition-dependent limits for various source charges, B, I_3, and $B - L$. It should be noted that, in general, limits on a coupling to lepton number are only marginally different than the limits for $B - L$ but with the sign of the coupling reversed. Since $\Delta\left({}^{B}/_{\mu}\right)$ is intrinsically small for bulk matter, we have $\Delta\left({}^{(B-L)}/_{\mu}\right) \approx -\Delta\left({}^{L}/_{\mu}\right)$. Furthermore, particularly for the lighter elements, we can roughly set $\left({}^{(B-L)}/_{\mu}\right) \sim {}^{L}/_{\mu} \sim 0.5$. Thus, to within about 20%, the $B - L$ plots with $+\alpha_0$ and $-\alpha_0$ interchanged yield the L limits.

The plots shown here skirt the issue of couplings to a general linear combination of the fundamental vector charges of bulk matter as given by Equation 2.37. Consideration of such linear combinations is necessary because of the regions where the

effective charge disappears for any particular detector and source combination. At the time of the Boynton and Thieberger experiments, it was noted by Boynton [88] that the two positive results could be made compatible for a coupling dominantly to isospin but with a small baryon content admixture. The reason for this, was that the effective charge for typical terrestrial sources disappears precisely in this region, thus making the acceptable range of coupling strengths quite large. The local source mass experiments, with their ability to specify both the source and detector charges, end up being the source of constraints in that region. At the present time, the various detector and source charge combinations which have been employed, have placed significant limits for all values of θ_5 in Equation 2.37. The reader is referred to the excellent review by Adelberger, *et al.* [151], for a summary of these results.

In summary, there is no experimental support for a new composition-dependent interaction acting over ranges of meters to kilometers. For ranges from a few meters to ten kilometers, torsion balance experiments place the best limits. For ranges greater than ten kilometers, the Galilean free fall experiments predominate. At present, the most difficult range to investigate is at tens of kilometers. At these distances the Galilean experiments do not "see" enough underlying mass to overcome their limited sensitivity to differential accelerations. In the case of torsion balance experiments, there are no terrestrial sources whose extent compares to the interaction range on those scales.

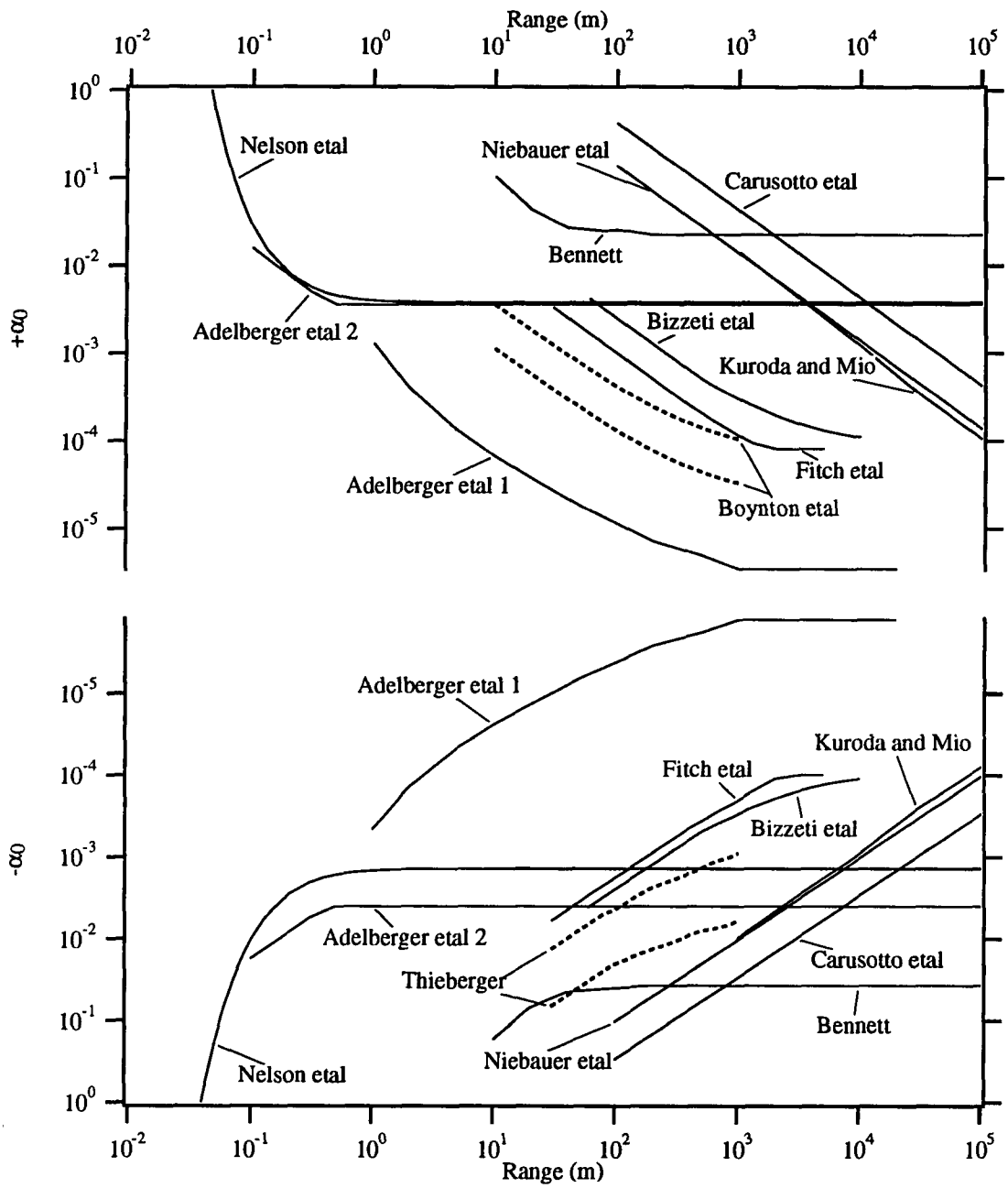

Figure 7.1: Composition-dependent limits on a Yukawa coupling to baryon number. The curves represent 2σ limits. The upper plot is for positive values of the strength parameter, α_0, corresponding to an attractive interaction while the lower plot is for a repulsive interaction. Excluded regions are above the solid limit curves in the upper plot and below the solid limit curves for the lower plot.

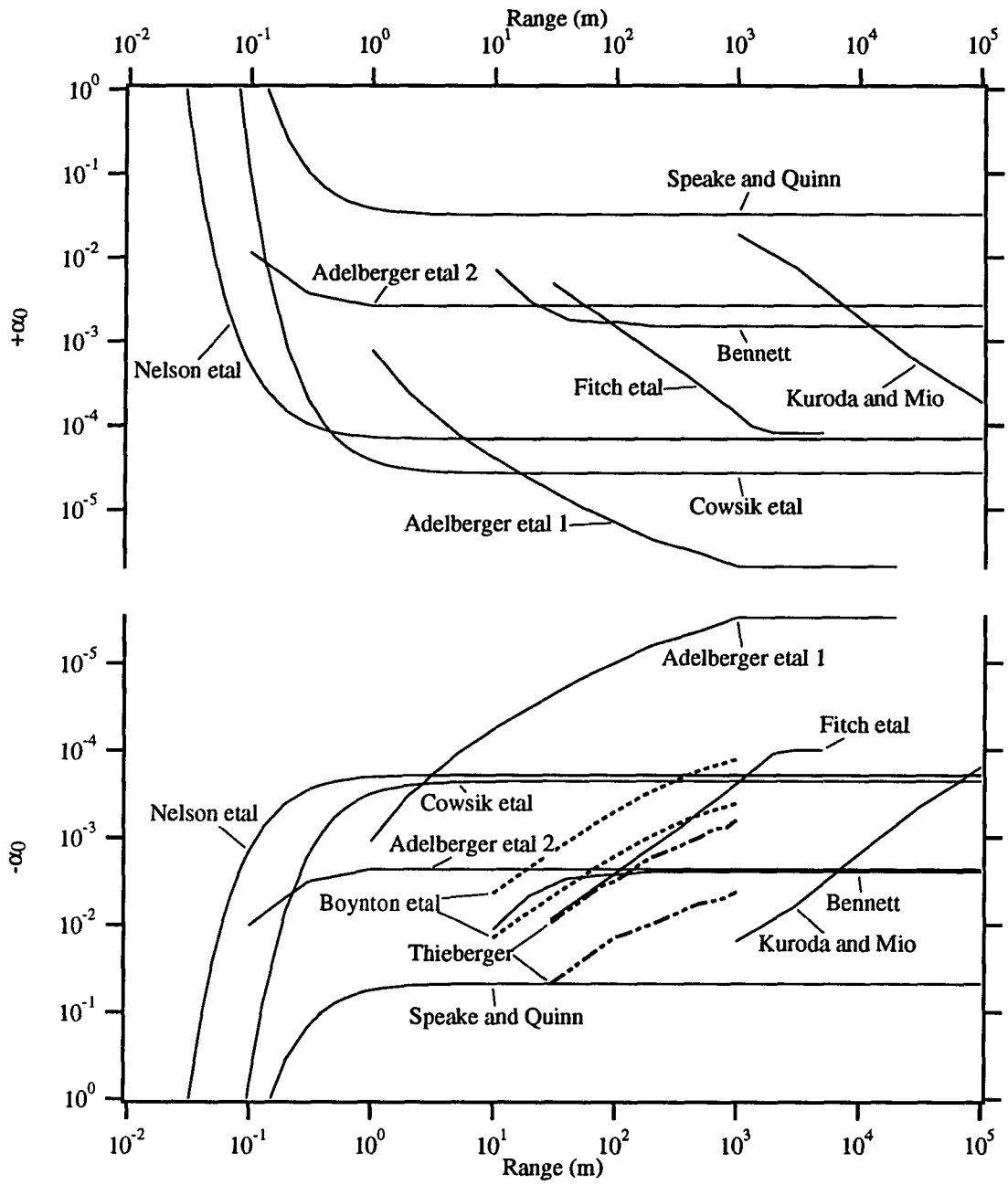

Figure 7.2: Composition-dependent limits on a Yukawa coupling to isospin content. The curves represent 2σ limits. The upper plot is for positive values of the strength parameter, α_0, corresponding to an attractive interaction while the lower plot is for a repulsive interaction. Excluded regions are above the solid limit curves in the upper plot and below the solid limit curves for the lower plot.

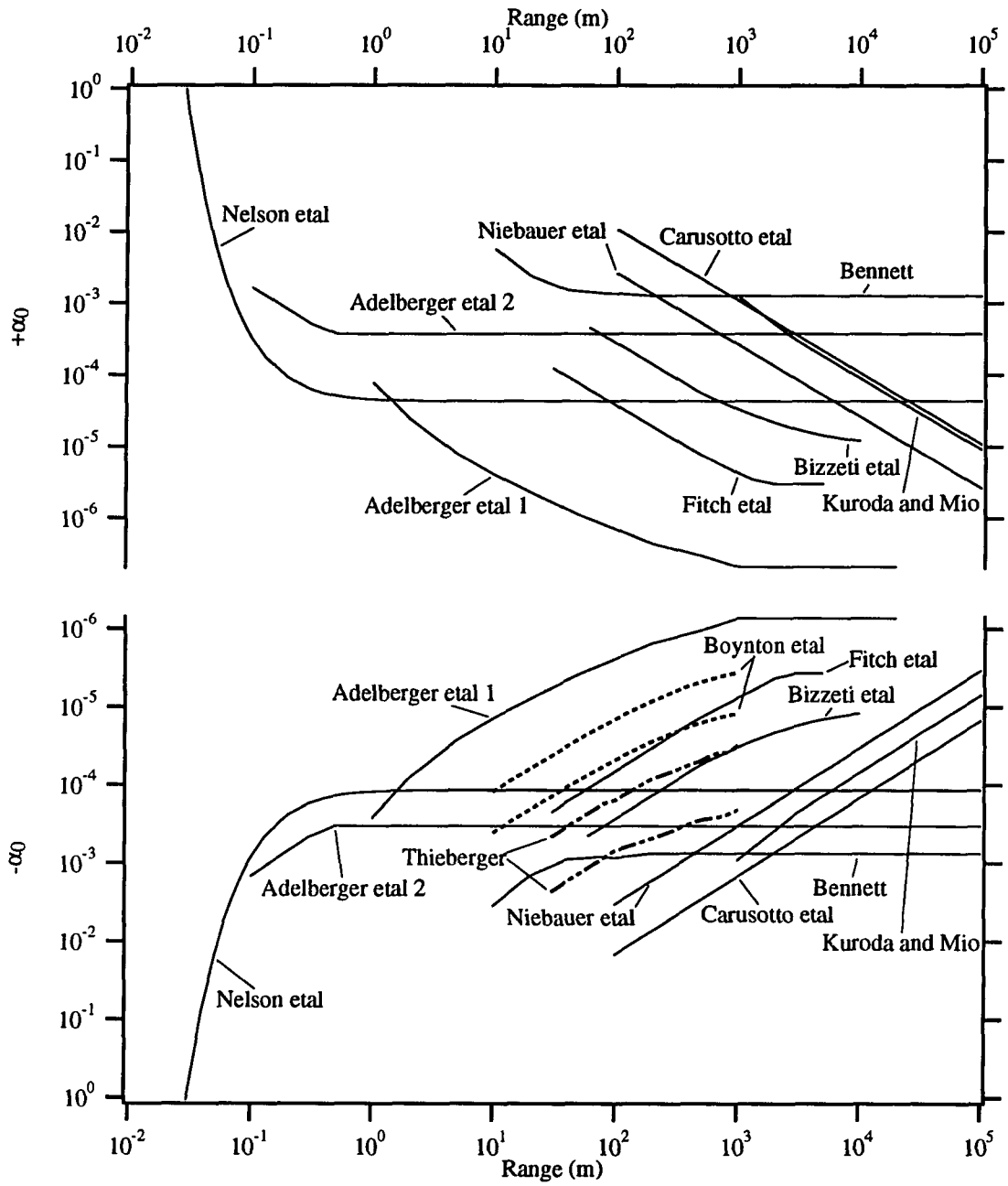

Figure 7.3: Composition-dependent limits on a Yukawa coupling to $B-L$. The curves represent 2σ limits. The upper plot is for positive values of the strength parameter, α_0, corresponding to an attractive interaction while the lower plot is for a repulsive interaction. Excluded regions are above the solid limit curves in the upper plot and below the solid limit curves for the lower plot. Recall that limits from a coupling to lepton number are negligibly different except that the positive and negative limit plots should be interchanged.

Chapter 8

Conclusion

In summary, we have placed limits on the strength of composition-dependent interactions with ranges of 25 meters to 5 kilometers. Our first detector was sensitive to differential accelerations of copper and polyethylene at the level of 4.9 nGal. We have interpreted an observed differential acceleration of

$$\Delta a = 3.0 \pm 4.9\,\mathrm{nGal}$$

in terms of couplings to the baryon, isospin, and $B - L$ content of the comparison materials. The corresponding limits are as follows:

For $25 < \lambda < 400\,\mathrm{m}$:

$$\alpha_0\lambda = \quad -0.04 \pm 0.07\,\mathrm{m} \qquad (\mathrm{B})$$

$$\alpha_0\lambda = \quad (-1.5 \pm 2.6) \times 10^{-3}\,\mathrm{m} \quad (\mathrm{B-L})$$

$$\alpha_0\lambda = \quad -0.06 \pm 0.011\,\mathrm{m} \qquad (\mathrm{N-Z})$$

At $\lambda = 1600\,\mathrm{m}$:

$$\alpha_0\lambda = \quad -0.05 \pm 0.09\,\mathrm{m} \qquad (\mathrm{B})$$

$$\alpha_0\lambda = \quad (-2 \pm 5) \times 10^{-3}\,\mathrm{m} \quad (\mathrm{B-L})$$

$$\alpha_0\lambda = \quad -0.05 \pm 0.09\,\mathrm{m} \qquad (\mathrm{N-Z})$$

For $1600 < \lambda < 5000\,\mathrm{m}$:

$$|\alpha_0| < \quad 10^{-4} \qquad (\mathrm{B})$$

$$|\alpha_0| < \quad 4 \times 10^{-6} \quad (\mathrm{B} - \mathrm{L})$$

$$|\alpha_0| < \quad 10^{-4} \quad (\mathrm{N} - \mathrm{Z})$$

In addition, we note that a coupling to L gives essentially the same limits as a coupling to $B - L$ but with the opposite sign, while a coupling to the bare quark and lepton masses is indistinguishable from a coupling to baryon number.

8.1 Torsion Balances

Torsion balances provide an extremely sensitive technique to look for small differential forces. They dominate the composition-dependent limits at ranges up to roughly 10 km. Nevertheless, it is not clear that they have reached their full potential. In our experiments, we have consistently noted that noise levels far exceed the thermal noise limit. Furthermore, the noise tends not to be the limiting factor in the experiment, but rather one has to deal with the elimination of extraneous systematic effects.

In the case of the dynamic apparatus, it is an open question whether the range of systematic effects to which it is susceptible can be overcome. If they can be eliminated, the data suggests that the apparatus can be operated with a sensitivity of a few times 10^{-10} Gal. Achieving a final sensitivity of 10^{-10} Gal would allow useful comparisons with existing limits using a terrestrial source.

8.2 Some General Comments

Seven years of intensive searches for a new fundamental interaction have failed to produce any solid evidence for its existence. At this point, it has been unequivocally shown that Newton's inverse-square law holds at terrestrial scales to roughly one part in a thousand. Techniques such as the gravity gradiometer of Paik, *et al.*, have the

potential to push these limits even further.

In terms of composition-dependent effects, all of the early non-null results have been contradicted by later tests. The conflict among the early results clearly illustrates the delicate nature, and corresponding sensitivity to systematic effects, of these experiments designed to measure extremely small forces. As a result, a number of complementary approaches and techniques had to be pursued in order to develop a clear understanding of the experimental situation. At present, stringent limits, reaching the part in 10^6 level in some cases, have been set for couplings to the vector charges of bulk matter. Furthermore, the wide variety of sources and detector materials which have now been employed in various experiments place significant limits on all possible linear combinations of these charges [151]. Thus there is little room for composition-dependent departures from Newtonian gravity at terrestrial scales.

Appendix A

Pre-1986 Limits

This appendix summarizes the sources of constraints on departures from the gravitational inverse-square law as they existed in early 1986 when the fifth force hypothesis was suggested. These limits define the unexplored window of possible ranges for new interactions which is shown in Figure 1.2. As such, they complement the limits described in Chapters 6 and 7. The treatment here concentrates on the experiments which set the most stringent limits. For an exhaustive bibliography of experiments (and theoretical speculations) relating to deviations from Newtonian gravity, the reader is referred to Reference 152.

At distances of 1 cm–10 m constraints on new interactions come from laboratory tests. The review by Newman [153] provides a compilation of these laboratory scale results. Of the techniques considered in that article, the best limits come from variants of the Cavendish technique where a mass quadrupole torsion balance is subjected to torques from an asymmetric external mass distribution. The limits labelled Irvine I and II [153] in Figure 1.2 dominate at ranges of millimeters to a fraction of a meter while the Moscow results [11] dominate at ranges up to several meters. The basic Cavendish geometry used to look for inverse-square law deviations is shown in Figure A.1. Two source masses, m and M, are located at distances from the torsion balance mass such that the opposing forces should cancel if the $1/r^2$ dependence of gravity holds. This technique allows the experimenter to probe range scales up to

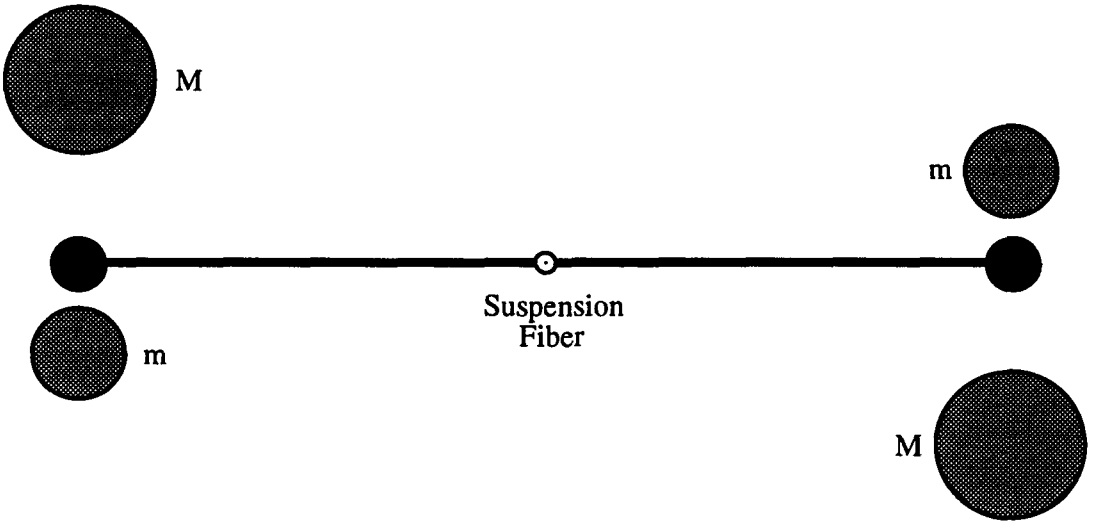

Figure A.1: The Cavendish technique as used to look for departures from the gravitational inverse-square law. The geometry shown is for a null experiment where the masses m and M are chosen to make the net torque on the balance zero if Newton's law of gravity holds.

roughly the size of the torsion balance arm. A straightforward way to present the results of such experiments is to quote the ratio of the observed Newtonian constant for the two mass separations, r_0 and r_1 used in the experiment:

$$X(r_0, r_1) = \frac{G(r_1)}{G(r_0)}. \tag{A.1}$$

In the presence of a Yukawa term in the gravitational potential, this can be written as

$$X(r_0, r_1) = \frac{1 + \alpha\left(1 + \frac{r_1}{\lambda}\right) e^{-r_1/\lambda}}{1 + \alpha\left(1 + \frac{r_0}{\lambda}\right) e^{-r_0/\lambda}} \tag{A.2}$$

which yields constraints on α as a function of λ.

For ranges of 10's to 100's of meters, geophysical measurements of the gravitational constant are the only means currently available for a composition-independent check of the $1/r^2$ dependence of Newtonian gravity. Nonzero deviations in such experiments at levels indicated by the region labelled Hilton Mine in Figure 1.2, however, were an

important part of the experimental motivation for the new round of searches in recent years. A detailed discussion of the geophysical techniques is provided in Chapter 6 where the results of more recent geophysical tests are considered.

For ranges of more than a few hundred meters, astrophysical measurements provide the excluded regions of Figure 1.2. From 1 km to over 10^6 km the limits come from the orbital measurements of the moon and satellites using laser rangefinding techniques. In particular, comparison of the values of $GM_\odot$, where $M_\odot$ is the mass of the earth, obtained at the earth's surface, from the orbit of the LAGEOS satellite and from the moon's orbit provide the most stringent limits [27]. To quantify the last statement, consider a spherically uniform earth and a potential given by Equation 1.3. An object at distance $r > R_\odot$ will experience a radial acceleration given by:

$$g(r) = -\frac{GM_\odot}{r^2}\left[1 + 3\alpha e^{-r/\lambda}\left(1 + \frac{r}{\lambda}\right) f\left(\frac{R_\odot}{\lambda}\right)\right] \tag{A.3}$$

where

$$f(x) = x^{-3}\left(x\cosh x - \sinh x\right). \tag{A.4}$$

The values of $r^2 g(r)$ are compared for the different satellite measurements. If no anomalous force were present, the results would all yield $GM_\odot$ to within experimental error. Discrepancies of the various measurements yield limits on α as a function of the range, λ, through Equation A.3. The limits labelled Earth-Lageos and Moon-Lageos in Figure 1.2 are based on the $GM_\odot$ values summarized in Reference 27 (Also see the references therein).

For yet longer ranges, up to about 10^{14} m, the limits are obtained by considering how well General Relativity describes the precession of the perihelions of the planetary and asteroid orbits, in particular those of Mercury and Icarus. The precession induced

by an interaction of the form under consideration can be obtained by considering the classsical orbital equation of motion[1]

$$\frac{d^2u}{d\theta^2} + u + \frac{m}{\ell^2 u^2} F(u) = 0, \tag{A.5}$$

where $u = r^{-1}$, ℓ is the angular momentum and$F(u)$ is the central force. For a $1/r^2$ force law the solution is given by:

$$GMmu = 1 + \varepsilon \cos\theta \tag{A.6}$$

where ε is the eccentricity of the orbit. We can use the method of successive approximations to obtain the dominant term in the perihelion shift from equation A.5 for a force law of the form in Equation 1.4. The Yukawa portion gives, to first order in ε, a secular solution of the form:

$$u_{sec} = \frac{1}{\chi}\left[1 + \varepsilon\cos\theta + \frac{\alpha\varepsilon}{2}\left(\frac{\chi}{\lambda}\right)^2 e^{-\chi/\lambda}\,\theta\sin\theta\right] \tag{A.7}$$

$$\cong \frac{1}{\chi}\left\{1 + \varepsilon\cos\left[\theta + \frac{\alpha\varepsilon}{2}\left(\frac{\chi}{\lambda}\right)^2 e^{-\chi/\lambda}\,\theta\right]\right\} \tag{A.8}$$

where

$$\frac{1}{\chi} = \frac{GMm^2}{\ell^2} \tag{A.9}$$

with M the mass of the sun, m the mass of the planet or asteroid, and ℓ the angular momentum. The orbital precession is immediately obvious as

$$\delta\theta_{prec} = -\pi\alpha\varepsilon\left(\frac{a}{\lambda}\right)^2 e^{-a/\lambda} \tag{A.10}$$

where I have set $\chi = a$, with a the semimajor axis of the orbit, which holds to 1st order in ε. Values for the deviation of the orbital precessions of Icarus and Mercury from the general relativistic predictions were taken from the reference of Mikkelsen and Newman [9] and used to produce the limits shown in Figure 1.2.

[1]The treatment here closely follows that of Marion [98].

For ranges greater than the scale set by the solar system, the limits on coupling strengths comparable to gravity disappear. In fact, orbital measurements at the galactic scale are the source of one of the most perplexing problems in astrophysics today—rotation curves of galaxies, assuming a standard Newtonian potential, require the presence of large amounts of invisible "dark" matter in galaxies. At such ranges the only limits that can be set rely on a composition-dependent behavior of α in Equation 1.3. In this formulation the Roll, Krotkov and Dicke (RKD) and the Braginsky and Panov (BP) experiments are sensitive to

$$\Delta\alpha = \alpha_2 - \alpha_1 = \alpha_0 \left(\frac{C_\otimes}{\mu_\otimes}\right)\left(\frac{C_2}{\mu_2} - \frac{C_1}{\mu_1}\right) \tag{A.11}$$

where indices 1 and 2 represent the pair of test materials which each group employed and $\otimes$ represents the sun. If the deviation from $1/r^2$ behavior results from a coupling to mass, these experiments set no limits at all. If, however, the coupling is composition-dependent, then these experiments require $\Delta\alpha < 3\times10^{-11}$ (RKD) and $\Delta\alpha < 9\times10^{-13}$ (BP) for ranges greater than 1.5×10^8 km. When considering a coupling to baryon content this translates to $\alpha_0 < 6 \times 10^{-8}$ and $\alpha_0 < 2 \times 10^{-9}$, respectively.

Appendix B

Charge Content of the Stable Elements

This appendix presents a listing of the charge content of the stable elements for several effective charges. These charges have been considered as possibilities for the source of a new composition-dependent intermediate-range interaction acting between bulk matter. Note that the values are averaged over the contributions of the various isotopes of each element and normalized to the hydrogen mass (as opposed to the atomic mass unit) which is the normalization convention of Fischbach, *et al.* [38]. The isotope fractions were obtained from Reference 154.

Element	Z	Mass†	B/μ‡	(N-Z)/μ‡	(B-L)/μ‡
H	1	1.00797	1.000000	-0.999702	0.000149
He	2	4.0026	1.007170	-0.000000	0.503585
Li	3	6.939	1.005511	0.134231	0.569871
Be	4	9.0122	1.006462	0.111829	0.559146
B	5	10.811	1.006892	0.074921	0.540906
C	6	12.01115	1.007822	0.000929	0.504375
N	7	14.0067	1.007605	0.000264	0.503934
O	8	15.9994	1.008145	0.000280	0.504213
F	9	18.9984	1.007910	0.053048	0.530479
Ne	10	20.183	1.008207	0.008942	0.508575
Na	11	22.9898	1.008274	0.043838	0.526056
Mg	12	24.312	1.008453	0.013461	0.510957
Al	13	26.9815	1.008515	0.037352	0.522934
Si	14	28.086	1.008657	0.003904	0.506281
P	15	30.9738	1.008679	0.032538	0.520608
S	16	32.064	1.008709	0.002909	0.505809
Cl	17	35.453	1.008731	0.042203	0.525467
Ar	18	39.948	1.008774	0.100543	0.554658
K	19	39.102	1.008764	0.029325	0.519044
Ca	20	40.08	1.008771	0.002880	0.505826
Sc	21	44.956	1.008813	0.067254	0.538034
Ti	22	47.90	1.008911	0.082735	0.545823
V	23	50.942	1.008934	0.098872	0.553903
Cr	24	51.996	1.008974	0.078610	0.543792
Mn	25	54.9380	1.008962	0.091724	0.550343
Fe	26	55.847	1.008994	0.070598	0.539796
Co	27	58.9332	1.008968	0.085506	0.547237
Ni	28	58.71	1.008962	0.047575	0.528269

† quoted in amu ‡ μ normalized to m($_1H^1$)=1.00782519 amu

Table B.1: The Stable Elements and Their Charges

Element	Z	Mass†	B/μ‡	(N-Z)/μ‡	(B-L)/μ‡
Cu	29	63.54	1.008951	0.089077	0.549014
Zn	30	65.37	1.008944	0.084149	0.546547
Ga	31	69.72	1.008906	0.112640	0.560773
Ge	32	72.59	1.008904	0.120837	0.564871
As	33	74.9216	1.008880	0.121066	0.564973
Se	34	78.96	1.008881	0.141279	0.575080
Br	35	79.909	1.008868	0.125957	0.567412
Kr	36	83.80	1.008883	0.142978	0.575931
Rb	37	85.47	1.008874	0.136278	0.572576
Sr	38	87.62	1.008903	0.134699	0.571801
Y	39	88.905	1.008892	0.124695	0.566793
Zr	40	91.22	1.008872	0.125045	0.566959
Nb	41	92.906	1.008841	0.119325	0.564083
Mo	42	95.94	1.008815	0.125953	0.567384
Tc*	43	98.9062			
Ru	44	101.07	1.008771	0.131244	0.570007
Rh	45	102.905	1.008751	0.127318	0.568034
Pd	46	106.4	1.008732	0.137555	0.573144
Ag	47	107.870	1.008713	0.130462	0.569588
Cd	48	112.40	1.008690	0.148093	0.578391
In	49	114.82	1.008669	0.148467	0.578568
Sn	50	118.69	1.008653	0.159843	0.584248
Sb	51	121.75	1.008620	0.164344	0.586482
Te	52	127.60	1.008577	0.187332	0.597954
I	53	126.9044	1.008584	0.166774	0.587679
Xe	54	131.30	1.008555	0.179525	0.594040
Cs	55	132.905	1.008543	0.174410	0.591476
Ba	56	137.34	1.008522	0.186570	0.597546

† quoted in amu ‡ μ normalized to m($_1H^1$)=1.00782519 amu

* unstable

Table B.1: The Stable Elements and Their Charges (*Continued*)

Element	Z	Mass†	B/μ‡	(N-Z)/μ‡	(B-L)/μ‡
La	57	138.91	1.008506	0.181381	0.594943
Ce	58	140.12	1.008503	0.174130	0.591316
Pr	59	140.907	1.008486	0.164505	0.586495
Nd	60	144.24	1.008446	0.169995	0.589221
Pm*	61	144.913**			
Sm	62	150.35	1.008373	0.177251	0.592812
Eu	63	151.96	1.008352	0.172721	0.590536
Gd	64	157.25	1.008312	0.187983	0.598147
Tb	65	158.924	1.008299	0.183904	0.596101
Dy	66	162.50	1.008272	0.189607	0.598940
Ho	67	164.930	1.008250	0.189429	0.598840
Er	68	167.26	1.008235	0.188774	0.598504
Tm	69	168.934	1.008217	0.184939	0.596578
Yb	70	173.04	1.008185	0.192776	0.600481
Lu	71	174.97	1.008167	0.190233	0.599200
Hf	72	178.49	1.008136	0.195060	0.601598
Ta	73	180.948	1.008115	0.194939	0.601527
W	74	183.85	1.008093	0.196753	0.602423
Re	75	186.2	1.008070	0.196239	0.602154
Os	76	190.2	1.008041	0.202791	0.605416
Ir	77	192.2	1.008024	0.200573	0.604298
Pt	78	195.09	1.008009	0.202082	0.605046
Au	79	196.967	1.007996	0.199553	0.603774
Hg	80	200.59	1.007979	0.204118	0.606048
Tl	81	204.37	1.007954	0.209125	0.608540
Pb	82	207.19	1.007942	0.210314	0.609128
Bi	83	208.980	1.007920	0.207371	0.607645

† quoted in amu ‡ μ normalized to m($_1H^1$)=1.00782519 amu

* unstable ** mass of most stable isotope

Table B.1: The Stable Elements and Their Charges (*Continued*)

Appendix C

Toroid and Sphere Scaling Relations

This appendix provides details of the scaling relations discussed in Section 3.2. First let us consider a toroidal balance of rectangular cross section. The mass of such a balance scales as $M \propto R \cdot \Delta R \cdot h$ where ΔR is the radial thickness of the toroid and h is its height. A differential torque will then scale as $R^2 \cdot \Delta R \cdot h$ and can be maximized by making ΔR and h as small as reasonable fabrication tolerances will allow so that R can be as large as possible. Thus for balances of dimension larger than some characteristic length scale, ℓ, which is determined largely by available fabrication techniques (ℓ is, say, a fraction of an inch or half a centimeter), the mass scales as $M \propto R \cdot \ell^2 \propto r^2$ so that $R \propto r^2/\ell^2$ and the expression for the balance sensitivity becomes:

$$S \propto \frac{MR}{\left(r^4/L\right)} \approx \frac{r^4}{\left(r^4/L\right)} = L, \tag{C.1}$$

independent of balance size.

In the case of a spherical shell torsion balance, a similar argument applies. To some substantial degree the thickness of the shell is determined by fabrication capabilities. If we again call this "fabrication dimension" ℓ, we see that the mass of a balance of some size larger than ℓ scales as $M \propto R^2 \cdot \ell$ and we have $R \propto r$. The torque on the balance then looks like $\tau_5 \propto MR \propto R^3 \propto r^3$ and we obtain the following scaling of

the balance sensitivity:

$$S \propto \frac{MR}{\left(r^4/L\right)} \approx \frac{r^3}{\left(r^4/L\right)} = \frac{L}{r}, \tag{C.2}$$

which is a somewhat less strong dependence on the fiber size than obtained in the general scaling argument given in Section 3.2.

Appendix D

Thermal Noise in a Period Measurement

In this appendix, we consider the impact of thermal noise on a measurement of the period of a simple harmonic oscillator. If a timing measurement is started at $t = 0$ when the oscillator passes through its equilibrium position, we only need to retain the first term in Equation 3.2. At this point the oscillator has some amplitude θ_0 which we take to be large in comparison to the thermal noise amplitude. Figure D shows the effect of a small noise amplitude, $\Delta\theta$, on the phase of an oscillator with amplitude θ_0 and natural frequency ω.[1] The shift in oscillator phase is given by

$$\Delta\phi = \frac{\Delta\theta}{\theta_0}\cos\psi. \tag{D.1}$$

The angle ψ will be random so we immediately substitute the RMS value of $1/2$ for $\cos\psi$ in Equation D.1. We may now write the phase shift in the oscillator, due to noise, as

$$\phi(t) = \frac{1}{\sqrt{2}}\int_0^t \dot{\theta}_n(t')dt' \tag{D.2}$$

where $\dot{\theta}_n$ is the angular velocity due to thermal noise and where, because of our specified initial conditions, we have set $\phi(0) = 0$. Thus we are examining the continuum limit of a random-walk process. To obtain the mean-square value of ϕ, we consider

[1]This phasor treatment of the noise is similar to Yariv's treatment of laser noise in He-Ne lasers [155, p. 327].

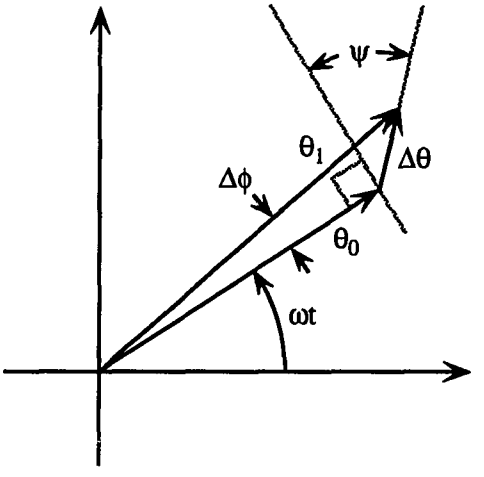

Figure D.1: Phasor Treatment of Noise in the Oscillator Phase: The oscillator initially has amplitude, θ_0, but a small additional amplitude, θ_n, due to noise contributes to a resultant amplitude, θ_1, which is shifted in phase by $\Delta\phi$. The phase of the noise relative to the oscillator is given by the angle $\pi - \psi$.

the autocorrelation function [156]

$$\langle \phi(t)\,\phi(t+\Delta t)\rangle = \frac{1}{2\theta_0^2}\int_0^t dt' \int_0^{t+\Delta t} dt'' \left\langle \dot{\theta}(t')\,\dot{\theta}(t'')\right\rangle \tag{D.3}$$

where $\Delta t > 0$. We employ the Wiener-Khintchine theorem to write

$$\left\langle \dot{\theta}(t')\,\dot{\theta}(t'')\right\rangle = \frac{1}{2\pi}\int_0^\infty J_{\dot{\theta}}(\omega)\cos\omega\,(t''-t')\,d\omega \tag{D.4}$$

where $J_{\dot{\theta}}$ is the spectral density of $\dot{\theta}$. We can consider

$$\left\langle \dot{\theta}^2\right\rangle = \frac{1}{2\pi}\int_0^\infty J_{\dot{\theta}}(\omega)\,d\omega \tag{D.5}$$

to be the definition of $J_{\dot{\theta}}$. This, however, is an expression that we know how to calculate using Nyquist's theorem and some linear circuit theory [89]. Equation 3.16 gives the spectral density of the thermal noise torque for our oscillator. In complete analogy with electrical circuits, we may write the relation between the torque and the angular velocity as

$$\tau(\omega) = Z(\omega)\,\dot{\theta}(\omega) \tag{D.6}$$

where $Z(\omega)$ is the impedance. The formula for the impedance follows from a comparison of our situation with that for an LRC circuit:

$$Z(\omega) = 2\beta I + i\omega I - \frac{i\kappa}{\omega} \tag{D.7}$$

and we have:

$$\left\langle \dot{\theta}^2 \right\rangle = \frac{2k_B T (2\beta I)}{\pi} \int_0^\infty \frac{\left(\omega^2/\kappa^2\right) d\omega}{\left(1 - \frac{\omega^2}{\omega_0^2}\right)^2 + \frac{\omega^2}{\omega_0^2 Q^2}} \tag{D.8}$$

which allows us to make the identification

$$J_{\dot{\theta}}(\omega) = \frac{4k_B T (2\beta I) \left(\omega^2/\kappa^2\right)}{\left(1 - \frac{\omega^2}{\omega_0^2}\right)^2 + \frac{\omega^2}{\omega_0^2 Q^2}}. \tag{D.9}$$

If we use this expression to rewrite Equation D.3, integrate over the time variables and let $\Delta t \to 0$, we obtain

$$\left\langle \phi^2(t) \right\rangle = \frac{1}{2\pi\theta_0^2} \int_0^\infty \frac{J_{\dot{\theta}}(\omega)(1 - \cos\omega t)}{\omega^2} d\omega \tag{D.10}$$

where we will take t to span an integer number of periods, N. Integration yields:

$$\left\langle \phi^2 \right\rangle_{N\ cycles} = \frac{\pi N k_B T}{\kappa Q \theta_0^2} \tag{D.11}$$

which leads to a corresponding timing uncertainty given by:

$$\left\langle \left(\frac{\Delta P}{P}\right)^2 \right\rangle \approx \frac{k_B T}{4\pi N \kappa Q \theta_0^2}. \tag{D.12}$$

Appendix E

The Effects of Fluid Oscillations

In order to calculate the forces exerted on an oscillating torsion balance by the fluid in which it is immersed, we must consider the time-dependent solutions to the the Navier-Stokes equation. The torsion balance used in the dynamic experiment is a thin spherical shell. Thus we want to consider the effects of both the external and internal volumes of fluid on the rotational and translational oscillations of the balance. Landau and Lifshitz have outlined the calculations and results for the external effects in both types of motion and the effect of the internal fluid on rotational oscillations [96, See the text and problems in Sections 20 and 24]. The calculation for the fourth case, a hollow sphere undergoing translational oscillations, will be described in some detail here and the results in the other three cases summarized.

E.1 A Summary of the Oscillatory Solutions

The primary characteristic of oscillatory solutions is the penetration depth of waves in the fluid

$$\delta = \sqrt{\frac{2\nu}{\omega}} \tag{E.1}$$

where ν is the kinematic viscosity of the fluid and ω is the frequency of the oscillations. For situations involving a sphere of radius R, the forces (torques) exerted on the sphere can be expressed in terms of the ratio R/δ.

We first consider the forces on a spherical shell, with fluid inside and out, of radius R undergoing translational oscillations. The force exerted on the sphere by the external fluid is

$$F = -6\pi\eta R\left(1+\frac{R}{\delta}\right)u - 3\pi R^2\sqrt{\frac{2\eta\rho}{\omega}}\left(1+\frac{2R}{9\delta}\right)\dot{u} \tag{E.2}$$

while that exerted by the internal fluid volume (See below) is

$$\begin{aligned} F &= 6\pi\eta R\left[1-\left(\frac{R}{\delta}\right)\frac{\sinh\left(\frac{2R}{\delta}\right)+\sin\left(\frac{2R}{\delta}\right)}{\cosh\left(\frac{2R}{\delta}\right)-\cos\left(\frac{2R}{\delta}\right)}\right]u \\ &\quad +3\pi R^2\sqrt{\frac{2\eta\rho}{\omega}}\left[\frac{2}{3}\left(\frac{R}{\delta}\right)-\frac{\sinh\left(\frac{2R}{\delta}\right)-\sin\left(\frac{2R}{\delta}\right)}{\cosh\left(\frac{2R}{\delta}\right)-\cos\left(\frac{2R}{\delta}\right)}\right]\dot{u} \end{aligned} \tag{E.3}$$

where $u = u_0 e^{-i\omega t}$ is the velocity of the sphere. The $\dot{u}$ terms represent inertial forces due to the mass of the gas (naturally these contributions are relatively small due to the low densities involved) while the u terms give the viscous damping. The situation of interest for our experiments corresponds to $R/\delta \gg 1$. In this limit we see that the viscous damping on a translational mode is

$$F_{viscous} = -6\pi\eta R\left(\frac{2R}{\delta}\right)u \tag{E.4}$$

which can greatly exceed the Stokes' Law value, $6\pi\eta Ru$, valid for a sphere in uniform motion.

For a spherical shell undergoing rotational oscillations, the torque exerted by the external fluid is

$$T = -8\pi\eta R^3\Omega\left[\frac{1+\frac{2R}{\delta}+2\left(\frac{R}{\delta}\right)^2+\frac{2}{3}\left(\frac{R}{\delta}\right)^3-\frac{2i}{3}\left(\frac{R}{\delta}\right)^2\left(1+\frac{R}{\delta}\right)}{1+\frac{2R}{\delta}+2\left(\frac{R}{\delta}\right)^2}\right] \tag{E.5}$$

while the torque from the internal fluid is

$$T = -8\pi\eta R^3\Omega\left(\frac{\sin kR - kR\cos kR - \frac{k^2R^2}{3}\sin kR}{kR\cos kR - \sin kR}\right) \tag{E.6}$$

where $k = (1+i)/\delta$ and the angular velocity of the balance is $\Omega = \Omega_0 e^{-i\omega t}$. The real parts of these expressions give the viscous damping forces while the imaginary parts represent inertial torques due to the induced rotation of the fluid. For the torsion mode of our balances, we are primarily interested in the regime with $R/\delta < 1$. Hence we write the total viscous damping force as

$$T = -8\pi\eta R^3\Omega \left[\frac{1 + \frac{2R}{\delta} + 2\left(\frac{R}{\delta}\right)^2 + \frac{2}{3}\left(\frac{R}{\delta}\right)^3}{1 + \frac{2R}{\delta} + 2\left(\frac{R}{\delta}\right)^2} + \frac{4}{525}\left(\frac{R}{\delta}\right)^4 \right] \tag{E.7}$$

where the last term is due to the internal fluid. We note that, as we are primarily interested in the limit $\omega \to 0$ (*i.e.*, we are primarily interested in the regime with $R/\delta \to 0$), damping from the internal fluid disappears as that volume co-rotates with the sphere while damping from the external fluid approaches the steady-state value of $8\pi\eta R^3\Omega$.

E.2 Fluid Oscillations Within a Hollow Sphere

The following treatment closely parallels the related calculations in Reference 96. We work in the limit of small Reynolds' number (a reasonable approximation for the pendulum and vertical oscillation modes of our torsion balances) which allows us to ignore the convective derivative term in the complete Navier-Stokes equation. Thus we are left with

$$\frac{\partial \vec{v}}{\partial t} = \frac{-\vec{\nabla} p}{\rho} + \nu \nabla^2 \vec{v} \tag{E.8}$$

where $\vec{v}$, p, ρ and ν are the fluid velocity, pressure, density and kinematic viscosity, respectively. We also treat the fluid as incompressible. Taking the curl of both sides of Equation E.8 gives the differential equation for the fluid velocity

$$\vec{\nabla} \times \frac{\partial \vec{v}}{\partial t} = \nu \left(\vec{\nabla} \times \nabla^2 \vec{v} \right). \tag{E.9}$$

Now we take the velocity of the sphere to be of the form

$$\vec{u} = \vec{u}_0 e^{-i\omega t} \tag{E.10}$$

and work in the frame where $r = 0$ is the instantaneous position of the sphere's center. We look for a solution, $\vec{v}(\vec{r})$, of the form[1]

$$\vec{v} = e^{-i\omega t}\vec{\nabla} \times \vec{\nabla} \times (f\vec{u}_0) \tag{E.11}$$

where f is a function only of the radial coordinate. Substitution of E.11 into E.9 yields

$$\left(\Delta^2 + \frac{2i}{\delta^2}\Delta\right)\vec{\nabla} f = 0 \tag{E.12}$$

where we recall from above that $\delta = \sqrt{\frac{2\nu}{\omega}}$ is the penetration depth of waves in the fluid. Integrating once then gives

$$\left(\Delta^2 + \frac{2i}{\delta^2}\Delta\right) f = constant \tag{E.13}$$

Since there is no steady state contribution to the velocity inside the sphere, we may immediately set the constant to zero. Letting

$$g = \Delta f, \tag{E.14}$$

we solve the differential equation and take the solution which is well-behaved at the origin. This gives

$$g(r) = \frac{A}{r}\sin kr \tag{E.15}$$

[1]This form is completely specified by the nature of $\vec{v}$ and $\vec{u}$. As described in Reference 96, p. 59, since both quantities are divergenceless, their difference can be written as the curl of another vector, $\vec{A}$. The velocities are polar vectors so $\vec{A}$ must be axial. The only characteristic direction in the problem is $\vec{u}$. Thus the only axial vector, linear in $\vec{u}$, which can be formed is

$$\vec{\nabla} f \times \vec{u}$$

where f is a function only of the radial coordinate. Some manipulation then yields Equation E.11.

where $k = (1+i)/\delta$ and A is a constant. Substituting back into Equation E.14, and noting that only the derivatives of f enter into the velocity, we write

$$\frac{\partial f'}{\partial r} + \frac{2}{r} f' = \frac{A}{r} \sin kr, \tag{E.16}$$

which yields

$$f'(r) = \frac{1}{r^2}\left[\frac{A}{k^2}(\sin kr - kr\cos kr) + B\right] \tag{E.17}$$

where B is a constant. Now, using E.11, the fluid velocity may be written as

$$\begin{aligned} \vec{v} &= e^{-i\omega t}\left\{\frac{\vec{u}_0}{r}\left[A\left(\frac{1}{k^2r^2}-1\right)\sin kr - \frac{A}{kr}\cos kr + \frac{B}{r^2}\right]\right. \\ &\left. + \frac{\vec{r}\,(\vec{u}_0\cdot\vec{r})}{r^3}\left[A\left(1-\frac{3}{k^2r^2}\right)\sin kr + \frac{3A}{kr}\cos kr - \frac{3B}{r^2}\right]\right\}. \end{aligned} \tag{E.18}$$

Matching the boundary conditions at $r = R$ specifies the constants of integration as:

$$\begin{aligned} A &= -\frac{3R}{2\sin kR} \\ B &= -R^3\left[\left(\frac{1}{2}-\frac{3}{2k^2R^2}\right) + \frac{3\cos kR}{2kR\sin kR}\right] \end{aligned} \tag{E.19}$$

Substituting $\vec{v}$ into E.8 lets us write the pressure in the fluid as

$$p(\vec{r},t) = p_0 + \frac{iB\omega\rho}{r^2}(\vec{u}_0\cdot\vec{r})\,e^{-i\omega t}. \tag{E.20}$$

Armed with expressions for the velocity and pressure, we can now calculate the forces exerted on the spherical surface by the fluid with a suitable integration over the components of the fluid stress tensor, σ. The force on the surface at radius R is given by

$$F = \oint_S (\sigma_{rr}\cos\theta - \sigma_{r\theta}\sin\theta)ds \tag{E.21}$$

where

$$\sigma_{rr} = -p + 2\eta\frac{\partial v_r}{\partial r} \tag{E.22}$$

and

$$\sigma_{r\theta} = \eta \left(\frac{1}{r}\frac{\partial v_r}{\partial \theta} + \frac{\partial v_\theta}{\partial r} - \frac{v_\theta}{r} \right). \tag{E.23}$$

Carrying out the integration yields

$$F = 6\pi\eta R u_0 e^{-i\omega t} \left[1 - (1+i)\left(\frac{R}{\delta}\right)\frac{\cos kR}{\sin kR} - \frac{2i}{3}\left(\frac{R}{\delta}\right)^2 \right] \tag{E.24}$$

Separating this into real and complex parts gives

$$\begin{aligned} [\,] \;\rightarrow\; & 1 - \left(\frac{R}{\delta}\right)\frac{\sinh\left(\frac{2R}{\delta}\right) + \sin\left(\frac{2R}{\delta}\right)}{\cosh\left(\frac{2R}{\delta}\right) - \cos\left(\frac{2R}{\delta}\right)} \\ & + i\left[\left(\frac{R}{\delta}\right)\frac{\sinh\left(\frac{2R}{\delta}\right) - \sin\left(\frac{2R}{\delta}\right)}{\cosh\left(\frac{2R}{\delta}\right) - \cos\left(\frac{2R}{\delta}\right)} - \frac{2}{3}\left(\frac{R}{\delta}\right)^2\right] \end{aligned} \tag{E.25}$$

where the real part of the expression gives the viscous damping force and the imaginary part represents an inertial correction due to accelerating the mass of the fluid. The inertial corrections are intrinsically small and can be ignored for our purposes. If we consider the limiting case of $R/\delta \gg 1$, the damping force exerted on the sphere is given by

$$F_{viscous} \rightarrow -6\pi\eta R u \left(\frac{R}{\delta}\right), \qquad \frac{R}{\delta} \gg 1. \tag{E.26}$$

For $R/\delta \rightarrow 0$, taking the limiting value of the second term in E.25 gives

$$F_{viscous} \rightarrow 0. \tag{E.27}$$

These results agree with our intuition. For penetration depths which are much larger than the size of the sphere, the internal fluid moves with the sphere and there is no damping. For small penetration depths, however, energy imparted to the fluid in the form of wave motion is rapidly dissipated within the fluid volume resulting in significant viscous drag.

Appendix F

Scaling of the Nonlinearity

This appendix estimates how the nonlinearity associated with a $|\phi|^3$ term in the torsion potential scales with the size of the fiber. We can estimate the scaling in analogy with the standard calculation of the torsion constant of a cylindrical fiber. We consider the stress in a thin cylindrical shell due to twisting the ends at an angle ϕ relative to each other. In the linear approximation we have

$$S = \mu \frac{r\phi}{L} \tag{F.1}$$

where μ is the shear modulus and r and L are the radius and length of the shell, respectively. We consider the case where the shear is of the form

$$S = \mu \frac{r\phi}{L} + \lambda \left(\frac{r}{L}\right)^2 |\phi|\, \phi. \tag{F.2}$$

The corresponding torque on a solid cylinder is then given by

$$T = \int_0^r r S dA = 2\pi \int_0^r r^2 S dr. \tag{F.3}$$

Integrating yields

$$T = \frac{\pi \mu r^4}{2L} \phi + \frac{2\pi \lambda r^5}{5L^2} |\phi|\, \phi \tag{F.4}$$

We can now identify κ and α as the coefficients of ϕ and $|\phi|\, \phi$. The nonlinear dependence is then characterized by

$$\frac{\alpha}{\kappa} = \frac{4\lambda r}{5\mu L} \tag{F.5}$$

Thus the nonlinearities should scale roughly as r/L of the torsion fiber.

Bibliography

[1] R.V. Wagoner, Physical Review D **1** (1970) 3209–3216.

[2] Y. Fujii, Nature **234** (1971) 5–7.

[3] Y. Fujii, Annals of Physics **69** (1972) 494–521.

[4] J. O'Hanlon, Physical Review Letters **29** (1972) 137–138.

[5] Y. Fujii, Physical Review D **9** (1974) 874–876.

[6] J. Scherk, in Supergravity, ed. P. van Nieuwenhúizen and D.Z. Freedman, (North-Holland Publishing Company, Amsterdam, 1979), pp. 43–51.

[7] J. Scherk, Physics Letters **88B** (1979) 265–267.

[8] J. Scherk, in Unification of the Fundamental Particle Interactions, ed. S. Ferrara, J. Ellis and P. van Nieuwenhuizen, (Plenum Press, New York, 1980), pp. 381–409.

[9] D.R. Mikkelsen and M.J. Newman, Physical Review D **16** (1977) 919–926.

[10] D.R. Long, Nature **260** (1976) 417–418.

[11] V.I. Panov and V.N. Frontov, Soviet Physics JETP **50** (1979) 852–856.

[12] R. Spero, J.K. Hoskins, R.D. Newman, J. Pellam and J. Schultz, Physical Review Letters **44** (1980) 1645–1648.

[13] F.D. Stacey and G.J. Tuck, Nature **292** (1981) 230–232.

[14] S.C. Holding and G.J. Tuck, Nature **307** (1984) 714–716.

[15] J.K. Hoskins, R.D. Newman, R. Spero and J. Schultz, Physical Review D **32** (1985) 3084–3095.

[16] E. Fischbach, D. Sudarsky, A. Szafer, C. Talmadge and S. H. Aronson, Physical Review Letters **56** (1986) 3–6.

[17] R.v. Eötvös, D. Pekár and E. Fekete, Annalen der Physik (Leipzig) **68** (1922) 11–66.

[18] P.G. Roll, R.V. Krotkov and R. H. Dicke, Annals of Physics **26** (1964) 442–517.

[19] V. B. Braginsky and V. I. Panov, Soviet Physics JETP **34** (72) 463–466.

[20] Isaac Newton, Philosophiae Naturalis Principia Mathematica, 1687, as translated in *Newton's Principia and Newton's System of the World*, 1st American Edition of the translation by Andrew Motte, (Daniel Adee, New York, 1846).

[21] Albert Einstein, in The Principle of Relativity, ed. W. Perrett and G. B. Jeffery, (Dover Publications, Inc., Toronto, Canada, 1952), pp. 109–164.

[22] S. Weinberg, Gravitation and Cosmology: Principles and Applications of the General Theory of Relativity, (John Wiley and Sons, Inc., New York, 1972).

[23] The Laws of Gravitation: Memoirs by Newton, Bouguer and Cavendish, ed. A.S. Mackenzie, (American Book Company, New York, 1900).

[24] G.G. Luther and W.R. Towler, Physical Review Letters **48** (1982) 121–123.

[25] G.W. Gibbons, B.F. Whiting, Nature **291** (1981) 636–638.

[26] F.D. Stacey, Science Progress **69** (1984) 1–17.

[27] A. De Rújula, Physics Letters B **180** (1986) 213–220.

[28] C. Talmadge, J.-P. Berthias, R.W. Hellings and E. M. Standish, Physical Review Letters **61** (1988) 1159–1162.

[29] S. H. Aronson, G.J. Bock, H.-Y. Cheng and E. Fischbach, Physical Review Letters **48** (1982) 1306–1309.

[30] E. Fischbach, H.-Y. Cheng, S.H. Aronson and G.J. Bock, Physics Letters **116B** (1982) 73–76.

[31] S.H. Aronson, G.J. Bock, H.-Y. Cheng and E. Fischbach, Physical Review D **28** (1983) 476–494.

[32] S.H. Aronson, G.J. Bock, H.-Y. Cheng and E. Fischbach, Physical Review D **28** (1983) 495–523.

[33] L. Bod, E. Fischbach, G. Marx and Maria Náray-Ziegler, Acta Physica Hungarica **69** (1991) 335–355.

[34] D.H. Eckhardt, Physical Review Letters **57** (1986) 2868.

[35] M. Milgrom, Nuclear Physics **B277** (1986) 509–512.

[36] P. Thieberger, Physical Review Letters **56** (1986) 2347–2349.

[37] E. Fischbach, D. Sudarsky, A. Szafer, C. Talmadge and S.H. Aronson, Physical Review Letters **56** (1986) 2424.

[38] E.Fischbach, D. Sudarsky, A. Szafer, C. Talmadge and S.H.Aronson, Annals of Physics **182** (1988) 1–89.

[39] H.H. Thodberg, Physical Review Letters **56** (1986) 2423.

[40] P.T. Keyser, T.M. Niebauer, J.E. Faller, Physical Review Letters **56** (1986) 2425.

[41] S.Y. Chu and R.H. Dicke, Physical Review Letters **57** (1986) 1823–1824.

[42] E. Fischbach, C. Talmadge and S.H. Aronson, Physical Review Letters **57** (1986) 2869.

[43] H. Cavendish, Philosophical Transactions of the Royal Society of London (1798) 469–526, as reproduced in *The Laws of Gravitation*, ed. A.S. Mackenzie, (American Book Company, New York, 1900).

[44] C.V. Boys, Philosophical Transactions of the Royal Society of London (A) **186** (1895) 1–72.

[45] R.H. Dicke, Physical Review **126** (1962) 1875–1877.

[46] P. Jordan, Zeitschrift für Physik **157** (1959) 112–121.

[47] C. Brans and R.H. Dicke, Physical Review **124** (1961) 925–935.

[48] R.H. Dicke, Physical Review **125** (1961) 2163–2167.

[49] R.H. Dicke, Physical Review **126** (1962) 1580–1581.

[50] R.H. Dicke, in Evidence for Gravitational Theories, Proceedings of the International School of Physics "Enrico Fermi", Course XX, ed. C. Moller, (Academic Press, Villa Monastero, 1962), pp. 1–49.

[51] R.D. Peccei, J. Solà and C. Wetterich, Physics Letters B **195** (1987) 183–190.

[52] S. Weinberg, Physical Review Letters **40** (1978) 223–226.

[53] F. Wilczek, Physical Review Letters **40** (1978) 279–282.

[54] E.W. Kolb and M.S. Turner, The Early Universe, (Addison-Wesley Publishing Company, Redwood City, CA, 1990).

[55] J.M. Pendlebury, K.F. Smith, R. Golub, J. Byrne, T.J.L. McComb, T.J. Sumner, S.M. Burnett, A.R. Taylor, B. Heckel, N.F. Ramsey, K. Green, J. Morse, A.I. Kilvington, C.A. Baker, S. A. Clark, W. Mampe, P. Ageron and P.C. Miranda, Physics Letters **136B** (1984) 327–330.

[56] J.E. Moody and F. Wilczek, Physical Review D **30** (1984) 130–138.

[57] J.E. Moody, Axion Forces, Gravity Experiments and T Violation, Ph.D. thesis, Princeton University, 1984.

[58] D. Chang, R.N. Mohapatra and S. Nussinov, Physical Review Letters **55** (1985) 2835–2838.

[59] T.R. Taylor and G. Veneziano, Physics Letters B **213** (1988) 450–454.

[60] R.D. Peccei, Cosmons and Fifth Forces, 1988, Unpublished.

[61] T.D. Lee and C.N. Yang, Physical Review **98** (1955) 1501.

[62] C.N. Yang and R. Mills, Physical Review **96** (1954) 191–195.

[63] Y. Néeman, Physical Review **134** (1964) 1355–1357.

[64] J. Bernstein, N. Cabibbo and T.D. Lee, Physics Letters **12** (1964) 146–148.

[65] J.S. Bell and J.K. Perring, Physical Review Letters **13** (1964) 348–349.

[66] S. Weinberg, Physical Review Letters **13** (1964) 495–497.

[67] S. Weinberg, Physics Letters **9** (1964) 357–359.

[68] S. Weinberg, Physical Review **135** (1964) 1049–1056.

[69] S. H. Aronson, E. Fischbach, D. Sudarsky and C. Talmadge, in Festi-Val—Festschrift for Val Telegdi, ed. K. Winter, (Elsevier, New York, 1988), pp. 1–16.

[70] M.S. Atiya, I.-H. Chiang, J.S. Frank, J.S. Haggerty, M.M. Ito, T.F.Kycia, K.K. Li, L.S. Littenberg, A. Sambamurti, A. Stevens, R.C. Strand, W.C. Louis, D.S. Akerib, D.R. Marlow, P.D. Meyers, M.A. Selen, F.C. Shoemaker, A.J.S. Smith, E.W. Blackmore, D.A. Bryman, L. Felawka, P. Kitching, A. Konaka, Y. Kuno, J.A. Macdonald, T. Numao, P. Padley, J.-M. Poutissou, J. Roy, R. Soluk and A.S. Turcot, Physical Review Letters **70** (1993) 2521–2524.

[71] S.H. Aronson, E. Fischbach, D. Sudarsky and C. Talmadge, in 5th Force-Neutrino Physics, Proceedings of the XXIIIrd Rencontre de Moriond, ed. O. Fackler and J. Trân Thanh Vân, (Editions Frontières, Gif-sur-Yvette, 1988), pp. 593–602.

[72] P. Fayet, Physics Letters **69B** (1977) 489–494.

[73] P. Fayet, Physics Letters **84B** (1979) 417–420.

[74] P. Fayet, Physics Letters **95B** (1980) 285–289.

[75] P. Fayet, Physics Letters B **171** (1986) 261–266.

[76] P. Fayet, Physics Letters B **172** (1986) 363–368.

[77] P. Fayet, in Tests of Fundamental Laws of Physics, Proceedings of the XXIVth Rencontre de Moriond, ed. O. Fackler and J. Trân Thanh Vân, (Editions Frontières, Gif-sur-Yvette, 1989), pp. 561–587.

[78] I. Bars and M. Visser, Physical Review Letters **57** (1986) 25–28.

[79] M.M. Nieto, T. Goldman and R.J. Hughes, in New and Exotic Phenomena, Proceedings of the XXIInd Rencontre de Moriond, ed. O. Fackler and J. Trân Thanh Vân, (Editions Frontières, Gif-sur-Yvette, 1987), pp. 613–619.

[80] M.M. Nieto, T. Goldman and R.J. Hughes, Physical Review D **36** (1987) 3684–3687.

[81] M.M. Nieto, T. Goldman and R.J. Hughes, Physical Review D **36** (1987) 3688–3693.

[82] M.M. Nieto and T. Goldman, Physics Reports **205** (1991) 221–281.

[83] E.G. Adelberger, B.R. Heckel, D.W. Stubbs and Y. Su, Physical Review Letters **66** (1991) 850–853.

[84] J. Strong, Procedures in Experimental Physics, (Prentice-Hall, Inc., New York, 1945).

[85] CRC Handbook of Chemistry and Physics, ed. R.C. Weast, (CRC Press, Inc., Boca Raton, Florida, 63rd edition, 1982).

[86] Handbook of Materials and Processes for Electronics, pp. 9.48–9.49, ed. Charles A. Harper, (McGraw-Hill, New York, 1970).

[87] Practical Handbook of Materials Science, p. 274, ed. Charles T. Lynch, (CRC Press, Inc., Boca Raton, Florida, 1989).

[88] P.E. Boynton, in 5th Force Neutrino Physics, Proceedings of the XXIIIrd Rencontre de Moriond, ed. O. Fackler and J. Trân Thanh Vân, (Editions Frontières, Gif-sur-Yvette, 1988), pp. 431–444.

[89] H.B. Callen and T.A. Welton, Physical Review **83** (1951) 34–40.

[90] Metals Handbook, ed. H.E. Boyer and T.L. Gall, (American Society for Metals, Metals Park, Ohio, 1985).

[91] V.L. Fitch, M.V. Isaila and M.A. Palmer, Physical Review Letters **60** (1988) 1801–1804.

[92] J.L. Wooden, P.A. Mueller, D.K. Hunt and D.R. Bowes, Montana Bureau of Mines and Geology Special Publication 84, 1982, p. 45.

[93] P.A. Mueller, J.L. Wooden, A.L. Odom and D.R. Bowes, Montana Bureau of Mines and Geology Special Publication 84, 1982, p. 69.

[94] R.B. Berg, D.C. Lawson, F.P. Jones and R.I. Smith, Progress Report on Clays and Shales of Montana, 1968–1969, (Samples 636 to 727).

[95] Well logs from the area were obtained from Petroleum Information, Log Division, Denver, Colorado.

[96] L.D. Landau and E.M. Lifshitz, Fluid Mechanics, volume 6 of *Course of Theoretical Physics*, (Pergamon Press, Oxford, second edition, 1987).

[97] S. Strong, Measuring Asymmetries of a Spherical Mass Shell, Princeton University Physics Dept. Generals Project, unpublished, 1989.

[98] J.B. Marion, Classical Dynamics of Particles and Systems, (Academic Press, New York, 1970).

[99] E.G. Adelberger, C.W. Stubbs, B.R. Heckel, Y. Su, H.E. Swanson, G. Smith, J.H. Gundlach and W.F. Rogers, Physical Review D **42** (1990) 3267–3292.

[100] H.J. Paik, Physical Review D **19** (1979) 2320–2324.

[101] H. A. Chan, M.V. Moody and H.J. Paik, Physical Review Letters **49** (1982) 1745–1748.

[102] M.V. Moody, H. A. Chan and H.J. Paik, Journal of Applied Physics **60** (1986) 4308–4315.

[103] H.J. Paik, Q. Kong, M.V. Moody and J.W. Parke, in 5th Force-Neutrino Physics, Proceedings of the XXIIIrd Rencontre de Moriond, ed. O. Fackler and J. Trân Thanh Vân, (Editions Frontières, Gif-sur-Yvette, 1988), pp. 531–547.

[104] M.V. Moody and H.J. Paik, Physical Review Letters **70** (1993) 1195–1198.

[105] I. Marson and J.E. Faller, Journal of Physics E **19** (1986) 22–32.

[106] G.I. Moore, F.D. Stacey, G.J. Tuck, B.D. Goodwin and A. Roth, Journal of Physics E: Scientific Instruments **21** (1988) 534–539.

[107] G.I. Moore, F.D. Stacey, G.J. Tuck, B.D. Goodwin, N.P. Linthorne, M.A. Barton, D.M. Reid and G.D. Agnew, Physical Review D **38** (1988) 1023–1029.

[108] G. Müller, W. Zürn, K. Lindner and N. Rösch, Physical Review Letters **63** (1989) 2621–2624.

[109] J. Thomas, Physical Review D **40** (1989) 1735–1740.

[110] A.J. Romaides, C. Jekeli, A.R. Lazarewicz, D.H. Eckhardt and R.W. Sands, Journal of Geophysical Research **94** (1989) 1563–1572.

[111] J.D. Jackson, Classical Electrodynamics, (John Wiley and Sons, Inc., New York, 1962).

[112] W.A. Heiskanen, H. Moritz, Physical Geodesy, (W.H. Freeman and Company, San Francisco, 1967).

[113] D.H. Eckhardt, C. Jekeli, A.R. Lazarewicz, A.J. Romaides and R.W. Sands, Physical Review Letters **60** (1988) 2567–2570.

[114] D.H. Eckhardt, C. Jekeli, A.R. Lazarewicz, A.J. Romaides and R.W. Sands, in 5th Force-Neutrino Physics, Proceedings of the XXIIIrd Rencontre de Moriond, ed. O. Fackler and J. Trân Thanh Vân, (Editions Frontières, Gif-sur-Yvette, 1988), pp. 577–583.

[115] D.F. Bartlett and W.L. Tew, in Tests of Fundamental Laws of Physics, Proceedings of the XXIVth Rencontre de Moriond, ed. O. Fackler and J. Trân Thanh Vân, (Editions Frontières, Gif-sur-Yvette, 1989), pp. 543–548.

[116] C. Jekeli, D.H. Eckhardt and A.J. Romaides, Physical Review Letters **64** (1990) 1204–1206.

[117] J. Thomas, P. Kasameyer, O. Fackler, D. Felske, R. Harris, J. Kammeraad, M. Millett and M. Mugge, Physical Review Letters **63** (1989) 1902–1905.

[118] C.C. Speake, T.M. Niebauer, M.P. McHugh, P.T. Keyser, J.E. Faller, J.Y.Cruz, J.C. Harrison, J. Mäkinen and R.B. Beruff, in New and Exotic Phenomena '90, Proceedings of the XXVth Rencontre de Moriond, ed. O. Fackler and J. Trân Thanh Vân, (Editions Frontières, Gif-sur-Yvette, 1990), pp. 255–262.

[119] C.C. Speake, T.M. Niebauer, M.P. McHugh, P.T. Keyser, J.E. Faller, J.Y. Cruz, J.C. Harrison, J. Mäkinen and R.B. Beruff, Physical Review Letters **65** (1990) 1967–1971.

[120] S.C. Holding, F.C. Stacey and G.J. Tuck, Physical Review D **33** (1986) 3487–3494.

[121] F.D. Stacey, G.J. Tuck and G.I. Moore, Journal of Geophysical Research **93** (1988) 10,575–10,587.

[122] E.G. Adelberger, in General Relativity and Gravitation, 1989, Proceedings of the 12th International Conference on General Relativity and Gravitation, ed. N. Ashby, D.F. Bartlett and W. Wyss, (Cambridge University Press, Cambridge, 1990), pp. 273–294.

[123] J.E. Faller, in General Relativity and Gravitation, 1989, Proceedings of the 12th International Conference on General Relativity and Gravitation, ed. N. Ashby, D.F. Bartlett and W. Wyss, (Cambridge University Press, Cambridge, 1990), pp. 345–348.

[124] A.T. Hsui, Science **237** (1987) 881–882.

[125] M.E. Ander, M.A. Zumberge, T.V. Lautzenhiser, R.L. Parker, C.L.V. Aiken, M.R. Gorman, M.M. Nieto, A.P.R. Cooper, J.F. Ferguson, E. Fisher, G.A. McMechan, G.S. Sasagawa, J.M. Stevenson, G. Backus, A.D. Chave, J. Greer, P. Hammer, B.L. Hansen, J.A. Hildebrand, J.R. Kelty, C. Slides and J. Wirtz, Physical Review Letters **62** (1989) 985–988.

[126] J. Thomas, R.Vogel and P. Kasameyer, in 5th Force-Neutrino Physics, Proceedings of the XXIIIrd Rencontre de Moriond, ed. O. Fackler and J. Trân Thanh Vân, (Editions Frontières, Gif-sur-Yvette, 1988), pp. 585–592.

[127] J. Thomas and P. Vogel, Physical Review Letters **65** (1990) 1173–1176.

[128] M.A. Zumberge, J.A. Hildebrand, J.M. Stevenson, R.L. Parker, A.D. Chave, M.E. Ander and F.N. Spiess, Physical Review Letters **67** (1991) 3051–3054.

[129] E.G. Adelberger, C.W. Stubbs, W.F. Rogers, F.J. Raab, B.R. Heckel, J.H. Gundlach, H.E. Swanson and R. Watanabe, Physical Review Letters **59** (1987) 849–852.

[130] K. Kuroda and N. Mio, Physical Review D **42** (1990) 3903–3907.

[131] T.M. Niebauer, M.P. McHugh and J.E. Faller, Physical Review Letters **59** (1987) 609–612.

[132] S. Carusotto, V. Cavasinni, A. Mordacci, F. Perrone, E. Polacco, E. Iacopini and G. Stefanini, Physical Review Letters **69** (1992) 1722–1725.

[133] C.W. Stubbs, E.G. Adelberger, F.J. Raab, J.H. Gundlach, B.R. Heckel, K.D. McMurry, H.E. Swanson and R. Watanabe, Physical Review Letters **58** (1987) 1070–1073.

[134] B.R. Heckel, E.G. Adelberger, C.W. Stubbs, Y. Su, H.E. Swanson, G. Smith and W.F. Rogers, Physical Review Letters **63** (1989) 2705–2708.

[135] P.E. Boynton, D. Crosby, P. Ekstrom and A. Szumilo, Physical Review Letters **59** (1987) 1385–1389.

[136] P.E. Boynton and S.H. Aronson, in New and Exotic Phenomena '90, Proceedings of the XXVth Rencontre de Moriond, ed. O. Fackler and J. Trân Thanh Vân, (Editions Frontières, Gif-sur-Yvette, 1990), pp. 207–224.

[137] R. Cowsik, N. Krishnan, S.N. Tandon and S. Unnikrishnan, Physical Review Letters **64** (1990) 336–339.

[138] R. Cowsik, in 5th Force-Neutrino Physics, Proceedings of the XXIIIrd Rencontre de Moriond, ed. O. Fackler and J. Trân Thanh Vân, (Editions Frontières, Gif-sur-Yvette, 1988), pp. 481–488.

[139] R. Cowsik, N. Krishnan, S.N. Tandon and C.S. Unnikrishnan, Physical Review Letters **61** (1988) 2179–2181.

[140] C.W. Stubbs, E.G. Adelberger, B.R. Heckel, W.F. Rogers, H.E. Swanson, R. Watanabe, J.H. Gundlach and F.J. Raab, Physical Review Letters **62** (1989) 609–612.

[141] P.G. Nelson, D.M. Graham and R.D. Newman, Physical Review D **42** (1990) 963–976.

[142] L.B. Kreuzer, Physical Review **169** (1968) 1007–1012.

[143] D.A. Neufeld, Physical Review Letters **56** (1986) 2344–2346.

[144] C.C. Speake and T.J. Quinn, Physical Review Letters **61** (1988) 1340–1343.

[145] P. Thieberger, Physical Review Letters **58** (1987) 1066–1069.

[146] H.J. Maris, Physical Review Letters **60** (1988) 964.

[147] P. Thieberger, Physical Review Letters **60** (1988) 965.

[148] P.T. Keyser, Physical Review Letters **62** (1989) 2332.

[149] P. Thieberger, Physical Review Letters **62** (1989) 2333.

[150] P.G. Bizzeti, A.M. Bizzeti-Sona, T. Fazzini, A. Perego and N. Taccetti, Physical Review Letters **62** (1989) 2901–2904.

[151] E.G. Adelberger, B.R. Heckel, C.W. Stubbs and W.F. Rogers, Annual Review of Nuclear and Particle Science **41** (1991) 269–320.

[152] E. Fischbach, G.T. Gillies, D.E. Krause, J.G. Schwan and C. Talmadge, Metrologia **29** (1992) 213–260.

[153] R.D. Newman, in Proceedings of the Third Marcel Grossmann Meeting on General relativity, ed. N. Hu, (Science Press and North-Holland Publishing Company, Amsterdam, 1983), pp. 755–769.

[154] Handbook of Physics, pp. 65–87, ed. E.U. Condon and H. Odishaw, (McGraw-Hill, New York, 1967).

[155] A. Yariv, Optical Electronics, (Holt, Rinehart and Winston, New York, 1985).

[156] M.J. Buckingham, Noise in Electronic Devices and Systems, (Ellis Horwood Limited, Chichester, 1983).